

Advanced Space Concepts Laboratory  
Department of Mechanical and Aerospace Engineering  
University of Strathclyde, Glasgow, Scotland, United Kingdom

# PRELIMINARY DESIGN METHODOLOGIES FOR HYBRID PROPULSION TRAJECTORIES

Steven Robert Owens

Submitted in fulfilment of the requirements for

the degree of Doctor of Philosophy

2014

# DECLARATION OF AUTHENTICITY AND AUTHOR'S RIGHTS

This thesis is the result of the author's original research. It has been composed by the author and has not been previously submitted for examination which has led to the award of a degree.

The copyright of this thesis belongs to the author under the terms of the United Kingdom Copyright Acts as qualified by University of Strathclyde Regulation 3.50. Due acknowledgement must always be made of the use of any material contained in, or derived from, this thesis.

Signed:

A handwritten signature in black ink, appearing to read 'Henry Jones', written over a faint dotted grid background.

Date: 02/09/2014

# ACKNOWLEDGEMENTS

Pursuing this PhD is an adventure I could not have enjoyed without the support and help of many people. Firstly I would like to thank my supervisor Dr Malcolm Macdonald for providing research ideas and his support and guidance throughout the entire process. I would also like to thank my fellow colleagues for their contribution and advice when I've needed it.

For financial support, I would like to thank the Scottish Funding Council for funding my PhD and conference travel expenses over the course of three years. Additionally, I would like to thank the following bodies in no particular order for support in helping me present my research at international conferences: The Institution of Mechanical Engineers (x2 awards), Royal Aeronautical Society (x1), The Institution of Engineering and Technology (x1) and the European Space Agency (x1).

I would also like to thank all my friends and family for their continued support and interest in my work. A massive thank you is due to my parents and sister for supporting me in everything I have done: Thank you for being fantastic and always encouraging me to reach for the stars, I will be eternally grateful and I hope I have made you proud. Finally I would like to thank Alison who has been my rock throughout this whole endeavour. Words cannot express my appreciation and the support I feel with you by my side. This is your achievement also as without you and the sacrifices you have made to allow me to pursue my dream, this could not have happened. I look forward to the future and many more adventures together.

# ABSTRACT

In this dissertation, the Hohmann and bi-elliptic transfers are considered with the inclusion of a plane change. The evolution of critical limits which determine the transfer offering the lowest velocity requirement, previously defined for a co-planar analysis, is shown with the inclusion of a plane change. This has not been possible in previous work as analyses have been dependent on the intermediate orbit and numerical optimisation of the plane change distribution between impulses. It is shown that the critical limits found for the co-planar analysis reduce at different rates with increasing plane change and converge on a point where both transfers offer the same velocity requirement for a given final to initial orbit ratio and plane change. Between the two limits the Area Of Uncertainty (AOU) found for the co-planar analysis is shown to reduce to the convergence point which beyond, a second AOU emerges. A detailed analysis of these critical limits, determining when each transfer should be used is performed and a simple figure is presented which would allow a mission designer to select the fuel optimal transfer dependent on the final to initial orbit ratio and plane change only. The dissertation then introduces a novel orbit transfer using both high and low-thrust propulsion systems to accommodate the current development of platforms with this technology on-board. An analytical model is created which determines when the system offers a fuel mass saving compared to a single propulsion high-thrust only transfer. In addition to this, a critical limit analysis is performed which determines the limitations of analytical models based on a quasi-circular assumption. This analysis is developed into a numerical optimisation procedure which extends the application of the transfer to allow for eccentric orbits throughout the duration of the low-thrust phase. Case studies are presented which demonstrate substantial fuel mass savings compared to the single propulsion transfer: the largest fuel mass saving is found to be 27% of the spacecraft wet mass for a transfer from a Sun-Synchronous Orbit to a highly elliptical polar orbit.

# TABLE OF CONTENTS

DECLARATION OF AUTHENTICITY AND AUTHOR'S RIGHTS .....	I
ACKNOWLEDGEMENTS .....	II
ABSTRACT .....	III
TABLE OF CONTENTS .....	IV
LIST OF ACRONYMS.....	IX
LIST OF SYMBOLS .....	X
LIST OF FIGURES.....	XVII
LIST OF TABLES .....	XXV
CHAPTER 1 .....	1
INTRODUCTION.....	1
1.1. BACKGROUND .....	1
1.2. THESIS OBJECTIVES .....	2
1.3. CONTRIBUTION TO KNOWLEDGE .....	2
1.4. PUBLISHED WORK .....	3
CHAPTER 2 .....	5
LITERATURE REVIEW.....	5
2.1. HIGH-THRUST TRANSFERS.....	6

2.2.	LOW-THRUST TRANSFERS.....	15
2.3.	HYBRID PROPULSION TRANSFERS.....	17
2.4.	HIGH-THRUST PROPULSION SYSTEMS.....	19
2.5.	LOW-THRUST PROPULSION SYSTEMS.....	21
2.6.	LOW-THRUST TRAJECTORY DESIGN.....	26
2.7.	HYBRID PROPULSION TRAJECTORY OPTIMISATION.....	37
CHAPTER 3.....		39
HOHMANN AND BI-ELLIPTIC TRANSFER COMPARISON.....		39
3.1.	PLANE CHANGE DISTRIBUTION THEORY.....	40
3.2.	HOHMANN TRANSFER WITH PLANE CHANGE.....	46
3.3.	BI-ELLIPTIC TRANSFER WITH PLANE CHANGE.....	49
3.4.	ANALYSIS.....	51
3.5.	CASE STUDIES.....	63
3.6.	SUMMARY.....	72
CHAPTER 4.....		74
THE HOHMANN SPIRAL TRANSFER.....		74
4.1.	GENERAL CRITICAL SPECIFIC IMPULSE DERIVATION.....	75
4.2.	CO-PLANAR.....	77

4.3. PLANE CHANGE.....	86
4.4. HST WITH HIGH-THRUST PLANE CHANGE.....	87
4.5. HST WITH LOW-THRUST PLANE CHANGE.....	102
4.6. HST ONLY CRITICAL RATIO.....	128
4.7. CRITICAL RATIO COMPARISONS.....	135
4.8. LOW-THRUST PLANE CHANGE METHOD COMPARISON.....	137
4.9. TIME RESTRICTED TRANSFERS.....	141
4.10. ANALYTICAL LIMIT ANALYSIS.....	144
4.11. SUMMARY.....	148
CHAPTER 5.....	150
NUMERICAL ANALYSIS AND OPTIMISATION.....	150
5.1. NUMERICAL INTEGRATION PROCEDURE.....	150
5.2. OPTIMISATION METHOD.....	151
5.3. SUMMARY.....	158
CHAPTER 6.....	159
CASE STUDIES.....	159
6.1. ANALYTICAL.....	159
6.2. NUMERICAL OPTIMISATION.....	178

6.3. SUMMARY .....	207
CHAPTER 7 .....	209
CONCLUSIONS AND FUTURE WORK.....	209
7.1. CONCLUSIONS .....	209
7.2. RECOMMENDATIONS AND FUTURE WORK .....	210
REFERENCES.....	212
A.1. OPTIMISATION STUDY RESULTS.....	228
A.1.1. LEO-GEO.....	228
A.1.2. GTO-GEO .....	230
A.2. TRANSFER PROFILES.....	233
A.2.1. LEO-GEO.....	233
A.2.1.1. HIGH-THRUST PLANE CHANGE.....	233
A.2.1.1.1. WET MASS = 3299.69 KG .....	233
A.2.1.1.2. WET MASS = 4402.27 KG .....	235
A.2.1.1.3. WET MASS = 5504.85 KG .....	237
A.2.1.2. LOW-THRUST PLANE CHANGE.....	238
A.2.1.2.1. WET MASS = 3299.69 KG .....	238
A.2.1.2.2. WET MASS = 5504.85 KG .....	242

A.2.2.	GTO-GEO .....	244
A.2.2.1.	HIGH-THRUST PLANE CHANGE.....	244
A.2.2.1.1.	WET MASS = 2037.42 KG .....	244
A.2.2.1.2.	WET MASS = 2547.7 KG .....	246
A.2.2.2.	LOW-THRUST PLANE CHANGE.....	248
A.2.2.2.1.	WET MASS = 1527.13 KG .....	248
A.2.2.2.2.	WET MASS = 2037.42 KG .....	250
A.2.3.	SSO – HIGHLY ELLIPTICAL POLAR ORBIT .....	252
A.2.3.1.	12 HOUR ORBIT - HST WITH HIGH-THRUST PLANE CHANGE .....	252
A.2.3.2.	16 HOUR ORBIT - HST WITH LOW-THRUST PLANE CHANGE .....	254

# LIST OF ACRONYMS

---

---

<b>Acronym</b>	<b>Description</b>
ARTEMIS	Advanced Relay and Technology Mission Satellite
A <sup>n</sup> D	Accessibility and Deficit
EP	Electric Propulsion
ESA	European Space Agency
GEO	Geostationary Earth Orbit
GOCE	Gravity field and steady-state Ocean Circulation Explorer
GTO	Geostationary Transfer Orbit
LEO	Low Earth Orbit
HST	Hohmann Spiral Transfer
JAXA	Japan Aerospace Exploration Agency
MEO	Medium Earth Orbit
SSO	Sun Synchronous Orbit
SSTO	SuperSynchronous Transfer Orbit

# LIST OF SYMBOLS

---

---

Symbol	Description
$a$	Semi-major axis, m
$a_s$	Low-thrust system acceleration, $\text{m/s}^2$
$a_{target}$	Target semi-major axis, m
A	Limit line A
AOU1	Area of Uncertainty 1
AOU2	Area of Uncertainty 2
B	Limit line B
$\beta_0$	Initial thrust vector angle for low-thrust phase, rad
$\beta$	thrust vector angle at any given time throughout low-thrust phase, rad
CoA	Co-planar limit point A
CoB	Co-planar limit point B
$\Delta I$	Plane change, rad
$\Delta i$	Plane change at any given time throughout the low-thrust phase, rad
$\Delta I_i$	Plane change for initial velocity requirement, rad
$\Delta I_f$	Plane change for final velocity requirement, rad
$\Delta I_{C1^*}$	Critical point 1 plane change, rad
$\Delta I_{C2^*}$	Critical point 2 plane change, rad

---

---

$\Delta I_{C3^*}$	Critical point 3 plane change, rad
$\Delta I_{CS^*}$	Switching point plane change, rad
$\Delta I_{CA}$	critical point calculated analytically, rad
$\Delta I_{CNA}$	critical point calculated numerically, rad
$\Delta I_{po}$	Plane change per orbital revolution, rad
$\Delta V$	Velocity requirement for given transfer, m/s
$\Delta V_B$	Velocity requirement for bi-elliptic transfer, m/s
$\Delta V_{BT}$	Total velocity requirement for bi-elliptic transfer
$\Delta V_H$	Velocity requirement for Hohmann transfer, m/s
$\Delta V_{HC}$	High-thrust only transfer velocity requirement for circular initial orbit, m/s
$\Delta V_{HE}$	High-thrust only transfer velocity requirement for elliptical initial orbit, m/s
$\Delta V_{HSTHC}$	HST high-thrust phase velocity requirement for circular initial orbit, m/s
$\Delta V_{HSTHE}$	HST high-thrust phase velocity requirement for elliptical initial orbit, m/s
$\Delta V_{HSTHPC}$	HST critical specific ratio only - high-thrust phase velocity requirement with plane change starting in a circular initial orbit, m/s
$\Delta V_{HSTHPE}$	HST critical specific ratio only - high-thrust phase velocity requirement with plane change starting in an elliptical initial orbit, m/s
$\Delta V_{HSTHCPC}$	HST critical specific ratio only - high-thrust phase velocity requirement without plane change starting in a circular initial orbit, m/s
$\Delta V_{HSTHCPE}$	HST critical specific ratio only - high-thrust phase velocity requirement without plane change starting in an elliptical initial orbit, m/s
$\Delta V_{HSTL}$	HST low-thrust phase velocity requirement , m/s

$\Delta V_{HSTPL}$	Velocity requirement to perform low-thrust plane change only, m/s
$\Delta V_{HSTSL}$	Low-thrust spiral-in with no plane change section velocity requirement, m/s
$\Delta V_{HT}$	Total velocity requirement for Hohmann transfer, m/s
$\Delta V_{\infty}$	Total velocity requirement for parabolic transfer
$\Delta V_{\infty e}$	Escape velocity requirement, m/s
$\Delta V_{\infty r}$	Return velocity requirement, m/s
$\Delta V_{INC}$	Plane change only manoeuvre velocity requirement, m/s
$\Delta V_i$	Initial velocity requirement, m/s
$\Delta V_f$	Final velocity requirement, m/s
$\Delta V_L$	Velocity requirement for low-thrust transfer, m/s
$e$	Eccentricity
$e_{re}$	Allowable eccentricity error
$E$	Eccentric anomaly
$f$	Force, N
$f$	Modified equinoctial element
$g$	Modified equinoctial element
$i$	Inclination, rad
$I_{sp}$	Specific impulse, s
$I_{spH}$	Specific impulse of high-thrust propulsion system, s
$I_{spL}$	Specific impulse of low-thrust propulsion system, s

$k$	Modified equinoctial element
$L$	Modified equinoctial element
$m_0$	Initial mass, kg
$\hat{\lambda}_b$	Blended control law unit vector
$\hat{\lambda}_\sigma$	Variational element unit vector
$m_{02}$	Spacecraft mass at the beginning of low-thrust phase, kg
$m_1$	Final mass, kg
$m_{dry}$	Spacecraft dry mass, kg
$m_{HF}$	High-thrust transfer only fuel mass, kg
$m_{HSTF}$	HST fuel mass, kg
$m_{wet}$	Wet mass, kg
$N$	Normal thrust, N
$NOO$	Number of orbital revolutions required to perform specified plane change
$\nu$	True anomaly, rad
$\omega$	Argument of perigee, rad
$p$	Semi-latus rectum, m
$r$	Auxiliary positive variable (radius), m
$r$	Orbit radius
$r_i$	Initial orbit radius, m
$r_c$	Intermediate orbit radius, m

$r_c$	Intermediate orbit radius, m
$r_f$	Final orbit radius, m
$r_p$	Radius of perigee, m
$r_t$	Intermediate orbit radius, m (Hohmann and bi-elliptic analysis)
$r_t$	Target orbit radius, m
$r_x$	Intermediate orbit perigee for optimisation study, m
$R$	Radial thrust, N
$R$	Final to initial orbit ratio (Hohmann and bi-elliptic analysis)
$R_A$	Intermediate to initial orbit ratio analytical approximation of limit A
$R_B$	Intermediate to initial orbit ratio analytical approximation of limit B
$R_{C1^*}$	Critical intermediate to initial orbit ratio at critical point 1
$R_{C2^*}$	Critical intermediate to initial orbit ratio at critical point 2
$R_{C3^*}$	Critical intermediate to initial orbit ratio at critical point 3
$R_{CS^*}$	Critical intermediate to initial orbit ratio switching point
$R^*$	Intermediate to initial orbit radius
$R^*_{AOU1}$	Critical intermediate to initial orbit ratio for AOU1
$R^*_{AOU2}$	Critical intermediate to initial orbit ratio for AOU2
$R1$	Target to initial orbit ratio
$R2$	Intermediate to initial orbit ratio
$R2_{max}$	Maximum orbit ratio R2 using Edelbaum's method

$R3$	Current orbit to initial orbit radius ratio
$R3_{max}$	Maximum orbit ratio achieved throughout duration of low-thrust phase
$s$	Fraction of plane change conducted for initial velocity requirement
$\sigma$	Variational element
$t$	Transfer time at any given point, s
$t_B$	Bi-elliptic transfer duration, s
$t_H$	Hohmann transfer duration, s
$t_{HSTC}$	HST total transfer time for circular initial orbit, s
$t_{HSTE}$	HST total transfer time for elliptical initial orbit, s
$t_{HSTH}$	HST high-thrust transfer phase time, s
$t_{HSTL}$	HST low-thrust transfer phase time, s
$t_L$	Lower transfer time bound for optimisation, s
$t_l$	Low-thrust transfer duration, s
$t_{MAX}$	Maximum allowable transfer time, s
$t_{Rmax}$	Transfer time at which largest orbit ratio occurs, s
$t_{period}$	Orbital period, s
$t_U$	Upper transfer time bound for optimisation, s
$T$	Transverse thrust, N
$Tr$	Thrust due to low-thrust propulsion system, N
$\tau$	Auxiliary positive variable

$v_i$	Initial orbit velocity, m/s
$v_e$	Exhaust velocity, m/s
$v_f$	Final orbit velocity, m/s
$V$	Orbital velocity at any given time throughout low-thrust phase, m/s
$V_i$	Initial orbit velocity, m/s
$V_f$	final orbit velocity, m/s
$v_{trans_i}$	Transfer orbit velocity at perigee, m/s
$v_{trans_f}$	Transfer orbit velocity at apogee, m/s
$v_{transA}$	Velocity requirement at node A, m/s
$v_{trans1A'}$	Velocity requirement at transfer orbit 1 node A', m/s
$v_{trans1B'}$	Velocity requirement at transfer orbit 1 node B', m/s
$v_{trans2B'}$	Velocity requirement at transfer orbit 2 node B', m/s
$v_{transC}$	Velocity requirement at node C, m/s
$v_{trans2C'}$	Velocity requirement at transfer orbit 2 node C', m/s
$W_\sigma$	Control law weighting constant

# LIST OF FIGURES

Figure 2-1 Variation in rocket equation due to vehicle engine's specific impulse .....	6
Figure 2-2 Co-planar Hohmann transfer .....	8
Figure 2-3 Co-planar bi-elliptic transfer .....	10
Figure 2-4 Finite burn losses due to gravity compared with impulsive burn transfer .....	12
Figure 2-5 Liquid and solid rocket engines .....	20
Figure 2-6 Definition of classical orbital elements .....	32
Figure 2-7 RTN co-ordinate reference frame .....	33
Figure 3-1 Hohmann and bi-elliptic transfers with plane change at first and second impulses .....	40
Figure 3-2 Total velocity requirement comparison for circular orbit with plane change only .....	45
Figure 3-3 Relative percentage error of Eq. (3.6) compared to Eq. (3.2) with numerical method .....	46
Figure 3-4 Hohmann and parabolic transfer comparison with critical limits (verified with [9]) .....	49
Figure 3-5 Hohmann and parabolic transfer comparison for range of plane changes and orbit ratios.....	52
Figure 3-6 All transfers for varying orbit ratios at a plane change, $\Delta I = 0^\circ$ .....	54

Figure 3-7 All transfers for varying orbit ratios at a plane change, $\Delta I = 21.152^\circ$ .....	55
Figure 3-8 All transfers for varying orbit ratios at a plane change, $\Delta I = 31.852^\circ$ .....	55
Figure 3-9 Hohmann and bi-elliptic transfers' velocity requirement for varying orbit ratio, $R^*$ and plane change, $\Delta I$ .....	57
Figure 3-10 Hohmann, parabolic and bi-elliptic ( $R^*$ specified) transfer comparison.....	58
Figure 3-11 Transfer selection graph with areas of uncertainty and critical points .....	59
Figure 3-12 Characteristics of AOUI for a transfers specification of $R = 12$ & $\Delta I = 0.3rad (17.19^\circ)$ .....	64
Figure 3-13 Characteristics of AOUII for a transfers specification of $R = 2$ & $\Delta I = 0.8rad (45.84^\circ)$ .....	65
Figure 3-14 Limit B - $R > RC1^*$ for a transfer specification of $R = 10$ & $\Delta I = 0.556 rad (31.86^\circ)$ .....	66
Figure 3-15 Limit B - $RCS^* < R < RC1^*$ for a transfer specification of $R = 5.7$ & $\Delta I = 0.754 rad (43.20^\circ)$ .....	67
Figure 3-16 Limit B - $RC2^* < R < RCS^*$ for a transfer specification of $R = 3$ & $\Delta I = 0.761 rad (43.60^\circ)$ .....	68
Figure 3-17 Limit B - $R < RC2^*$ for a transfer specification of $R = 1.2$ & $\Delta I = 0.670 rad (38.39^\circ)$ .....	69
Figure 3-18 Limit A - $R > RCS^*$ for a transfer specification of $R = 8$ & $\Delta I = 0.555 rad (31.8^\circ)$ .....	70

Figure 3-19 Limit A - $RC3 * < R < RCS *$ for a transfer specification of $R = 4.2$ & $\Delta I = 0.809 \text{ rad}$ (46.35°) .....	71
Figure 3-20 Limit A - $R < RC3 *$ for a transfer specification of $R = 2$ & $\Delta I = 0.867 \text{ rad}$ (49.68°) .....	72
Figure 4-1 Critical specific impulse ratio superscript methodology .....	76
Figure 4-2 Co-planar HST with circular initial orbit .....	78
Figure 4-3 Co-planar HST with elliptical initial orbit .....	79
Figure 4-4 Co-planar Hohmann and HST critical specific impulse ratio for circular and elliptical initial orbit.....	82
Figure 4-5 Co-planar bi-elliptic and HST critical specific impulse ratio for circular and elliptical initial orbit.....	84
Figure 4-6 Hohmann and HST and bi-elliptic and HST critical ratio intersection .....	85
Figure 4-7 HST with plane change comparison chart.....	86
Figure 4-8 HST with high-thrust inclination change, Hohmann and bi-elliptic (plane change at nodes 1 and 2) transfer schematic .....	88
Figure 4-9 HST and Hohmann critical specific impulse ratio, Eq. (4.19), variation for $R1 = 6.42$ (LEO - GEO) .....	94
Figure 4-10 HST and bi-elliptic with plane change at first and second impulses critical specific impulse ratio, Eq. (4.21), variation for $R1 = 6.42$ (LEO – GEO) .....	95
Figure 4-11 HST and bi-elliptic with plane change at first and second impulses critical specific impulse ratio, Eq. (4.23), variation for $R1 = 6.42$ (LEO – GEO) .....	95

Figure 4-12 HST and Hohmann critical specific impulse ratio, Eq. (4.26), variation for $R1 = 6.42$ (GTO – GEO).....	101
Figure 4-13 HST and bi-elliptic with plane change at first and second impulses critical specific impulse ratio, Eq. (4.28), variation for $R1 = 6.42$ (GTO – GEO).....	102
Figure 4-14 HST and bi-elliptic with plane change at first and second impulses critical specific impulse ratio, Eq. (4.30), variation for $R1 = 6.42$ (GTO – GEO).....	102
Figure 4-15 HST with low-thrust plane change schematic.....	104
Figure 4-16 HST and Hohmann critical specific impulse ratio, Eq. (4.39), variation for $R1 = 6.42$ (LEO – GEO) .....	111
Figure 4-17 HST and bi-elliptic with plane change at first and second impulses critical specific impulse ratio, Eq. (4.40), variation for $R1 = 6.42$ (LEO – GEO) .....	111
Figure 4-18 HST and bi-elliptic with plane change at second and third impulses critical specific impulse ratio, Eq. (4.41), variation for $R1 = 6.42$ (LEO – GEO) .....	112
Figure 4-19 HST and Hohmann critical specific impulse ratio, Eq. (4.43), variation for $R1 = 6.42$ (GTO – GEO).....	115
Figure 4-20 HST and bi-elliptic with plane change at first and second impulses critical specific impulse ratio, Eq. (4.44), variation for $R1 = 6.42$ (GTO – GEO).....	115
Figure 4-21 HST and bi-elliptic with plane change at first and second impulses critical specific impulse ratio, Eq. (4.45), variation for $R1 = 6.42$ (GTO – GEO).....	116
Figure 4-22 HST and Hohmann critical specific impulse ratio, Eq. (4.55), variation for $R1 = 6.42$ (GTO – GEO).....	123

Figure 4-23 HST and Hohmann critical specific impulse ratio, Eq. (4.56), variation for $R1 = 6.42$ (GTO – GEO).....	123
Figure 4-24 HST and Hohmann critical specific impulse ratio, Eq. (4.57), Variation for $R1 = 6.42$ (GTO – GEO).....	124
Figure 4-25 HST and Hohmann critical specific impulse ratio, Eq. (4.58), variation for $R1 = 6.42$ (GTO – GEO).....	127
Figure 4-26 HST and Hohmann critical specific impulse ratio, Eq. (4.59), variation for $R1 = 6.42$ (GTO – GEO).....	127
Figure 4-27 HST and Hohmann critical specific impulse ratio, Eq. (4.60), variation for $R1 = 6.42$ (GTO – GEO).....	128
Figure 4-28 HST only critical specific impulse ratio variation for $R1 = 6.42$ (LEO – GEO), plane change performed at largest orbit radius .....	131
Figure 4-29 HST only critical specific impulse ratio variation for $R1 = 6.42$ (GTO – GEO), plane change performed at largest orbit radius .....	132
Figure 4-30 HST only critical specific impulse ratio variation for $R1 = 6.42$ (LEO – GEO) .....	135
Figure 4-31 HST only critical specific impulse ratio variation for $R1 = 6.42$ (GTO – GEO) .....	135
Figure 4-32 Comparison of critical specific impulse ratios, HST and Hohmann with high and low-thrust plane changes for $R1 = 6.42$ (GTO – GEO).....	137
Figure 4-33 HST only critical ratio with both low-thrust plane change methods, circular initial orbit, $R1 = 6.42$ (LEO – GEO).....	138

Figure 4-34 HST only critical ratio with both low-thrust plane change methods, elliptical initial orbit, $R1 = 6.42$ (GTO – GEO) .....	138
Figure 4-35 HST only critical ratio with both low-thrust plane change methods, circular initial orbit, $R1 = 3.21$ (LEO – MEO) .....	140
Figure 4-36 HST Only critical ratio with both low-thrust plane change methods, circular initial orbit, $R1 = 1.09, \Delta I = 98.6$ (LEO – SSO) .....	140
Figure 4-37 Critical orbit radius at specified eccentricity error tolerances with varying spacecraft acceleration .....	147
Figure 4-38 Maximum initial orbit radius with varying spacecraft acceleration. Error represents final orbit eccentricity .....	148
Figure 5-1 HST optimisation method with high-thrust plane change .....	155
Figure 5-2 HST optimisation method with low-thrust plane change .....	157
Figure 6-1 Critical specific impulse ratio comparison .....	162
Figure 6-2 Hohmann and HST only critical specific impulse ratio comparison .....	162
Figure 6-3 Critical $R2$ limit for varying spacecraft accelerations at the beginning of phase 2 .....	164
Figure 6-4 Orbit ratio, $R3$ , variation over low-thrust phase for wet mass of 5000 kg .....	167
Figure 6-5 Thrust angle, $\beta$ , variation over low-thrust phase for wet mass of 5000 kg .....	167
Figure 6-6 Plane change, $\Delta i$ , variation over low-thrust phase for wet mass of 5000 kg .....	168
Figure 6-7 Maximum allowable wet mass for specified transfer time .....	170

Figure 6-8 Hohmann and HST only critical specific impulse ratio comparison.....	173
Figure 6-9 LEO – GEO, intermediate orbit eccentricity for wet masses specified in ascending order.....	183
Figure 6-10 LEO – GEO, percentage fuel mass savings for wet masses specified in ascending order.....	184
Figure 6-11 LEO – GEO, $r_2$ for wet masses specified in ascending order.....	184
Figure 6-12 GTO – GEO, intermediate orbit eccentricity for wet masses specified in ascending order.....	188
Figure 6-13 GTO – GEO, percentage fuel mass savings for wet masses specified in ascending order.....	188
Figure 6-14 GTO – GEO, $R_2$ for wet masses specified in ascending order.....	189
Figure 6-15 GTO – GEO, HST with high-thrust plane change.....	190
Figure 6-16 GTO-GEO, HST with low-thrust plane change.....	191
Figure 6-17 GTO – GEO, HST with high-thrust plane change acceleration profiles.....	191
Figure 6-18 GTO – GEO, HST with low-thrust plane change acceleration profiles.....	192
Figure 6-19 GTO – GEO, HST with high-thrust plane change orbit radius profile.....	193
Figure 6-20 GTO – GEO, HST with low-thrust plane change orbit radius profile.....	194
Figure 6-21 GTO – GEO, HST with high-thrust plane change orbital element profiles.....	195
Figure 6-22 GTO – GEO, HST with low-thrust plane change orbital element profiles.....	195

Figure 6-23 12 hour polar orbit transfer, HST with low-thrust plane change.....	203
Figure 6-24 16 hour polar orbit transfer, HST with high-thrust plane change.....	203
Figure 6-25 12 hour polar orbit transfer, HST with low-thrust plane change orbit radius profile.....	204
Figure 6-26 16 hour polar orbit transfer, HST with high-thrust plane change radius profile .....	204
Figure 6-27 12 hour polar orbit transfer, HST with low-thrust plane change orbit element profiles .....	205
Figure 6-28 16 hour polar orbit transfer, HST with high-thrust plane change orbital element profiles .....	205
Figure 6-29 12 hour polar orbit transfer, HST with low-thrust plane change acceleration profiles .....	206
Figure 6-30 16 hour polar orbit transfer, HST with high-thrust plane change acceleration profiles .....	206

# LIST OF TABLES

Table 4-1 Subscript notation detailing critical specific impulse ratio transfer specification .	77
Table 4-2. Low-thrust plane change at largest orbit radius validation study specification..	107
Table 4-3 Low-thrust plane change at largest orbit radius validation study results.....	107
Table 4-4 Critical limit validation study parameters.....	146
Table 6-1 Circular initial orbit case study specification (LEO-GEO) from Xichang launch port.....	160
Table 6-2 Critical $R_2$ and transfer time for specified wet mass and thrust .....	164
Table 6-3 HST performance for different wet masses .....	169
Table 6-4 HST performance for maximum allowable wet masses .....	171
Table 6-5 HST performance for specified dry masses using HST with high-thrust plane change .....	172
Table 6-6 Critical $R_2$ and transfer time for specified wet mass and thrust .....	174
Table 6-7 HST performance for different wet masses .....	175
Table 6-8 HST performance for maximum allowable wet masses .....	176
Table 6-9 HST performance for specified dry masses using HST with high-thrust plane change .....	177
Table 6-10 Numerical study parameters .....	179

Table 6-11 2000 kg wet mass specified LEO – GEO comparison. A – Analytical, HTPC – High-Thrust Plane Change, LTPC – Low-Thrust Plane Change .....	180
Table 6-12 5000 kg wet mass specified LEO – GEO comparison. A – Analytical, HTPC – High-Thrust Plane Change, LTPC – Low-Thrust Plane Change .....	181
Table 6-13 9100 kg wet mass specified LEO – GEO comparison. A – Analytical, HTPC – High-Thrust Plane Change, LTPC – Low-Thrust Plane Change .....	181
Table 6-14 2600 kg wet mass specified GTO – GEO Comparison. A – Analytical, HTPC – High-Thrust Plane Change, LTPC – Low-Thrust Plane Change .....	185
Table 6-15 3800 kg wet mass specified GTO – GEO Comparison. A – Analytical, HTPC – High-Thrust Plane Change, LTPC – Low-Thrust Plane Change .....	186
Table 6-16 5500 kg wet mass specified GTO – GEO Comparison. A – Analytical, HTPC – High-Thrust Plane Change, LTPC – Low-Thrust Plane Change .....	186
Table 6-17 GTO – GEO velocity requirement and fuel mass phase breakdown. HTPC – High-Thrust Plane Change, LTPC – Low-Thrust Plane Change .....	196
Table 6-18 Optimisation data. HTPC – High-Thrust Plane Change, LTPC – Low-Thrust Plane Change .....	196
Table 6-19 Highly elliptical polar observation orbit.....	198
Table 6-20 Transfer specification and propulsion system performance .....	199
Table 6-21 Optimisation results for 12 and 16 hour orbit transfers .....	201

# Chapter 1

---

## INTRODUCTION

### 1.1. Background

In recent years space technology has matured allowing a substantial rise in space based services such as Earth-monitoring, satellite communications and surveillance. As such, there has been extensive research studying the most efficient way to deliver these payloads to their working orbit so that the cost for operators and therefore users is kept at a minimum. Such research focuses on optimising the trajectory of the spacecraft from its initial to final working orbit with the aim of minimising fuel mass. Until recently, these trajectories have been designed on the basis that chemical systems are the primary propulsion system and this has led to a great deal of research in the area [1]–[8]. Different transfer methods, such as the Hohmann and bi-elliptic transfer, have been proposed and investigated to determine the minimum fuel transfer [9], [10, Sec. 6.3]; however, there is often ambiguity as to which transfer should be used as no general solution exists, something which this dissertation will address.

As the fuel-efficiency of the chemical propulsion systems used for the aforementioned transfers tends to be poor, there has been significant development of low-thrust propulsion systems such as Solar Electric Propulsion (SEP) offering a far better efficiency. While the use of a low-thrust propulsion system reduces fuel consumption, it radically alters the trajectory and for certain transfers can result in a substantially increased transfer time. For commercial space based services, this increased transfer time can result in delayed income from the satellite which can be problematic, especially for commercial satellites. A multi-

objective approach, addressing both the fuel and time minimisation constraints, is to consider both high and low-thrust propulsion systems on-board the spacecraft. Such transfers have been studied previously however there has been limited work on a hybrid propulsion transfer based on the bi-elliptic transfer ethos; travelling from the initial to a far removed orbit and returning to the target orbit which can provide a benefit over a direct transfer from the initial to target orbit.

## 1.2. Thesis Objectives

This thesis has the following objectives:

- Determine a general solution for the evolution of critical limits, previously realised for a co-planar analysis, which determine if the Hohmann or bi-elliptic transfer offers the lowest fuel consumption, with the introduction of a plane change.
- Use general and special perturbation techniques to investigate if a hybrid propulsion transfer, based on the bi-elliptic transfer ethos, can reduce spacecraft fuel mass when compared to a single propulsion technology transfer without significant adverse effects on the trajectory duration.

## 1.3. Contribution To Knowledge

The key contribution of this dissertation can be summarised as follows:

- Where previous work in the literature has been case specific and required a numerical optimisation technique to determine the best transfer, this dissertation provides a general solution, based on simple analytical expressions, to determine when the Hohmann or bi-elliptic transfer is better with a plane change.

- The introduction and derivation of a hybrid propulsion transfer similar to the bi-elliptic transfer which is shown to outperform a single propulsion system transfer with fuel mass savings up to 27% of the initial wet mass.
- The development of a hybrid propulsion transfer optimisation methodology which can be implemented without engineering experience to provide rapid preliminary trajectory results.

## 1.4. Published Work

### 1.4.1. Journal Papers

- Owens, Steven Robert and Macdonald, Malcolm (2013) Analogy to Bi-Elliptic Transfers Incorporating High- And Low-Thrust. *Journal of Guidance, Control and Dynamics*, 36 (3). pp. 890-894. ISSN 0731-5090. doi: 10.2514/1.57917
- Owens, Steven Robert and Macdonald, Malcolm (2013) A Complete Overview of the Hohmann Spiral Transfer. To be submitted. *Journal of Guidance, Control and Dynamics*.

### 1.4.2. Conference Papers

- Owens, Steven Robert and Macdonald, Malcolm (2011) A Novel Approach to Hybrid Propulsion Transfers. In: 62<sup>nd</sup> International Astronautical Congress 2011, 2011-10-03 - 2011-10-07, Cape Town.
- Owens, Steven Robert and Macdonald, Malcolm (2012) An Extension and Numerical Analysis of the Hohmann Spiral Transfer. In: 63<sup>rd</sup> International Astronautical Congress, 2012-10-01 - 2012-10-05, Naples.

- Owens, Steven Robert and Macdonald, Malcolm (2013) Hohmann Spiral Transfer with Inclination Change Performed by Low-Thrust System. In: 23<sup>rd</sup> AAS/AIAA Space Flight Mechanics Conference, 2013-02-10 - 2013-02-14, Kauai, Hawaii.
- Owens, Steven Robert and Macdonald, Malcolm (2013) Novel Numerical Optimisation of the Hohmann Spiral Transfer. In: 64<sup>th</sup> International Astronautical Congress 2013, 2013-09-23 - 2013-09-27, Beijing.

### 1.4.3. Statement of Work Distribution

The content of the journal publications titled '*Analogy to Bi-Elliptic Transfers Incorporating High- and Low-Thrust*'; '*A Complete Overview of the Hohmann Spiral Transfer*' and all conference papers are part of the work considered in Chapter 4-6.

# Chapter 2

---

## LITERATURE REVIEW

The foundations of the modern space age can be attributed to Russian astronautics pioneer Konstantin Eduardovich Tsiolkovsky. In 1897 he independently derived the well-known rocket equation describing the motion of a body with variable mass, and went on to use it in his most famous publication titled ‘The exploration of cosmic space by means of reaction devices which was published in 1903 [11]. The full derivation will not be given here but the ideal rocket equation is defined as

$$\Delta V = v_e \ln \frac{m_0}{m_1} \quad (2.1)$$

where  $m_{0/1}$  are initial and final mass respectively. The exhaust velocity of the body,  $v_e$ , can be defined in terms of the specific impulse and gravity at sea level,  $v_e = g_0 I_{sp}$ . This equation allows the total velocity requirement for any given manoeuvre to be determined based on the initial and final mass of the body. Alternatively, as the total velocity change for any given manoeuvre can be calculated by other means as discussed throughout this chapter, the equation can be re-arranged to determine the spacecraft mass ratio dependent on the total velocity change to perform a manoeuvre and spacecraft exhaust velocity,

$$\frac{m_1}{m_0} = e^{\left[ \frac{-\Delta V}{g_0 I_{sp}} \right]} \quad (2.2)$$

It is interesting to note that the mass ratio has a strict dependency on the spacecraft’s engine specific impulse. Considering Figure 2-1 for an arbitrary  $\Delta V$ , it is evident the mass ratio can be increased with a larger specific impulse.

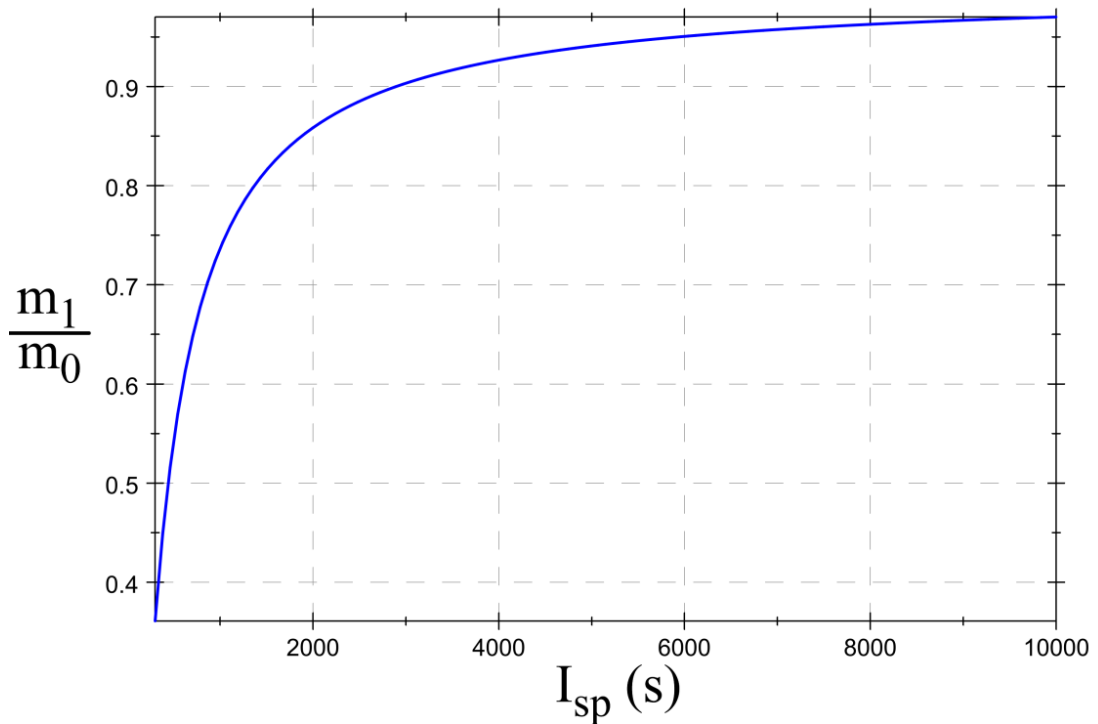


Figure 2-1 Variation in rocket equation due to vehicle engine's specific impulse

This is an important observation for this dissertation as it opens up the opportunity to investigate different propulsion systems with different engine characteristics.

## 2.1. High-Thrust Transfers

The term high-thrust transfer refers to a propulsion system which can offer a thrust to weight ratio of 0.5 to 1 [12, Sec. 6.3]. Commonly known as chemical propulsion systems, they have been successfully used to insert satellites into Earth orbits as well as on interplanetary orbit transfers, like that of Voyager 1 and 2, since the beginning of spaceflight. As these propulsion transfers can easily overcome the local gravity of a central body, they can often be treated as impulsive transfers. Two such transfers are the Hohmann and bi-elliptic transfers. As the comparison of these transfers is a major topic within this dissertation, it is necessary to establish the fundamentals of each and identify the research already conducted within the field.

## 2.1.1. Hohmann Transfer

One of the most common orbit transfers is the Hohmann transfer [13]. It has been proven to be the fuel optimal two-impulsive, circular to circular, transfer using many different theorems [2], [4], [7], [12, Sec. 5.4], [14]–[19], however this does mean that it takes longer than any other possible transfer orbit between the same two circular orbits [20, Sec. 3.3]. Considering the co-planar circular to circular orbit transfer detailed in Figure 2-2 it is evident the Hohmann transfer has one burn that is tangent to the initial orbit. This occurs at the transfer orbit perigee and inserts the spacecraft on an elliptical transfer orbit whose orbit apogee aligns with the target orbit. At point 2, the transfer ellipse apogee, another tangential burn is applied allowing the spacecraft to enter the target orbit.

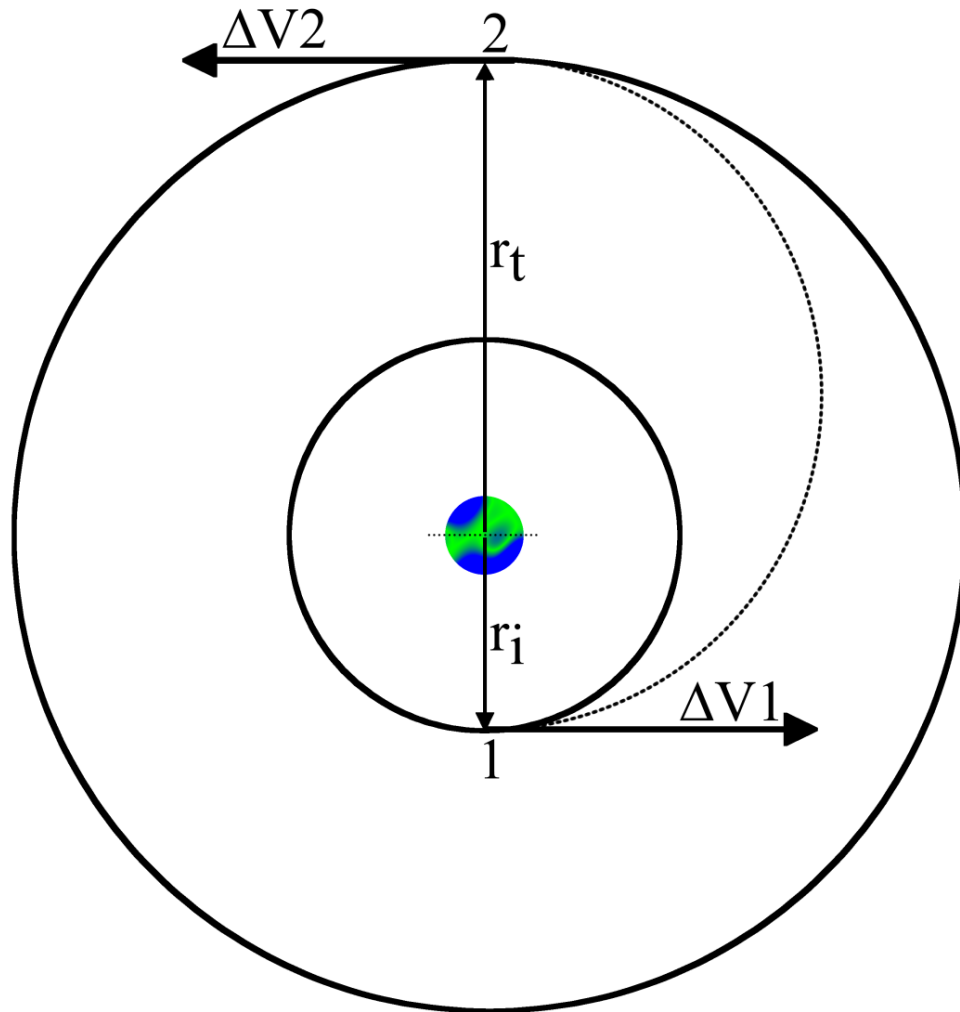


**Figure 2-2 Co-planar Hohmann transfer**

The Hohmann transfer can also be used for transfers between elliptical orbits or a combination of circular and elliptical orbits; so long as the major axes of the initial and final orbits align. For circular to elliptical orbits, the Hohmann transfer has also been shown to be the optimal transfer dependent on the transfer configuration [6]. For elliptical to elliptical orbit transfers however, there is no guarantee the Hohmann transfer is the optimal transfer [21], [22, Sec. 11], [23]. In the elliptical to elliptical case it is often necessary to employ numerical methods in order to determine the optimum transfer. However as this case is not a focus of this dissertation, it will not be discussed in detail. The total change in velocity to perform a Hohmann transfer, as shown in Figure 2-2, is

$$\Delta V_H = \left[ \sqrt{\frac{2\mu}{r_i} - \frac{2\mu}{r_i+r_t}} - \sqrt{\frac{\mu}{r_i}} \right] + \left[ \sqrt{\frac{\mu}{r_t}} - \sqrt{\frac{2\mu}{r_t} - \frac{2\mu}{r_i+r_t}} \right] \quad (2.3)$$

and the transfer time, which is simply half the elliptical orbit period, is defined as

$$t_H = \pi \sqrt{\frac{(r_i+r_t)^3}{\mu}}. \quad (2.4)$$

The fuel mass consumption of the Hohmann transfer can then be calculated from the rocket equation defined in Eq. (2.2).

## 2.1.2. Bi-elliptic Transfer

Another transfer, similar to the Hohmann as it also makes use of tangential impulsive burns, is the bi-elliptic. The bi-elliptic transfer was independently devised by Ehricke [24], Hoelker and Silber [8] and Shternfeld [25], who each found it could offer energy savings over the Hohmann transfer in a co-planar scenario for certain orbit configurations. Similar to the Hohmann transfer, the bi-elliptic transfer can also be used for a combination of circular and elliptical initial and final orbits so long as the major axes of both orbits align. The optimal transfer once again depends on the orbit configuration; as will be discussed in detail in Section 2.1.4. The co-planar bi-elliptic transfer is a three-impulse transfer as shown in Figure 2-3.

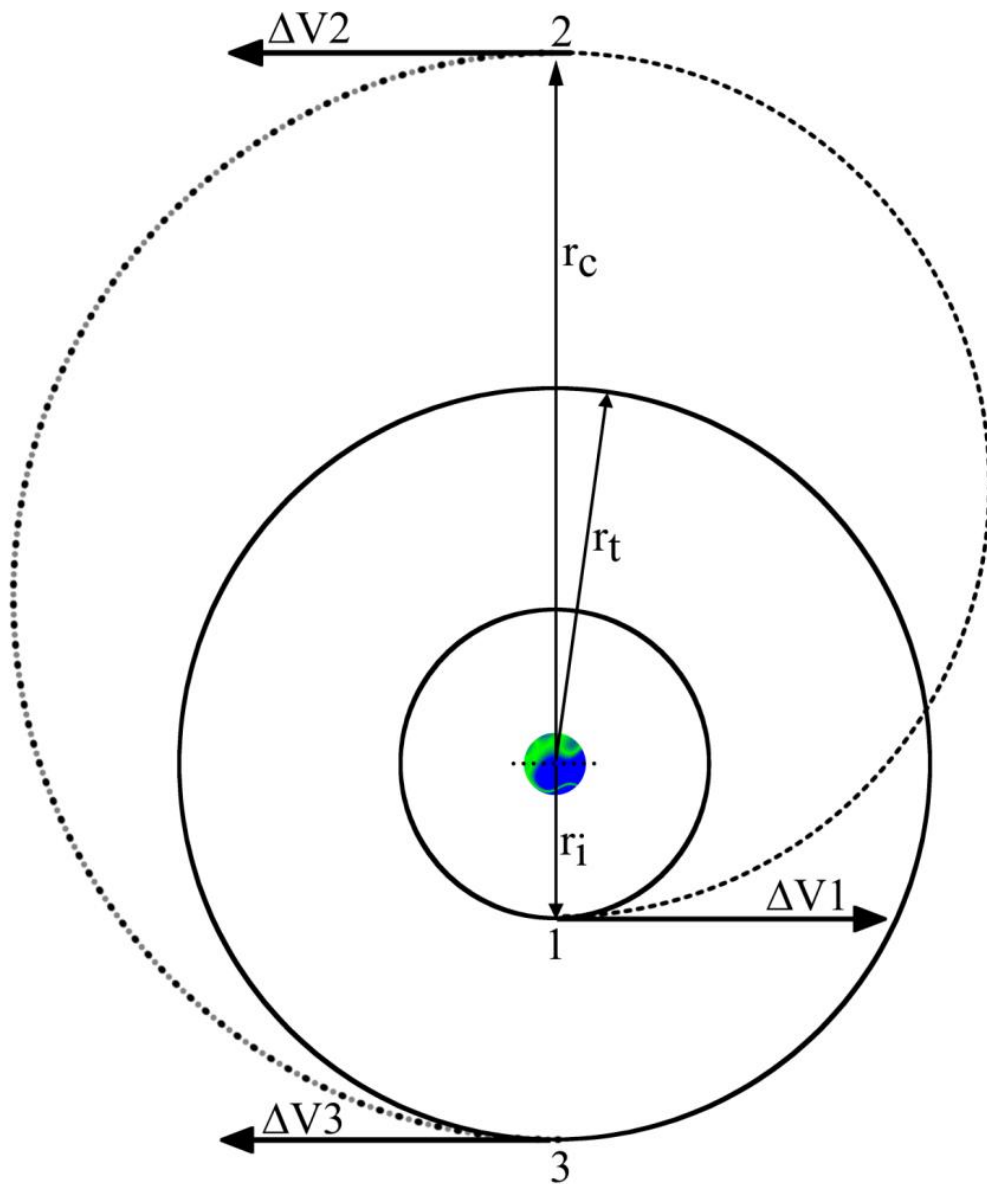


**Figure 2-3 Co-planar bi-elliptic transfer**

In this transfer the first impulse is again tangential to the initial orbit and occurs at the perigee of the first transfer orbit, however due to its larger magnitude the spacecraft is placed on an elliptical transfer orbit to a far removed point beyond the target orbit. At this far removed point, the apogee of the first and second transfer ellipse, a second tangential impulse is applied which moves the spacecraft from the first transfer orbit to the second; whose perigee aligns with the target orbit. At point 3, as shown in Figure 2-3, a third tangential impulse is applied, however in the direction opposite to the spacecraft motion;

allowing the spacecraft to enter the final orbit. The total change in velocity for the bi-elliptic transfer, corresponding to Figure 2-3, is

$$\Delta V_B = \left[ \sqrt{\frac{2\mu}{r_i} - \frac{2\mu}{r_i+r_c}} - \sqrt{\frac{\mu}{r_i}} \right] + \left[ \sqrt{\frac{2\mu}{r_c} - \frac{2\mu}{r_t+r_c}} - \sqrt{\frac{2\mu}{r_c} - \frac{2\mu}{r_i+r_c}} \right] + \left[ \sqrt{\frac{2\mu}{r_t} - \frac{2\mu}{r_t+r_c}} - \sqrt{\frac{\mu}{r_t}} \right] \quad (2.5)$$

and the transfer time, which is the sum of half the orbit period of the first transfer ellipse and half the orbit period of the second transfer ellipse, is

$$t_B = \frac{\pi}{\sqrt{\mu}} \left[ \sqrt{(r_i + r_c)^3} + \sqrt{(r_t + r_c)^3} \right]. \quad (2.6)$$

The fuel mass fraction of the bi-elliptic transfer can be calculated with the application of the rocket equation defined in Eq. (2.2).

The limiting bi-elliptic case is found by setting the intermediate orbit radius,  $r_c$ , in Eq. (2.7) equal to infinity,

$$\Delta V_B|_{r_c \rightarrow \infty} = \sqrt{\frac{\mu}{r_i}}(\sqrt{2} - 1) + \sqrt{\frac{\mu}{r_t}}(\sqrt{2} - 1) \quad (2.7)$$

where it is found the total velocity is simply the sum of the initial and target orbit velocities scaled by the factor  $(\sqrt{2} - 1)$ . The transfer time would also be infinite for this case.

### 2.1.3. Finite burn Losses

For both high-thrust impulsive transfers described previously, it is assumed that the impulse is delivered instantaneously. This however is not true, due to the inability of a spacecraft to provide infinite thrust, and leads to losses due to the effect of gravity on the spacecraft propulsion system [12, Sec. 6.3]. In reality, the thrust impulse would be delivered over a thrust arc around the ideal impulsive location over a finite time period as shown in Figure 2-4. At the centre of the arc  $\gamma \cong 0$  as desired, however at the start and end of the arc the  $\sin \gamma$  contribution may be significant. The thrust direction could be varied throughout the

burn so that  $\gamma = 0$  however this would lead to the spacecraft following a non-optimal trajectory.

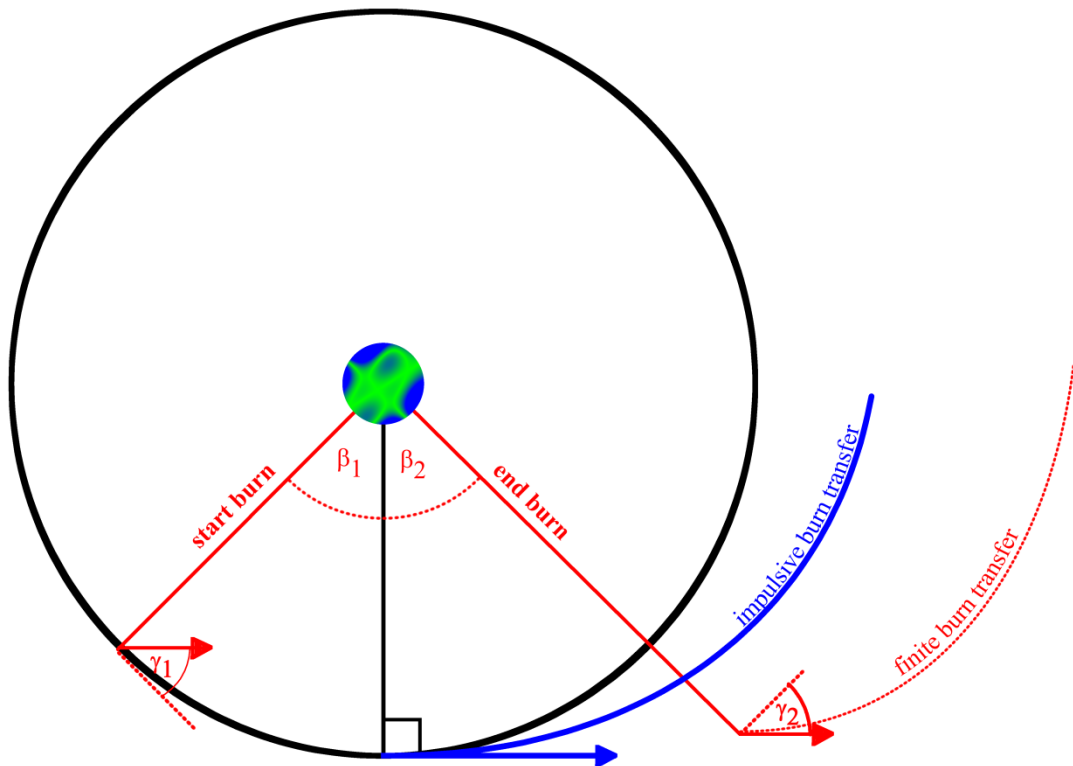


Figure 2-4 Finite burn losses due to gravity compared with impulsive burn transfer

This would have the effect of increasing the total velocity change for an impulsive transfer. A method of reducing the gravity losses is to split the total manoeuvre into several smaller manoeuvres. This would mean that a fraction of the total required change in velocity would be performed over a smaller burn arc. As the spacecraft approaches the perigee after one full revolution, another velocity increase impulse is performed again over a smaller burn arc and so on. In general, the greater the number of burns, the smaller the increase in velocity change required to account for gravity losses. The effect of these gravity losses can be quantified by the thrust to weight ratio as defined in Section 2.1. As for high-thrust transfers the thrust to weight ratio is generally between 0.5 and 1, the impulsive method can be said to offer a reasonably accurate representation of the orbit transfer, demonstrating the ‘best case scenario’. In a preliminary analysis this is more than ample and only in a detailed mission

design process, or for a significantly lower thrust to weight ratio, would the finite burn losses have to be taken into account. In some cases an acceptable velocity change penalty error can be specified so that certain limits can be derived in which the impulsive analysis is sufficiently accurate [26], [27]. As this dissertation is not concerned with detailed mission studies, impulsive manoeuvres are deemed acceptable whenever high-thrust transfers are considered.

## 2.1.4. Hohmann and Bi-elliptic Transfer Comparison

As Chapter 3 compares the Hohmann and bi-elliptic transfers, it is necessary to review the research previously conducted in this area. The transfers, between circular orbits, have been considered in a co-planar scenario where it has been shown there are critical ratios, dependent on the orbit transfer configuration, that determine which transfer offers the lowest velocity requirement [9], [10, Sec. 6.3]. In these analyses, two critical ratios are determined. The first is where the velocity of the Hohmann transfer is maximised, and occurs at a target to initial orbit ratio of 15.58. The second limit is calculated as a target to initial orbit ratio of 11.94. This limit is found by setting the Hohmann transfer velocity change equal to the limiting bi-elliptic transfer case [Eq.(2.3) = Eq. (2.7)], and solving for the resultant ratio. These limits have also been confirmed in the circular to elliptical case when comparing the Hohmann and limiting bi-elliptic case, also known as the parabolic transfer [6].

The transfers have also been considered between inclined planar orbits, however this work has either assumed the plane change is performed fully at the transfer apogee or has been optimally split between impulses and numerically determined [1], [28], [29]. While this approach yields accurate solutions, the analysis is dependent on the bi-elliptic intermediate orbit and precludes a general solution to the problem. In [28], the author describes two modified Hohmann transfers as well as the bi-elliptic with plane change. The first

modification to the Hohmann transfer performs the full plane change at the apogee of the transfer orbit. This occurs simultaneously with the orbit raise manoeuvre as this has been proven to be more fuel effective than performing each separately [24, Sec. 6.5]. The second modification splits the plane change between the first and second manoeuvres, with the majority of the plane change performed at the apogee of the transfer orbit. Upon investigation, it was found that this method always outperformed the prior [1], [10, Sec. 6.5], [28]–[30]. Using this method however requires an optimisation procedure for different orbit configurations and hence adds a numerical step to the analysis as mentioned previously. In [28], similar modifications are also applied to the bi-elliptic transfer. The first modification performs the full plane change at the intermediate orbit apogee. As this is a bi-elliptic transfer, this apogee is larger than the target orbit radius. If this apogee occurs at infinity then no velocity is required to perform the plane change and the total velocity requirement is the same as that defined in Eq. (2.7). The second modification is to split the plane change over all three impulses. This however results in the usage of Lagrange multipliers and once again requires a numerical step based on a specified intermediate orbit apogee; precluding a general solution. In [29], the author investigates the bi-elliptic transfer in great detail and delivers minimum velocity solutions with use of an iterative method. While this paper again highlights the benefits of the bi-elliptic transfer, it is again restricted by the need for a numerical method and a specific intermediate orbit apogee to determine a solution. Due to this, a general solution, based on the initial and final orbits, is again not possible. In [1], the author considers the bi-elliptic compared to the Hohmann transfer and a modified Hohmann transfer which accounts for a rendezvous scenario. In this case the orbit raising from the initial and target orbits is a standard co-planar Hohmann transfer. An additional burn is then applied at the line of nodes to change the orbital plane. As this is a rendezvous manoeuvre, the second orbit raise and plane change burn cannot be combined. This paper only considers a maximum intermediate orbit apogee ten times larger than the initial orbit radius and therefore does not consider the region in which the limits, described earlier in the chapter,

exist. The work in [1] also determines the optimum plane change split via a numerical method and therefore again precludes a general solution to which transfer offers the lowest total change in velocity for a set orbit transfer.

In Chapter 3 an analysis of the Hohmann and bi-elliptic transfers, compared in a non-co-planar transfer configuration, is presented. The aim of which is to determine a reference method to be used to determine the fuel optimal transfer based on the initial and target specification only. This removes the analysis dependence on the bi-elliptic intermediate orbit which has previously resulted in the transfers being compared with a case by case approach.

## 2.2. Low-thrust Transfers

Low-thrust transfers are somewhat different to high-thrust transfers in their application and resultant trajectories. As the title implies, low-thrust transfers are brought about by the application of a propulsion system with a low acceleration; less than the magnitude of the local body's gravitational acceleration. This provides a thrust to weight ratio of approximately  $10^{-2} \rightarrow 10^{-5}$  [12, Sec. 6.3]. Due to this small acceleration, these transfers require the propulsion system to be activated for large time periods; another major difference between low and high-thrust transfers. Similar to high-thrust transfers, coast-arcs can also be introduced to low-thrust transfers. To ensure its reliability, it is common for a low-thrust system to be tested for operational runtimes of tens of thousands of hours with multiple on/off cycles incorporated. This has been shown both in the development stages but also through previous missions [31]–[36]. Another major difference compared to high-thrust transfers is the resultant trajectory; normally a geometric transfer similar to a spiral.

When analysing low-thrust transfers, several assumptions, to reduce the complexity and thus provide general solutions, can be made. One such assumption for co-planar analyses involves constraining the thrust vector to the transverse direction. Although this is a

simplifying assumption, early research suggested this as the most effective way, in terms of fuel mass, to perform a co-planar orbit raise where no eccentricity is considered in the analysis [37]. In fact, in the same work it was shown that the spacecraft thrusting in the radial direction can consume more than double the fuel of a spacecraft using a tangential thrust direction vector.

As a result of the acceleration magnitude and the spacecraft only thrusting in the tangential direction, it can be said the transfer is quasi-circular and hence the orbit eccentricity is maintained  $\cong 0$  throughout the transfer. In this case the total velocity requirement for a transfer between two circular orbits, where  $r_i < r_t$ , is simply the difference in the orbital velocities

$$\Delta V_L = \sqrt{\frac{\mu}{r_i}} - \sqrt{\frac{\mu}{r_t}} \quad (2.8)$$

and if the spacecraft acceleration is assumed constant the transfer time can be calculated as

$$t_l = \frac{\Delta V_L}{a_s}. \quad (2.9)$$

Analytical solutions for the total change in velocity have also been developed for inclined circular orbit transfers based on averaging solutions [30]

$$\Delta V_L = \sqrt{V_i^2 - 2V_iV_f \cos\left(\frac{\pi\Delta I}{2}\right) + V_f^2}. \quad (2.10)$$

This again considered a spacecraft with a constant acceleration and was constrained by the thrust vector maintaining the same magnitude of angle for each orbital revolution i.e. the thrust direction was switched at the anti-nodes. For this case, the transfer time can also be calculated using Eq. (2.9). The fuel mass fraction for either case can be calculated using the rocket equation defined in Eq. (2.2). The constant thrust angle was addressed and resolved in [38] and the work was extended to include variation in constant acceleration due to

propellant expenditure. Further work has explored variable specific impulse and thrust [39], [40] as well as considering Earth-shadow effects [41], [42]. More recent work has developed a model for mass optimised circular co-planar transfers which has reduced complex trajectories to simple semi-analytical relationships and thus can be used quickly and effectively to determine optimal transfer parameters [43].

Where the design of the spacecraft trajectory is necessary, there are several additional techniques which can be utilized. This is addressed in Section 2.6.

## 2.3. Hybrid Propulsion Transfers

Although there has been substantial development of low-thrust propulsion transfers and the physical engines, as discussed in Section 2.2 and 2.5 respectively, there has also been research focused on coupling high and low-thrust propulsion technologies to form a hybrid propulsion system. The advantages of coupling are obvious; reducing the transfer time compared to only low-thrust propulsion, providing a fuel mass saving compared to only chemical propulsion and reducing the time the spacecraft spends in the Van Allen radiation belts, which can cause significant power degradation to the solar panels used by certain EP systems. The first indication of using the systems together was in 1962 by Theodore Edelbaum [44], around the time when Electric Propulsion (EP) systems were starting to be considered as a feasible propulsion system for spacecraft [45]. Early work on the transfer method, such as the analysis in [44], assumed the high-thrust segments were impulsive and patched with the low-thrust transfers to form the trajectory. This was also the case in proceeding work [46], [47]. In using this method, the transversality condition used in the optimisation process offered some conditions for patching the segments together. Other work has made use of primer vector theory, which can provide similar results; however in a more general and direct manner without the need to patch sections together [48]. This was based on a switching function that could be used to switch between propulsion systems and also

allow the spacecraft to enter a coast period. This switching methodology was also identified in [49] and [50] and the similarities between [48]–[50] were described in [51].

In recent years, work has also been able to consider the practicalities of implementing hybrid propulsion systems, that is, performing an analysis based on launch vehicle technology, spacecraft power availability and efficiencies of current low thrust systems. This has allowed for realistic studies of transfers from Earth to the Moon using chemical-electric systems and also nuclear-electric systems [52]–[54]. These studies have again identified the advantage of such a propulsion system. In addition to Earth – Moon transfers, there have also been studies of combined propulsion systems for orbit transfers within the Earth’s sphere of influence; most notably, transfers to GEO. This research has considered the use of a chemical system on-board the satellite in conjunction with an EP system, also on-board the satellite but for the main use of station keeping manoeuvres, to perform part of the orbit raise manoeuvre [55], [56]. In addition, work has considered the effect of the launch vehicle on the transfer [57]. In order to maximise the satellite dry mass and hence minimise the fuel mass, these studies have also considered the effect of varying the propulsion system specification which has shown there could be some advantage to an EP system with variable specific impulse and thrust. The work in [57] also found the optimum EP system specific impulse depends strongly on the chemical propulsion system specific impulse which is due to a trade-off between minimum fuel mass and minimum time. This is interesting as the hybrid propulsion analysis in this dissertation is dependent on the ratio of the high and low-thrust system’s specific impulses; however, it is expected that a similar trend will not be observed as the analysis in this dissertation considers a minimum fuel optimisation satisfying a user specified time constraint. The radiation reduction on the power degradation issue was studied in [58] where it was confirmed the time spent in the radiation belts can be reduced drastically by employing a hybrid system as opposed to low-thrust only. The introduction of the high-thrust system does impose a mass penalty but this can be offset again by the reduction in radiation

effects on the spacecraft. There have also been studies considering interplanetary travel using hybrid propulsion which have mainly focused on the application of such systems for transfers to Mars [59]–[61]. Several studies have also considered hybrid propulsion with the use of two low-thrust propulsion technologies. This has predominantly been studied to consider interplanetary transfers but it has also been found it can enable several missions that were not possible with chemical propulsion with Earth as the central body [62]–[67].

As the primary purpose of this dissertation is to consider novel hybrid transfers around the Earth, it is worth revisiting the work discussed on transfers to GEO. This research has mainly focused on transfers which use high-thrust burns to achieve an intermediate orbit somewhere between the initial injection and target orbits. This method then uses an outward spiral trajectory towards the target orbit. However by considering the bi-elliptic transfer ethos and how it can save fuel mass by using an intermediate orbit far greater than the target orbit, it is worthwhile studying a similar hybrid transfer. In this case, the high-thrust section is used to propel the spacecraft beyond the target to an intermediate orbit, with both perigee and apogee larger than the target, and then the low-thrust system propulsion system is used to spiral back in-towards the target. This means the low-thrust system is used with a larger thrust to weight ratio than most normal hybrid transfers; ultimately improving the effectiveness of the low-thrust system. As such, Chapter 4 considers such a transfer in greater detail, deriving the theory behind the method and noting its limitation before applying it to different case studies.

## 2.4. High-Thrust Propulsion Systems

As discussed earlier in the text, a high-thrust propulsion system has been predominantly used for spacecraft since the beginning of the space age. The most common high-thrust propulsion system is the rocket engine, which is normally an internal heat combustion engine. Rockets carry their own oxidant in addition to the fuel; separating them from the likes of air breathing

jet engines which require an external source of oxygen. There are three main types of rocket engine: liquid, solid and hybrid [68]. The liquid engine, as the name suggests, carries liquid forms of the fuel and usually oxidant, which are kept separate until mixed in the combustion chamber. The solid rocket engine contains a solid of mixed fuel and oxidant and finally the hybrid rocket engine requires either the fuel or oxidant to be liquid with the other being solid. The most effective oxidant is found to be in liquid form so the standard arrangement is solid fuel and liquid oxidant [68, Sec. 4.8]. As hybrid rocket engines are rarely used in orbit, only the liquid and solid variants will be discussed in further detail. A schematic of the liquid and solid rocket engines is given in Figure 2-5 highlighting the key differences between each system.

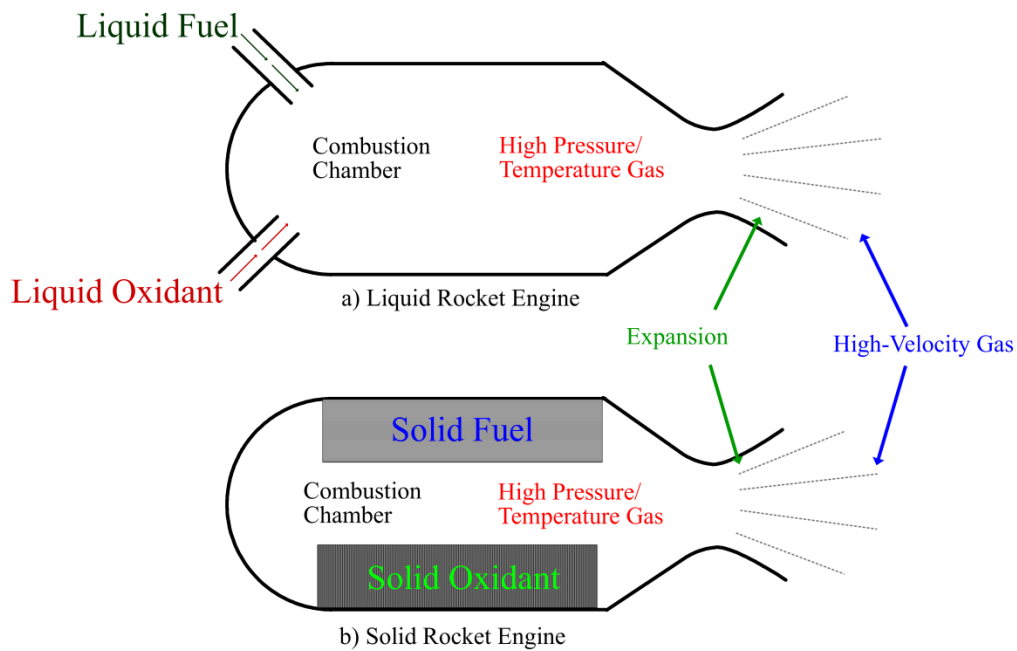


**Figure 2-5 Liquid and solid rocket engines**

The liquid rocket engine is used as it typically offers higher performance when compared to the solid rocket engine [68, Ch. 3]. In the case of a bi-propellant rocket, both the propellant and oxidant in liquid form are stored away from the combustion chamber as highlighted in Figure 2-5. For the case of a monopropellant rocket, only the propellant is stored away from the combustion chamber. In the case of the solid rocket engine, both the propellant and

oxidiser are stored within the combustion chamber as also shown in Figure 2-5. The liquid rocket engine is safer due to the propellant being stored externally however this proves more expensive than the solid rocket engine due to the complex injection systems required to move the propellant from their storage tanks to the combustion chamber. Some variations of the liquid rocket engine do offer the versatility of being able to start and stop the engine, something not possible with solid rocket engines, which is a significant benefit in delivering spacecraft to different orbit specifications [68, Ch. 3]. The applications of the solid rocket engine are for small to medium launchers where a simple reliable system is required however they are often strapped to a heavy lift launcher as a booster system [68, Ch. 4].

## 2.5. Low-Thrust Propulsion Systems

The advantage of low-thrust propulsion in comparison to high-thrust is the massive reduction in fuel mass required. This fuel mass reduction can enable a variety of new missions that are not possible with chemical propulsion. It can also allow a platform to house additional payload or quite simply, reduce the spacecraft mass and potentially launch costs.

### 2.5.1. An Historical Perspective

The application of EP for spacecraft missions has been studied for over 100 years now [45]. The first known record of using electrically charged particles as a form of propulsion was in 1906 by rocket pioneer Robert H. Goddard [69, Sec. 1] and although further research was conducted thereafter, it was the chemical rocket that developed rapidly and therefore has been used on the majority of space missions to date. A demonstration mission of an electrostatic gridded-ion propulsion system, known as SERT 1 (Space Electric Rocket Test), was launched in 1964 and followed up by SERT 2 in 1970 [70]. The first deep space mission to utilise the technology however, was not launched until 1998 [34], [71], [72]. The spacecraft, Deep Space 1, was the first flight of NASA's Millennium project; set up to

demonstrate and flight-validate high-risk technologies that could be used to future space missions. Its primary mission was to validate the SEP engine developed as part of NASA's Solar Electric Propulsion Technology Application Readiness (NSTAR) program. Following the success of Deep Space 1, the NSTAR gridded ion engine was used again on the DAWN mission, launched in 2007, as the sole propulsion system for an exploratory mission [73].

The former Soviet Union was also heavily involved in research and development of EP and had flown the system successfully on many missions prior to the acceptance of it in the wider space community [45]. This research is still on going in Russia but the main focus of the research is on Hall-effect thrusters [74].

Other agencies have also used EP on missions as the main propulsion system. In 2003 the Japanese Aerospace Exploration Agency (JAXA) launched the sample and return Hayabusa mission to the asteroid 25143 Itokawa with four gridded ion-engines as the primary propulsion system [32], [75]. In the same year the European Space Agency (ESA) launched the Moon impact satellite mission SMART 1 (Small Missions for Advanced Research in Technology 1) which had Snecma's PPS-1350-G Hall-effect thruster as its main propulsion system [35]. Due to these advancements, and the work of the Soviet Union, EP has slowly made its way on to satellite platforms, mainly as a propulsion system for station keeping. Inadvertently, this secondary propulsion system has also 'saved' satellites that were thought lost due to a failure in their main chemical engine [76]. One of the most notable instances of this was the ESA satellite ARTEMIS (Advanced Relay and Technology Mission Satellite) which, due to a failure in the launch vehicle, was left in an unusually low-transfer orbit. As the chemical propulsion system did not possess enough fuel to adequately raise the satellite to its final orbit, the gridded ion EP station keeping engines were used to achieve this: albeit over a longer period of time than originally planned [77]. However it is only more recently that EP is becoming accepted as the primary propulsion system for many satellites. In 2012, Boeing announced a new member to its Geostationary satellite's family; the 702 SP. This

satellite is Boeing's first satellite to utilise an all-electric propulsion system on board the satellite [78] and signals the intent of the manufacturer to utilise the benefits of the propulsion system.

In Britain, QinetiQ have developed two versions of the gridded-ion thruster; the T5 and T6. The T5 thruster has successfully flown on ESA's Gravity field and steady-state Ocean Circulation Explorer (GOCE) mission where its function was to provide drag free attitude control to achieve the scientific mission objectives [79], [80]. For this mission the T5 had a thrust range of 1 to 20 mN, operated within a specific impulse range of 500s - 3500s and had a mass of 2.95 kg [81]. The T6 has a thrust range of 30-210 mN, operates at a specific impulse of 4300s and has a mass of approximately 8.1 kg [82]. The T6 thruster is to be the main thruster on ESA's bepi-columbo mission, planned for launch in 2014 [82]–[84] as well as provide the propulsion system for the next generation of communication platforms, Alphasat [84], [85].

It is clear there has been significant progress in the development of EP devices and that different systems can deliver benefits over conventional chemical systems. As this dissertation will only consider Solar Electric Propulsion (SEP) systems, they can be categorised as electromagnetic, electrothermal or electrostatic. The following sections will briefly discuss the advantages and disadvantages of each and recommend a propulsion system, based on current technology, suitable for the analyses conducted throughout this dissertation.

## 2.5.2. Electromagnetic Propulsion Systems

Electromagnetic thrusters offer a variety of different configurations in comparison to electrostatic and electrothermal systems. In terms of potential, they outperform both electrothermal and electrostatic. Their exhaust velocities are much higher than that of electrothermal and their thrust density is much larger than that of electrostatic [31]. However

these advantages and myriad possible configurations are severely compromised by the complexity that is required to implement the system. This is highlighted by the few number of devices that have made it through theoretical and experimental studies conducted since the 1950s. In addition to the system complexity, electromagnetic devices have fallen short in terms of the required efficiency, reliability and range of performance necessary for a spacecraft engine. Only one method has been extensively researched and that is the MagnetoPlasmaDynamic (MPD) thruster. Put simply, the device operates by accelerating a plasma propellant by either an internal or external magnetic field which acts on an internal arc current [31]. The device has a demonstrated specific impulse range of 1500-8000s, through ground testing [31] and has had considerable academic interest. However, due to the high-power required to operate efficiently (in excess of hundreds of kilowatts) it has attracted very little commercial interest. Due to this, only one device has been developed [86], [87] and successfully flown as a spacecraft's primary propulsion system [88]. This device's maximum specific impulse was only 1000s however.

### 2.5.3. Electrothermal Propulsion Systems

Electrothermal propulsion systems work on the premise that the propellant is electrically heated in some chamber and then expanded through a nozzle [31], [33]. There are three types of electrothermal propulsion engines: the resistojet, arcjet and the inductively and radioactively heated devices. However, due to the poor efficiencies associated with the latter, only resistojets and arcjets will be discussed. In a resistojet the heat is transferred to the propellant from a solid surface, either a chamber or a heater coil whereas the propellant in an arcjet engine is heated through an electric arc that is passed through it. A problem associated with all electrothermal systems is the loss associated with frozen flow. These losses are characterised by energy that is unattainable due to it being 'frozen' in the internal modes and also dissociation of the molecules. With respect to resistojets, the main constraints are: the chamber temperatures are limited by the associated materials and maintaining the integrity of

the insulator and the chamber heating surfaces [31]. In terms of performance, the resistojet can offer a specific impulse up to 500s which in comparison to other low-thrust propulsion systems is low and can be attributed to the method of heating [36]. Arcjets have efficiency problems that can be associated to the viscous effects within the fluid [31], offering a specific impulse up to 700s. Again this is low compared to other low-thrust propulsion systems.

## 2.5.4. Electrostatic Propulsion Systems

Although there are several systems that fall under the title of electrostatic propulsion systems, only two systems can be considered for primary propulsion systems due to their high exhaust velocity and specific impulse. These are gridded ion and hall-effect thrusters, where hall effect thrusters are effectively grid-less ion thrusters [33]. In their simplest form, ion thrusters accelerate a beam of atomic ions with an electric field which is then neutralised by an equal flow of electrons [31]. Gridded-ion thrusters use a permeable grid to electrostatically extract ions from a plasma flow and accelerate them to high velocities at voltages up to and exceeding 10 kV [36]. Hall-effect thrusters use a cross-field discharge (hall-effect) to generate the plasma and an electric field is created perpendicular to a magnetic field which accelerates ions to high exhaust velocities. Ion thrusters have a high efficiency, from 60% to >80% while providing extremely high specific impulses, from 2000s to over 10,000s. The efficiency and specific impulse range of the Hall-effect thruster is lower than the Gridded ion however it offers a higher thrust at a given power and is much simpler to operate [36]. Although the gridded ion thrusters are more complex, they have been developed and flown more than any other EP system as can be seen in the brief discussion at the beginning of this section. For this reason, this will be the primary propulsion system considered whenever low-thrust systems are referenced in this dissertation.

## 2.6. Low-Thrust Trajectory Design

Where high-thrust transfers are relatively straightforward to predict due to their impulsive nature, low-thrust transfers require continuous thrust to generate a similar velocity requirement, which can result in many orbital revolutions. This spiral trajectory leads to numerically intensive methods in order to determine a solution to any particular transfer problem. Several techniques have therefore been developed which reduce their complexity and produce trajectories which are near-optimal. These methods are good for determining an initial solution to a proposed trajectory problem or forming an initial guess to be used as part of a detailed optimisation study.

### 2.6.1. Shape-Based Methods

In [89] it was shown that an exponential sinusoidal function can be used as a shape based method to generate trajectories with a gravity assist segment. This was used as a simple analysis of a transfer and also used as an initial guess for a direct optimisation method whose minimum fuel solution could be correlated to the initial solution. Other methods include using inverse 5<sup>th</sup> and 6<sup>th</sup> degree polynomials to represent the trajectory in a two-dimensional frame [90], [91]. The work in [90], [91] showed the method could provide near optimal trajectories and in the case where the transfer time is fixed, was shown to be similar to the high-thrust impulsive Lambert's problem [90], [91]. It was also found to provide a good initial guess when being used in conjunction with an optimisation process, improving the chance of convergence. A slightly different approach which doesn't specify a shape to represent a transfer but instead determines a shape based on a finite Fourier series expansion is defined in [92]. By implementing the shape based method in this manner allows thrust constraints to be addressed which is not possible in the previously defined methods. An approach which addresses three dimensional transfers and uses a shaping method defined in spherical co-ordinates is shown in [93]. In this work, the method is coupled with a linear

quadratic controller which can determine the feasibility of transfers between any two orbits. As is the same with all shape based methods however, there is a restriction on the complexity of trajectories they can actually model. In addition to this, only [92] managed to determine trajectories based on explicit thrust constraints. As such, the applicability of shape-based methods for trajectories which rely heavily on the specific propulsion system used is limited.

## 2.6.2. Orbit Averaging Methods

Orbital averaging techniques, as previously mentioned in this Chapter, can also be used to generate trajectories with a reduction in complexity. In this method the change in any orbital element is calculated over one orbit which is then divided by the orbital period to give the average rate of change of the element per orbit. This method determines the element's mean time rate of change with the assumption that all other orbital elements are held constant. While this method reduces the complexity, a consequence of applying it is the spacecraft's position at a given time cannot be determined [94, Sec. 5]. Orbital averaging techniques have been employed through many different techniques. In [95], [96], the method uses an averaged Hamiltonian which provides accurate solutions over large transfer time, multi-revolution transfers as expected. However it is shown in [96] that it can also provide reasonably accurate solutions for short time-scale problems, while noting that the accuracy decreases with decreasing transfer time. The averaging method was also shown to take into account the effect of the Earth's oblateness where it was investigated to determine how this affected the nodal procession of the orbit transfer with both the semi-major axis and inclination changing [97]. A study of different transfers using averaging techniques is shown in [98] where the analysis again accounts for the effect of the Earth's oblateness, however it also accounts for the shadow effect. These transfers were also investigated from a minimum time and fuel perspective. With the development of the technique, it was demonstrated it could provide rapid and accurate approximations when used within a numerical integration model [99]. This was further investigated within an optimisation procedure, where the

averaged equations were re-derived with respect to the eccentric anomaly, allowing the mass flow rate to be accounted for [100]. This method was also found to offer accurate approximation of the time histories of the non-secular orbital elements however it experienced some problems when the semi-major axis was large as the averaging assumption breaks down. It was also found that this method is unable to model hyperbolic trajectories and eccentricities of zero as the argument or perigee becomes undefined. Orbit averaging was also shown to be coupled with a numerical optimisation method to provide trajectory solutions for Earth-Moon transfers [101].

In general, orbit averaging is a very powerful tool in the generation of low-thrust trajectories, even more so when it is to be coupled with an optimisation process. However, there are certain limitations as was highlighted previously. In addition to the lack of non-secular time histories, barring that identified in [100] which showed the time histories could be generated up to a certain point, averaging methods are also only able to model certain trajectories. As was discussed in [100] and is applicable for all averaging methods, they cannot accurately represent trajectories with velocities close to escape. In [100], this meant that the models were limited to within a few revolutions of orbital escape conditions where it was shown they demonstrated good accuracy up to a semi-major axis equivalent to twenty Earth Radii.

### 2.6.3. Locally Optimal Control Laws

Locally optimal control laws can also be used for trajectory generation. These control laws maximise the rate of change of a given orbit element and can be specified in closed analytical form. This can then be used as the optimal thrust direction vector. The advantage of such control laws is the speed of which they can be implemented in a trajectory problem and the primary disadvantage is the sub-optimal nature of the resulting solution. They can be developed from the variational equations of the orbital elements as will be shown in the proceeding section. Previous work developed a form of the control laws for semi-major axis,

inclination and radius of perigee using the equinoctial elements to avoid singularities associated with the classical elements [102]. In [103], this was extended to include the eccentricity control law which, combined with orbital averaging, was used in an optimisation process. The control laws were then explained in an analytical form by the same author in [104]. The control laws have also been derived for use with another form of low-thrust propulsion: solar-sailing [105]. This work was further extended to define the control laws in modified equinoctial elements [106]–[108] and applied to many novel missions only possible with a solar-sail [109].

Due to the quick implementation and versatility of locally optimal control laws, they will be used within this dissertation whenever trajectory design is required. Although they are sub-optimal by nature, it was demonstrated in [102], [103], [109] they exhibit an accuracy  $\leq 2.5\%$  from the optimal solution; an acceptable accuracy for the work scope within this dissertation.

## 2.6.4. Modified Equinoctial Elements

Modified equinoctial elements are used to derive the equations of motion used for spacecraft trajectories in this dissertation as they are non-singular except when  $i = \pi$  radians [110]. The modified equinoctial elements defined in keplerian elements are

$$p = a(1 - e^2) \quad (2.11)$$

$$f = \cos(\omega + \Omega) \quad (2.12)$$

$$g = e \sin(\omega + \Omega) \quad (2.13)$$

$$h = \tan \frac{i}{2} \cos \Omega \quad (2.14)$$

$$k = \tan \frac{i}{2} \sin \Omega \quad (2.15)$$

$$L = \Omega + \omega + \nu, \quad (2.16)$$

which, used with the positive auxiliary variables defined in Eq. (2.17)-(2.21), can define the equations of motion of any satellite.

$$s^2 = 1 + h^2 + k^2 \quad (2.17)$$

$$w = 1 + f \cos L + g \sin L \quad (2.18)$$

$$r = \frac{p}{w} \quad (2.19)$$

$$\tau = \sqrt{h^2 + k^2} \quad (2.20)$$

$$\alpha^2 = h^2 - k^2. \quad (2.21)$$

The equations of motion defined in modified equinoctial elements in the Gaussian form are therefore defined as

$$\frac{dp}{dt} = \frac{2p}{w} \sqrt{\frac{p}{\mu}} [R \quad T \quad N] \begin{bmatrix} 0 \\ 1 \\ 0 \end{bmatrix} \quad (2.22)$$

$$\frac{df}{dt} = \frac{1}{w} \sqrt{\frac{p}{\mu}} [R \quad T \quad N] \begin{bmatrix} w \sin L \\ (w + 1) \cos L + f \\ -g(h \sin L - k \cos L) \end{bmatrix} \quad (2.23)$$

$$\frac{dg}{dt} = \frac{1}{w} \sqrt{\frac{p}{\mu}} [R \quad T \quad N] \begin{bmatrix} -w \cos L \\ (w + 1) \sin L + g \\ f(h \sin L - k \cos L) \end{bmatrix} \quad (2.24)$$

$$\frac{dh}{dt} = \frac{s^2}{2w} \sqrt{\frac{p}{\mu}} [R \quad T \quad N] \begin{bmatrix} 0 \\ 0 \\ \cos L \end{bmatrix} \quad (2.25)$$

$$\frac{dk}{dt} = \frac{s^2}{2w} \sqrt{\frac{p}{\mu}} [R \quad T \quad N] \begin{bmatrix} 0 \\ 0 \\ \sin L \end{bmatrix} \quad (2.26)$$

$$\frac{dL}{dt} = \sqrt{\mu p} \left(\frac{w}{p}\right)^2 + \frac{1}{w} \sqrt{\frac{p}{\mu}} [R \quad T \quad N] \begin{bmatrix} 0 \\ 0 \\ h \sin L - k \cos L \end{bmatrix}. \quad (2.27)$$

These equations of motion were derived in [110] but contained some typographical errors. As such, these have since been amended in [111] to give the form provided in this dissertation. It is noted that if there are no perturbations, Eqs. (2.22) - (2.26) are zero and Eq. (2.27) reduces to the angular momentum term.

## 2.6.5. Derivation of Locally Optimal Control Laws

Although locally optimal control laws have been derived in [104], [106]–[108], the specific control laws used within this dissertation, semi-major axis, eccentricity, inclination and radius of perigee, will be re-derived here for completeness. Only these control laws are required as this dissertation does not consider specific orbit insertion requirements. The control laws are derived in modified equinoctial elements as the trajectory is propagated using the equations of motion defined in modified equinoctial elements in Section 2.6.4 to avoid singularities associated with the classical elements.

The variational equation of any element is

$$\frac{d\sigma}{dt} = \mathbf{f} \cdot \hat{\boldsymbol{\lambda}}_{\sigma}, \quad (2.28)$$

where  $\sigma$  represents the respective element. For clarification, the classical orbital elements are shown in Figure 2-6.

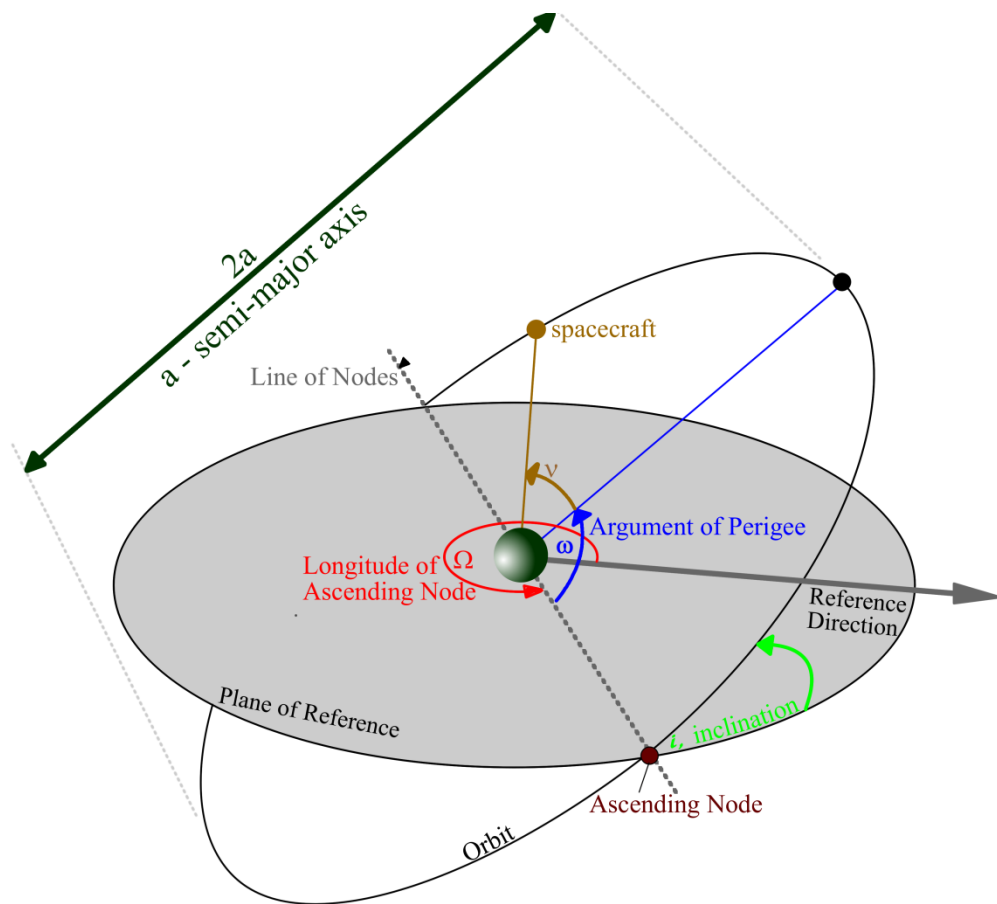


**Figure 2-6 Definition of classical orbital elements**

The required force,  $f$ , in the Radial, Transverse and Normal Axes (RTN), demonstrated in Figure 2-7, to maximise the rate of change of  $\sigma$ , is a unit vector defined by  $\hat{\lambda}_\sigma$ . By maximising the force along  $\hat{\lambda}_\sigma$ , the instantaneous rate of  $\sigma$  is also maximised. The variational equations are defined in Gaussian form as this allows each component of the perturbing acceleration to be identified [112], [113].

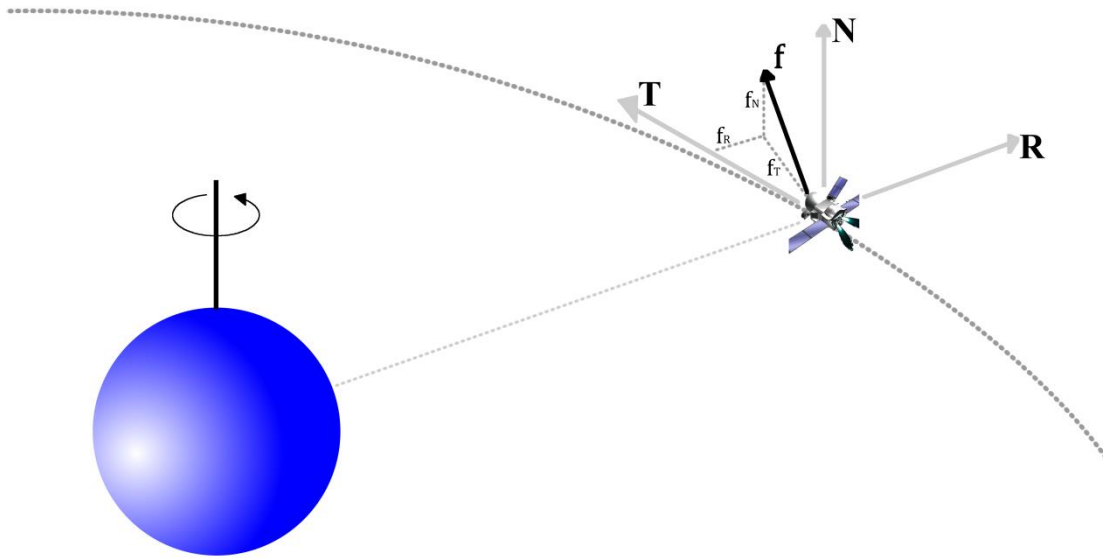


Figure 2-7 RTN co-ordinate reference frame

### 2.6.5.1. *Semi-Major Axis Control Law*

The semi-major axis variational equation can be defined in classical elements

$$\frac{da}{dt} = \frac{2a^2}{\sqrt{\mu p}} [R \quad T \quad N] \begin{bmatrix} e \sin \nu \\ 1 + e \sin \nu \\ 0 \end{bmatrix}. \quad (2.29)$$

By then identifying  $\lambda_a$  and converting to modified equinoctial elements, the maximised direction vector is

$$\lambda_a = \begin{bmatrix} e \sin \nu \\ 1 + e \sin \nu \\ 0 \end{bmatrix} = \begin{bmatrix} f \sin L - g \cos L \\ 1 + (f \cos L + g \sin L) \\ 0 \end{bmatrix}. \quad (2.30)$$

This can now be used to generate a locally optimal control law which will maximise the semi-major axis. This is also known as the energy gain control law as it gives a locally optimal variation in orbit energy.

### 2.6.5.2. Eccentricity Control Law

The eccentricity variational equation, defined in classical elements is

$$\frac{de}{dt} = \frac{p}{\mu} [R \quad T \quad N] \begin{bmatrix} \sin v \\ \cos v + \cos E \\ 0 \end{bmatrix}. \quad (2.31)$$

By identifying  $\lambda_e$  and converting to modified equinoctial elements, the maximised thrust direction vector is

$$\lambda_e = \begin{bmatrix} \sin v \\ \cos v + \cos E \\ 0 \end{bmatrix} = \begin{bmatrix} \frac{f \sin L - g \cos L}{\sqrt{f^2 + g^2}} \\ \frac{[f \sin L + g \cos L] \left[1 + \frac{r}{p}\right]}{\sqrt{f^2 + g^2}} + \frac{r\sqrt{f^2 + g^2}}{p} \\ 0 \end{bmatrix}. \quad (2.32)$$

### 2.6.5.3. Inclination Control Law

The inclination control law varies to the two previously defined. It depends only on the out of plane perturbation and as such a switching term is required in order to maintain the chosen rate of change; either positive or negative. It will change according to the argument of latitude. The variational equation for inclination defined in classical elements can be defined as

$$\frac{di}{dt} = \frac{r}{\sqrt{\mu p}} [R \quad T \quad N] \begin{bmatrix} 0 \\ 0 \\ \cos(v + \omega) \end{bmatrix}. \quad (2.33)$$

Identifying  $\lambda_i$ , converting to modified equinoctial elements and applying the switching term as discussed, the maximised thrust direction vector is

$$\lambda_i = \begin{bmatrix} 0 \\ 0 \\ \text{sgn}[\cos(v + \omega)] \end{bmatrix} = \begin{bmatrix} 0 \\ 0 \\ \text{sgn} \left[ \frac{h \cos(L) + k \sin(L)}{\tau} \right] \end{bmatrix}. \quad (2.34)$$

$$\text{where } \tau = \sqrt{h^2 + k^2}$$

#### 2.6.5.4. *Radius of Perigee Control Law*

The radius of perigee variational equation is formed of the semi-major axis and eccentricity equations in classical elements as

$$\frac{dr_p}{dt} = \frac{da}{dt} (1 - e) \frac{de}{dt} = a \sqrt{\frac{p}{\mu}} [R \quad T \quad N] \begin{bmatrix} \frac{2ae(1-e) \sin v}{p} - \sin v \\ \frac{2ae(1-e)(1-\cos v)}{p} - \cos v + \cos E \\ 0 \end{bmatrix}. \quad (2.35)$$

By identifying  $\lambda_{r_p}$  and converting to modified equinoctial elements, the maximised thrust direction vector is

$$\lambda_{r_p} = \begin{bmatrix} \frac{2ae(1-e) \sin v}{p} - \sin v \\ \frac{2ae(1-e)(1-\cos v)}{p} - \cos v + \cos E \\ 0 \end{bmatrix} = \begin{bmatrix} f \sin L - g \cos L \left[ \frac{2(1-\sqrt{f^2+g^2})}{1-f^2-g^2} - \frac{1}{\sqrt{f^2+g^2}} \right] \\ \frac{2(1-\sqrt{f^2+g^2})(1+f \cos L + g \sin L)}{1-f^2-g^2} + \left( \frac{f \cos L + g \sin L}{\sqrt{f^2+g^2}} + \cos E \right) \\ 0 \end{bmatrix}. \quad (2.36)$$

#### 2.6.5.5. *Blending Method*

As was discussed previously, locally optimal control laws can be used to generate complex trajectories with varying mission constraints. However the effectiveness, and therefore optimality of these control laws, is often dependent on how they are combined or ‘blended’ to form a near optimal thrust direction vector. It is possible to generate trajectories without blending, as was shown in [102] where the control laws were used sequentially, however these will only be near-optimal for specific trajectories. One method demonstrated in [103] applies weighting constants to each control law as part of the blending procedure. These weighting constants are then optimised in a numerical optimisation process. Although this can offer accurate solutions, it results in weighting constants that are dependent on time and

therefore could not function as a fully autonomous guidance controller. Furthermore, the optimisation process would be intensive due to the optimal weights being calculated at every time step. This method was modified slightly in [104] so that the weighting constants were determined through additional user defined constants so as to avoid an optimisation procedure. However the resultant weighting constants were still dependent on time and required sound engineering judgment to determine the constants. In [114] a ‘time-to-go’ concept was introduced which was based around comparing the current and final orbit states. In [106] a blending method known as (A<sup>n</sup>D) was suggested for use in generating solar sail trajectories with a constrained thrust direction vector. It was proposed in this work that weighting constants be calculated as a function of the osculating elements as opposed time; thus enabling the potential controller to account for unforeseen perturbations in the trajectory. This method calculated the weights for each control law based on the sail’s time to target if it solely used that control law and its effective use of the sail. A user defined constant was again used here to tailor the trajectories to suit certain mission specifications.

The method implemented in this dissertation is closely related to that of [106] but does incorporate some of the ideas discussed in [103], [104], [114]. It is adopted here to suit low-thrust technologies without the limitations of a sail i.e. the thrust can be directed in any direction as and when it is required. Firstly, the deficit (time to target) of each control law is calculated based on the maximised thrust vector if it were solely used and assuming a constant rate of change. These are then normalised with respect to the largest, resulting with each control law receiving a score between zero and one: zero meaning the control law has achieved its target and one meaning it is furthest, in terms of time, from its target value. The control laws are then multiplied by a constant,  $W_{\sigma}$ , based on mission specification before finally being blended using the averaging technique

$$\hat{\lambda}_b = \frac{\sum W_{\sigma} \hat{\lambda}_{\sigma}}{\|\sum W_{\sigma} \hat{\lambda}_{\sigma}\|} \quad (2.37)$$

where  $\sigma = a, e, r_p, i$ .

This now forms the maximised thrust direction vector. Again this method is dependent on a weighting constant which somehow needs to be determined. However, as this constant is independent of time and is specified at the beginning of the trajectory design, it can easily be determined in a non-intensive optimisation procedure as will be discussed in Chapter 5.

## 2.7. Hybrid Propulsion Trajectory Optimisation

Several of the papers already discussed in Section 2.3 have considered different methods of addressing the issues associated with optimisation of hybrid propulsion transfers. In addition, there has been research that used a pre-calculated transfer array which can be interpolated in order to speed up the transfer analysis [56]. The initial analysis in this method was therefore computationally heavy but for any other transfers it meant there was a rapid estimation available. This method obviously has a speed advantage but it is limited as it can only evaluate transfers in the region of the initial analysis. The accuracy of the resultant interpolated solutions is also dependent on the discretisation of the initial solutions. Other papers have used a patching method allowing the high and low-thrust transfer sections to be decoupled and hence reducing the overall optimisation complexity as each section is analysed individually as discussed previously [52]–[54]. Although this patching method can offer near-optimal solutions, it still requires a large amount of user time and knowledge to ensure the different trajectories can be connected. There is however a program which has been developed to optimise a full hybrid propulsion transfer. This is called SEPSHOT and was developed at the NASA Glen research facility [115]. In coupling the high thrust section this program assumes the spacecraft begins in a circular orbit and can impart a maximum of two high-thrust impulses before the low-thrust system is activated. The total velocity change for the high-thrust section is specified and if the first required impulse is equal or greater than this then the high-thrust section is restricted to one impulse. If the first required impulse

is less, then the transfer is a two burn orbit raise. In this case the second burn is the difference between the total specified velocity change and the first burn velocity change. Several problems have been identified with SEPSHOT however, specifically related to its sensitivity to the initial guesses and convergence problems [103].

To avoid the need for user input and sensitivity issues, this dissertation will develop a new hybrid propulsion transfer optimiser which models the high-thrust phase as a Hohmann transfer and generates the low-thrust trajectory using locally optimal control laws. The optimisation process is detailed in Chapter 5.

# Chapter 3

---

## HOHMANN AND BI-ELLIPTIC TRANSFER COMPARISON

In Chapter 2 the Hohmann and bi-elliptic transfers were introduced and a detailed discussion of previous research comparing the transfers was presented. In particular, it was shown that critical limits were determined for the co-planar analysis and these determine when each transfer should be used to ensure the lowest velocity requirement. Obvious progression is to investigate the transfers with the introduction of a plane change and while there has been extensive research in this area, a general solution for the evolution of the critical limits has not been explicitly determined. This chapter will therefore further investigate the Hohmann and bi-elliptic transfers with the inclusion of a plane change, to determine the evolution of the critical limits determined for the co-planar analysis. The chapter builds on the knowledge of the transfers introduced in Chapter 2 by introducing the relevant theory for transfers with combined orbit raise and plane change manoeuvres. An analytical method is detailed in Section 3.1.1 that determines the distribution of plane change between two impulses and is compared to a full numerical approach in Section 3.1.2 to validate its use within the work presented. With use of this analytical plane change distribution method, the derivation of simple analytical expressions for the velocity requirement of the Hohmann and bi-elliptic transfers is given in Sections 3.2 and 3.3 respectively. Finally the chapter determines the evolution of critical limits with varying plane change and provides an explicit general solution to when each transfer should be used.

## 3.1. Plane Change Distribution Theory

### 3.1.1. Analytical Methodology

As was discussed in Chapter 2 when transferring between two non-co-planar orbits, it is more efficient to perform the plane change over two impulses rather than entirely at the transfer orbit apogee [1], [28]–[30], [116]. It has also been shown that that the orbit raise and plane change manoeuvres should be coupled, where possible, as this is more fuel effective than performing each separately [116]. With this in mind, a schematic of the transfers is shown in Figure 3-1.

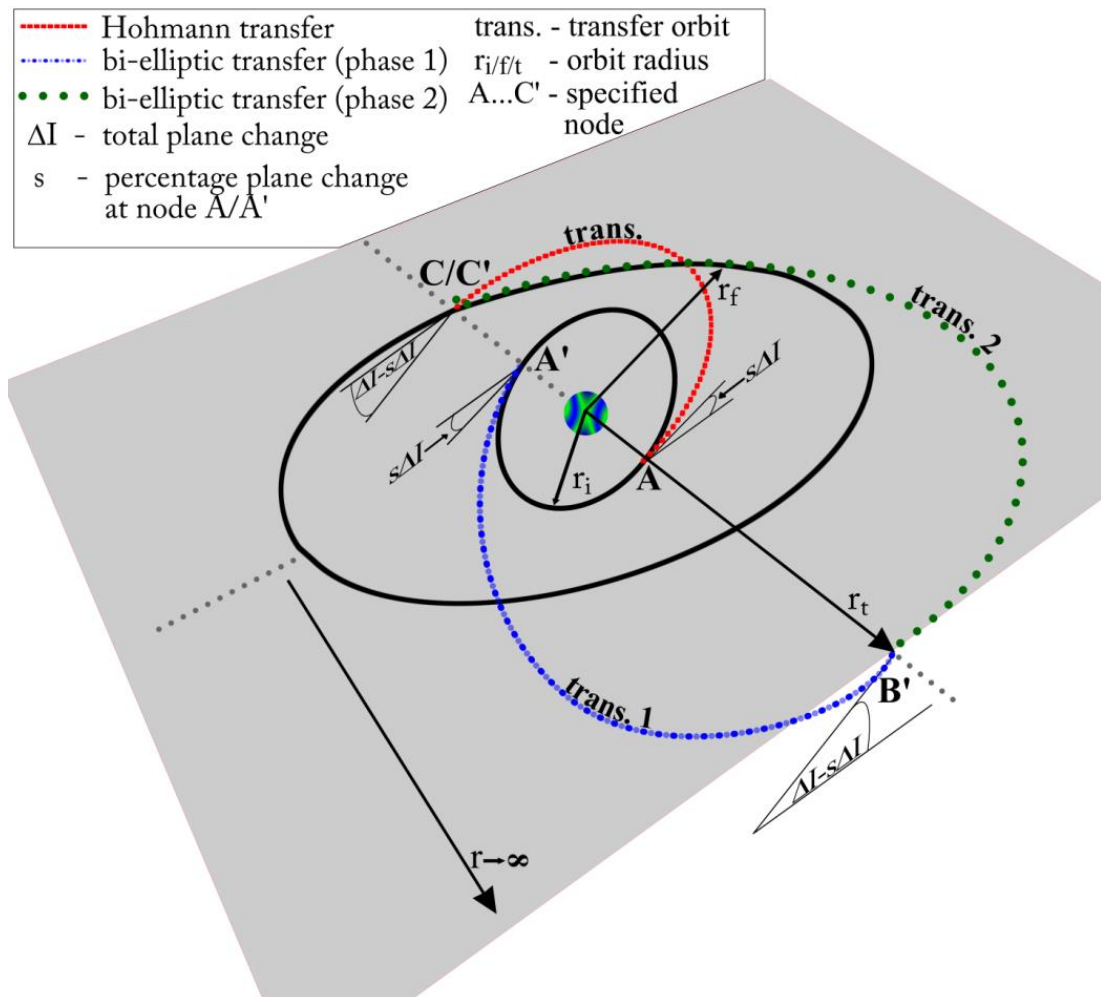


Figure 3-1 Hohmann and bi-elliptic transfers with plane change at first and second impulses

To derive simple equations that describe the velocity requirement of the Hohmann and bi-elliptic transfers with the inclusion of a plane change, an analytical approximation of the plane change distribution based on the orbit configuration is used [116]. This is compared to the numerical approach in Section 3.1.2 for a specific transfer to validate its use and highlight its limitations. It is of note that the referenced method used is enhanced to account for transfers other than circular-circular.

The velocity requirement to perform a combined orbit raise and plane change is calculated by comparing the initial and final velocity vectors, as well as the plane change required. The general case is defined in Eq. (3.1) and is applicable for both the Hohmann and bi-elliptic transfers, with the bi-elliptic transfer performing the plane change over the first two impulses and the third impulse being a co-planar manoeuvre. While it is recognised that the optimal bi-elliptic transfer will split the plane change across all three impulses [28]–[30], [117], this would again prevent a general solution to the evolution of the critical limits. In the optimal plane change distribution case detailed in [29], it is shown that the largest plane change is conducted at the second impulse<sup>1</sup> (largest apogee) with the plane change conducted at the third impulse always less than that at the first impulse. It is therefore logical to assume that by splitting the plane change across the first two impulses, the total velocity requirement is only slightly greater than that of the optimal case. By doing this the analysis is simplified, allowing the use of the velocity requirement equations defined hereafter and therefore enabling the determination of the evolution of the critical limits. Equation (3.1) is an extension of the cosine law as part of vector analysis [118], where  $\Delta V_i$  and  $\Delta V_f$  represent the velocity requirement to enter the transfer orbit and then the final/intermediate orbit respectively,

---

<sup>1</sup> In [29] it is shown for  $r_f/r_i = 1$ ,  $r_t/r_i = 2$  and  $\Delta I \leq 10^\circ$ , the plane change is optimally split between the first and third impulses with no plane change conducted at the second impulse. This is not relevant in this analysis however as the evolution of the critical limits at  $r_f/r_i = 1$  determine  $\Delta I > 35^\circ$  as shown later in this chapter.

$$\begin{aligned}\Delta V &= \Delta V_i + \Delta V_f = \\ &\sqrt{v_i^2 + v_{trans_i}^2 - 2v_i v_{trans_i} \cos(\Delta I_i)} + \\ &\sqrt{v_f^2 + v_{trans_f}^2 - 2v_f v_{trans_f} \cos(\Delta I_f)}.\end{aligned}\tag{3.1}$$

As the orbit raise and plane change manoeuvre is conducted using two impulses, one to enter a transfer orbit and one to capture a target orbit, which in the case of a bi-elliptic transfer is a second transfer orbit, the question arises as to how much plane change to impart at each impulse of the manoeuvre. The analytical approximation, which distributes the plane change across two impulses, introduces a scaling term,  $s$ , dependent on the orbit geometry which defines the fraction of plane change to be performed with the first orbit raise manoeuvre. In Eq. (3.1),  $\Delta I_i$  becomes  $s\Delta I$  and  $\Delta I_f$  becomes  $(1 - s)\Delta I$  to give

$$\begin{aligned}\Delta V &= \Delta V_i + \Delta V_f = \\ &\sqrt{v_i^2 + v_{trans_i}^2 - 2v_i v_{trans_i} \cos(s\Delta I)} + \\ &\sqrt{v_f^2 + v_{trans_f}^2 - 2v_f v_{trans_f} \cos((1 - s)\Delta I)}.\end{aligned}\tag{3.2}$$

To gain the analytical approximation, begin by squaring the two velocities in Eq. (3.2) to remove the square roots. Ignoring the cross product terms ( $2\Delta V_i \Delta V_f$ ), allows simplification to,

$$\begin{aligned}\Delta V_i^2 + \Delta V_f^2 &\approx v_i^2 + v_{trans_i}^2 - 2v_i v_{trans_i} \cos(s\Delta I) + v_f^2 + v_{trans_f}^2 - \\ &2v_f v_{trans_f} \cos((1 - s)\Delta I).\end{aligned}\tag{3.3}$$

Equation (3.3) can then be differentiated with respect to  $s$  and set equal to zero in order to determine when the function is a minimum,

$$\frac{\partial(\Delta V_i^2 + \Delta V_f^2)}{\partial s} \approx 2\Delta I v_i v_{trans_i} \sin(s\Delta I) - 2\Delta I v_f v_{trans_f} \sin((1 - s)\Delta I) = 0.\tag{3.4}$$

Collecting terms and rearranging gives

$$\frac{\sin(s\Delta I)}{\cos(s\Delta I)} \approx \frac{v_f v_{trans_f} \sin(\Delta I)}{v_i v_{trans_i} + v_f v_{trans_f} \cos(\Delta I)} \quad (3.5)$$

which, with further simplification, gives the analytical approximation for the fraction inclination split as

$$s \approx \frac{1}{\Delta I} \tan^{-1} \left[ \frac{\sin(\Delta I)}{X + \cos(\Delta I)} \right]. \quad (3.6)$$

where  $X = \frac{v_i v_{trans_i}}{v_f v_{trans_f}}$ .

As discussed previously,  $X$  can be modified depending on the transfer scenario under consideration by introducing the velocity formulas representative of the transfer. This allows Eq. (3.6) to be extended to the application of non-circular orbits. For the bi-elliptic transfer, this is accounted for and  $X$  is adjusted accordingly. The total velocity requirement, with Eq. (3.6) substituted to account for  $s$ , is therefore given in Eq. (3.7), which has been divided by the initial orbit velocity to provide a convenient non-dimensional form.

$$\begin{aligned} \frac{\Delta V}{v_i} = & \sqrt{1 + \frac{v_{trans_i}^2}{v_i^2} - 2 \frac{v_{trans_i}}{v_i} \cos \left( \tan^{-1} \left[ \frac{\sin(\Delta I)}{\frac{v_i v_{trans_i}}{v_f v_{trans_f}} + \cos(\Delta I)} \right] \right)} + \\ & \sqrt{\frac{v_f^2}{v_i^2} + \frac{v_{trans_f}^2}{v_i^2} - 2 \frac{v_f v_{trans_f}}{v_i^2} \cos \left( \Delta I - \tan^{-1} \left[ \frac{\sin(\Delta I)}{\frac{v_i v_{trans_i}}{v_f v_{trans_f}} + \cos(\Delta I)} \right] \right)} \end{aligned} \quad (3.7)$$

### 3.1.2. Numerical Validation

To verify Eq. (3.7) it is necessary to perform a numerical analysis to determine the plane change performed at the first impulse, that is, without the removal of the cross product term that enables the simplification to Eq. (3.3). This allows the error over a range of plane changes to be determined. To perform the numerical analysis, Eq. (3.2) can be partially

differentiated with respect to  $s$  and set equal to zero to determine when the function is a minimum,

$$\sin s\Delta I = \frac{\Delta V_i v_f v_{transf} \sin((1-s)\Delta I)}{\Delta V_f v_i v_{transi}}. \quad (3.8)$$

As  $\sin s\Delta I$  appears on both sides, it is necessary to perform an iterative root-finding method to determine the fraction of plane change performed at the first impulse,  $s$ . This optimal value is then substituted into Eq. (3.2) to give the total velocity requirement to perform the orbit raise and plane change.

Before comparing the two approaches for coupled orbit raise and plane change manoeuvres however, the numerical method can be verified by comparing its velocity requirement with that of Eq. (3.9), for a plane change manoeuvre alone,

$$\frac{\Delta V_{INC}}{v_i} = 2 \sin\left(\frac{\Delta I}{2}\right). \quad (3.9)$$

Equation (3.9) has been divided by the initial orbit velocity to give a non-dimensional form similar to Eq. (3.7). From Figure 3-2 it is seen that the numerical method maintains the same characteristics as the analytical plane change, Eq. (3.9), for a range of plane change values. Although not visible in Figure 3-2, the maximum relative percentage error between the numerical method, with a solution tolerance of  $1 \times 10^{-5}$ , and Eq. (3.9) is 0.02% for plane changes up to  $\pi/2$  rad ( $90^\circ$ ). An upper limit of  $90^\circ$  is imposed as retrograde orbits are not considered in this analysis. This error is small enough that Eq. (3.2), where  $s$  is numerically determined, can be used to verify Eq. (3.7).

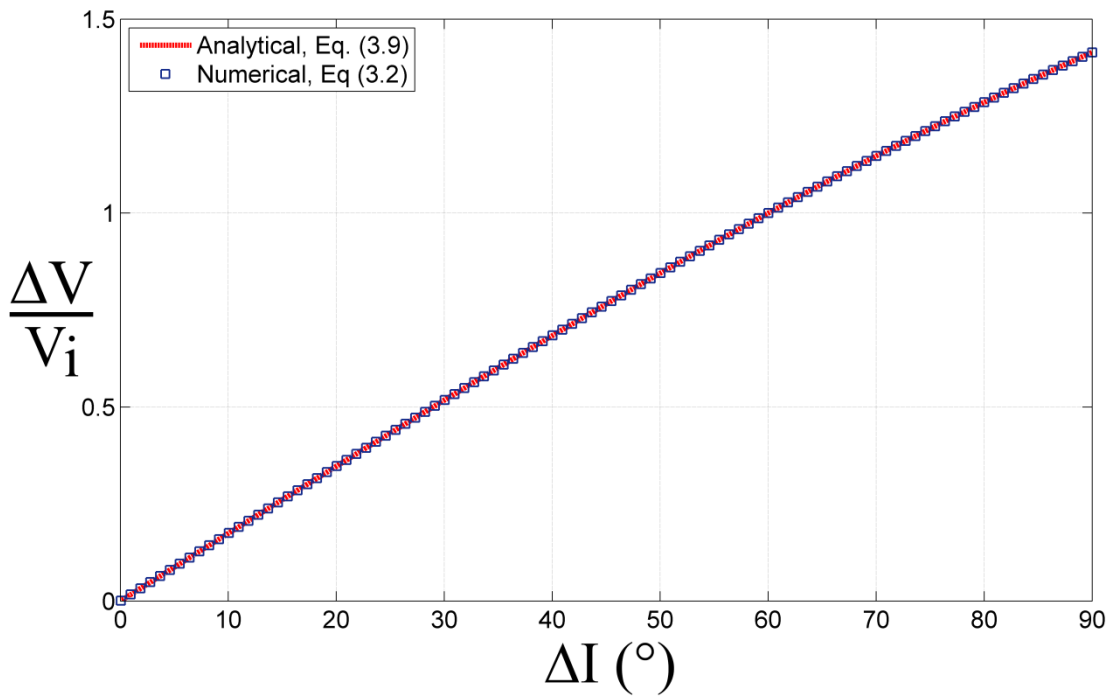


**Figure 3-2 Total velocity requirement comparison for circular orbit with plane change only**

The relative percentage error of total velocity requirement for a range of coupled orbit raise and plane change manoeuvres is shown in Figure 3-3. It can be seen that the largest error is found for large plane changes and small orbit ratios ( $r_f/r_i \rightarrow 1, \Delta I \rightarrow \pi/2 \text{ rad } (90^\circ)$ ) with a maximum relative percentage error of 12.36%. The average relative percentage error for the range considered in Figure 3-3 is 0.81%. If considering transfers with  $r_f/r_i$  approaching unity and large plane changes then a numerical approach should be adopted, however this scenario is very unlikely and hence the analytical method is deemed acceptable for this analysis.

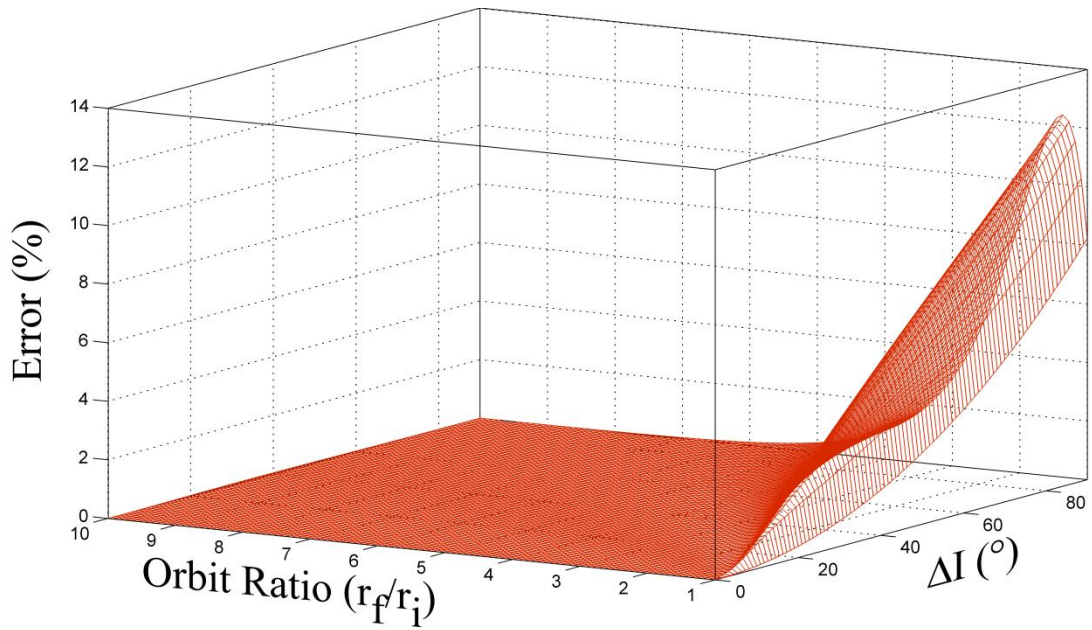


Figure 3-3 Relative percentage error of Eq. (3.6) compared to Eq. (3.2) with numerical method

## 3.2. Hohmann Transfer with Plane Change

Using the analytical plane change distribution theory from the previous section, the equations describing the Hohmann transfer can be defined as

$$v_i = \sqrt{\frac{\mu}{r_i}} \quad (3.10)$$

$$v_{transA} = \sqrt{\frac{2\mu}{r_i} - \frac{2\mu}{r_i+r_f}}. \quad (3.11)$$

Equation (3.10) gives the initial orbit velocity and Eq. (3.11), the transfer velocity at point A, defined in Figure 3-1. Equations (3.12) and (3.13) describe the transfer velocity at point C and the final orbit velocity respectively.

$$v_{transC} = \sqrt{\frac{2\mu}{r_f} - \frac{2\mu}{r_i+r_f}} \quad (3.12)$$

$$v_f = \sqrt{\frac{\mu}{r_f}} \quad (3.13)$$

The total velocity requirement to perform the Hohmann transfer with plane change is therefore given in Eq. (3.14). Note that an orbit ratio  $R$  ( $r_f/r_i$ ) has been introduced for the

purposes of simplification and the equation has been divided by the initial circular velocity,  $v_i$ , to give a convenient non-dimensional form as before,

$$\frac{\Delta V_{HT}}{V_i} = \sqrt{1 + \frac{2R}{1+R} - \sqrt{\frac{8R}{1+R}} \cos\left(\tan^{-1}\left[\frac{\sin(\Delta I)}{\sqrt{R^3 + \cos(\Delta I)}}\right]\right)} + \sqrt{\frac{1}{R} + \frac{2}{R^2+R} - \sqrt{\frac{8}{R^2+R^3}} \cos\left(\Delta I - \tan^{-1}\left[\frac{\sin(\Delta I)}{\sqrt{R^3 + \cos(\Delta I)}}\right]\right)} \quad (3.14)$$

To verify this equation, the plane change can be assumed to equal zero and the equation shown to simplify to represent the same result as [9]. Further validation can be sought by differentiating Eq. (3.14) with respect to  $R$ , and solving to find the location of the stationary point. It is found that  $R = 15.58171874$  which is the same value found in [9] using the co-planar equation. The stationary point, from this point forward known as limit CoB to represent the co-planar limit on limit B (introduced later in the chapter), is found to be a maximum and determines the orbit ratio,  $R$ , beyond which the velocity requirement starts to reduce. This suggests that travelling to a far removed orbit ( $r_t > r_f$ ) and returning to the target may offer a reduction in the required change of velocity and is the origin of the bi-elliptic transfer which will be discussed in more detail in the next section. Considering the limiting case for an intermediate orbit at infinite distance, the initial velocity requirement is the velocity necessary to escape the initial orbit that is simply the limit of Eq. (3.14) assuming  $R \rightarrow \infty$  and scaled by  $v_i$ ,

$$\Delta V_{\infty e} = (\sqrt{2} - 1)V_i. \quad (3.15)$$

The final velocity requirement is the velocity necessary to return from infinity to the target orbit but scaled by the target orbit velocity,  $v_f$ ,

$$\Delta V_{\infty r} = (\sqrt{2} - 1)V_f. \quad (3.16)$$

The total velocity requirement is therefore the sum of Eqns. (3.15) and (3.16) and once again divided by  $V_i$  to give a non-dimensional form,

$$\frac{\Delta V_{\infty}}{V_i} = (\sqrt{2} - 1) \left( 1 + \sqrt{\frac{1}{R}} \right). \quad (3.17)$$

This is the same result, in a slightly different form, as was introduced in Eq.(2.7) in Chapter 2 and although Eq. (3.14) contains a term for the plane change, the limiting case as shown in Eq. (3.17) does not due to the plane change being performed at infinity where no change in velocity is required. This is representative of a parabolic transfer. Equation (3.17) is highlighted in Figure 3-4 along with the Hohmann transfer velocity requirement. An intersection point is found by equating Eq. (3.14), with no plane change, with Eq. (3.17) and solving for  $R$ . This is found to be  $R = 11.93876547$  which is again the same value found in [9] and represents a limit of the Hohmann transfer, from here onwards known as limit CoA to represent the co-planar limit on limit A (introduced later in the text). For any  $R < 11.93876547$ , the Hohmann transfer will always have the lowest velocity requirement. Both transfer limits CoA and CoB are highlighted in Figure 3-4.

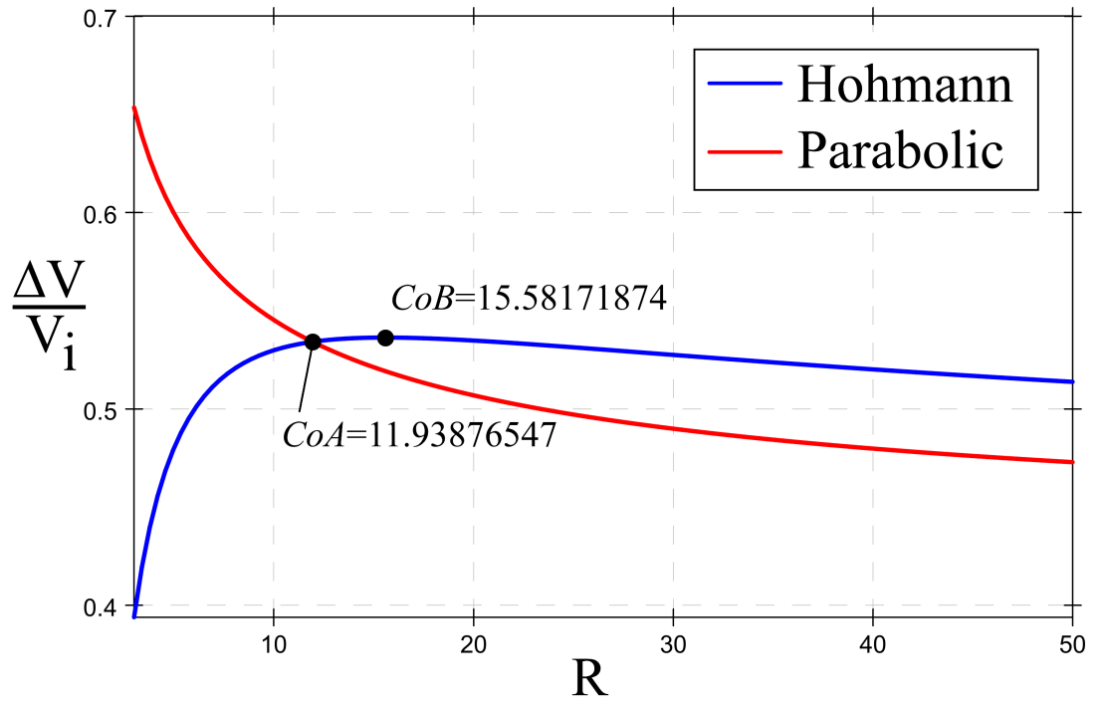


Figure 3-4 Hohmann and parabolic transfer comparison with critical limits (verified with [9])

### 3.3. Bi-elliptic Transfer with Plane Change

The analytical plane change distribution methodology can again be used when considering the bi-elliptic transfer with plane change. As was discussed previously however, the plane change is distributed between the first two impulse burns with the third being a co-planar manoeuvre. To determine the total velocity requirement equation, the initial and final orbit velocities remain the same as those given in Eqns. (3.10) and (3.13) respectively. The orbit velocities at nodes  $A'$  and  $B'$ , as detailed in Figure 3-1, are

$$v_{trans1A'} = \sqrt{\frac{2\mu}{r_i} - \frac{2\mu}{r_i+r_t}} \quad (3.18)$$

$$v_{trans1B'} = \sqrt{\frac{2\mu}{r_t} - \frac{2\mu}{r_i+r_t}} \quad (3.19)$$

As was discussed when introducing the co-planar bi-elliptic transfer in Chapter 2, the spacecraft is propelled on an initial elliptical trajectory with apogee radius greater than the target orbit radius. At this transfer apogee,  $r_t$ , the spacecraft enters a new ellipse and travels

back towards the target. The velocities at points  $B'$  and  $C'$ , as defined in Figure 3-1 are therefore

$$v_{trans2B'} = \sqrt{\frac{2\mu}{r_t} - \frac{2\mu}{r_t+r_f}} \quad (3.20)$$

$$v_{trans2C'} = \sqrt{\frac{2\mu}{r_f} - \frac{2\mu}{r_t+r_f}} \quad (3.21)$$

The total velocity requirement to perform the bi-elliptic is then the sum of the impulses required to transfer to each orbit. The total velocity requirement for the bi-elliptic transfer with plane change, in non-dimensional form, is given in Eq. (3.22). Note an additional orbit ratio between the intermediate orbit and initial orbit,  $R^*$  ( $r_t/r_i$ ), has been introduced in order to simplify the expression as it is now only dependent on  $R, R^*$  and  $\Delta I$ . This additional orbit ratio must always be greater than  $r_f/r_i$  i.e. ( $R^* > R$ ) for this analysis.

$$\begin{aligned} \frac{\Delta V_{BT}}{V_i} = & \sqrt{1 + \frac{2R^*}{1+R^*} - \sqrt{\frac{8R^*}{1+R^*}} \cos(\sigma_1)} + \sqrt{\frac{2}{R^{*2}+R^*} + \frac{2R}{R^{*2}+RR^*} - \frac{4}{\sqrt{R^{*3}}} \sqrt{\frac{RR^*}{R^{*2}+RR^*+R+R^*}} \cos(\sigma_2)} + \\ & \sqrt{\frac{1}{R} \left[ \sqrt{\frac{2R^*}{R+R^*}} - 1 \right]} \end{aligned} \quad (3.22)$$

where

$$\sigma_1 = \tan^{-1} \left[ \frac{\sin(\Delta I)}{\frac{\sqrt{R^{*3}\sqrt{R+R^*}}}{\sqrt{2R}} + \cos(\Delta I)} \right]$$

$$\sigma_2 = \Delta I - \tan^{-1} \left[ \frac{\sin(\Delta I)}{\frac{\sqrt{R^{*3}\sqrt{R+R^*}}}{\sqrt{2R}} + \cos(\Delta I)} \right].$$

In order to verify this equation, the same technique as before can be adopted. By setting the orbit ratio  $R^* = R$  and plane change  $\Delta I = 0$ , the equation reduces to give the same representation as the co-planar Hohmann equation.

### 3.4. ANALYSIS

The Hohmann and Parabolic transfers are shown for a varying range of orbit ratios and plane changes in Figure 3-5. It can be seen that the parabolic transfer maintains the same characteristics at all plane change angles as this manoeuvre is performed at infinity, as discussed previously. It can also be seen that these two surfaces intersect for a range of plane changes ( $\Delta I = 0 \rightarrow \cong 50^\circ$ ). This intersection is an extension of the co-planar limit CoA ( $R = 11.93876547$  at  $\Delta I = 0^\circ$ ), also shown in the figure. This non-co-planar limit will be known as limit A from this point forward. As can be seen in Figure 3-5, several points of limit A are shown which highlight the evolution of the limit with increasing plane change. To determine the equation representing limit A, Eq. (3.14) and Eq. (3.17) can be set equal to each other,

$$\frac{\Delta V_{HT}}{V_i} = \frac{\Delta V_\infty}{V_i}. \quad (3.23)$$

The intersection of the two surfaces at an orbit ratio of  $R = 1$ , as shown in Figure 3-5, is considered the lower boundary of limit A as  $R < 1$  (inward transfer) is not considered in this analysis. This intersection indicates for a plane change greater than this point, and any  $R \geq 1$ , the parabolic transfer has a lower velocity requirement than the Hohmann. The critical plane change at  $R = 1$  can be calculated numerically using Eq. (3.23), or analytically by setting Eq. (3.9) to equal Eq. (3.17), where it is a condition  $R = 1$  as Eq. (3.9) is valid for a plane change only manoeuvre. Using the analytical approach the plane change of the intersection at  $R = 1$  is found as  $\Delta I_{CA} = 0.854$  rad ( $48.94^\circ$ ) where the subscripts represent the critical point calculated analytically. As no explicit analytical solution was found to be possible for the plane change,  $\Delta I$ , using Eq. (3.23), it can be solved for  $R = 1$  using a Newton iteration method [119] to give  $\Delta I_{CNA} = 0.834$  rad ( $47.78^\circ$ ). The subscripts introduced represent the numerical calculation of the critical point using the limit A

equation. The relative percentage error between the numerical, with a solution tolerance of  $1 \times 10^{-5}$ , and analytical methods is found as 2.34% and is due to the plane change methodology assumption described in the Section 3.1. As the analytical approach discussed is only valid for  $R = 1$ , Eq. (3.23) will be used whenever Limit A is referred to throughout the text. It should be noted that from this point forward, values calculated for all analyses are rounded to three decimal places. For calculations dependent on a previous result however, the number with at least seven decimal places is used to eliminate significant rounding errors.

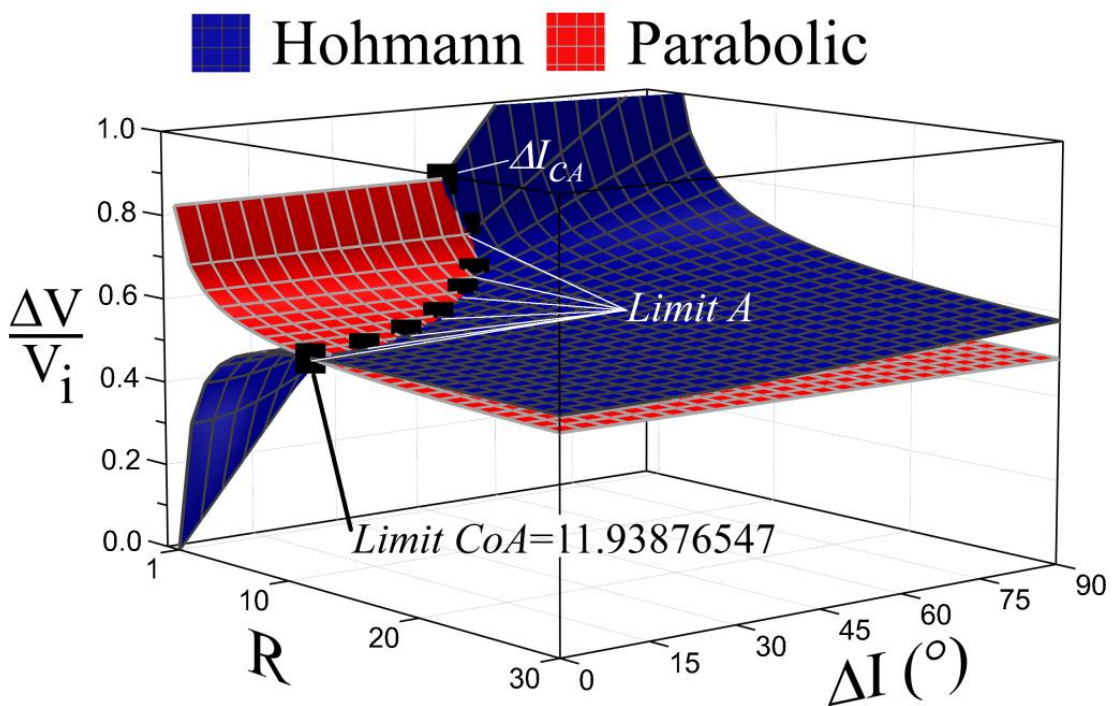


**Figure 3-5 Hohmann and parabolic transfer comparison for range of plane changes and orbit ratios**

Figure 3-6 - Figure 3-8 highlight the variation of the Hohmann, bi-elliptic and parabolic transfers for a range of orbit ratios,  $R$ , and plane changes,  $R^*$ . The Hohmann transfer is the blue line defined by  $R^* = R$ , the parabolic red with  $R^* = \infty$  and the bi-elliptic with different  $R^*$  values is black, as shown in each figure. In all figures it can be seen for  $R^* = 40$  there is an intersection at  $R = 40$  which again confirms the bi-elliptic equation reduces to the Hohmann. Beyond this intersection  $R > R^*$  and, as shown in the figures, the Hohmann offers

the lowest velocity requirement. This transfer would have a target orbit larger than both the initial and intermediate orbits and as a result, as found in [9], [116], the Hohmann transfer will always outperform the bi-elliptic. As discussed in [116], such transfers are ultimately phasing orbits and can be shown to be variants of the Hohmann transfer. This would also be the case beyond  $R = R^* = 200$ .

In Figure 3-6, it can be seen the bi-elliptic transfer, with an intermediate orbit,  $R^* = 15.58171874$  is coincident with the Hohmann transfer ( $R^* = R$ ) at  $R = 15.58171874$ . This is the co-planar limit CoB as discussed earlier and is found by differentiating the bi-elliptic transfer velocity requirement with respect to  $R^*$ , then setting  $R^* = R$  and solving to determine the turning point,

$$\frac{\partial \frac{\Delta V_{BT}}{V_i}}{\partial R^*} = 0 \Big|_{R^*=R}. \quad (3.24)$$

Equation (3.24) determines when the bi-elliptic transfer velocity requirement function is a turning point for a given transfer specification (specific  $R$  and  $\Delta I$ ) and has the same velocity requirement as the Hohmann transfer ( $R^* = R$ ). This equation can then be used to determine the evolution of the co-planar limit into the non-co-planar realm, known as limit B from this point forward, as shown in Figure 3-7 and Figure 3-8 as the black dot at the point of coincidence with the Hohmann transfer line. This occurs at an orbit ratio,  $R = 13$ , for a plane change,  $\Delta I = 21.152^\circ$  in Figure 3-7 and an orbit ratio,  $R = 10$ , for a plane change,  $\Delta I = 31.852^\circ$  in Figure 3-8. The orbit ratios,  $R$ , used in Figure 3-7 and Figure 3-8 were arbitrary values chosen so that Eq. (3.24) could be solved to determine the corresponding plane change,  $\Delta I$ , which defines limit B. Both Figure 3-7 and Figure 3-8 show that with increasing plane change, the orbit ratio,  $R$ , which beyond the bi-elliptic transfer offers the lowest velocity requirement, is reducing.

It was found earlier in the chapter that limit CoB could also be calculated by solving Eq. (3.14), differentiated with respect to  $R$ , and set equal to zero i.e. a maximum turning point on the Hohmann transfer velocity requirement function. However, by comparing this approach with that of Eq. (3.24) for different plane changes, it is found that Eq. (3.14) is only valid for  $\Delta I = 0^\circ$ . Although not shown in Figure 3-7 and Figure 3-8, the location of the maximum turning points are  $R = 12.642$  and  $R = 9.13$  respectively.

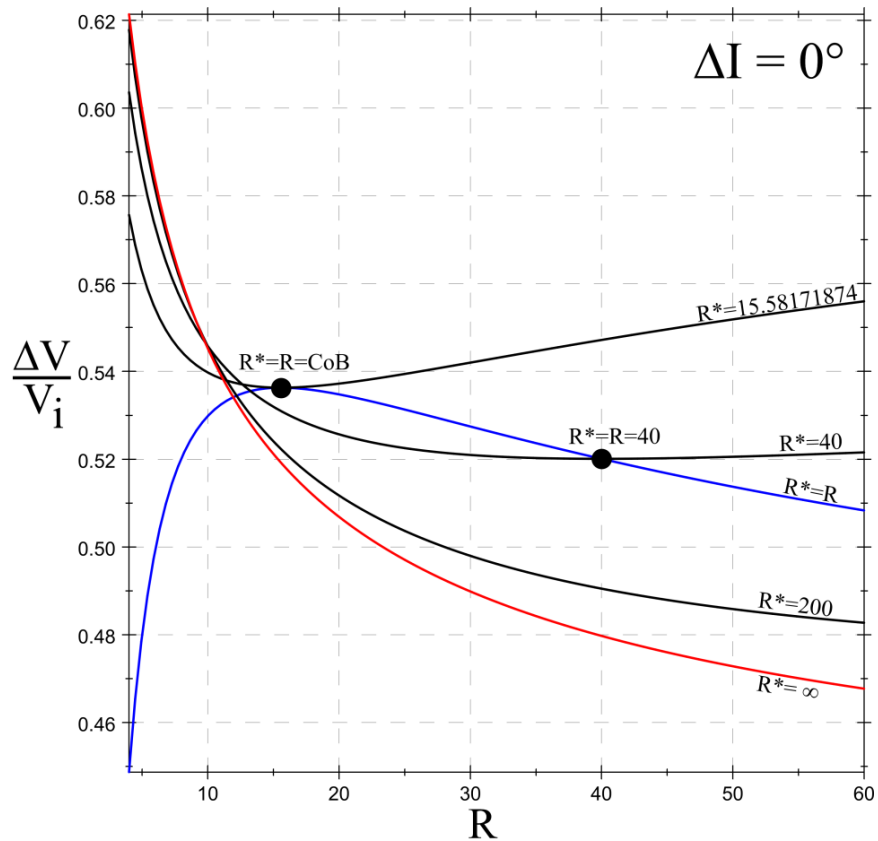


Figure 3-6 All transfers for varying orbit ratios at a plane change,  $\Delta I = 0^\circ$

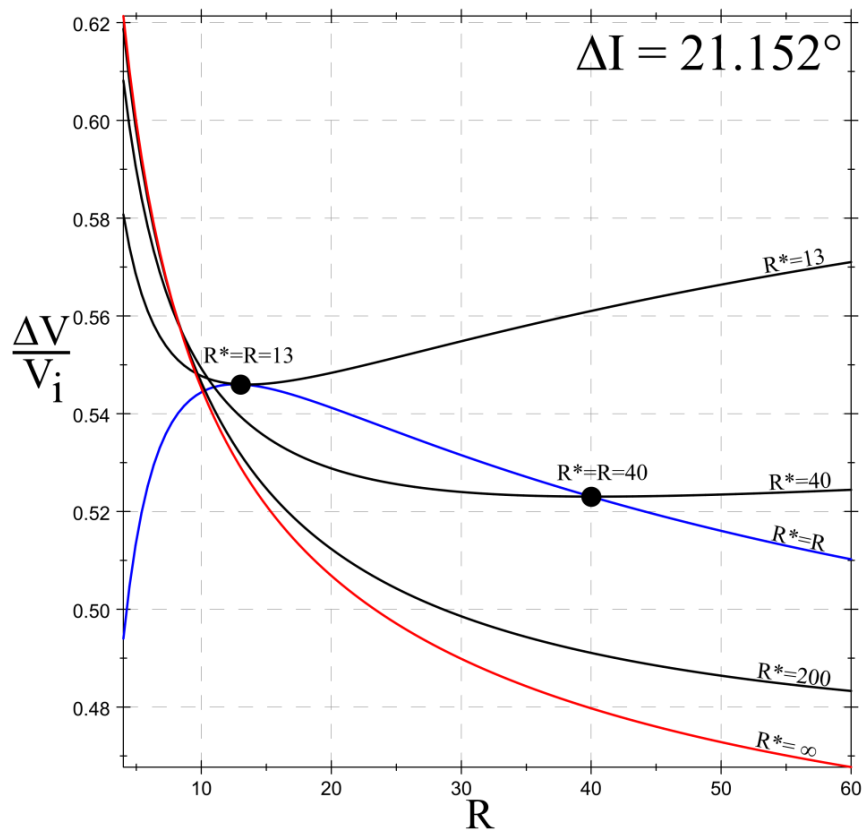


Figure 3-7 All transfers for varying orbit ratios at a plane change,  $\Delta I = 21.152^\circ$

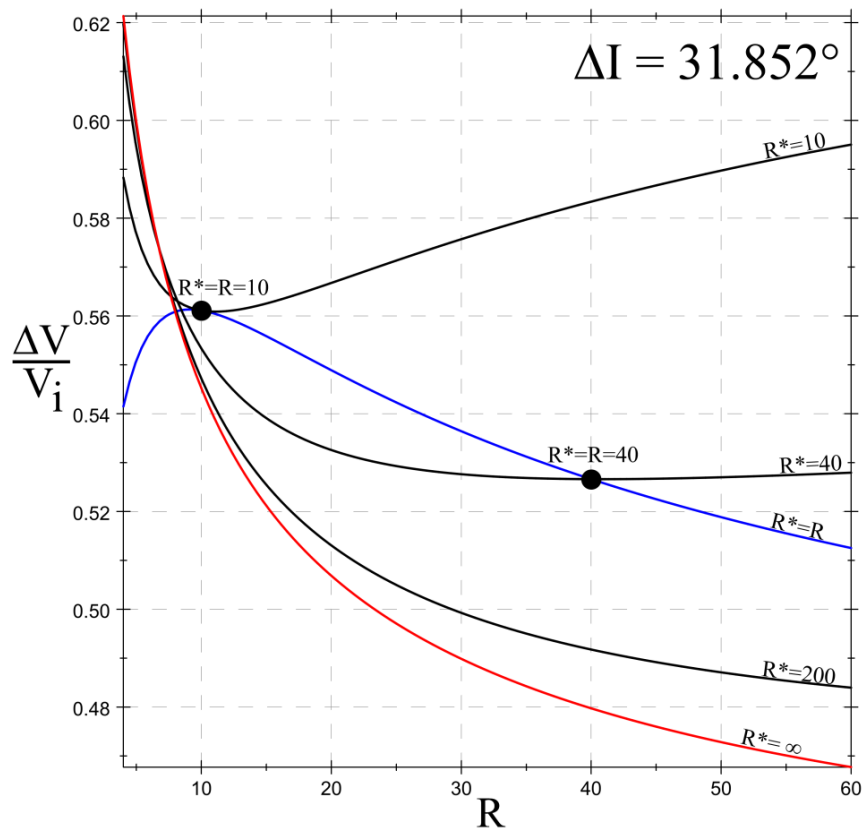


Figure 3-8 All transfers for varying orbit ratios at a plane change,  $\Delta I = 31.852^\circ$

Figure 3-9 offers a slightly different perspective of the cases detailed in Figure 3-6 - Figure 3-8 as it displays the velocity requirement for a varying  $R^*$  as opposed to  $R$ . The lines in blue represent the Hohmann transfer for the plane changes specified while the red lines represent a bi-elliptic transfer for the plane change specified. For each plane change,  $\Delta I = 0^\circ, 21.152^\circ$  and  $31.852^\circ$ , there are coincidence points between the Hohmann and bi-elliptic transfers at orbit ratios  $R = 15.5817187410, 13$  and  $10$ , respectively. This point of coincidence is calculated using Eq. (3.24) and, for the cases shown, the bi-elliptic transfer velocity requirement function is a maximum turning point. This means for any  $R^* > R$ , the bi-elliptic transfer will have a lower velocity requirement than the Hohmann. By increasing the  $R^*$  distance, the velocity requirement saving can be increased as shown in Figure 3-9 as the difference between the red bi-elliptic transfer line and the black dotted line representing the Hohmann transfer velocity requirement for the specified orbit ratio,  $R$ . This is discussed in detail later in the section but where the Hohmann and bi-elliptic functions intersect does again show the evolution of limit B.

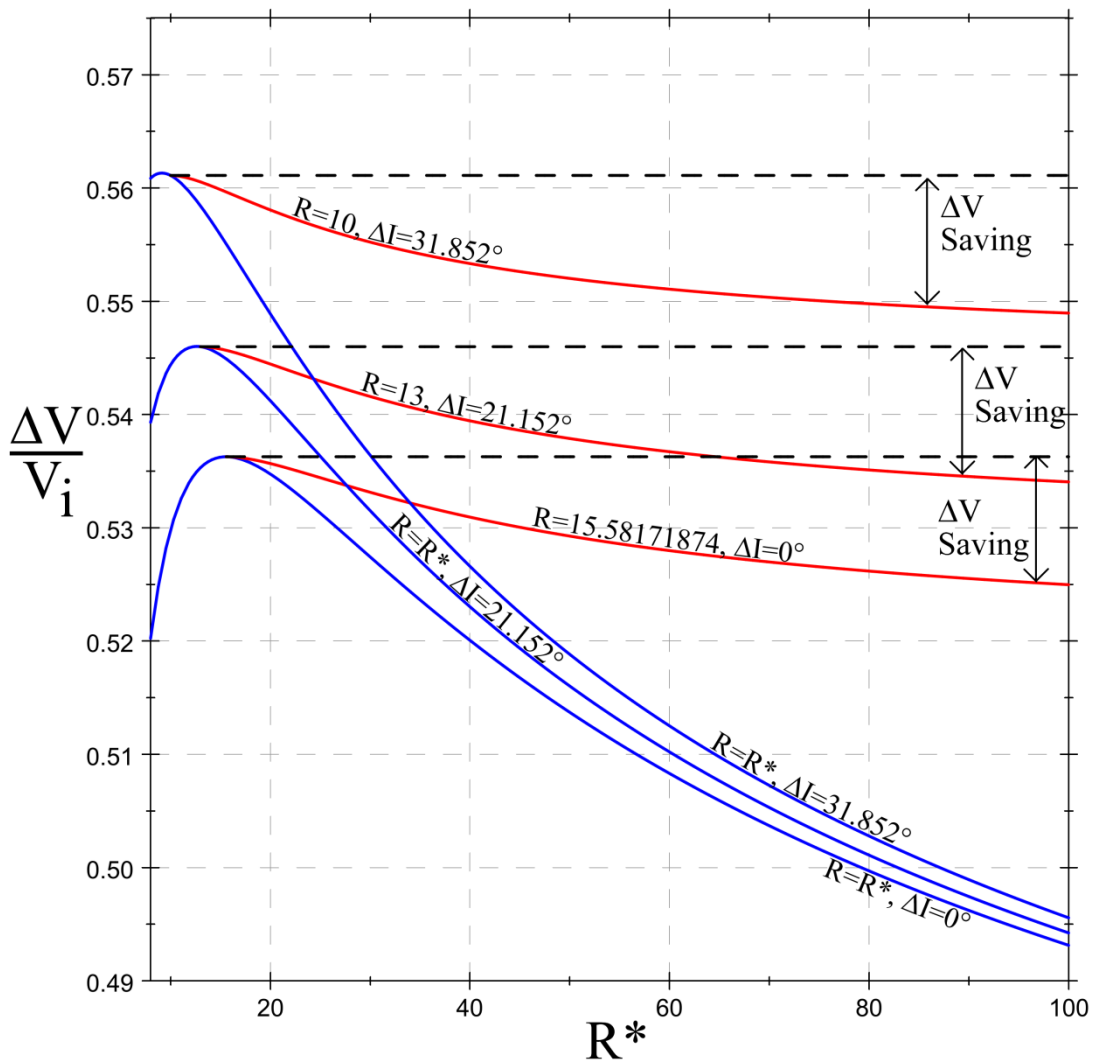
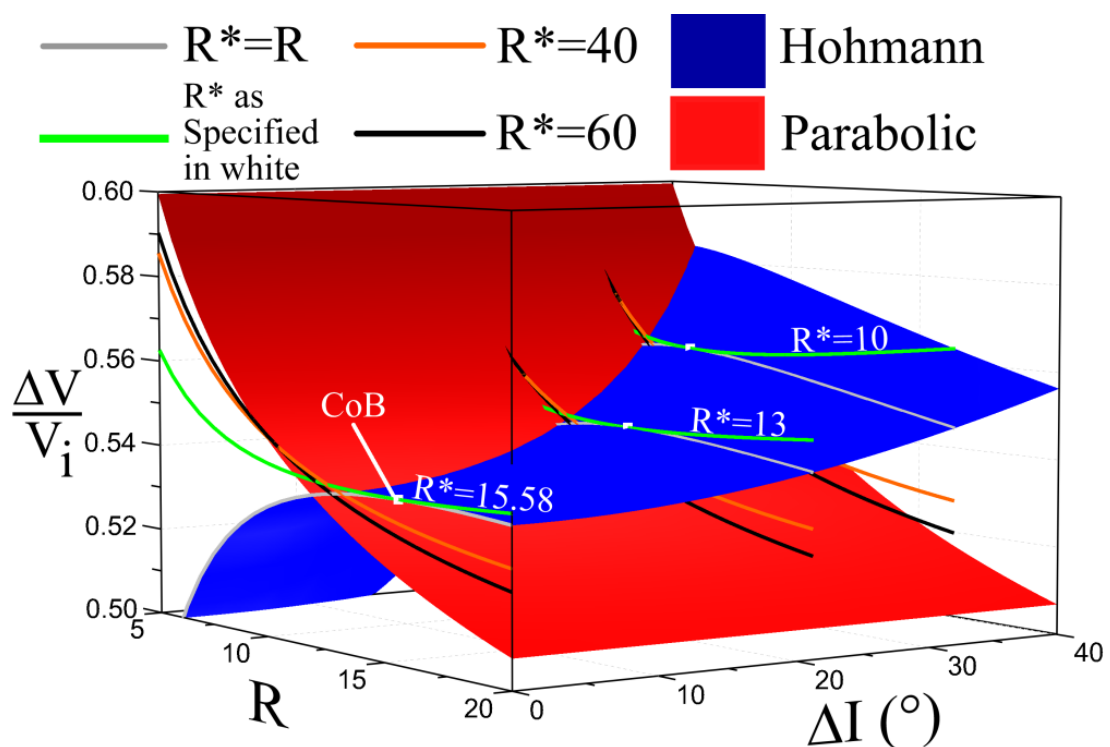


Figure 3-9 Hohmann and bi-elliptic transfers' velocity requirement for varying orbit ratio,  $R^*$  and plane change,  $\Delta I$

Figure 3-10 shows a comparison of the Hohmann, parabolic and bi-elliptic transfers over a range of orbit ratios,  $R$ , and plane changes,  $\Delta I$ . It builds on Figure 3-5- Figure 3-8 as it demonstrates both limits A and B on one single plot. The bi-elliptic transfer is represented by the lines for different intermediate to initial orbit ratios,  $R^*$ , as specified in the legend. The two surface plots are the same as that detailed in Figure 3-5; over a smaller range on all axes, most notably the  $\Delta V/v_i$  axis. The co-planar bi-elliptic orbit ratio limit, CoB, is represented as the white square at the coincident point between the grey line on the Hohmann surface and green line at  $\Delta I = 0 \text{ rad}$ . The grey line represents a co-planar Hohmann transfer and the green line is a co-planar bi-elliptic transfer with an intermediate orbit,

$R^* = \text{CoB} (15.58171874)$ , as specified in the white writing. It can be seen in the figure that the coincident point occurs at  $R = R^*$  as expected. This was also demonstrated in Figure 3-6.

The two remaining coincident points between the grey lines on the Hohmann surface and green lines with  $R^* = 13$  and  $10$  are the same coincident points that were shown in Figure 3-7 and Figure 3-8. They are represented by the white squares and are an extension of limit CoB and, as before, demonstrate the orbit ratio limit, at which the bi-elliptic transfer becomes the most effective transfer, is reducing. Again it can be seen the coincident points occur at  $R = R^*$  as expected.



From Figure 3-11, which is a two-dimensional projection of limit A and B, it is clear that both critical limits reduce at different rates for a range of plane change values, leading to two distinct Areas of Uncertainty (AOU). In order to determine the properties associated with each AOU, from here on defined as Area of Uncertainty 1 (AOU1) and Area of Uncertainty 2 (AOU2), it is necessary to consider the critical limits independently. Out with the two

AOU, it is clear from the figure which transfer should be selected to achieve the lowest velocity requirement for a transfer with a specific orbit ratio,  $R$ , and plane change,  $\Delta I$ .

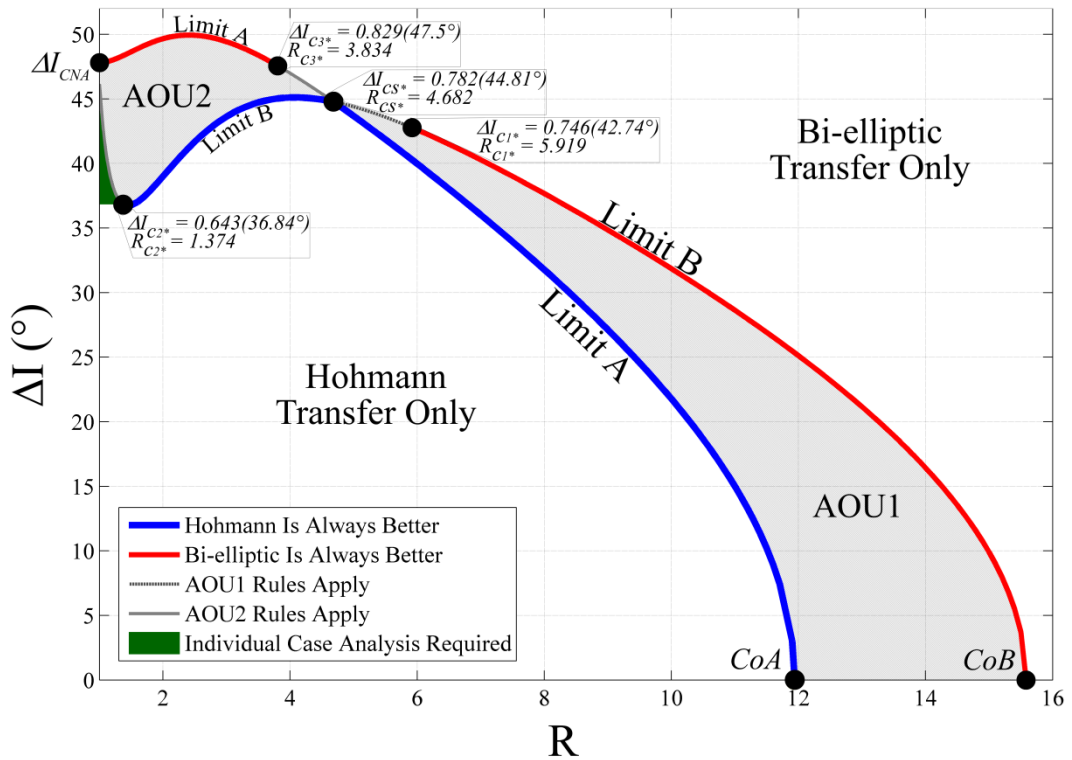


Figure 3-11 Transfer selection graph with areas of uncertainty and critical points

Considering AOU1, a test is required to determine which transfer has the lowest velocity requirement. This test was identified in [9] for the co-planar only analysis but is also applicable for transfers that include a plane change. It is conducted by setting the Hohmann and bi-elliptic transfer velocity requirement equations equal to each other, that is Eqs. (3.14) and (3.22) respectively,

$$\frac{\Delta V_{HT}}{V_i} = \frac{\Delta V_{BT}}{V_i} \quad (3.25)$$

and solving for  $R^*(R^*_{AOU1})$  for a given  $R$  and  $\Delta I$ . As no analytical solution was found for  $R^*$ , this is done numerically as before. Any intermediate to initial orbit ratio that exceeds this limit ( $R^* > R^*_{AOU1}$ ) ensures the bi-elliptic transfer velocity requirement is lower than the Hohmann. Below this point a Hohmann transfer is more effective. For AOU2 the same test

applies, however the bi-elliptic transfer only has a lower velocity requirement than the Hohmann for any intermediate orbit ratio that is less than this limit ( $R < R^* < R^*_{AOU2}$ ). In effect, the rules are opposite to that of AOU1 as the boundary lines have intersected. The change between the areas of uncertainty can be determined by simultaneously solving Eqs. (3.23) and (3.24); determining the switching point to have a transfer specification with an orbit ratio of  $R_{CS^*} = 4.682$  and plane change of  $\Delta I_{CS^*} = 0.782 \text{ rad}$  ( $44.81^\circ$ ).  $R_{C1/2^*}$  and  $\Delta I_{C1/2^*}$ , as specified in Figure 3-11, define the transfer specifications for critical point 1 and 2 respectively. These critical points describe the orbit transfer specification at which the function describing limit B, Eq. (3.24), changes from being a maximum turning point to a minimum. For any transfer specifications which lie on the limit line defined by Eq. (3.24), with an orbit ratio greater than the critical point 1 ( $R > R_{C1^*}$ ) and plane change less than critical point 1 ( $\Delta I < \Delta I_{C1^*}$ ) (i.e. the right-hand-side of critical point 1 on the boundary line of AOU1), the bi-elliptic transfer will always have a lower velocity requirement than the Hohmann. For the region between the switching point where AOU1 transitions into AOU2 and critical point 1 ( $R_{CS^*} > R > R_{C1^*}$ ), any combination of orbit ratio and plane change on limit B defined by Eq. (3.24) requires the same test using Eq. (3.25), as detailed previously for AOU1, to determine when the bi-elliptic outperforms the Hohmann transfer. For any transfer specification that lies on the line bounding AOU2, between critical point 2 and the switching point ( $R_{C2^*} < R < R_{CS^*}$ ), the bi-elliptic will never outperform the Hohmann transfer. For any transfer specification on the line bounding AOU2, between critical point 2 and the graph axis at  $R = 1$  ( $1 < R < R_{C2^*}$ ), the same test using Eq. (3.25), as required for a point lying within AOU2, must be used to determine when the bi-elliptic transfer outperforms the Hohmann. The critical points can be determined by simultaneously solving Eqs. (3.24) and (3.26).

$$\left. \frac{\partial^2 \frac{\Delta V_{BT}}{V_i}}{\partial R^{*2}} = 0 \right|_{R^*=R} \quad (3.26)$$

As before, the first order partial derivative represents the point where the bi-elliptic velocity requirement function is a turning point and the second order partial derivative determines the transfer specification at which this turning point changes from a maximum to minimum. As shown in Figure 3-11, the critical transfer specifications are found as  $R_{C1^*} = 5.919$  and  $\Delta I_{C1^*} = 0.746 \text{ rad}$  ( $42.74^\circ$ ) for the boundary line of AOU1 and  $R_{C2^*} = 1.374$  and  $\Delta I_{C2^*} = 0.643 \text{ rad}$  ( $36.84^\circ$ ) for the boundary line of AOU2. The dark green shaded region between  $R_{C2^*}$ , limit B and the graph axis requires an individual test, dependent on the orbit ratio,  $R$ , and plane change,  $\Delta I$ , to determine which transfer has the lowest velocity requirement. This can be performed by comparing Eqs. (3.14) and (3.22), which determine the total velocity requirement for the Hohmann and bi-elliptic transfers respectively, for an orbit ratio,  $R$ , and plane change,  $\Delta I$ , lying in the region. It is of note that this corresponds to the region where plane change error is maximum as discussed in Section 3.1.2. It is found for a transfer specification, where  $R > R_{CS^*}$  and  $\Delta I < \Delta I_{CS^*}$ , on limit A, the bi-elliptic will never outperform the Hohmann transfer. For a transfer specification, where  $R_{C3^*} < R < R_{CS^*}$  and  $\Delta I_{CS^*} < \Delta I < \Delta I_{C3^*}$ , on limit A, it is found that the same rules as AOU2 apply to determine when the bi-elliptic will outperform the Hohmann transfer. For  $R < R_{C3^*}$  and the corresponding  $\Delta I$  that defines a transfer specification on limit A, it is found that the bi-elliptic transfer has a lower velocity requirement than the Hohmann.

It should be noted that the transfer specification defining critical point 3 with an orbit ratio,  $R_{C3^*}$ , and plane change,  $\Delta I_{C3^*}$ , is found with an adaptation of the numerical bi-section root-finding method as opposed to the Newton iteration method. This is done using Eqs. (3.23) and (3.25) to an accuracy of three decimal places [119]. Firstly Eq. (3.23) is used to determine the plane change for a given orbit ratio,  $R$ , on limit A. The numerical bi-section method then uses the same test as given in Eq. (3.25) for these given values to solve for the intermediate orbit ratio,  $R^*$ . Depending on if only one root, the same as the transfer orbit ratio ( $R = R^*$ ), or two are found, one being ( $R = R^*$ ), then the search region is refined and

the process repeated in order to locate the point where this switch is located. This critical point is found as  $R_{C3^*} = 3.834$  and  $\Delta I_{C3^*} = 0.829 \text{ rad}$  (47.5°).

The limits defined in Figure 3-11 were suggested to exist in [28] when comparing the Hohmann and bi-elliptic transfers with a plane change conducted only at the apogee of the transfer orbit; however they were not explicitly defined or fully understood. By providing this reference graph, with plane change split over two impulses as was shown to always be more efficient than conducting the plane change at the transfer apogee [1], [28]–[30], [116], the transfer with the lowest velocity requirement can easily be selected for a given transfer specification.

To gain an analytical approximation of limit A and B, a best-fit polynomial is used. Eq. (3.27) shows a 7<sup>th</sup> order polynomial for limit A, which gives a mean relative percentage error of 0.15%

$$\begin{aligned}
 R_A(\Delta I) = & -3.076538341261905 \times 10^{-6} \Delta I^7 + 1.310418848093121 \times 10^{-4} \Delta I^6 - \\
 & 0.002252267968691 \Delta I^5 + \\
 & 0.019845311738719 \Delta I^4 - 0.093329276789302 \Delta I^3 + \\
 & 0.211562089144509 \Delta I^2 - 0.182784045887656 \Delta I + 0.878407397664127 .
 \end{aligned} \tag{3.27}$$

A 7<sup>th</sup> order polynomial is also used to represent limit B as

$$\begin{aligned}
 R_B(\Delta I) = & -1.116816225841078 \times 10^{-6} \Delta I^7 + 6.670356903870254 \times 10^{-5} \Delta I^6 - \\
 & 0.001622209813374 \Delta I^5 + \\
 & 0.020542764091578 \Delta I^4 - 0.143193345233860 \Delta I^3 + \\
 & 0.525841068740029 \Delta I^2 - 0.876667308099266 \Delta I + 1.195859374502926.
 \end{aligned} \tag{3.28}$$

The mean relative percentage error is found as 1.25%.

## 3.5. Case Studies

### 3.5.1. Area of Uncertainty 1

The transfer specification used to illustrate AOU1 has an orbit ratio of  $R = 12$  and plane change of  $\Delta I = 0.3 \text{ rad}$  ( $17.19^\circ$ ). By substituting these specified values, Eq. (3.25) can be solved to give  $R^*_{AOU1} = 31.602$ . This is the point at which the velocity requirement of the Hohmann and bi-elliptic transfers are equal. For comparison, if  $\Delta I = 0$ , then  $R^*_{AOU1} = 815.820$  which shows the bi-elliptic is more effective with increasing plane change. It can be shown that the bi-elliptic is always better, in terms of velocity requirement, than the Hohmann transfer when  $R^* > R^*_{AOU1}$  with a check of the derivative function of the bi-elliptic transfer velocity requirement with respect to  $R^*$ ,  $(\partial \Delta V_{BT}/V_i / \partial R^* |_{R^*=R^*_{AOU1}})$ . By substitution of the orbit transfer specification values, it is found the derivative is  $-0.0001$  which, due to the negative, means the function is decreasing at the point the Hohmann and bi-elliptic transfers' velocity requirements are equal, as shown in Figure 3-12. Before this point, the bi-elliptic transfer has a greater velocity requirement than the Hohmann transfer while beyond it, a smaller velocity requirement, as shown in Figure 3-12.

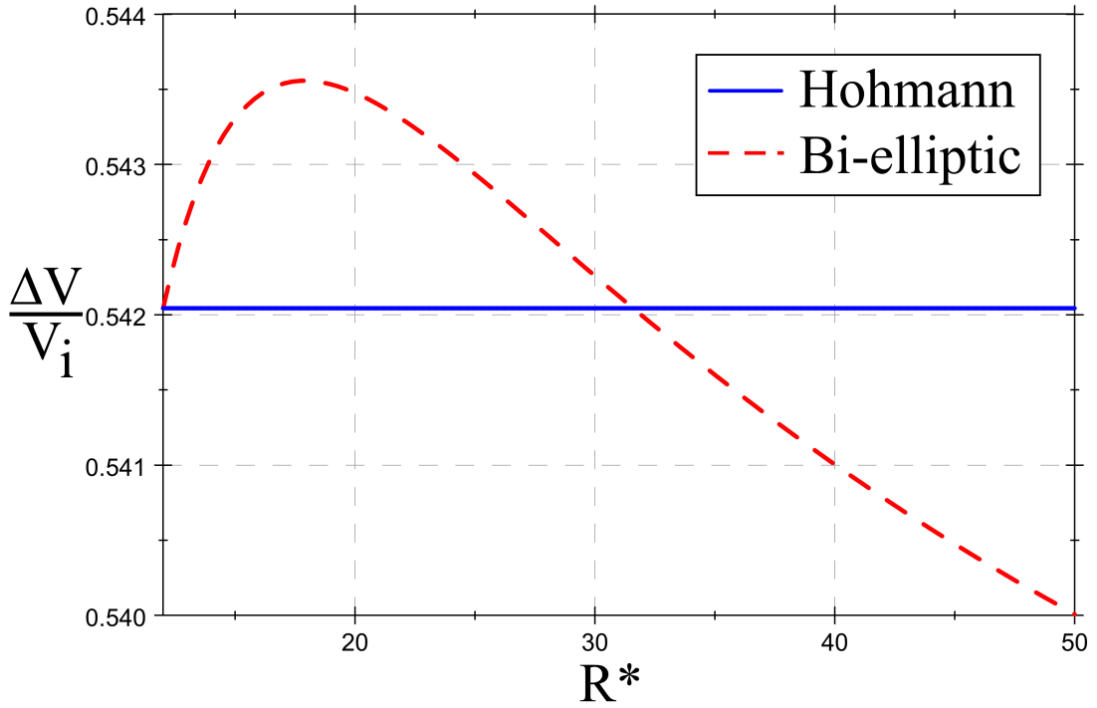


Figure 3-12 Characteristics of AOU1 for a transfers specification of  $R = 12$  &  $\Delta I = 0.3rad$  ( $17.19^\circ$ )

### 3.5.2. Area of Uncertainty 2

The orbit transfer specification used to illustrate AOU2 has an orbit ratio of  $R = 2$  and plane change of  $\Delta I = 0.8 rad$  ( $\cong 45.84^\circ$ ). Substituting these values into Eq. (3.25) and solving gives  $R^*_{AOU2} = 4.794$ . As is highlighted in the AOU1 case study, this is the point at which the velocity requirement of both the Hohmann and bi-elliptic transfer are equal. However, as discussed previously in this chapter and conversely to the AOU1 case study, it is for any  $R^* < R^*_{AOU2}$  that the bi-elliptic transfer outperforms the Hohmann. This is confirmed again with  $\partial \Delta V_{BT}/V_i / \partial R^* |_{R^*=R^*_{AOU1}}$  which is found as 0.031. As this is positive, the function is increasing at the point the Hohmann and bi-elliptic transfers' velocity requirements are equal. Before this point the bi-elliptic therefore outperforms the Hohmann whereas beyond it, the Hohman is better than the bi-elliptic. Figure 3-13 confirms this. The orbit ratio location of the greatest saving in velocity requirement is calculated by solving

$$\frac{\partial \frac{\Delta V_{BT}}{V_i}}{\partial R^*} = 0 \quad (3.29)$$

for  $R^*$  with the substitution of the relevant  $R$  and  $\Delta I$  for the given orbit transfer configuration.

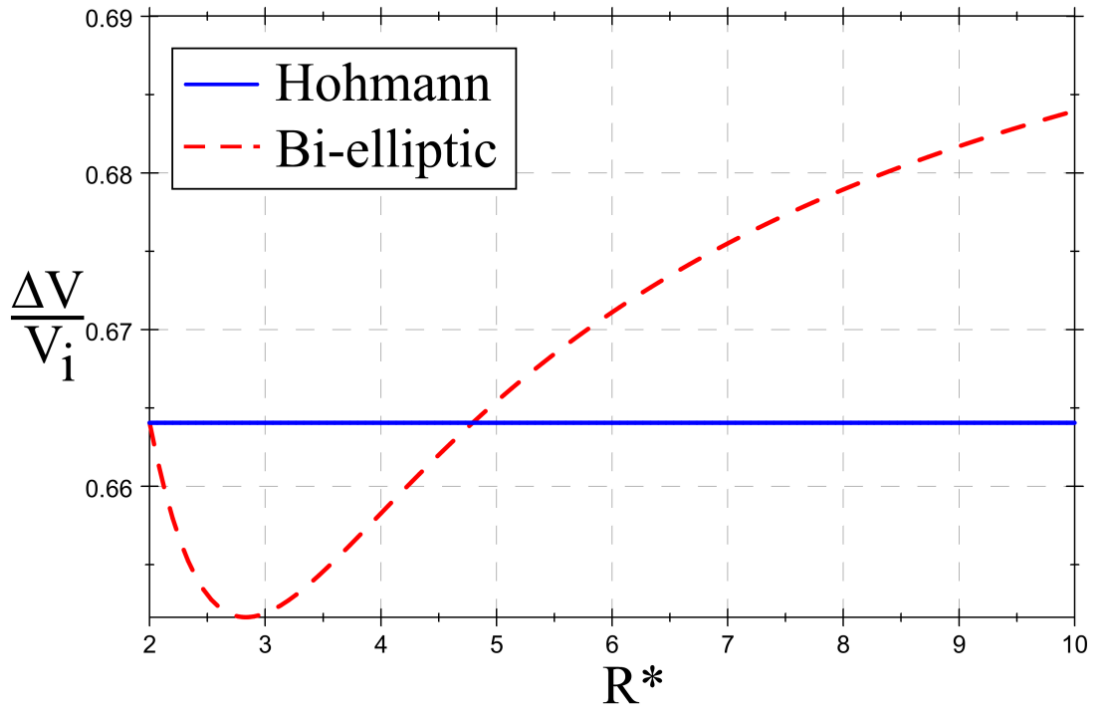


Figure 3-13 Characteristics of AOU2 for a transfers specification of  $R = 2$  &  $\Delta I = 0.8rad$  ( $45.84^\circ$ )

### 3.5.3. Limit B - $R > R_{C1}^*$

This scenario is slightly different from the previous two as it concerns the Limit B where  $R > R_{C1}^*$ . This divides AOUI and the bi-elliptic transfer only region, as detailed in Figure 3-11. For this case study it is necessary to select an orbit ratio,  $R$ , and solve for the corresponding plane change,  $\Delta I$ . This is done using Eq. (3.24) for an orbit transfer specification of  $R = 10$  and it is found  $\Delta I = 0.556 rad$  ( $31.86^\circ$ ). Using Eq. (3.24) ensures that at the point the Hohmann and bi-elliptic transfers' velocity requirements are equal, the bi-elliptic function is a turning point. By then using the second order partial derivative, as given in Eq. (3.26), it can be determined whether the function is a maximum or minimum. In this case it is found that the function is a maximum. This confirms that, on the right hand side of critical point 1 and on the critical line defined by Eq. (3.24) ( $R > R_{C1}^*$  and  $\Delta I < \Delta I_{C1}^*$ ), any  $R^* > R$  will ensure the bi-elliptic function outperforms the Hohmann transfer.

In-effect, this part of the critical line is the same as the bi-elliptic only region as shown in Figure 3-14.

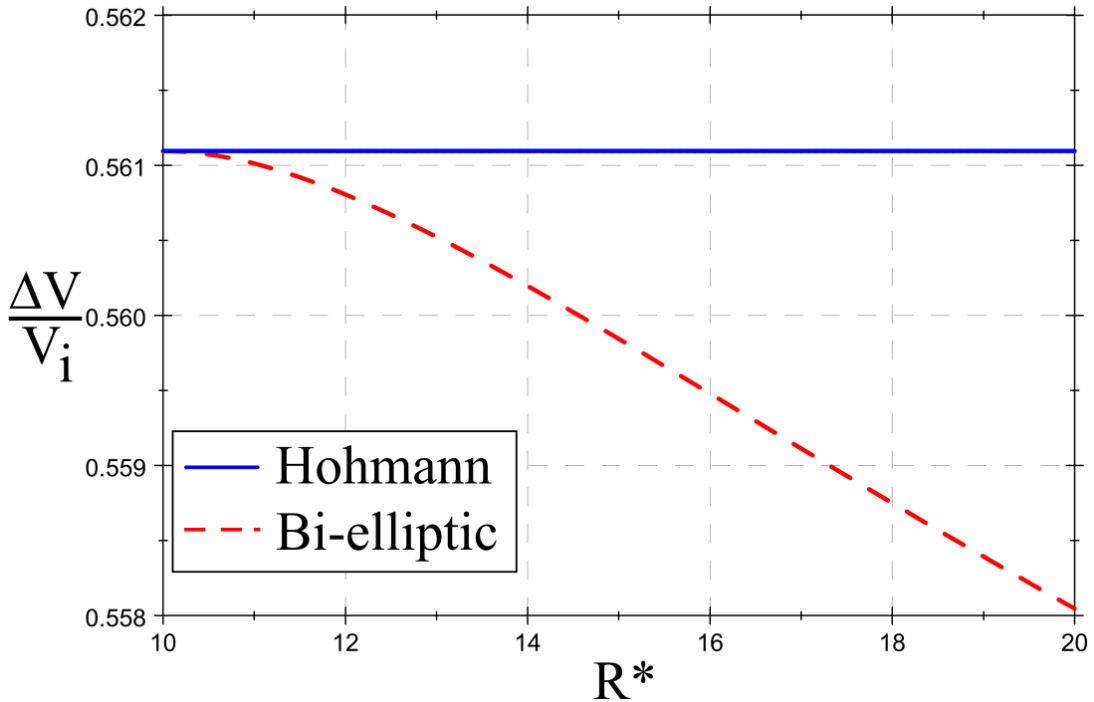


Figure 3-14 Limit B -  $R > R_{C1^*}$  for a transfer specification of  $R = 10$  &  $\Delta I = 0.556 \text{ rad}$  ( $31.86^\circ$ )

### 3.5.4. Limit B - $R_{CS^*} < R < R_{C1^*}$

This scenario is similar to the previous as it is again concerned with Limit B, but between critical point 1 and the switching point, ( $R_{CS^*} < R < R_{C1^*}$ ). Similarly, it is necessary to select an orbit ratio,  $R$ , and solve for  $\Delta I$  using Eq. (3.24). For  $R = 5.7$  it is found that  $\Delta I = 0.754 \text{ rad}$  ( $43.20^\circ$ ). As Eq. (3.24) gives the location of a turning point it is necessary to use Eq. (3.26) to determine whether it is a maximum or minimum, which for the given values it is found to be a minimum location. This confirms that for any transfer specification lying on the line between  $R_{C1^*}$  and  $R_{CS^*}$ , the test given in Eq. (3.25) has to be used to determine when the bi-elliptic has a lower velocity requirement than the Hohmann transfer. In-effect, this section of the critical line obeys the same rules as AOU1, as shown in Figure 3-15, and so long as  $R^* > R_{AOU1}^*$ , the bi-elliptic transfer will outperform the Hohmann.

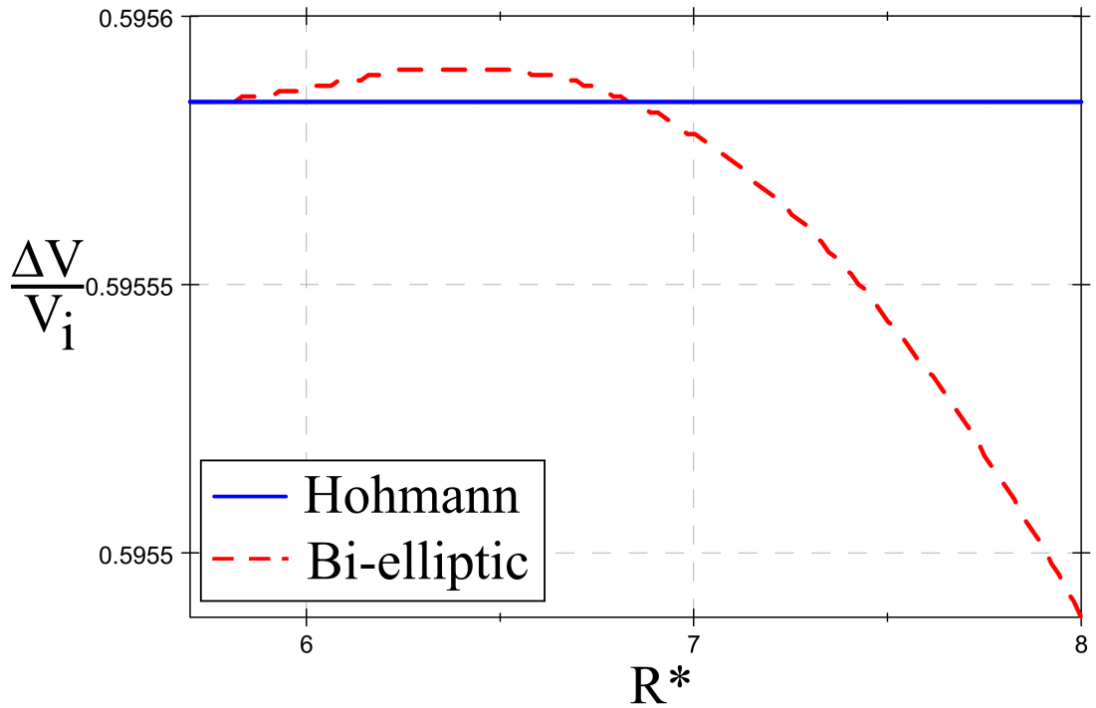


Figure 3-15 Limit B -  $R_{CS^*} < R < R_{C1^*}$  for a transfer specification of  $R = 5.7$  &  $\Delta I = 0.754 \text{ rad}$  ( $43.20^\circ$ )

### 3.5.5. Limit B - $R_{C2^*} < R < R_{CS^*}$

This scenario is concerned with Limit B between critical point 2 and the switching point, ( $R_{C2^*} < R < R_{CS^*}$ ), as shown in Figure 3-11. For  $R = 3$  and by using Eq. (3.24) it is found that  $\Delta I = 0.761 \text{ rad}$  ( $43.60^\circ$ ). Once again, Eq. (3.26) is used to determine whether this turning point is a maximum or minimum; it is found it is a minimum turning point. As this is the border of AOU2, it confirms that the bi-elliptic transfer is never better than the Hohmann. In effect, if a certain orbit configuration is selected which lies directly on the line between  $R_{C2^*}$  and  $R_{CS^*}$ , then it obeys the same rules as the Hohmann only region. Figure 3-16 confirms this.

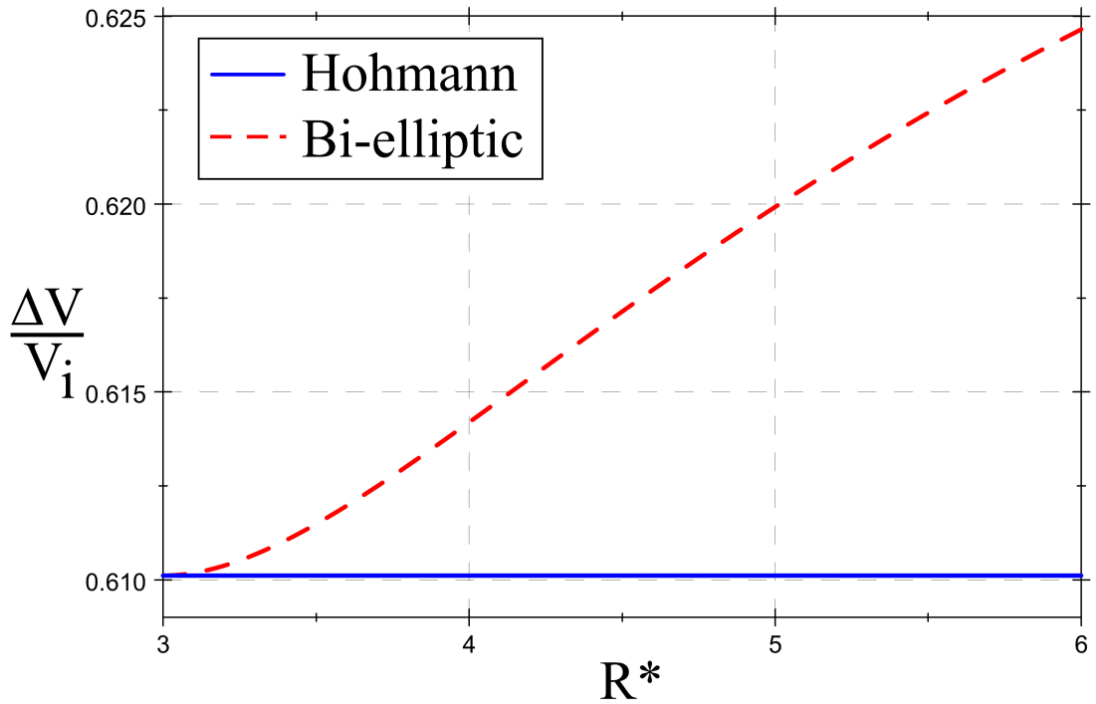


Figure 3-16 Limit B -  $R_{C2^*} < R < R_{CS^*}$  for a transfer specification of  $R = 3$  &  $\Delta I = 0.761 \text{ rad}$  ( $43.60^\circ$ )

### 3.5.6. Limit B - $R < R_{C2^*}$

This scenario is concerned with the limit B for  $R < R_{C2^*}$ , as shown in Figure 3-11. For  $R = 1.2$  and by using Eq. (3.24), it is found that  $\Delta I = 0.670 \text{ rad}$  ( $38.39^\circ$ ). As the use of Eq. (3.24) ensures this is a turning point, Eq. (3.26) is used to confirm it as a maximum turning point. As this is the border of AOU2, it confirms that any  $R^* < R_{AOU2}^*$  will ensure the bi-elliptic transfer has a lower velocity requirement than the Hohmann. In effect, this section of the line can be treated as if inside AOU2 as is shown in Figure 3-17.

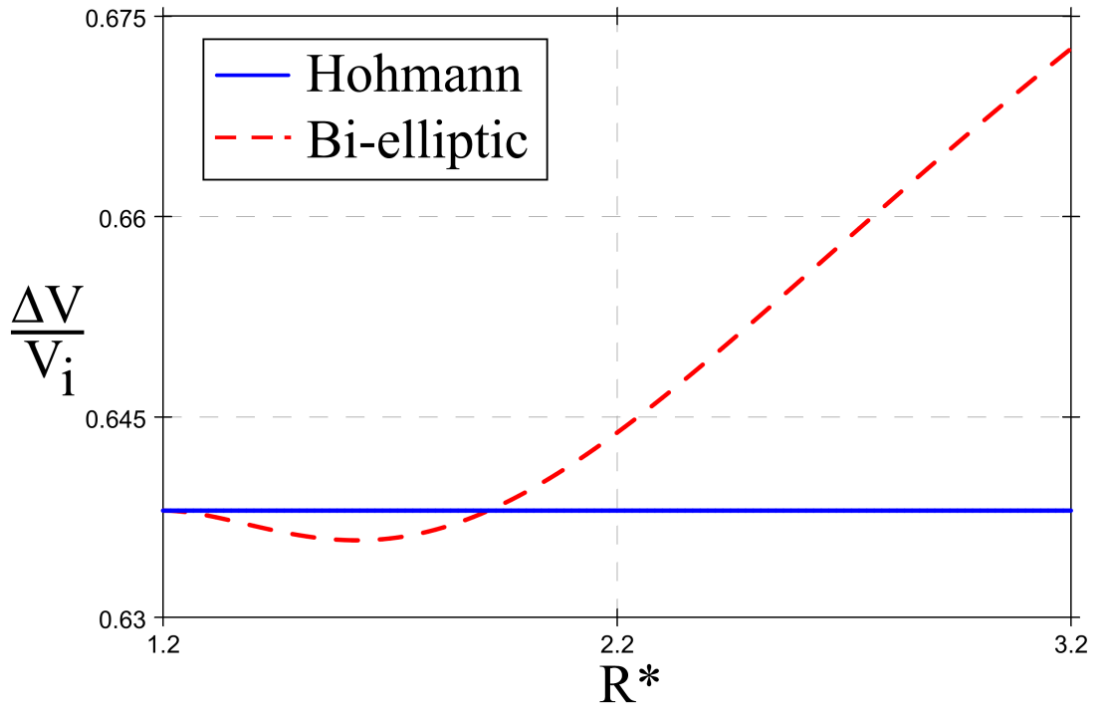


Figure 3-17 Limit B -  $R < R_{C2^*}$  for a transfer specification of  $R = 1.2$  &  $\Delta I = 0.670 \text{ rad}$  ( $38.39^\circ$ )

### 3.5.7. Limit A - $R > R_{CS^*}$

Now considering Limit A on the right hand side of the switching point, ( $R > R_{CS^*}$ ), it is found that the Hohmann transfer will always outperform the bi-elliptic. This can be confirmed by performing a case study with a transfer specification which lies directly on the line. For  $R = 8$ , Eq. (3.23) is used to determine  $\Delta I = 0.555 \text{ rad}$  ( $31.8^\circ$ ).  $\partial \Delta V_{BT}/V_i / \partial R^* |_{R^*=R}$ , at the point the bi-elliptic transfer's velocity requirement equals that of the Hohmann and parabolic, is found as 0.002 confirming that  $\Delta V_{BT}/V_i$  is increasing with increasing  $R^*$  as shown in Figure 3-18. It is also shown in Figure 3-18 as  $R^* \rightarrow \infty$ ,  $\Delta V_{BT}/V_i \rightarrow \Delta V_{HT}/V_i$ ; however it should be noted it is never less than the Hohmann.

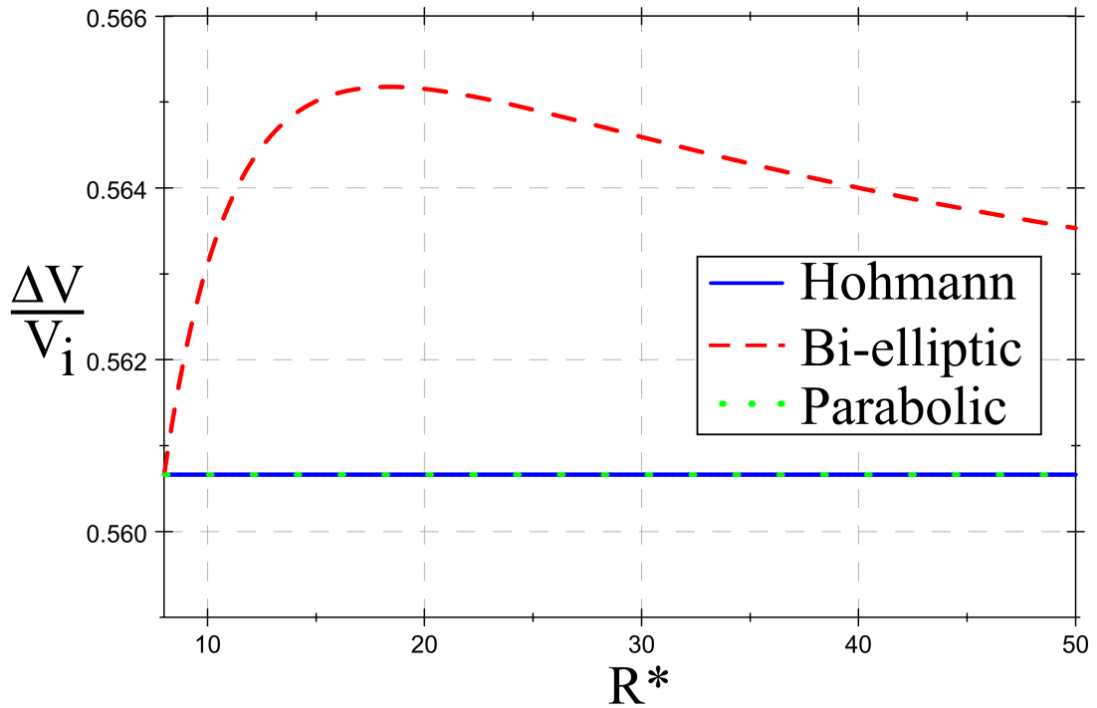


Figure 3-18 Limit A -  $R > R_{CS^*}$  for a transfer specification of  $R = 8$  &  $\Delta I = 0.555 \text{ rad}$  ( $31.8^\circ$ )

### 3.5.8. Limit A - $R_{C3^*} < R < R_{CS^*}$

Considering the region between  $R_{CS^*}$  and  $R_{C3^*}$ , on Limit A, it is found that the same rules as AOU2 apply. This is demonstrated by using  $R = 4.2$  and solving Eq. (3.23) to find  $\Delta I = 0.809 \text{ rad}$  ( $46.35^\circ$ ). By then using  $\partial \Delta V_{BT}/V_i / \partial R^* |_{R^*=R}$ , found as  $-0.002$ , it is confirmed that  $\Delta V_{BT}/V_i$  is decreasing at  $R^* = R$ . By then referring to Figure 3-19 it can be seen that  $\Delta V_{BT}/V_i$ , at some  $R^*$  dependent on  $R$ , does again exceed  $\Delta V_{HT}/V_i$  confirming that the same test for AOU2 is required to determine when a bi-elliptic transfer should be used. Once again, Eq. (3.29) can be used to determine the point at which the greatest velocity requirement saving is achieved.

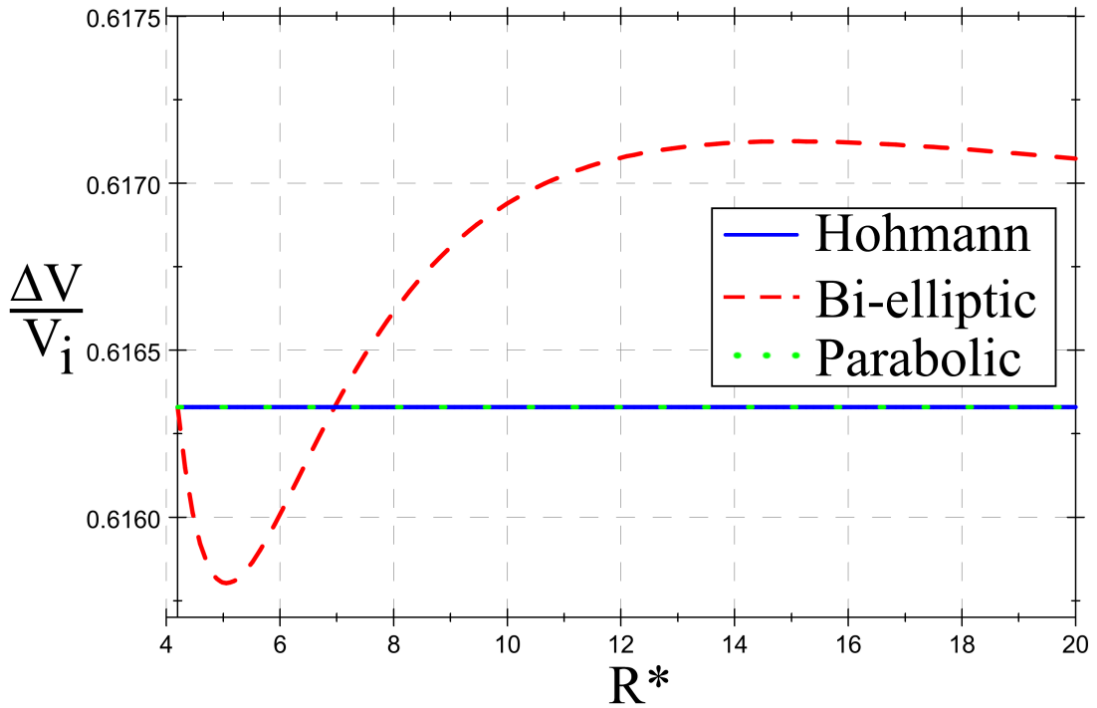


Figure 3-19 Limit A -  $R_{C3^*} < R < R_{CS^*}$  for a transfer specification of  $R = 4.2$  &  $\Delta I = 0.809 \text{ rad}$  ( $46.35^\circ$ )

### 3.5.9. Limit A - $R < R_{C3^*}$

This final scenario is concerned with the region from  $R = 1$  to  $R_{C3^*}$  on Limit A. For  $R = 2$ , and by using Eq. (3.23), it is found  $\Delta I = 0.867 \text{ rad}$  ( $49.68^\circ$ ). By then using  $\partial \Delta V_{BT}/V_i / \partial R^* |_{R^*=R}$ , found as  $-0.058$ , it is confirmed that  $\Delta V_{BT}/V_i$  is decreasing at  $R^* = R$  suggesting the bi-elliptic transfer outperforms the Hohmann. By then using Eq. (3.25) and finding that the only root is  $R^* = R$ , it is found that the bi-elliptic transfer will always possess a lower velocity requirement than the Hohmann or parabolic transfer on this section of Limit A. This is highlighted in Figure 3-20.

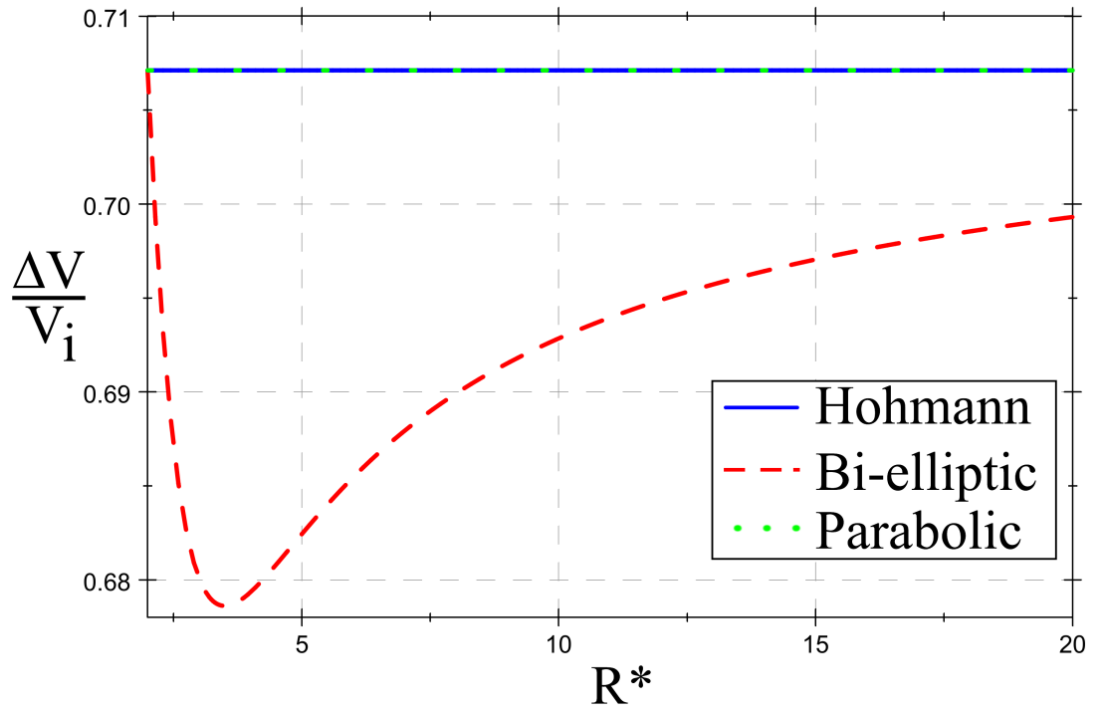


Figure 3-20 Limit A -  $R < R_{C3}$  for a transfer specification of  $R = 2$  &  $\Delta I = 0.867 \text{ rad}$  ( $49.68^\circ$ )

### 3.6. Summary

This chapter has reviewed two high-thrust orbit transfers: the Hohmann and the bi-elliptic, with the inclusion of a plane change. It has been shown that the area of uncertainty, determined for a co-planar analysis of the transfers, reduces in size with increasing plane change and converges on a point, beyond which a second area of uncertainty emerges. Previously, individual case analysis was required to determine which transfer offered the lowest velocity requirement when considering an optimal plane change split between impulses resulting in no general solution. In this chapter however, an analysis has produced a reference graph based on simple analytical expressions for the velocity requirement that, with knowledge of the orbit transfer required (ratio of target and initial orbit radius and plane change), can be used to determine which transfer should be used. The analytical expressions have been generated with use of a simple approximation which distributes the plane change over two impulses. The method is dependent on the orbit geometry and its use has been

validated by comparing it to a numerical approach. The theory has also been extended and used for orbit transfers other than circular-circular.

# Chapter 4

---

## THE HOHMANN SPIRAL TRANSFER

This chapter introduces a novel hybrid propulsion transfer named the Hohmann Spiral Transfer (HST). It is fundamentally different to previous hybrid propulsion transfers, as was discussed in Chapter 2, and is inspired by the high-thrust bi-elliptic transfer which was discussed in detail in Chapter 3. As the bi-elliptic transfer can offer a fuel mass saving by using an intermediate orbit apogee greater than the target orbit, it is worth considering if a similar principle is applicable to a hybrid transfer. As such, the high-thrust system is used to propel the spacecraft beyond the target to an intermediate orbit, with both perigee and apogee larger than the target, where the low-thrust propulsion system is activated and used to spiral back in-towards the target. This means the low-thrust system is used with a larger thrust to weight ratio than most prior hybrid transfers, which use an intermediate orbit radius less than the target; ultimately improving the effectiveness of the low-thrust system.

This chapter will first introduce the theory for the general case in Section 4.1 before applying this to a co-planar case in Section 4.2. It will then be applied to a non-co-planar case where the high-thrust system performs the full plane change in Sections 4.4 and then where the plane change is performed by only the low-thrust system in Section 4.5. The analytical method adopted allows the use of critical specific impulse equations that can be used to determine when the HST will offer a lower fuel mass fraction than either a Hohmann or bi-elliptic transfer. The analysis will also account for the transfer time in Section 4.9 and determine the limitations of the analytical analysis due to large orbit radii in Section 4.10.

## 4.1. General critical specific impulse derivation

Before the transfer can be fully investigated for the co-planar and plane change cases, it is necessary to define the general underlying theory. The following equations derive the general form of the critical specific impulse ratio, which can then be applied to each case independently. The high-thrust only (Hohmann and bi-elliptic) and HST fuel mass fractions can be written respectively as,

$$\frac{m_{HF}}{m_{wet}} = 1 - \exp\left(\frac{-\Delta V_{H(C/E)}}{g^{I_{spH}}}\right) \quad (4.1)$$

$$\frac{m_{HSTF}}{m_{wet}} = 1 - \exp\left(\frac{-\Delta V_{HSTH(C/E)}}{g^{I_{spH}}}\right) \exp\left(\frac{-\Delta V_{HSTL}}{g^{I_{spL}}}\right). \quad (4.2)$$

By equating Eqns. (4.1) and (4.2), it can be shown that the HST transfer is equivalent or better, in terms of fuel mass fraction, when

$$\exp\left(\frac{-\Delta V_{H(C/E)}}{g^{I_{spH}}}\right) \leq \exp\left(\frac{-\Delta V_{HSTH(C/E)}}{g^{I_{spH}}}\right) \exp\left(\frac{-\Delta V_{HSTL}}{g^{I_{spL}}}\right) \quad (4.3)$$

which can be simplified to give

$$\frac{I_{spL}}{I_{spH}} \geq \frac{\Delta V_{HSTL}}{\Delta V_{H(C/E)} - \Delta V_{HSTH(C/E)}} \quad (4.4)$$

confirming that a critical specific impulse ratio can be determined for the condition when the high-thrust only transfer fuel consumption is equal to the HST transfer fuel consumption. Thus, for a given set of initial conditions, any specific impulse ratio above this critical value will ensure the HST is more fuel-efficient than the compared transfer.

From Eq. (4.4) it can be seen that a singularity exists when the HST high-thrust velocity requirement equals that of the high-thrust only. Beyond this signifies the region where the HST requires more fuel than the high-thrust only transfer resulting in no mass saving. Due to the large number of equations that are generated for different transfer scenarios throughout

this chapter, a superscript system has been introduced to avoid confusion. The methodology behind the superscript system is described in Figure 4-1 and Table 4-1 details each transfer comparison considered and the associated superscript used. It should be noted that the equations representing the comparison of the HST only are labelled differently; these subscripts are found at the end of the table.

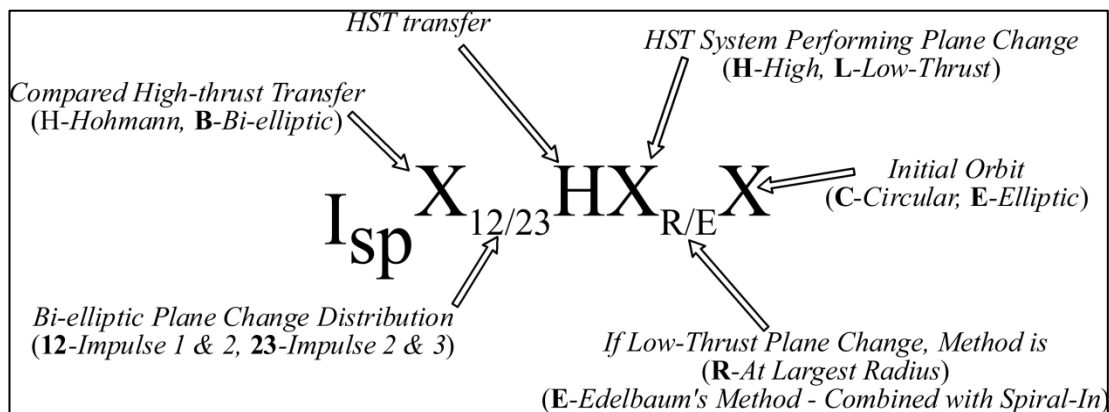


**Figure 4-1 Critical specific impulse ratio superscript methodology**

**Table 4-1 Subscript notation detailing critical specific impulse ratio transfer specification**

<b>Transfer Comparison Type</b>	<b>Superscript (<math>I_{sp}^{XXXX}</math>)</b>
Hohmann compared with HST ( <i>co-planar, circular initial orbit</i> )	<i>HH-C</i>
Bi-elliptic compared with HST ( <i>co-planar, circular initial orbit</i> )	<i>BH-C</i>
Hohmann compared with HST ( <i>co-planar, elliptical initial orbit</i> )	<i>HH-E</i>
Bi-elliptic compared with HST ( <i>co-planar, elliptical initial orbit</i> )	<i>BH-E</i>
Hohmann compared with HST ( <i>high-thrust system plane change, circular initial orbit</i> )	<i>HHHC</i>
Hohmann compared with HST ( <i>low-thrust system plane change - R, circular initial orbit</i> )	<i>HL<sub>R</sub>C</i>
Hohmann compared with HST ( <i>low-thrust system plane change - E, circular initial orbit</i> )	<i>HL<sub>E</sub>C</i>
Hohmann compared with HST ( <i>high-thrust system plane change, elliptical initial orbit</i> )	<i>HHHE</i>
Hohmann compared with HST ( <i>low-thrust system plane change - R, elliptical initial orbit</i> )	<i>HL<sub>R</sub>E</i>
Hohmann compared with HST ( <i>low-thrust system plane change - E, elliptical initial orbit</i> )	<i>HL<sub>E</sub>E</i>
Bi-elliptic with plane change at first and second impulse compared with HST ( <i>high-thrust system plane change, circular initial orbit</i> )	<i>B<sub>12</sub>HHC</i>
Bi-elliptic with plane change at first and second impulse compared with HST ( <i>low-thrust system plane change - R, circular initial orbit</i> )	<i>B<sub>12</sub>HL<sub>R</sub>C</i>
Bi-elliptic with plane change at first and second impulse compared with HST ( <i>low-thrust system plane change - E, circular initial orbit</i> )	<i>B<sub>12</sub>HL<sub>E</sub>C</i>
Bi-elliptic with plane change at first and second impulse compared with HST ( <i>high-thrust system plane change, elliptical initial orbit</i> )	<i>B<sub>12</sub>HHE</i>
Bi-elliptic with plane change at first and second impulse compared with HST ( <i>low-thrust system plane change - R, elliptical initial orbit</i> )	<i>B<sub>12</sub>HL<sub>R</sub>E</i>
Bi-elliptic with plane change at first and second impulse compared with HST ( <i>low-thrust system plane change - E, elliptical initial orbit</i> )	<i>B<sub>12</sub>HL<sub>E</sub>E</i>
Bi-elliptic with plane change at second and third impulse compared with HST ( <i>high-thrust system plane change, circular initial orbit</i> )	<i>B<sub>23</sub>HHC</i>
Bi-elliptic with plane change at second and third impulse compared with HST ( <i>low-thrust system plane change - R, circular initial orbit</i> )	<i>B<sub>23</sub>HL<sub>R</sub>C</i>
Bi-elliptic with plane change at second and third impulse compared with HST ( <i>low-thrust system plane change - E, circular initial orbit</i> )	<i>B<sub>23</sub>HL<sub>E</sub>C</i>
Bi-elliptic with plane change at second and third compared with HST ( <i>high-thrust system plane change, elliptical initial orbit</i> )	<i>B<sub>23</sub>HHE</i>
Bi-elliptic with plane change at second and third compared with HST ( <i>low-thrust system plane change - R, elliptical initial orbit</i> )	<i>B<sub>23</sub>HL<sub>R</sub>E</i>
Bi-elliptic with plane change at second and third compared with HST ( <i>low-thrust system plane change - E, elliptical initial orbit</i> )	<i>B<sub>23</sub>HL<sub>E</sub>E</i>
HST ( <i>high-thrust system plane change</i> ) compared with HST ( <i>low-thrust system plane change - R, circular initial orbit</i> )	<i>HSH<sub>R</sub>C</i>
HST ( <i>high-thrust system plane change</i> ) compared with HST ( <i>low-thrust system plane change - E, circular initial orbit</i> )	<i>HSH<sub>E</sub>C</i>
HST ( <i>high-thrust system plane change</i> ) compared with HST ( <i>low-thrust system plane change - R, elliptical initial orbit</i> )	<i>HSH<sub>R</sub>E</i>
HST ( <i>high-thrust system plane change</i> ) compared with HST ( <i>low-thrust system plane change - E, elliptical initial orbit</i> )	<i>HSH<sub>E</sub>E</i>

## 4.2. Co-planar

Firstly, the co-planar HST can be considered. Figure 4-2 and Figure 4-3 show the transfer for a circular and elliptical initial orbit. In each figure, the HST, Hohmann and bi-elliptic transfers are shown. In Figure 4-2 it can be seen that the Hohmann transfer is a simple two-impulse transfer connecting the initial and target orbits whereas the bi-elliptic transfer is a three impulse transfer using two elliptical transfer orbits to reach the target. These transfers

were discussed in detail in Chapter 3 and as such will not be discussed further here. It is noted that the HST is also shown in both Figure 4-2 and Figure 4-3 where it shown the high-thrust phase is the same as the first bi-elliptic phase. At this transfer orbit apogee the high-thrust system is used to enter a circular orbit prior to the low-thrust system being activated and sending the spacecraft on a spiral trajectory inward towards the target orbit.

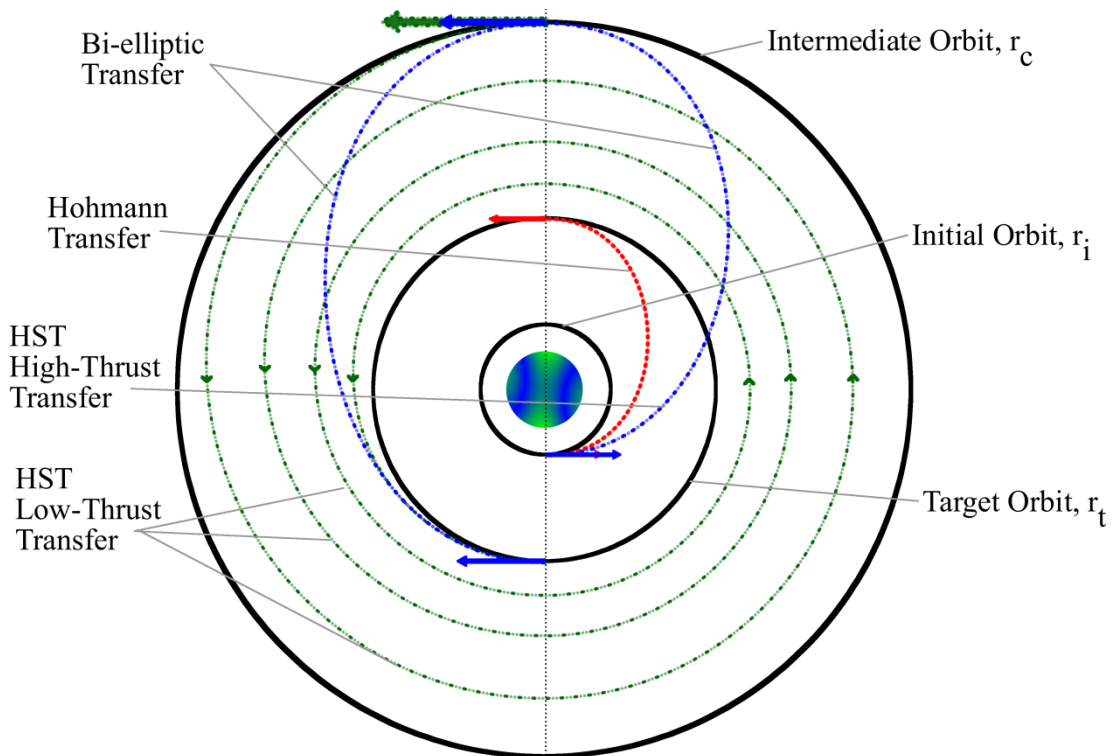


**Figure 4-2 Co-planar HST with circular initial orbit**

In Figure 4-3 it can be seen that the apogee of the initial elliptical orbit aligns with the target orbit radius. This changes the Hohmann transfer from two-impulses to one and is a necessary condition of the analytical analysis. This is a reasonable assumption as it is representative of a standard GTO to GEO [120].

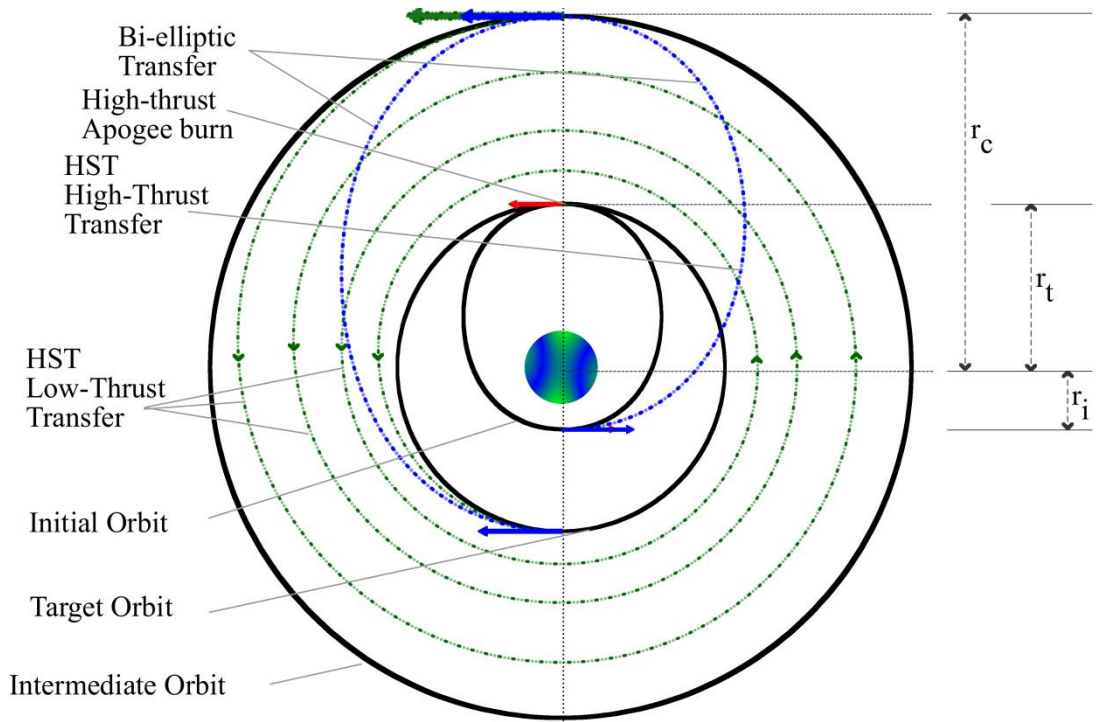


Figure 4-3 Co-planar HST with elliptical initial orbit

## 4.2.1. HST and Hohmann Critical Specific Impulse Ratio

Considering Figure 4-2 and Eq. (4.4) for a circular initial orbit, the following definitions give the velocity requirement,  $\Delta V$ , for the low and high-thrust phases of the HST respectively,

$$\Delta V_{HSTSL} = \sqrt{\frac{\mu}{r_t}} - \sqrt{\frac{\mu}{r_c}} \quad (4.5)$$

$$\Delta V_{HSTHC} = \sqrt{\frac{2\mu}{r_i} - \frac{2\mu}{r_i+r_c}} - \sqrt{\frac{\mu}{r_i}} + \sqrt{\frac{\mu}{r_c}} - \sqrt{\frac{2\mu}{r_c} - \frac{2\mu}{r_i+r_c}} \quad (4.6)$$

Additionally, the high-thrust Hohmann transfer used for the comparison can be defined as

$$\Delta V_{HC} = \sqrt{\frac{2\mu}{r_i} - \frac{2\mu}{r_i+r_t}} - \sqrt{\frac{\mu}{r_i}} + \sqrt{\frac{\mu}{r_t}} - \sqrt{\frac{2\mu}{r_t} - \frac{2\mu}{r_i+r_t}} \quad (4.7)$$

It should be noted that Eq. (4.5) is an approximate expression for the low-thrust velocity requirement. By then introducing the orbit ratios  $R1 (r_t/r_i)$  and  $R2 (r_c/r_i)$  to aid

simplification, Eq. (4.4), with the use of Eqs. (4.5) - (4.7) for this scenario, can be simplified to give

$$\frac{I_{spL}}{I_{spH}} = I_{sp}^{HH-C} = \frac{\sqrt{\frac{1}{2R1}} \sqrt{\frac{1}{2R2}}}{\sqrt{1 - \frac{1}{1+R1}} - \sqrt{1 - \frac{1}{1+R2}} - \sqrt{\frac{1}{R1} - \frac{1}{1+R1}} + \sqrt{\frac{1}{R2} - \frac{1}{1+R2}} + \sqrt{\frac{1}{2R1}} - \sqrt{\frac{1}{2R2}}} \quad (4.8)$$

It is of note that the orbit ratios defined here are the same as the orbit ratios,  $R$  and  $R^*$ , defined in Chapter 3 for the comparison of the Hohmann and bi-elliptic transfers. They have been redefined here to avoid confusion between the different chapters and hence transfers. For all scenarios considering the HST,  $R1$  and  $R2$  will be used when referring to these orbit ratios.

Equation (4.8) depends on only two variables,  $R1$  and  $R2$ . In the case where the initial and target orbits are known, the critical ratio is simply dependent on the target circular orbit radius value,  $r_c$ . Varying this will give a range of transfer orbits with a given critical specific impulse ratio defining the point where the HST is equivalent in terms of fuel mass fraction.

## 4.2.2. HST and Bi-Elliptic Critical Specific Impulse Ratio

Considering Figure 4-2, the case where the HST is compared to the bi-elliptic transfer can be considered. Equation (4.9) defines the bi-elliptic transfer velocity requirement while the HST's low and high thrust velocity requirements remain the same as defined in Eqs. (4.5) and (4.6) respectively.

$$\Delta V_{HC} = \sqrt{\frac{2\mu}{r_i} - \frac{2\mu}{r_i+r_c}} + \sqrt{\frac{2\mu}{r_c} - \frac{2\mu}{r_t+r_c}} - \sqrt{\frac{2\mu}{r_c} - \frac{2\mu}{r_i+r_c}} + \sqrt{\frac{2\mu}{r_t} - \frac{2\mu}{r_t+r_c}} - \sqrt{\frac{\mu}{r_t}} - \sqrt{\frac{\mu}{r_i}} \quad (4.9)$$

Using these equations together with the use of the orbit ratios  $R1$  and  $R2$  defined previously, the critical specific impulse ratio can be defined as

$$\frac{I_{spL}}{I_{spH}} = I_{sp}^{BH-C} = \frac{\sqrt{\frac{1}{2R_1} - \frac{1}{2R_2}}}{\sqrt{\frac{1}{R_1} - \frac{1}{R_1+R_2}} + \sqrt{\frac{1}{R_2} - \frac{1}{R_1+R_2}} - \sqrt{\frac{1}{2R_1}} - \sqrt{\frac{1}{2R_2}}}. \quad (4.10)$$

Similar to the HST and Hohmann transfer critical ratio, Eq. (4.10) is only dependent on the ratios  $R_1$  and  $R_2$ . If the initial and target orbits are known, then the equation will depend only on the intermediate orbit radius,  $r_c$ . By varying this orbit radius, a range of critical specific impulse ratios can be obtained which detail the point at which the HST consumes exactly the same amount of fuel mass as the bi-elliptic transfer.

### 4.2.3. HST and Hohmann Critical Specific Impulse Ratio (Elliptical Initial Orbit)

For the case of an elliptical initial orbit as shown in Figure 4-3, the velocity requirement for the one-impulse high-thrust Hohmann transfer is

$$\Delta V_{HE} = \sqrt{\frac{\mu}{r_t}} - \sqrt{\frac{2\mu}{r_t} - \frac{2\mu}{r_i+r_t}}. \quad (4.11)$$

The velocity requirement for the HST low thrust section is then unchanged from Eq. (4.5) but the high-thrust phase is given as

$$\Delta V_{HSTHE} = \sqrt{\frac{2\mu}{r_i} - \frac{2\mu}{r_i+r_c}} - \sqrt{\frac{2\mu}{r_i} - \frac{2\mu}{r_i+r_t}} - \sqrt{\frac{2\mu}{r_c} - \frac{2\mu}{r_i+r_c}} + \sqrt{\frac{\mu}{r_c}}. \quad (4.12)$$

Substituting these equations into Eq. (4.4) with the introduction of the orbit ratios previously defined allows the critical specific impulse ratio to be defined as

$$\frac{I_{spL}}{I_{spH}} = I_{sp}^{HH-E} = \frac{\sqrt{\frac{1}{2R_1} - \frac{1}{2R_2}}}{\sqrt{1 - \frac{1}{1+R_1}} - \sqrt{1 - \frac{1}{1+R_2}} - \sqrt{\frac{1}{R_1} - \frac{1}{1+R_1}} + \sqrt{\frac{1}{R_2} - \frac{1}{1+R_2}} + \sqrt{\frac{1}{2R_1}} - \sqrt{\frac{1}{2R_2}}}. \quad (4.13)$$

It is interesting to note that although the velocity requirement equations differ between the circular and elliptical cases, the critical ratio defined in Eq. (4.13) for the elliptical initial

orbit is the same as that defined for the circular initial orbit given in Eq. (4.8). The characteristics of the critical ratio for both the circular and elliptical initial orbits can therefore be seen in Figure 4-4. The general trend of the equation shows that the critical specific impulse ratio reduces with increasing intermediate to initial orbit ratio,  $R2$ , suggesting the further the spacecraft travels from the central body, the larger the fuel mass saving. This is also the case for increasing target to initial orbit ratio,  $R1$  however it can be seen as  $R1 \rightarrow 1$ , the function approaches a singularity, which beyond the Hohmann is more efficient than the HST and will therefore always offer a lower fuel mass fraction.

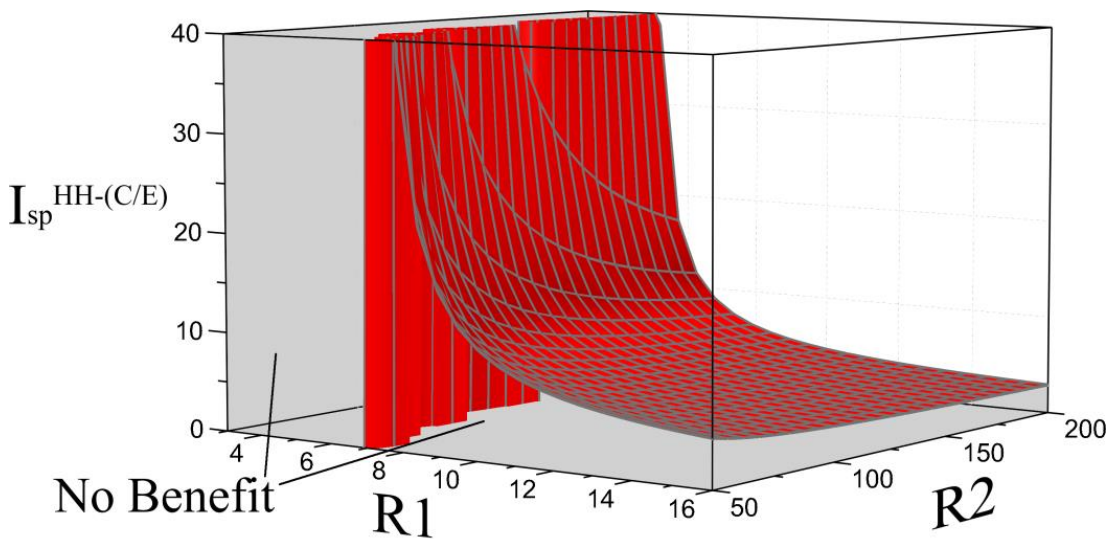


Figure 4-4 Co-planar Hohmann and HST critical specific impulse ratio for circular and elliptical initial orbit

#### 4.2.4. HST and Bi-Elliptic Critical Specific Impulse Ratio (Elliptical Initial Orbit)

Considering the case where the HST and bi-elliptic transfers are compared with an elliptical initial orbit as shown in Figure 4-3, the velocity requirement equation for the bi-elliptic transfer can be defined as

$$\Delta V_{HE} = \sqrt{\frac{2\mu}{r_i} - \frac{2\mu}{r_i+r_c}} - \sqrt{\frac{2\mu}{r_i} - \frac{2\mu}{r_i+r_t}} + \sqrt{\frac{2\mu}{r_c} - \frac{2\mu}{r_t+r_c}} - \sqrt{\frac{2\mu}{r_c} - \frac{2\mu}{r_i+r_c}} + \sqrt{\frac{2\mu}{r_t} - \frac{2\mu}{r_t+r_c}} - \sqrt{\frac{\mu}{r_t}}. \quad (4.14)$$

The equations representing the HST high and low thrust phases are the same as previously defined in Eqs. (4.12) and (4.5) respectively. Using these equations with the inclusion of the previously defined orbit ratios, the critical specific impulse ratio for the elliptical initial orbit can be defined,

$$\frac{I_{spL}}{I_{spH}} = I_{sp}^{BH-E} = \frac{\sqrt{\frac{1}{2R_1} - \frac{1}{2R_2}}}{\sqrt{\frac{1}{R_1} - \frac{1}{R_1+R_2}} + \sqrt{\frac{1}{R_2} - \frac{1}{R_1+R_2}} - \sqrt{\frac{1}{2R_1} - \frac{1}{2R_2}}}. \quad (4.15)$$

Similar to the case in Section 4.2.3, although the transfer velocity requirement equations differ, Eq. (4.15) is the same as that defined for the circular initial orbit in Eq. (4.10). The function can be seen in Figure 4-5 where it is shown that the critical specific impulse ratio reduces with increasing intermediate to initial orbit ratio,  $R_2$ . This suggests the further the spacecraft travels from the central body, the larger the possible fuel mass saving. Figure 4-5 also differs to Figure 4-4 as the critical specific impulse ratio increases with increasing  $R_1$ ; the significance of which is investigated in the next section.

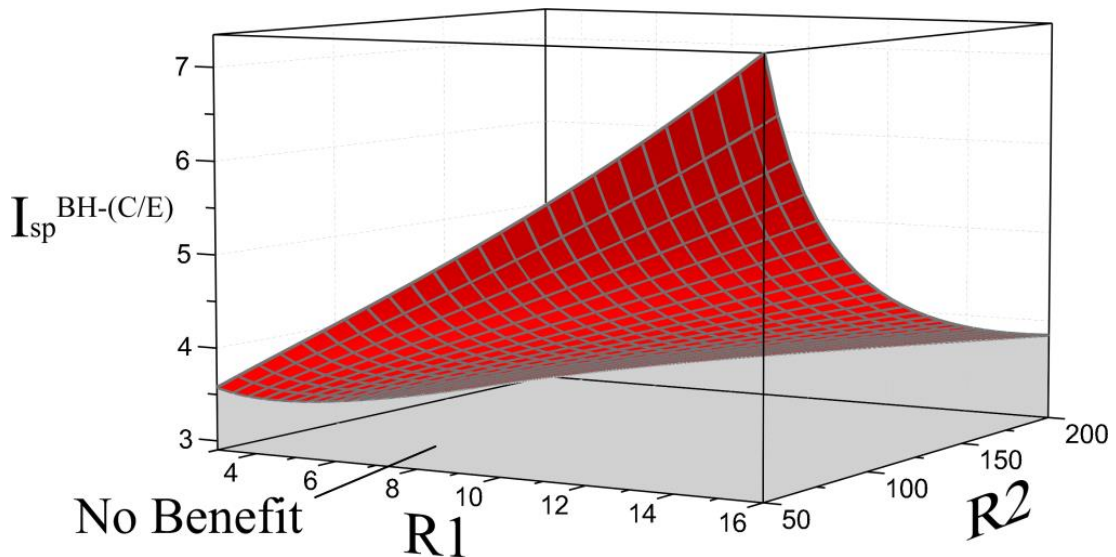


Figure 4-5 Co-planar bi-elliptic and HST critical specific impulse ratio for circular and elliptical initial orbit

#### 4.2.5. HST and Hohmann Compared with HST and Bi-Elliptic

In order for the HST to outperform both the Hohmann and bi-elliptic transfers it must exceed the largest critical specific impulse ratio. As such, there is a need to investigate the two functions together to determine if there are any general rules that dictate which transfer offers the lowest fuel consumption. Figure 4-6 illustrates both Eq. (4.13) and Eq. (4.15) for a varying range of  $R1$  and  $R2$  and shows an intersection between the two functions; highlighted by the black squares. As such, careful consideration must be given in this region to determine which critical specific impulse ratio has to be considered to ensure the HST offers the lowest fuel consumption.

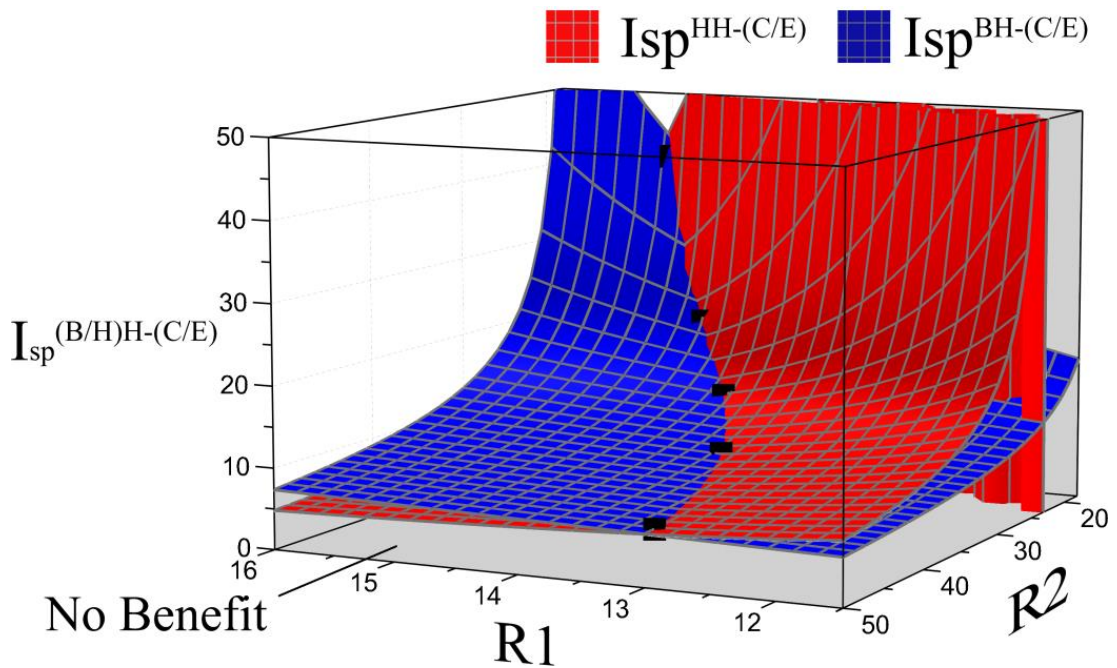


Figure 4-6 Hohmann and HST and bi-elliptic and HST critical ratio intersection

It is of note that a similar region of intersection, when  $11.938765474 < R1 < 15.58171874$ , was discussed in Chapter 3 when comparing the Hohmann and bi-elliptic transfers in a co-planar scenario. It was shown that around this intersection it was difficult to determine which transfer was more fuel effective and as such a test is required to determine the transfer with the lowest velocity requirement. Likewise, for the HST it can be determined, with use of a similar test, which critical ratio must be considered to ensure the HST is superior. The test is demonstrated by equating the critical ratios for each transfer type, in this case Eq. (4.13) and Eq. (4.15). It follows that

$$\sqrt{\frac{R2}{R2+1}} - \sqrt{\frac{R1}{R1+1}} + \sqrt{\frac{R1}{R2(R1+R2)}} + \sqrt{\frac{R2}{R1(R1+R2)}} + \sqrt{\frac{1}{R1(R1+1)}} - \sqrt{\frac{1}{R2(R2+1)}} - \sqrt{2} \sqrt{\frac{1}{R1}} = 0. \quad (4.16)$$

This can be solved for  $R2_0$ , corresponding to the zero of Eq. (4.16), within the defined range in order to identify the controlling critical equation. It can then be said that any  $R2$  value greater than  $R2_0$  will ensure the critical ratio, comparing the HST to bi-elliptic, has control of the system. Anything smaller will result in the critical ratio comparing the HST to a

Hohmann transfer assuming control. It is interesting to find that Eq. (4.16) gives  $R1 = 11.93876547$  when  $R2 \rightarrow \infty$ ; the same limit defined in Chapter 3. Similarly, it can be shown that if  $R1 \cong 15.58171874$  then  $R2 \cong 15.58171874$  which is again what was found in Chapter 3.

### 4.3. Plane Change

In addition to the critical ratios derived for the co-planar scenario, it is necessary to consider the HST with the introduction of a plane change. As the HST is a hybrid propulsion transfer, it is necessary to consider the transfer with the plane change performed by both the high and low-thrust systems. As such, this section derives critical specific impulse ratios for both the high and low-thrust system performing the plane change compared against either the Hohmann or bi-elliptic transfer. It should be noted that the HST is compared against the bi-elliptic with the plane change performed at the first and second impulses as well as at the second and third impulses. Critical ratios are also derived for all cases with a circular and elliptical initial orbit. Due to the large number of comparisons required, Figure 4-7 gives an overview of all the critical equations derived for a co-planar and non-co-planar scenario. It should be noted that the HST with low-thrust plane change accounts for the plane change performed at the largest orbit radius before the spiral-in phase and the combined plane change and spiral-in manoeuvre known as Edelbaum’s method.

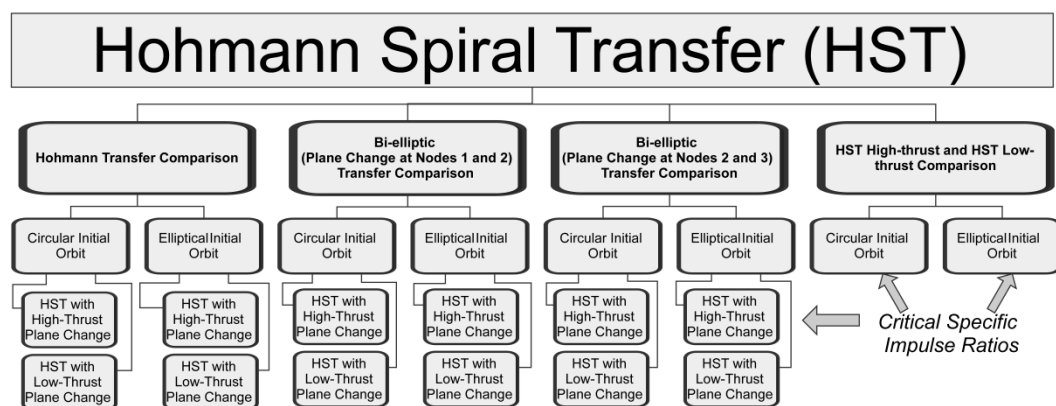


Figure 4-7 HST with plane change comparison chart

## 4.4. HST with High-Thrust Plane Change

Visual representations of the HST (high thrust plane change), Hohmann and bi-elliptic transfers are shown in Figure 4-8. It can be seen that the plane change for the HST is split between the first and second impulses; this is also the case for the compared Hohmann and bi-elliptic transfers. Although the case where the bi-elliptic plane change is split between the second and third nodes is not shown here, it is considered in this section as was mentioned previously. The analytical methodology used for the plane change distribution was introduced and validated in Section 3.1 in Chapter 3 and will therefore not be re-derived here.



$$\Delta V_{HSTHC} = \sqrt{\frac{\mu}{r_i} + \frac{2\mu r_c}{r_i(r_i+r_c)} - 2\sqrt{\frac{\mu}{r_i}}\sqrt{\frac{2\mu r_c}{r_i(r_i+r_c)}}\cos(\sigma_{1'})} + \sqrt{\frac{\mu}{r_c} + \frac{2\mu r_i}{r_c(r_i+r_c)} - 2\sqrt{\frac{\mu}{r_c}}\sqrt{\frac{2\mu r_i}{r_c(r_i+r_c)}}\cos(\Delta I - \sigma_{1'})}. \quad (4.17)$$

The velocity requirement for the HST low-thrust phase has been previously defined in Eq. (4.5) and the velocity requirement for the Hohmann transfer, which also uses the same analytical plane change distribution as the HST high-thrust phase, is found as

$$\Delta V_{HC} = \sqrt{\frac{\mu}{r_i} + \frac{2\mu r_t}{r_i(r_i+r_t)} - 2\sqrt{\frac{\mu}{r_i}}\sqrt{\frac{2\mu r_t}{r_i(r_i+r_t)}}\cos(\sigma_1)} + \sqrt{\frac{\mu}{r_t} + \frac{2\mu r_i}{r_t(r_i+r_t)} - 2\sqrt{\frac{\mu}{r_t}}\sqrt{\frac{2\mu r_i}{r_t(r_i+r_t)}}\cos(\Delta I - \sigma_1)} \quad (4.18)$$

where

$$\sigma_{1'/1} = s\Delta I = \tan^{-1} \left[ \frac{\sin(\Delta I)}{\frac{\sqrt{\frac{\mu}{r_i}}\sqrt{\frac{2\mu r_c/t}{r_i(r_i+r_c/t)}}}{\sqrt{\frac{\mu}{r_c/t}}\sqrt{\frac{2\mu r_i}{r_c/t(r_i+r_c/t)}}} + \cos(\Delta I)} \right].$$

By using the velocity requirements specified and substituting the orbit ratios  $R1$  and  $R2$  as defined previously, the critical specific impulse ratio, defined in Eq. (4.4) reduces to

$$\frac{I_{spL}}{I_{spH}} = I_{sp}^{HHHC} = \frac{1 - \sqrt{\frac{R1}{R2}}}{\sqrt{R1} \left[ \mathcal{A}_1 - \mathcal{A}_2 - \sqrt{\frac{1}{R2}} \mathcal{A}_3 \right] + \mathcal{A}_4}. \quad (4.19)$$

where

$$\mathcal{A}_1 = \sqrt{1 + \frac{2R1}{1+R1} - \sqrt{\frac{8R1}{1+R1}} \cos(\tan^{-1} \left[ \frac{\sin(\Delta I)}{\sqrt{(R1)^3 + \cos(\Delta I)}} \right])}$$

$$\mathcal{A}_2 = \sqrt{1 + \frac{2R2}{1+R2} - \sqrt{\frac{8R2}{1+R2}} \cos(\tan^{-1} \left[ \frac{\sin(\Delta I)}{\sqrt{(R2)^3 + \cos(\Delta I)}} \right])}$$

$$\mathcal{A}_3 = \sqrt{1 + \frac{2}{1+R2} - \sqrt{\frac{8}{1+R2}} \cos(\Delta I - \tan^{-1} \left[ \frac{\sin(\Delta I)}{\sqrt{(R2)^3 + \cos(\Delta I)}} \right])}$$

$$\mathcal{A}_4 = \sqrt{1 + \frac{2}{1+R1} - \sqrt{\frac{8}{1+R1}} \cos(\Delta I - \tan^{-1} \left[ \frac{\sin(\Delta I)}{\sqrt{(R1)^3 + \cos(\Delta I)}} \right])}$$

To verify Eq. (4.19), the plane change,  $\Delta I$ , can be set equal to zero and the equation is shown to reduce to the co-planar critical specific impulse ratio, Eq. (4.8), as expected. It can be seen that Eq. (4.19) depends on  $R1, R2$  and  $\Delta I$  and in the case where the initial orbit radius, target orbit radius and required plane change are known - common for most mission scenarios - the equation depends on only  $R2$  or more specifically, the intermediate circular orbit radius value,  $r_c$ . Varying this will give a range of transfer orbits with a given critical ratio defining the point where the HST, using the high-thrust system to impart the plane change, is equivalent in terms of fuel mass fraction to that of the Hohmann transfer. This statement is valid for all critical specific impulse equations derived in the following sections with the HST being equivalent, in terms of fuel mass fraction, to the compared transfer. The function graph is shown in Section 4.4.1.4.

#### 4.4.1.2. *HST and Bi-Elliptic Critical Specific Impulse Ratio[1-2]*

Considering the case where the bi-elliptic transfer is compared to the HST using the high-thrust system to perform the plane change and starting in a circular orbit, the velocity

requirements for the high and low-thrust sections of the HST are previously defined in Eqns. (4.17) and (4.5) respectively. The velocity requirement of the bi-elliptic transfer with plane change performed at both the first and second impulses is defined as

$$\Delta V_{HC} = \sqrt{\frac{\mu}{r_i} + \frac{2\mu r_c}{r_i(r_i+r_c)} - 2\sqrt{\frac{\mu}{r_i}}\sqrt{\frac{2\mu r_c}{r_i(r_i+r_c)}}\cos(\sigma_2)} + \sqrt{\frac{2\mu r_t}{r_c(r_c+r_t)} + \frac{2\mu r_i}{r_c(r_i+r_c)} - 2\sqrt{\frac{2\mu r_t}{r_c(r_c+r_t)}}\sqrt{\frac{2\mu r_i}{r_c(r_i+r_c)}}\cos(\Delta I - \sigma_2)}\sqrt{\frac{2\mu}{r_t} - \frac{2\mu}{r_c+r_t} - \sqrt{\frac{\mu}{r_t}}} \quad (4.20)$$

where

$$\sigma_2 = s\Delta I = \tan^{-1} \left[ \frac{\sin(\Delta I)}{\frac{\sqrt{\frac{\mu}{r_i}}\sqrt{\frac{2\mu r_c}{r_i(r_i+r_c)}}}{\sqrt{\frac{2\mu r_i}{r_c(r_i+r_c)}}\sqrt{\frac{2\mu r_t}{r_c(r_c+r_t)}} + \cos(\Delta I)}} \right].$$

By then substituting the orbit ratios defined previously, Eq. (4.5) reduces to

$$\frac{I_{spL}}{I_{spH}} = I_{sp}^{BHHC} = \frac{1 - \sqrt{\frac{R1}{R2}}}{\sqrt{R1} \left[ \sqrt{\frac{1}{R2} B_1} + \sqrt{\frac{2}{R2} B_2 - B_3 - \sqrt{\frac{1}{R2} F_4}} \right] + \sqrt{\frac{2R2}{R1+R2} - 1}} \quad (4.21)$$

where,

$$B_1 = \sqrt{1 + \frac{R2}{1+R2} - \sqrt{\frac{8R2}{1+R2}} \cos \left( \tan^{-1} \left[ \frac{\sin(\Delta I)}{\frac{\sqrt{R2^3}\sqrt{R1+R2}}{\sqrt{2R1}} + \cos(\Delta I)} \right] \right)}$$

$$B_2 = \sqrt{\frac{R1}{R1+R2} + \frac{1}{1+R2} - \sqrt{\frac{4R1}{R1+R2}} \sqrt{\frac{1}{1+R2}} \cos(\Delta I - \tan^{-1} \left[ \frac{\sin(\Delta I)}{\frac{\sqrt{R2^3}\sqrt{R1+R2}}{\sqrt{2R1}} + \cos(\Delta I)} \right])}$$

$$\mathcal{B}_3 = \sqrt{1 + \frac{2R2}{1+R2} - \sqrt{\frac{8R2}{1+R2}} \cos\left(\tan^{-1}\left[\frac{\sin(\Delta I)}{\sqrt{(R2)^3 + \cos(\Delta I)}}\right]\right)}$$

$$\mathcal{B}_4 = \sqrt{1 + \frac{2}{1+R2} - \sqrt{\frac{8}{1+R2}} \cos\left(\Delta I - \tan^{-1}\left[\frac{\sin(\Delta I)}{\sqrt{(R2)^3 + \cos(\Delta I)}}\right]\right)}.$$

The function graph is shown in Section 4.4.1.4.

#### 4.4.1.3. *HST and Bi-Elliptic Critical Specific Impulse Ratio* [2-3]

For the case when the bi-elliptic, with plane change performed at the second and third impulses, and HST, with plane change performed by the high-thrust system, are compared, the velocity requirement for the bi-elliptic transfer is

$$\Delta V_{HC} = \sqrt{\frac{2\mu r_c}{r_i(r_i+r_c)}} - \sqrt{\frac{\mu}{r_i}} + \sqrt{\frac{2\mu r_i}{r_c(r_i+r_c)} + \frac{2\mu r_t}{r_c(r_c+r_t)} - 2\sqrt{\frac{2\mu r_i}{r_c(r_i+r_c)}}\sqrt{\frac{2\mu r_t}{r_c(r_c+r_t)}}\cos(\sigma_3)} + \sqrt{\frac{\mu}{r_t} + \frac{2\mu r_c}{r_t(r_c+r_t)} - 2\sqrt{\frac{\mu}{r_t}}\sqrt{\frac{2\mu r_c}{r_t(r_c+r_t)}}\cos(\Delta I - \sigma_3)} \quad (4.22)$$

where

$$\sigma_3 = s\Delta I = \tan^{-1}\left[\frac{\sin(\Delta I)}{\frac{\sqrt{\frac{2\mu r_i}{r_c(r_i+r_c)}}\sqrt{\frac{2\mu r_t}{r_c(r_c+r_t)}}}{\sqrt{\frac{\mu}{r_t}}\sqrt{\frac{2\mu r_c}{r_t(r_c+r_t)}}} + \cos(\Delta I)}\right].$$

The HST high and low-thrust sections are previously defined in Eq. (4.17) and (4.5) respectively. Using these equations and the orbit ratios previously defined, the critical specific impulse ratio is

$$\frac{I_{spL}}{I_{spH}} = I_{sp}^{B_{23}HHC} = \frac{1 - \sqrt{\frac{R1}{R2}}}{\sqrt{R1} \left( \sqrt{\frac{2R2}{1+R2}} - 1 \right) + \sqrt{\frac{R1}{R2}} (C_1 - \sqrt{R2} C_2 - C_3) + C_4} \quad (4.23)$$

where

$$C_1 = \sqrt{\frac{2}{1+R2} + \frac{2R1}{R1+R2} - \sqrt{\frac{8}{1+R2}} \sqrt{\frac{2R1}{R1+R2}} \cos \left( \tan^{-1} \left[ \frac{\sin(\Delta I)}{\sqrt{\frac{2}{1+R2} \sqrt{\frac{R1^3}{R2^3} + \cos(\Delta I)}}} \right] \right)}$$

$$C_2 = \sqrt{1 + \frac{2R2}{1+R2} - \sqrt{\frac{8R2}{1+R2}} \cos \left( \tan^{-1} \left[ \frac{\sin(\Delta I)}{\sqrt{R2^3 + \cos(\Delta I)}} \right] \right)}$$

$$C_3 = \sqrt{1 + \frac{2}{1+R2} - \sqrt{\frac{8}{1+R2}} \cos \left( \Delta I - \tan^{-1} \left[ \frac{\sin(\Delta I)}{\sqrt{R2^3 + \cos(\Delta I)}} \right] \right)}$$

$$C_4 = \sqrt{1 + \frac{2R2}{1+R2} - \sqrt{\frac{8R2}{R1+R2}} \cos \left( \Delta I - \tan^{-1} \left[ \frac{\sin(\Delta I)}{\sqrt{\frac{2}{1+R2} \sqrt{\frac{R1^3}{R2^3} + \cos(\Delta I)}}} \right] \right)}$$

The function graph is shown in Section 4.4.1.4.

#### 4.4.1.4. *Circular Initial Orbit Function Graphs*

This section contains the graphs for the three functions starting in a circular orbit as detailed previously. Figure 4-9 corresponds to Eq. (4.19) and represents the HST and Hohmann critical specific impulse ratio. Figure 4-10 shows Eq. (4.21) and represents the critical specific impulse ratio for the HST and bi-elliptic with plane change at the first and second impulses. Figure 4-11 corresponds to Eq. (4.23) which represents the critical specific impulse ratio for the HST and bi-elliptic with plane change at second and third impulses. All critical ratios have a target to initial orbit radius ( $R1$ ) of 6.42 which is representative of a transfer from Low Earth Orbit (LEO) to GEO. For the HST to offer a lower fuel mass than

the compared transfer, the propulsion system on board the spacecraft must exceed the critical specific impulse ratio. To highlight this, each figure has a region which is shaded in grey and highlights where the HST will not offer a lower fuel mass than the compared transfer. Conversely, the region in white is where the HST will offer a benefit and in general, the larger the difference between the propulsion system specific impulse ratio and the critical specific impulse ratio, the larger the fuel mass saving. The general trend for all critical ratios shows the ratios reducing with increasing plane change,  $\Delta I$ , and intermediate to initial orbit ratio,  $R_2$ . As such the largest critical specific impulse ratios are found at small  $R_2$  and  $\Delta I$ . This implies that the HST becomes more efficient with an increasing plane change and orbit ratio,  $R_2$ . In Figure 4-9 it can be seen a singularity exist at small  $R_2$  and  $\Delta I$  which confirms the HST will never outperform the Hohmann transfer in the region beyond this.

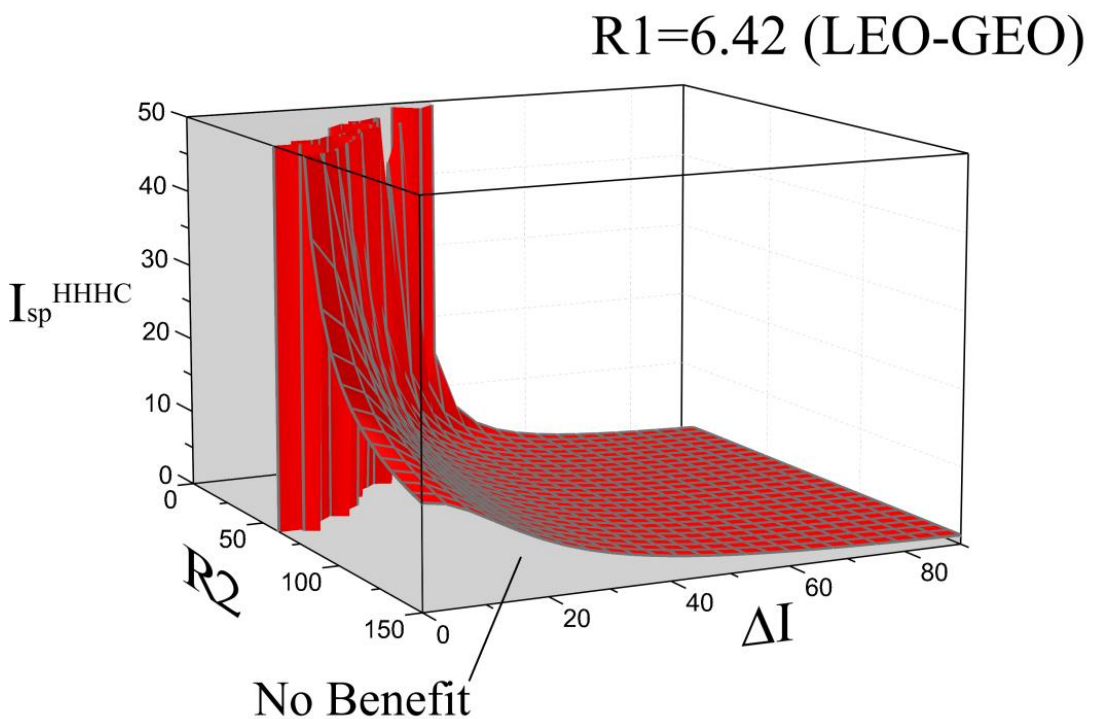
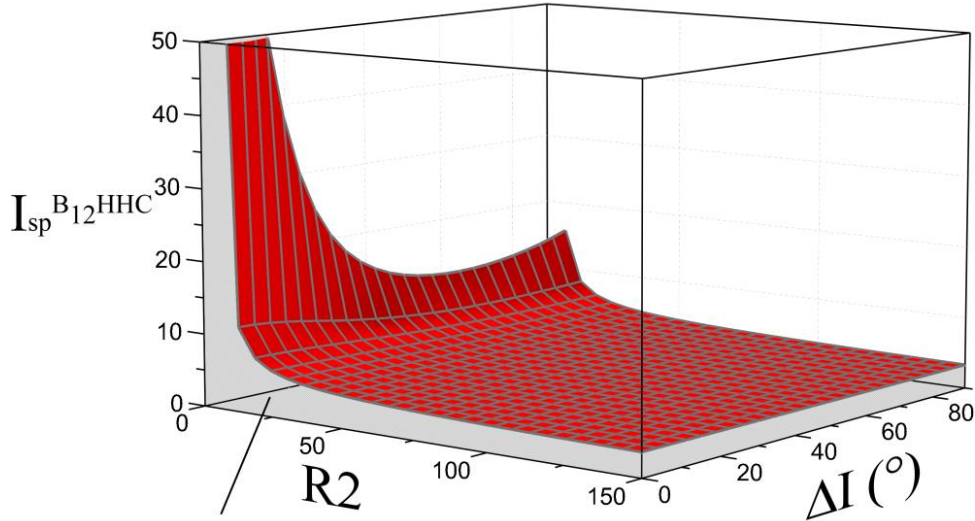


**Figure 4-9 HST and Hohmann critical specific impulse ratio, Eq. (4.19), variation for  $R_1 = 6.42$  (LEO - GEO)**

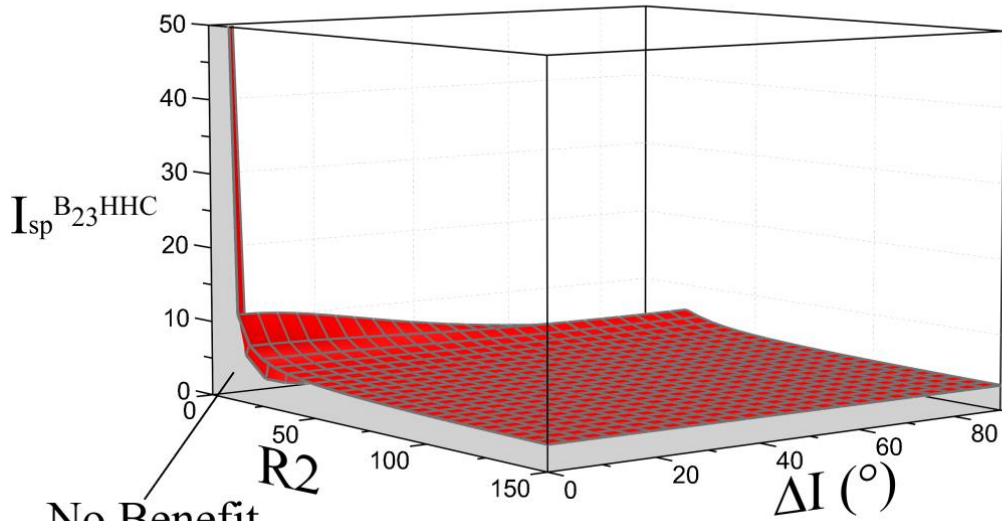
R1=6.42 (LEO-GEO)



No Benefit

Figure 4-10 HST and bi-elliptic with plane change at first and second impulses critical specific impulse ratio, Eq. (4.21), variation for R1 = 6.42 (LEO – GEO)

R1=6.42 (LEO-GEO)



No Benefit

Figure 4-11 HST and bi-elliptic with plane change at first and second impulses critical specific impulse ratio, Eq. (4.23), variation for R1 = 6.42 (LEO – GEO)

## 4.4.2. Elliptical Initial Orbit

### 4.4.2.1. *HST and Hohmann Critical Specific Impulse Ratio*

For the case when the spacecraft starts in an elliptical orbit and the high-thrust section of the HST performs the plane change, the high-thrust only Hohmann velocity requirement is

$$\Delta V_{HE} = \sqrt{\frac{2\mu r_i}{r_t(r_i+r_t)} + \frac{\mu}{r_t} - 2\sqrt{\frac{2\mu r_i}{r_t(r_i+r_t)}}\sqrt{\frac{\mu}{r_t}}\cos(\Delta I)} \quad (4.24)$$

and accounts for a single impulse burn at apogee. This burn circularises the orbit while also changing the inclination. It should be noted that this analytical analysis is only valid when the apogee of the initial orbit coincides with the final orbit radius. This is a reasonable assumption as it is representative of a standard orbit transfer from GTO to GEO [120].

The HST high-thrust section velocity requirement incorporating the plane change and accounting for the elliptical initial orbit is

$$\Delta V_{HSTHE} = \sqrt{\frac{\mu}{r_t}}\sqrt{\frac{R_1}{R_2}}(\sqrt{R_2}\mathcal{D}_1 + \mathcal{D}_2) \quad (4.25)$$

where

$$\mathcal{D}_1 = \sqrt{\frac{2R_1}{1+R_1} + \frac{2R_2}{1+R_2} - \sqrt{\frac{8R_1}{1+R_1}}\sqrt{\frac{2R_2}{1+R_2}}\cos\left(\tan^{-1}\left[\frac{\sin(\Delta I)}{\sqrt{\frac{2R_1R_2^3}{1+R_1} + \cos(\Delta I)}}\right]\right)}$$

$$\mathcal{D}_2 = \sqrt{1 + \frac{2}{1+R_2} - \sqrt{\frac{8}{1+R_2}}\cos\left(\Delta I - \tan^{-1}\left[\frac{\sin(\Delta I)}{\sqrt{\frac{2R_1R_2^3}{1+R_1} + \cos(\Delta I)}}\right]\right)}$$

The high-thrust burn is conducted at the initial orbit perigee and the orbit ratios, as previously defined, are used for simplification. For all elliptical cases considered in this dissertation, the orbit ratios  $R1$  and  $R2$  assume that  $r_i$  is the initial orbit perigee.

The low-thrust section of the HST transfer is the same as Eq. (4.5). Using these definitions, and substituting into Eq. (4.4) , the critical specific impulse ratio is

$$\frac{I_{spL}}{I_{spH}} = I_{sp}^{HHHE} = \frac{1 - \sqrt{\frac{R1}{R2}}}{\varepsilon_1 - \sqrt{\frac{R1}{R2}}(\sqrt{R2}\varepsilon_2 + \varepsilon_3)} \quad (4.26)$$

where

$$\varepsilon_1 = \sqrt{\frac{2}{1+R1} + 1 - 2\sqrt{\frac{2}{1+R1}} \cos(\Delta I)}$$

$$\varepsilon_2 = \sqrt{\frac{2R1}{1+R1} + \frac{2R2}{1+R2} - \sqrt{\frac{8R1}{1+R1}} \sqrt{\frac{2R2}{1+R2}} \cos\left(\tan^{-1}\left[\frac{\sin(\Delta I)}{\sqrt{\frac{2R1R2^3}{1+R1} + \cos(\Delta I)}}\right]\right)}$$

$$\varepsilon_3 = \sqrt{1 + \frac{2}{1+R2} - \sqrt{\frac{8}{1+R2}} \cos\left(\Delta I - \tan^{-1}\left[\frac{\sin(\Delta I)}{\sqrt{\frac{2R1R2^3}{1+R1} + \cos(\Delta I)}}\right]\right)}.$$

The function is shown in Section 4.4.3.1.

#### 4.4.2.2. *HST and Bi-Elliptic Critical Specific Impulse Ratio*

[1-2]

Deriving the critical specific impulse ratio for the comparison of a bi-elliptic transfer and the HST with high-thrust plane change starting in an elliptical orbit, the velocity requirement of the bi-elliptic transfer is

$$\Delta V_{HE} = \mathcal{F}_1 + \mathcal{F}_2 + \sqrt{\frac{2\mu r_c}{r_t(r_t+r_c)}} - \sqrt{\frac{\mu}{r_t}} \quad (4.27)$$

where

$$\mathcal{F}_1 = \sqrt{\frac{2\mu r_t}{r_i(r_i+r_t)} + \frac{2\mu r_c}{r_i(r_i+r_c)} - \sqrt{\frac{2\mu r_t}{r_i(r_i+r_t)}} \sqrt{\frac{2\mu r_c}{r_i(r_i+r_c)}} \cos \left( \tan^{-1} \frac{\sin(\Delta I)}{\sqrt{\frac{2\mu r_t}{r_i(r_i+r_t)} \sqrt{\frac{2\mu r_c}{r_i(r_i+r_c)}} + \cos(\Delta I)}} \right)}$$

$\mathcal{F}_2 =$

$$\sqrt{\frac{2\mu r_i}{r_c(r_i+r_c)} + \frac{2\mu r_t}{r_c(r_t+r_c)} - \sqrt{\frac{2\mu r_i}{r_c(r_i+r_c)}} \sqrt{\frac{2\mu r_t}{r_c(r_t+r_c)}} \cos \left( \Delta I - \tan^{-1} \frac{\sin(\Delta I)}{\sqrt{\frac{2\mu r_t}{r_i(r_i+r_t)} \sqrt{\frac{2\mu r_c}{r_i(r_i+r_c)}} + \cos(\Delta I)}} \right)}$$

The velocity requirements for the high and low-thrust sections of the HST are given in Eqs. (4.25) and (4.5) respectively. Using these equations and the orbit ratios previously defined, the critical specific impulse ratio can be determined as

$$\frac{I_{spL}}{I_{spH}} = I_{sp}^{BHHE} = \frac{1 - \sqrt{\frac{R1}{R2}}}{\sqrt{\frac{R1}{R2}}(\sqrt{R2}\mathcal{G}_1 + \mathcal{G}_2 - \sqrt{R2}\mathcal{G}_3 - \mathcal{G}_4) + \sqrt{\frac{2R2}{R1+R2}} - 1} \quad (4.28)$$

where

$$\mathcal{G}_1 = \sqrt{\frac{2R1}{1+R1} + \frac{2R2}{1+R2} - \sqrt{\frac{8R1}{1+R1}} \sqrt{\frac{2R2}{1+R2}} \cos \left( \tan^{-1} \left[ \frac{\sin(\Delta I)}{\sqrt{\frac{R2^3(R1+R2)}{1+R1} + \cos(\Delta I)}} \right]} \right)}$$

$$\mathcal{G}_2 = \sqrt{\frac{2}{1+R2} + \frac{2R1}{R1+R2} - \sqrt{\frac{8}{1+R2}} \sqrt{\frac{2R1}{R1+R2}} \cos \left( \Delta I - \tan^{-1} \left[ \frac{\sin(\Delta I)}{\sqrt{\frac{R2^3(R1+R2)}{1+R1} + \cos(\Delta I)}} \right]} \right)}$$

$$\mathcal{G}_3 = \sqrt{\frac{2R1}{1+R1} + \frac{2R2}{1+R2} - \sqrt{\frac{8R1}{1+R1}}\sqrt{\frac{2R2}{1+R2}} \cos\left(\tan^{-1}\left[\frac{\sin(\Delta I)}{\sqrt{\frac{2R1R2^3}{1+R1} + \cos(\Delta I)}}\right]\right)}$$

$$\mathcal{G}_4 = \sqrt{1 + \frac{2}{1+R2} - \sqrt{\frac{8}{1+R2}} \cos\left(\Delta I - \tan^{-1}\left[\frac{\sin(\Delta I)}{\sqrt{\frac{2R1R2^3}{1+R1} + \cos(\Delta I)}}\right]\right)}.$$

The function is shown in Section 4.4.3.1.

### 4.4.3. HST and Bi-Elliptic Critical Specific Impulse Ratio [2-3]

For an elliptical initial orbit, the bi-elliptic transfer with the plane change distributed between the second and third impulses has a velocity requirement of

$$\Delta V_{HE} = \sqrt{\frac{2\mu r_c}{r_i(r_i+r_c)} - \frac{2\mu r_t}{r_i(r_i+r_t)} + \sqrt{\frac{2\mu r_i}{r_c(r_i+r_c)} + \frac{2\mu r_t}{r_c(r_c+r_t)} - 2\sqrt{\frac{2\mu r_i}{r_c(r_i+r_c)}}\sqrt{\frac{2\mu r_t}{r_c(r_c+r_t)}} \cos(\sigma_4)} + \sqrt{\frac{\mu}{r_t} + \frac{2\mu r_c}{r_t(r_c+r_t)} - 2\sqrt{\frac{\mu}{r_t}}\sqrt{\frac{2\mu r_c}{r_t(r_c+r_t)}} \cos(\Delta I - \sigma_4)} \quad (4.29)$$

where

$$\sigma_4 = s\Delta I = \tan^{-1}\left[\frac{\sin(\Delta I)}{\frac{\sqrt{\frac{2\mu r_i}{r_c(r_i+r_c)}}\sqrt{\frac{2\mu r_t}{r_c(r_c+r_t)}}}{\sqrt{\frac{\mu}{r_t}}\sqrt{\frac{2\mu r_c}{r_t(r_c+r_t)}} + \cos(\Delta I)}}\right].$$

For the same initial orbit the HST's high and low-thrust velocity requirements have been previously defined in Eqs. (4.25) and (4.5) respectively. Using these equations and the orbit ratios previously defined, the critical specific impulse ratio can be determined as

$$\frac{I_{spL}}{I_{spH}} = I_{sp}^{B_{23}HHE} = \frac{1 - \sqrt{\frac{R_1}{R_2}}}{\sqrt{\frac{2R_1R_2}{1+R_2} - \sqrt{\frac{2R_1^2}{1+R_1} + \sqrt{\frac{R_1}{R_2}}(\mathcal{H}_1 - \sqrt{R_2}\mathcal{H}_2 - \mathcal{H}_3)} + \mathcal{H}_4}} \quad (4.30)$$

where

$$\mathcal{H}_1 = \sqrt{\frac{2}{1+R_2} + \frac{2R_1}{R_1+R_2} - \sqrt{\frac{8}{1+R_2}} \sqrt{\frac{2R_1}{R_1+R_2}} \cos \left( \tan^{-1} \left[ \frac{\sin(\Delta I)}{\sqrt{\frac{2}{1+R_2} \sqrt{\frac{R_1^3}{R_2^3} + \cos(\Delta I)}}} \right] \right)}$$

$$\mathcal{H}_2 = \sqrt{\frac{2R_1}{1+R_1} + \frac{2R_2}{1+R_2} - \sqrt{\frac{8R_1}{1+R_1}} \sqrt{\frac{2R_2}{1+R_2}} \cos \left( \tan^{-1} \left[ \frac{\sin(\Delta I)}{\sqrt{\frac{2R_1R_2^3}{1+R_1} + \cos(\Delta I)}} \right] \right)}$$

$$\mathcal{H}_3 = \sqrt{1 + \frac{2}{1+R_2} - \sqrt{\frac{8}{1+R_2}} \cos \left( \Delta I - \tan^{-1} \left[ \frac{\sin(\Delta I)}{\sqrt{\frac{2R_1R_2^3}{1+R_1} + \cos(\Delta I)}} \right] \right)}$$

$$\mathcal{H}_4 = \sqrt{1 + \frac{2R_2}{R_1+R_2} - \sqrt{\frac{8R_2}{R_1+R_2}} \cos \left( \Delta I - \tan^{-1} \left[ \frac{\sin(\Delta I)}{\sqrt{\frac{2}{1+R_2} \sqrt{\frac{R_1^3}{R_2^3} + \cos(\Delta I)}}} \right] \right)}$$

The function is shown in Section 4.4.3.1.

#### 4.4.3.1. *Elliptical Initial Orbit Function Graphs*

This section shows the graphs for the three previous functions described for an elliptical initial orbit. Figure 4-12 displays Eq. (4.26) and represents the HST and Hohmann critical specific impulse ratio. Figure 4-13 shows the evolution of Eq. (4.28) which is representative of the critical specific impulse ratio for the HST and bi-elliptic with plane change at the second and third impulses. Finally, Figure 4-14 shows Eq. (4.30) and is representative of the critical specific impulse ratio for the HST and bi-elliptic with plane change at the second and third impulses. For all transfers,  $R_1 = 6.42$  which is representative of a GTO-GEO transfer with the initial orbit radius in this case representing the perigee radius as discussed

previously. If compared with the circular initial orbit figures, it can be seen that each respective case is very similar. As such, the critical specific impulse ratio is shown to reduce for all cases, showing the HST becomes more efficient, with an increasing  $R2$  and  $\Delta I$ . For the HST and Hohmann critical specific impulse ratio it can also be seen that there is a singularity at small  $R2$  and  $\Delta I$  which again signifies that in the region beyond this the Hohmann transfer will always outperform the HST.

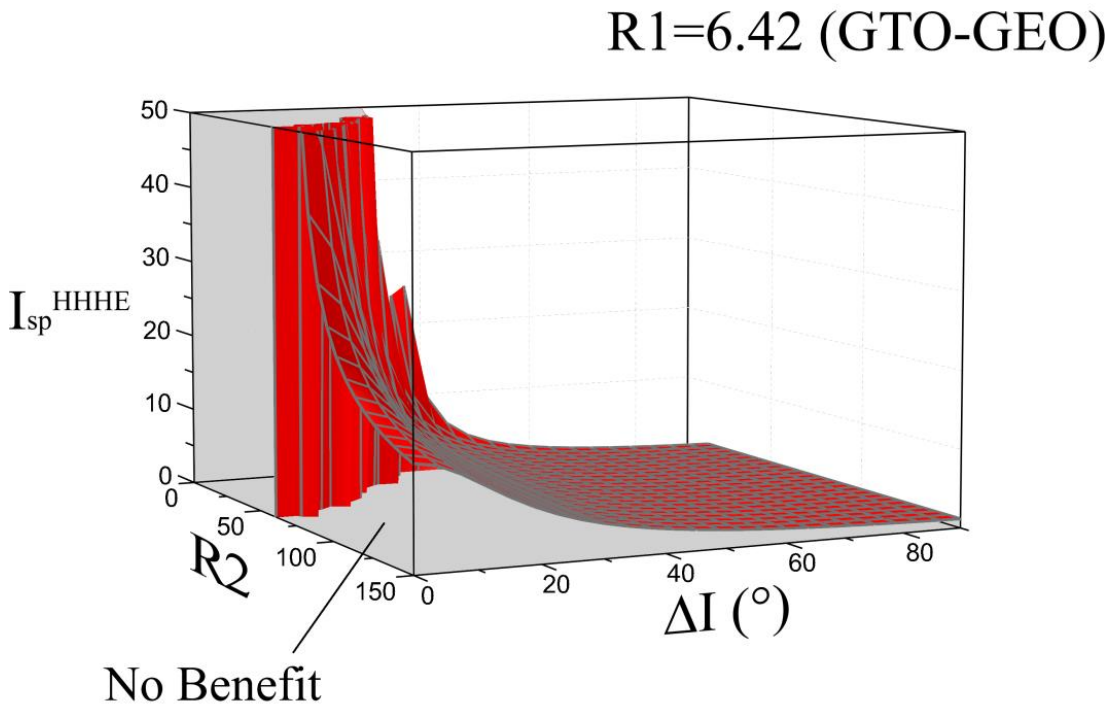
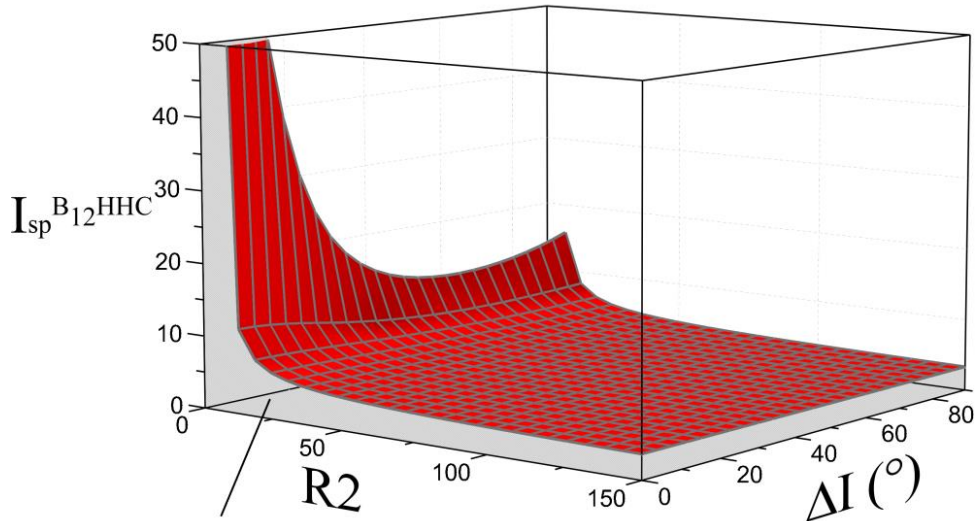


Figure 4-12 HST and Hohmann critical specific impulse ratio, Eq. (4.26), variation for  $R1 = 6.42$  (GTO – GEO)

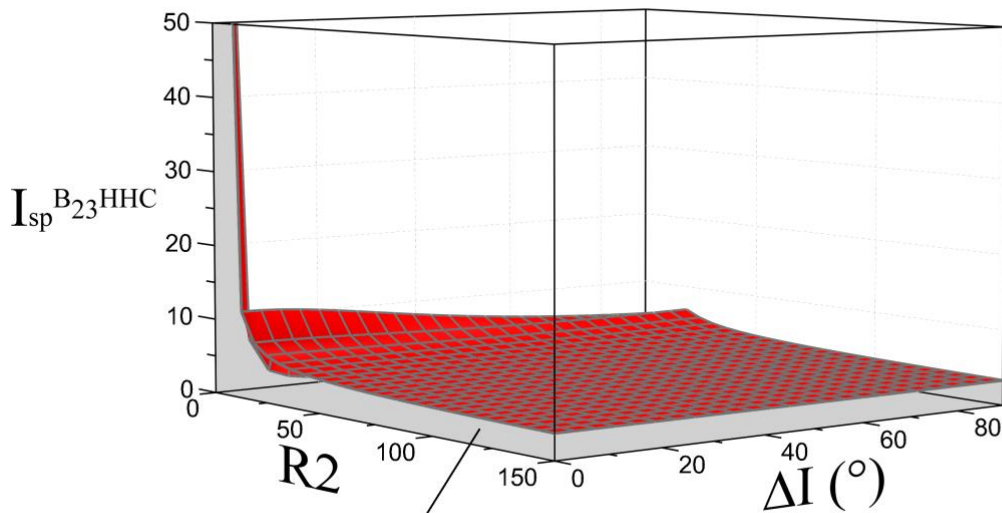
R1=6.42 (LEO-GEO)



No Benefit

Figure 4-13 HST and bi-elliptic with plane change at first and second impulses critical specific impulse ratio, Eq. (4.28), variation for  $R_1 = 6.42$  (GTO – GEO)

R1=6.42 (GTO-GEO)



No Benefit

Figure 4-14 HST and bi-elliptic with plane change at first and second impulses critical specific impulse ratio, Eq. (4.30), variation for  $R_1 = 6.42$  (GTO – GEO)

## 4.5. HST with Low-Thrust Plane Change

Considering the HST with the plane change performed by the low-thrust propulsion system, there are two analytical methods which can be used to perform the analysis. As the HST transfers the spacecraft to an intermediate orbit that is extremely large in comparison to the

target, the first method considers performing the full plane change at the largest orbit radius before spiralling-in towards the target. This allows the full plane change to be performed with the largest thrust to weight ratio before all the acceleration is then used to perform the spiral-in towards the target. The second method considers a combined plane change and spiral-in manoeuvre where the thrust vector is assumed to lie in the Transverse-Normal plane at some angle. This method was first suggested in [30] with the focus on outward orbit transfers at relatively small orbit ratios. As such, it is necessary to develop equations using both methods described and compare them to determine advantages of each approach. This section therefore derives equations that consider both circular and elliptical orbits compared to Hohmann and bi-elliptic transfers as was done in the high-thrust plane change section.

## 4.5.1. Plane Change at Greatest Radius

### 4.5.1.1. *Analytical Methodology*

A schematic of the HST with a plane change performed by the low-thrust propulsion is given in Figure 4-15. In this case the full plane change is performed at the largest orbit radius before the system is then used to spiral in toward the target orbit.

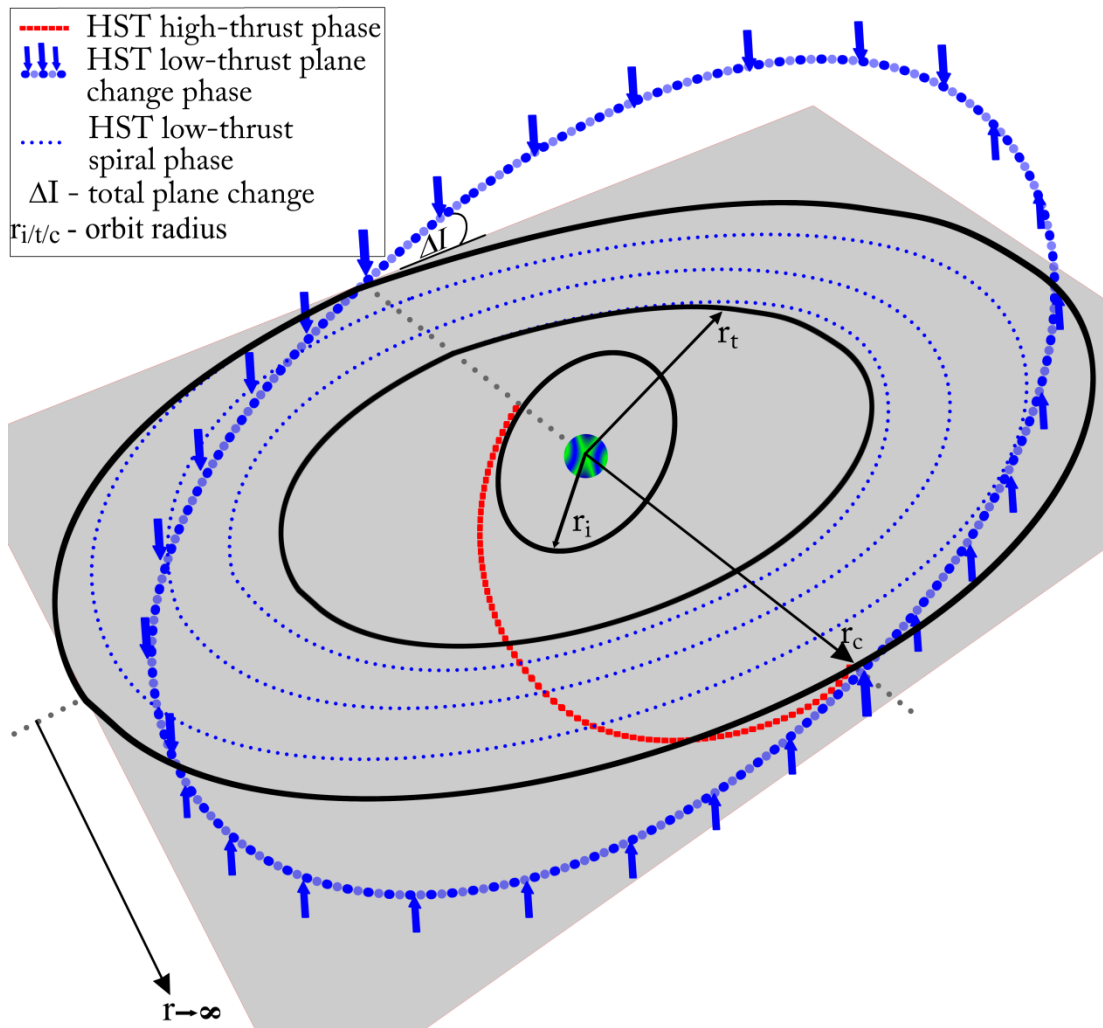


Figure 4-15 HST with low-thrust plane change schematic

To consider the plane change performed by the low-thrust system analytically, it is necessary to define the rate of change of inclination using the Gauss form of the Lagrange planetary equations, in terms of a spacecraft centred *RTN* coordinate system [121],

$$\frac{di}{dv} = \frac{r_c^3}{\mu p} \cos(v + \omega) N \quad (4.31)$$

where, for a circular orbit using the HST the semi-latus rectum is

$$p = r_c. \quad (4.32)$$

In this analysis the argument of perigee is assumed to be  $90^\circ$  as this resolves the issue of it being undefined for a circular intermediate orbit. Equation (4.31) can then be integrated over

one orbit to give the change in inclination. However, as the locally optimal control law states that the normal thrust switches sign depending on the argument of latitude, the integration is performed in two parts, from 0 to  $\pi$  radians and  $\pi$  to  $2\pi$  radians. The overall plane change for one orbit, a result of summing the magnitudes from each integration is therefore defined as

$$\Delta I_{po} = \frac{4r_c^2 a_s}{\mu}. \quad (4.33)$$

This can then be used with the orbital period and number of orbits required, defined respectively as

$$t_{period} = 2\pi \sqrt{\frac{r_c^3}{\mu}} \quad (4.34)$$

$$NOO = \frac{\Delta I}{\Delta I_{po}}, \quad (4.35)$$

to give the velocity requirement for the plane change as

$$\Delta V_{HSTPL} = a_s t_{period} NOO. \quad (4.36)$$

Summing this with Eq. (4.5), which is the velocity requirement to perform a spiral transfer between two circular orbits, gives the total change in velocity for the HST's low thrust section accounting for plane change and spiral-in as

$$\Delta V_{HSTL} = \sqrt{\frac{\mu}{r_t}} \left[ 1 - \sqrt{\frac{R1}{R2}} + \sqrt{\frac{R1}{R2}} \frac{\pi}{2} \Delta I \right]. \quad (4.37)$$

This equation can be used in the comparison of circular and elliptical initial orbits when the low-thrust system delivers the plane change as the low-thrust section will always begin from a circular orbit. By using this method it is assumed the spacecraft maintains a constant acceleration and thrust over the entire low-thrust phase i.e. the spacecraft mass is assumed to be constant.

### 4.5.1.2. *Numerical Validation*

It is necessary to validate the analytical approach to ensure it can be used for further analysis. To do this a benchmark comparison against a numerical model using the equations of motion defined in modified equinoctial elements is performed. Modified equinoctial elements are used to avoid singularities that exist when adopting the classical Lagrangian elements and have been described in detail in Section 2.6. Only the semi-major axis and inclination locally optimal control laws, that is Eqs (2.29) and (2.33) in Chapter 2, are required for this verification as the analytical methodology assumes that the spacecraft thrusts in the Tangential direction only and thus maintains an eccentricity  $\approx 0$ . Table 4-2 details the transfer specification used while Table 4-3 provides the results. The numerical verification was performed in two phases; the first phase used only the inclination control law to perform the plane change and the spiral-in second phase used the semi-major axis control law only. It should be noted that the numerical verification did not assume constant acceleration; allowing it to vary with the depletion of fuel mass. The transfer time for the HST is calculated using Eq. (4.75) which is defined in Section 4.9.2.

**Table 4-2. Low-thrust plane change at largest orbit radius validation study specification**

Gravitational Constant, $\mu$ ( $\text{m}^3/\text{s}^2$ )	$3.98604418 \times 10^{14}$
Initial Orbit, $r_i$ (m)	6,628,000 (257 km altitude)
Target Orbit, $r_t$ (m)	19,884,000 (13,516 km altitude)
Intermediate Orbit, $r_c$ (m)	33,140,000 (26,769 km altitude)
Target/Initial Orbit Ratio, $R1$	3
Intermediate/Initial Orbit Ratio, $R2$	5
Initial Mass, $m_{wet}$ (kg)	554
Low-Thrust System Specific Impulse, $I_{spL}$ (s)	4,500
Thrust, $Tr$ (mN)	150
Plane Change, $\Delta I$ (rad)	0.5236 ( $30^\circ$ )

In Table 4-3 it is seen that the fuel mass calculated by the analytical and numerical methods are very similar with a maximum relative error of 0.54%. There is a larger relative error of 5.16% associated with the calculated transfer time; this can be associated with the assumption that the analytical methodology maintains a constant acceleration throughout the whole of the low-thrust phase. As both errors are larger than the numerical method it is accepted that the analytical methodology offers a conservative analysis of the transfer.

**Table 4-3 Low-thrust plane change at largest orbit radius validation study results**

	Analytical	Numerical	Relative Error (%) w.r.t. Numerical
<b>Total Fuel Mass, (kg)</b>	46.4	46.15	0.54
<b>Total Transfer Time, (days)</b>	165.07	156.97	5.16

### 4.5.1.3. Circular Initial Orbit

#### 4.5.1.3.1. HST and Hohmann Critical Specific Impulse Ratio

The high-thrust only velocity requirement used to represent the Hohmann transfer in the comparison is given in Eq. (4.18). The high thrust velocity requirement phase of the HST with a circular initial orbit is defined as

$$\Delta V_{HSTHC} = \sqrt{\frac{2\mu}{r_i} - \frac{2\mu}{r_i + r_c}} - \sqrt{\frac{\mu}{r_i}} + \sqrt{\frac{\mu}{r_c}} - \sqrt{\frac{2\mu}{r_c} - \frac{2\mu}{r_i + r_c}} \quad (4.38)$$

whereas the HST low-thrust phase velocity requirement is defined in Eq. (4.37). By substituting the orbit ratios defined previously, Eq. (4.4) reduces to give the critical ratio for the scenario when the low-thrust system performs the plane change as

$$\frac{I_{spL}}{I_{spH}} = I_{sp}^{HHLC} = \frac{1 - \sqrt{\frac{R1}{R2}} + \frac{\pi}{2} \sqrt{\frac{R1}{R2}} \Delta I}{\sqrt{R1} J_1 + J_2 - \sqrt{2R1 - \frac{2R1}{1+R2}} + \sqrt{\frac{2R1}{R2} - \frac{2R1}{1+R2}} - \sqrt{\frac{R1}{R2}} + \sqrt{R1}} \quad (4.39)$$

where

$$J_1 = \sqrt{1 + \frac{2R1}{1+R1} - \sqrt{\frac{8R1}{1+R1}} \cos\left(\tan^{-1}\left(\frac{\sin(\Delta I)}{\sqrt{R1^3 + \cos(\Delta I)}}\right)\right)}$$

$$J_2 = \sqrt{1 + \frac{2}{1+R1} - \sqrt{\frac{8}{1+R1}} \cos\left(\Delta I - \tan^{-1}\left(\frac{\sin(\Delta I)}{\sqrt{R1^3 + \cos(\Delta I)}}\right)\right)} .$$

The function graph is shown in Section 4.5.1.3.4.

#### 4.5.1.3.2. HST and Bi-Elliptic Critical Specific Impulse Ratio [1-2]

Considering the scenario when the bi-elliptic is compared to the HST with the plane change of the bi-elliptic being performed at the first and second impulses and the plane change for

the HST being performed by the low-thrust system, the high and low-thrust velocity requirements for the HST remain the same as defined in Eqns. (4.38) and (4.37) respectively. The bi-elliptic velocity requirement remains the same as is given in Eq. (4.20). Using these definitions and the orbit ratios previously defined, the critical ratio for this scenario is

$$\frac{I_{spL}}{I_{spH}} = I_{sp}^{BHLC} = \frac{1 - \sqrt{\frac{R_1}{R_2} + \frac{\pi}{2} \sqrt{\frac{R_1}{R_2}}} \Delta I}{\sqrt{\frac{R_1}{R_2} (\sqrt{2R_2} J_1 + \sqrt{2} J_2 - 1)} + \sqrt{\frac{2R_2}{R_1 + R_2} - \sqrt{2R_1 - \frac{2R_1}{1+R_2}} + \sqrt{\frac{2R_1}{R_2} - \frac{2R_1}{1+R_2}} - 1}} \quad (4.40)$$

where

$$J_1 = \sqrt{1 + \frac{2R_2}{1+R_2} - \sqrt{\frac{8R_2}{1+R_2}} \cos\left(\tan^{-1}\left(\frac{\sin(\Delta I)}{\frac{\sqrt{R_2^3 \sqrt{R_1+R_2}}}{\sqrt{2R_1}} + \cos(\Delta I)}\right)\right)}$$

$$J_2 = \sqrt{\frac{R_1}{R_1+R_2} + \frac{1}{1+R_2} - \sqrt{\frac{4R_1}{R_1+R_2}} \sqrt{\frac{1}{1+R_2}} \cos\left(\Delta I - \tan^{-1}\left(\frac{\sin(\Delta I)}{\frac{\sqrt{R_2^3 \sqrt{R_1+R_2}}}{\sqrt{2R_1}} + \cos(\Delta I)}\right)\right)}$$

The function graph is shown in Section 4.5.1.3.4.

#### 4.5.1.3.3. HST and Bi-Elliptic Critical Specific Impulse Ratio [2-3]

For the case when the bi-elliptic, with plane change performed at the second and third impulses, is compared to the HST, using the low-thrust system to perform the plane change, the velocity requirements for each transfer have been previously defined in Eqs. (4.22), (4.38) and (4.37). The order of the equations represents the bi-elliptic, HST high-thrust section and HST low-thrust section velocity requirements respectively. The critical specific impulse ratio equation is then defined using these equations and the orbit ratios defined previously as

$$\frac{I_{spL}}{I_{spH}} = I_{sp}^{B_{23}HLC} = \frac{1 - \sqrt{\frac{R_1}{R_2} + \frac{\pi}{2} \sqrt{\frac{R_1}{R_2}}} \Delta I}{\sqrt{R_1} \sqrt{\frac{2R_2}{1+R_2} + \sqrt{\frac{R_1}{R_2}} (\mathcal{K}_1 - 1) + \mathcal{K}_2} - \sqrt{2R_1 - \frac{2R_1}{1+R_2}} + \sqrt{\frac{2R_1}{R_2} - \frac{2R_1}{1+R_2}}} \quad (4.41)$$

where

$$\mathcal{K}_1 = \sqrt{\frac{2}{1+R_2} + \frac{2R_1}{R_1+R_2} - \sqrt{\frac{8}{1+R_2}} \sqrt{\frac{2R_1}{R_1+R_2}} \cos \left( \tan^{-1} \left[ \frac{\sin(\Delta I)}{\sqrt{\frac{2}{1+R_2} \frac{R_1^3}{R_2^3} + \cos(\Delta I)}} \right] \right)}$$

$$\mathcal{K}_2 = \sqrt{1 + \frac{2R_2}{R_1+R_2} - \sqrt{\frac{8R_2}{R_1+R_2}} \cos \left( \Delta I - \tan^{-1} \left[ \frac{\sin(\Delta I)}{\sqrt{\frac{2}{1+R_2} \frac{R_1^3}{R_2^3} + \cos(\Delta I)}} \right] \right)}.$$

The function graph is shown in Section 4.5.1.3.4.

#### 4.5.1.3.4. *Circular Initial Orbit Function Graphs*

This section contains the graphs for the critical specific impulse ratio for the Hohmann and bi-elliptic transfers compared with the HST with a plane change performed by the low-thrust system at the largest orbit radius. All transfers begin in a circular orbit. Figure 4-16 shows Eq. (4.39) which represents the HST and Hohmann critical specific impulse ratio. Figure 4-17 shows Eq. (4.40) which is representative of the HST and bi-elliptic with plane change at first and second impulse. Figure 4-18 shows the function describing the HST and bi-elliptic with plane change at the second and third impulse. All transfers have an orbit ratio,  $R_1$ , of 6.42, as was the case for the HST with high-thrust plane change, and are shown for a varying  $R_2$  and  $\Delta I$ . In general, all equations exhibit similar behaviour to the critical specific impulse ratios with high-thrust plane change. As such, the largest critical ratios are found at small  $R_2$  and  $\Delta I$  for all cases. The HST and Hohmann critical specific impulse ratio contains a singularity which signifies in the region beyond that the HST will never outperform the Hohmann transfer. The lowest ratios for all cases are found at large  $R_2$  and  $\Delta I$  as was the case for the critical specific impulse ratios with a high-thrust plane change and signifies that the HST becomes more efficient with increasing  $R_2$  and  $\Delta I$ .

R1=6.42 (LEO-GEO)

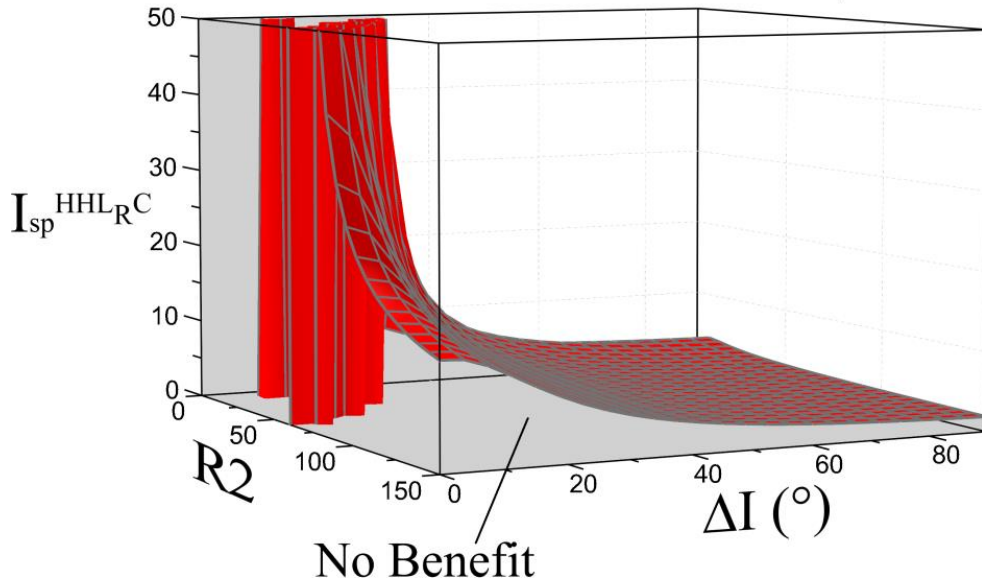


Figure 4-16 HST and Hohmann critical specific impulse ratio, Eq. (4.39), variation for  $R_1 = 6.42$  (LEO – GEO)

R1=6.42 (LEO-GEO)

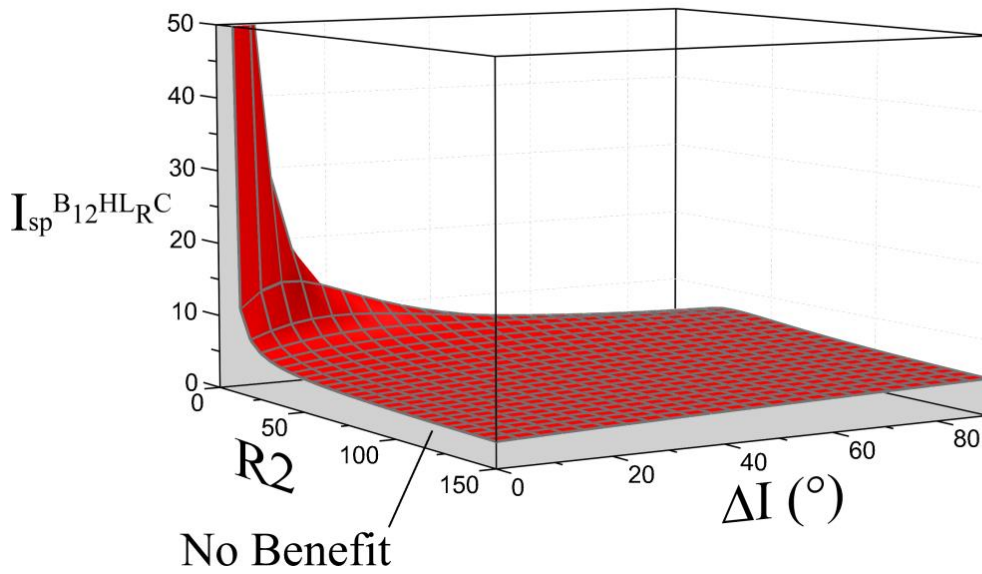


Figure 4-17 HST and bi-elliptic with plane change at first and second impulses critical specific impulse ratio, Eq. (4.40), variation for  $R_1 = 6.42$  (LEO – GEO)

R1=6.42 (LEO-GEO)

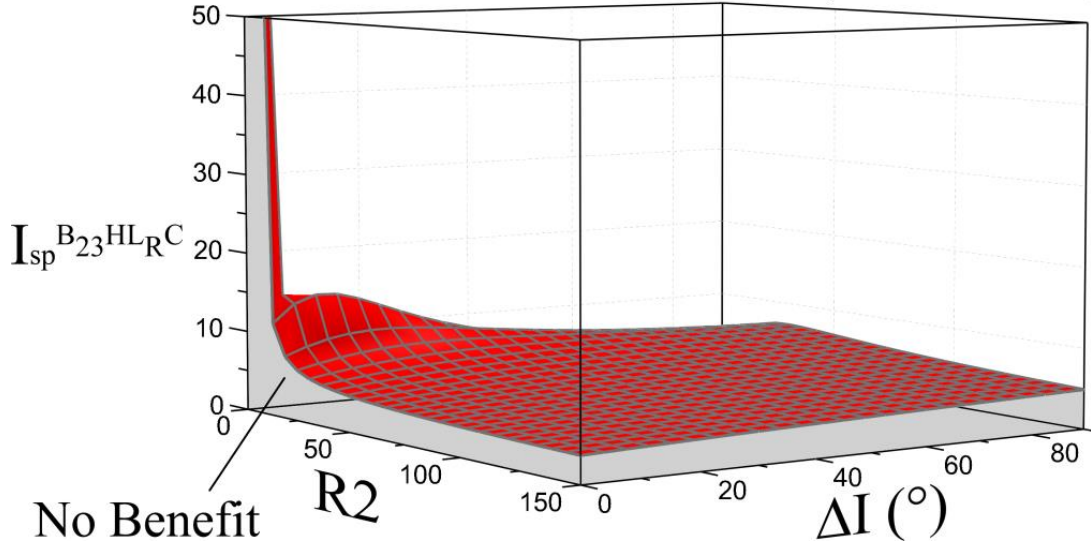


Figure 4-18 HST and bi-elliptic with plane change at second and third impulses critical specific impulse ratio, Eq. (4.41), variation for R1 = 6.42 (LEO – GEO)

#### 4.5.1.4. Elliptical Initial Orbit

##### 4.5.1.4.1. HST and Hohmann Critical Specific Impulse Ratio

For the case when the spacecraft starts in an elliptical orbit and the low-thrust section of the HST performs the plane change, the high-thrust only Hohmann velocity requirement is given in Eq. (4.24) and accounts for a single impulse burn at apogee. The same restrictions as detailed in Section 4.4.2 also apply. The low-thrust section of the HST is equal to Eq. (4.37). The high-thrust section of the HST is given as

$$\Delta V_{HSTHE} = \sqrt{\frac{2\mu r_c}{r_i(r_i+r_c)}} + \sqrt{\frac{\mu}{r_c}} - \sqrt{\frac{2\mu r_t}{r_i(r_i+r_t)}} - \sqrt{\frac{2\mu r_i}{r_c(r_i+r_c)}} \quad (4.42)$$

By then using the orbit ratios as previously defined the critical specific impulse ratio is

$$\frac{I_{spL}}{I_{spH}} = I_{sp}^{HHLE} = \frac{1 - \sqrt{\frac{R_1}{R_2} + \frac{\pi}{2} \sqrt{\frac{R_1}{R_2}} \Delta I}}{\mathcal{L}_1 - \sqrt{\frac{R_1}{R_2}} \left[ \sqrt{R_2} \left( \sqrt{\frac{2R_2}{1+R_2}} - \sqrt{\frac{2R_1}{1+R_1}} \right) - \sqrt{\frac{2}{1+R_2} + 1} \right]} \quad (4.43)$$

where,

$$\mathcal{L}_1 = \sqrt{\frac{2}{1+R_1} + 1 - 2\sqrt{\frac{2}{1+R_1}} \cos(\Delta I)}.$$

The function graph is shown in Section 4.5.1.4.4.

#### 4.5.1.4.2. HST and Bi-Elliptic Critical Specific Impulse Ratio [1-2]

For the scenario comparing the bi-elliptic transfer to the HST using low-thrust to impart the plane change and starting in an elliptical orbit, the velocity requirement for the bi-elliptic transfer has been previously described in Eq. (4.27). The high and low-thrust sections of the HST have been described in Eqns. (4.42) and (4.37) respectively. Using these and the orbit ratios previously defined, the critical specific impulse ratio is

$$\frac{I_{spL}}{I_{spH}} = I_{sp}^{BHLE} = \frac{1 - \sqrt{\frac{R_1}{R_2}} + \frac{\pi}{2} \sqrt{\frac{R_1}{R_2}} \Delta I}{\sqrt{\frac{R_1}{R_2} \left( \sqrt{R_2} \mathcal{M}_1 + \mathcal{M}_2 - \sqrt{R_2} \left[ \sqrt{\frac{2R_2}{1+R_2}} - \sqrt{\frac{2R_1}{1+R_1}} \right] + 1 - \sqrt{\frac{2}{1+R_2}} \right) + \sqrt{\frac{2R_2}{R_1+R_2} - 1}}} \quad (4.44)$$

where

$$\mathcal{M}_1 = \sqrt{\frac{2R_1}{1+R_1} + \frac{2R_2}{1+R_2} - \sqrt{\frac{8R_1}{1+R_1}} \sqrt{\frac{2R_2}{1+R_2}} \cos \left( \tan^{-1} \left[ \frac{\sin(\Delta I)}{\sqrt{\frac{R_2^3(R_1+R_2)}{1+R_1} + \cos(\Delta I)}} \right]} \right)}$$

$$\mathcal{M}_2 = \sqrt{\frac{2}{1+R_2} + \frac{2R_1}{R_1+R_2} - \sqrt{\frac{8}{1+R_2}} \sqrt{\frac{2R_1}{R_1+R_2}} \cos \left( \Delta I - \tan^{-1} \left[ \frac{\sin(\Delta I)}{\sqrt{\frac{R_2^3(R_1+R_2)}{1+R_1} + \cos(\Delta I)}} \right]} \right)}.$$

The function graph is shown in Section 4.5.1.4.4.

#### 4.5.1.4.3. HST and Bi-Elliptic Critical Specific Impulse Ratio [2-3]

Considering an elliptical initial orbit for the case when the bi-elliptic, with plane change at the second and third impulses, is compared to the HST, using the low-thrust system to perform the plane change, the velocity requirement equation for the bi-elliptic equation with

plane change at the second and third impulses has already been defined in Eq. (4.29). The HST's high and low-thrust velocity requirements have also been defined previously in Eqs. (4.42) and (4.37) respectively. The critical specific impulse ratio, using the previously defined orbit ratios, for this case is then defined as

$$\frac{I_{spL}}{I_{spH}} = I_{sp}^{B_{23}HLE} = \frac{1 - \sqrt{\frac{R_1}{R_2} + \frac{\pi}{2}} \sqrt{\frac{R_1}{R_2}} \Delta I}{\sqrt{\frac{2R_1R_2}{1+R_2}} \sqrt{\frac{2R_1^2}{1+R_1} + \frac{R_1}{R_2}} \left[ \mathcal{N}_1 - \left( \sqrt{R_2} \left( \sqrt{\frac{2R_2}{1+R_2}} \sqrt{\frac{2R_1}{1+R_1}} - \sqrt{\frac{2}{1+R_2} + 1} \right) \right) \right] + \mathcal{N}_2} \quad (4.45)$$

where

$$\mathcal{N}_1 = \sqrt{\frac{2}{1+R_2} + \frac{2R_1}{R_1+R_2} - \sqrt{\frac{8}{1+R_2}} \sqrt{\frac{2R_1}{R_1+R_2}} \cos \left( \tan^{-1} \left[ \frac{\sin(\Delta I)}{\sqrt{\frac{2}{1+R_2}} \sqrt{\frac{R_1^3}{R_2^3} + \cos(\Delta I)}} \right] \right)}$$

$$\mathcal{N}_2 = \sqrt{1 + \frac{2R_2}{R_1+R_2} - \sqrt{\frac{8R_2}{R_1+R_2}} \cos \left( \Delta I - \tan^{-1} \left[ \frac{\sin(\Delta I)}{\sqrt{\frac{2}{1+R_2}} \sqrt{\frac{R_1^3}{R_2^3} + \cos(\Delta I)}} \right] \right)}.$$

The function graph is shown in Section 4.5.1.4.4.

#### 4.5.1.4.4. *Elliptical Initial Orbit Function Graphs*

All graphs in this section show the HST, with plane change performed by the low-thrust system at the largest orbit radius, compared with the Hohmann and bi-elliptic transfers. All transfers begin in an elliptical initial orbit. Figure 4-19 shows Eq. (4.43) which represents the HST and Hohmann critical specific impulse ratio. Figure 4-20 highlights Eq. (4.44) which is the HST and bi-elliptic transfer with plane change at first and second impulse. Finally, Figure 4-21 demonstrates Eq. (4.45) which is the HST and bi-elliptic with plane change at the second and third impulse. As was the case for all equations described previously, the largest plane changes are found at small  $R_2$  and  $\Delta I$ . The HST and Hohmann critical specific impulse ratio again has a singularity which, in the region beyond, the Hohmann transfer will

always have a lower fuel mass than the HST. The smallest critical specific impulse ratios are found at large  $R2$  and  $\Delta I$ . This signifies that the HST becomes more efficient in all cases for large  $R2$  and  $\Delta I$ .

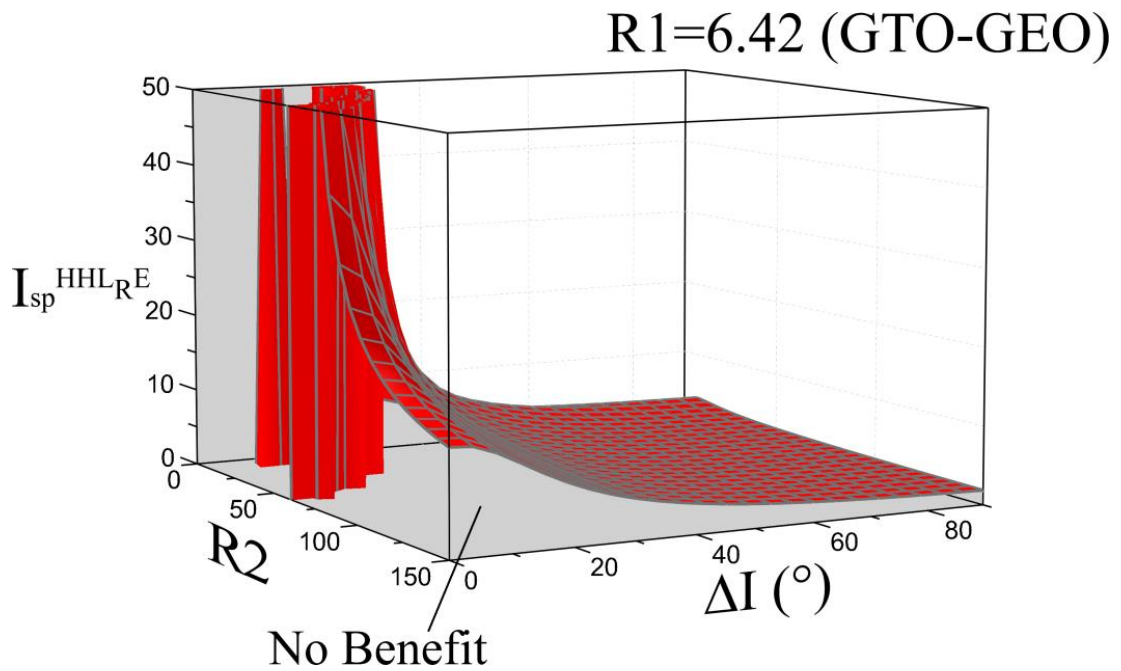


Figure 4-19 HST and Hohmann critical specific impulse ratio, Eq. (4.43), variation for  $R1 = 6.42$  (GTO – GEO)

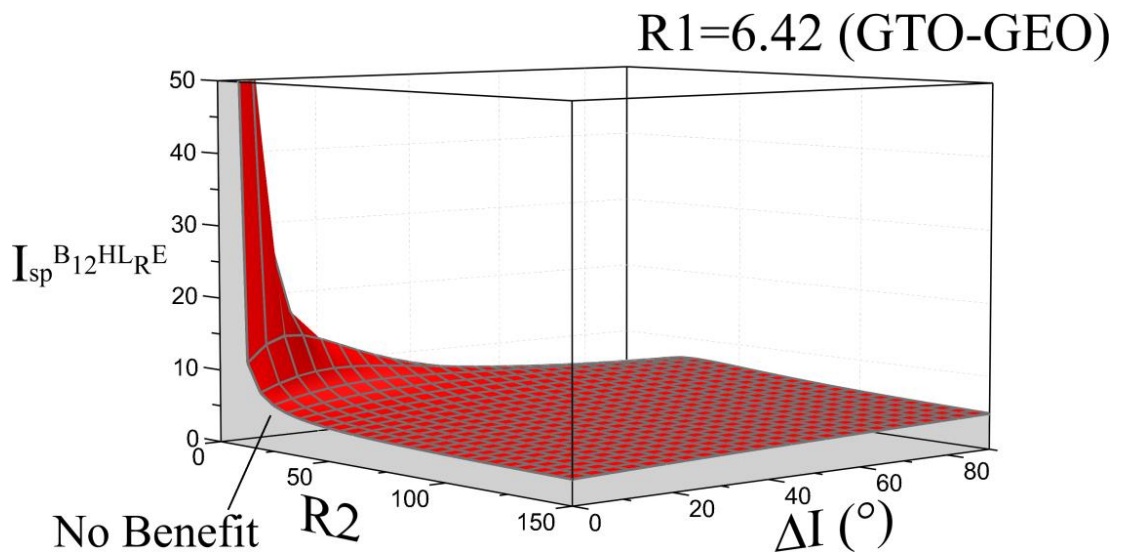


Figure 4-20 HST and bi-elliptic with plane change at first and second impulses critical specific impulse ratio, Eq. (4.44), variation for  $R1 = 6.42$  (GTO – GEO)

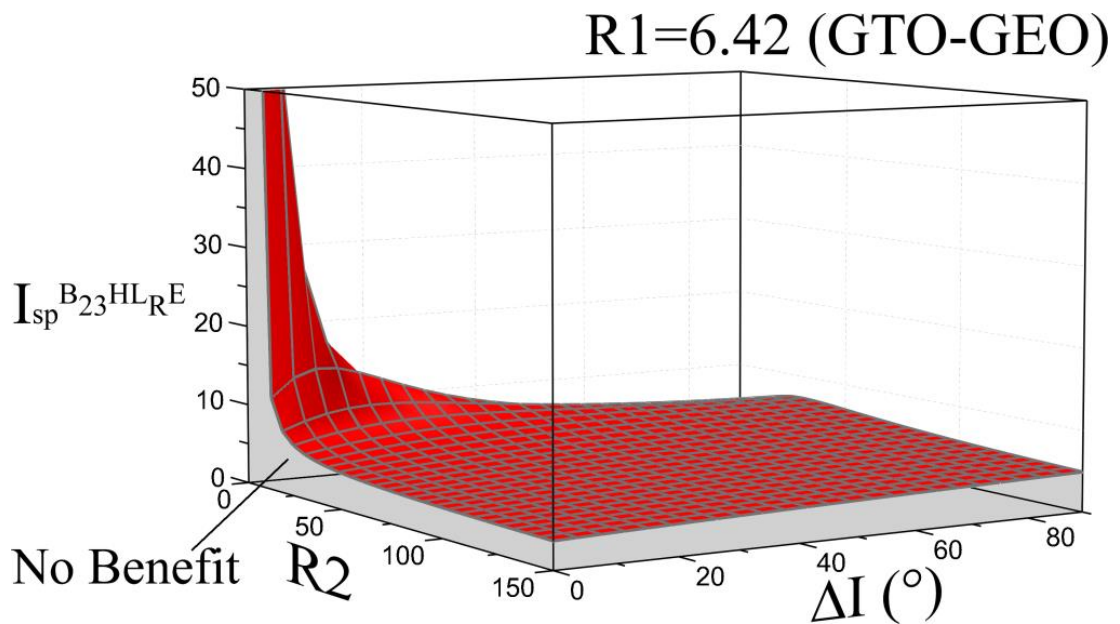


Figure 4-21 HST and bi-elliptic with plane change at first and second impulses critical specific impulse ratio, Eq. (4.45), variation for  $R1 = 6.42$  (GTO – GEO)

## 4.5.2. Edelbaum's Method (Combined Plane Change and Orbit Raise Manoeuvre)

### 4.5.2.1. Methodology

The alternative method to determine the velocity requirement for the low-thrust section is to use the method described in [30] as was briefly discussed in Chapter 2. Recapping and elaborating on the previous description, this method combines the plane change and orbit raise sections and is derived using orbit averaging and calculus of variations with time as a constraint and inclination as the maximisation variable. The spacecraft acceleration is assumed constant over the entire transfer and the thrust angle, which is accounted for in the derivation of the total velocity requirement equation, is held constant over each orbital revolution. The full derivation can be found in both [30] and [12, Sec. 14] so will not be reproduced here. The total velocity requirement equation is defined in Eq. (2.10) in Chapter 2, however with the inclusion of the orbit ratios  $R1$  and  $R2$  previously defined; the equation can be simplified to give

$$\Delta V_L = \sqrt{1 + \frac{R_1}{R_2} - 2\sqrt{\frac{R_1}{R_2}} \cos\left(\frac{\pi\Delta I}{2}\right)}. \quad (4.46)$$

Equation (4.46) can then be used to determine the total velocity requirement for a low-thrust transfer between two inclined orbits with a relative plane change in the region  $0 < \Delta I < 114.6^\circ$  ( $2 \text{ rad}$ ) without any ambiguity. As such, it is used to determine the low-thrust phase of the HST in the derivation of the critical specific impulse ratios derived in this section. The limit of  $\Delta I < 114.6^\circ$  ( $2 \text{ rad}$ ) is necessary as the derivation of the plane change in Eq. (4.46) involves an inverse-sine function which is double-valued in the region  $0 \rightarrow 2\pi$ . This means that two expressions, detailed in [30], must be used to cover the range of large plane change manoeuvres if the time history of the plane change is required.

It should be noted that by adopting Edelbaum's method, the transfer has the flexibility to expand the orbit greater than the  $R_2$  orbit ratio used within the equation. This happens with large plane changes where it is more efficient to perform the plane change further from the central body than the intermediate orbit radius defined by  $R_2$ . This means the high-thrust propulsion system propels the spacecraft from the initial orbit to the intermediate orbit where the low-thrust system is activated. At this point, the low-thrust system can perform the plane change while spiralling in towards the target or, if the plane change is large enough, spiral outwards to perform the majority of the plane change at a lower orbital velocity and then spiralling inwards to reach the desired target orbit thus acting as an enhanced HST.

To remove the double-valued problem, Edelbaum's analysis was re-formulated using optimal control theory in [42]. In this work Edelbaum's equations were shown to be exactly equivalent to the equations derived using optimal control theory. As such the next section shows how to obtain additional orbit transfer characteristics using the method. It should be noted that although a new equation representing the velocity requirement was also derived in

[42], Eq. (4.46) is still used as it is simpler and a relative plane change  $\Delta I \geq 114.6^\circ$  ( $2 \text{ rad}$ ) will never be considered with the HST.

#### 4.5.2.1.1. Determining Orbital Characteristics

To determine if the low-thrust system will choose to either spiral inwards or outwards at the beginning of the low-thrust phase, the initial thrust angle can be calculated using

$$\beta_0 = \tan^{-1} \left[ \frac{\sin\left[\left(\frac{\pi}{2}\right)\Delta I\right]}{\sqrt{\frac{R1}{R2}} - \cos\left[\left(\frac{\pi}{2}\right)\Delta I\right]} \right]. \quad (4.47)$$

If this is less than  $90^\circ$  the spacecraft will continue to spiral outwards until the thrust direction vector reaches  $90^\circ$  which represents a pure plane change with no increase in orbit semi-major axis. An initial thrust direction greater than  $90^\circ$  will mean that the low-thrust system will be constantly decreasing the semi-major axis and as such the orbit ratio,  $R2$ , will be the largest orbit ratio achieved throughout the duration of the transfer. To determine if the orbit ratio,  $R2$ , is the largest achieved throughout the transfer, Eq. (4.47) can be re-arranged for  $R2$  as the subject and as  $\beta_0 \rightarrow 90^\circ$ ,  $\tan(\beta_0) \rightarrow \infty$ , shown to equal

$$R2_{max} = \frac{R1}{\cos^2\left[\left(\frac{\pi}{2}\right)\Delta I\right]}. \quad (4.48)$$

If it is found that the largest fuel mass saving is achieved with an orbit ratio,  $R2$ , less than that defined in Eq. (4.48), then the following process can be used to determine the maximum orbit ratio achieved throughout the transfer. First, the thrust angle history can be defined, in terms of  $R1$  and  $R2$ , as

$$\beta = \tan^{-1} \left[ \frac{\sqrt{\frac{\mu}{r_t}} \sqrt{\frac{R1}{R2}} \sin(\beta_0)}{\sqrt{\frac{\mu}{r_t}} \sqrt{\frac{R1}{R2}} \cos(\beta_0) - \frac{m_{02} t}{Tr}} \right] \quad (4.49)$$

where  $\beta_0$  is defined in Eq. (4.47),  $m_{02}$  is the spacecraft mass at the beginning of the low-thrust phase,  $Tr$  is the available spacecraft thrust and  $t$  is the time variable from the

beginning to the end of phase 2. The total transfer time of phase 2 is calculated using the equation defined in Section 4.9 of this chapter and will not be discussed further here. This equation can then be re-arranged for  $t$  to enable the determination of the transfer time of the maximum orbit ratio. This is done similar to before by noting as  $\beta_0 \rightarrow 90^\circ$ ,  $\tan(\beta_0) \rightarrow \infty$ , and simplifying to give

$$t_{Rmax} = \frac{m_{02} \sqrt{\frac{\mu}{r_t} \sqrt{\frac{R1}{R2}} \cos(\beta_0)}}{Tr} \quad (4.50)$$

where  $\beta_0$  is again defined in Eq. (4.47). Now defining the variation of orbital velocity throughout the transfer as

$$V = \sqrt{\frac{\mu}{r_t} \frac{R1}{R2} - 2 \sqrt{\frac{\mu}{r_t} \sqrt{\frac{R1}{R2}}} \left(\frac{Tr}{m_{02}}\right) t \cos(\beta_0) + \left(\frac{Tr}{m_{02}}\right)^2 t^2} \quad (4.51)$$

and noting that the current orbital velocity,  $V$ , at any given point is defined by  $\sqrt{\mu/r}$ , where  $r$  is the current orbit radius, Eq. (4.51) can be re-defined as

$$r = \frac{\mu}{\frac{\mu}{r_t} \frac{R1}{R2} - 2 \sqrt{\frac{\mu}{r_t} \sqrt{\frac{R1}{R2}}} \left(\frac{Tr}{m_{02}}\right) t \cos(\beta_0) + \left(\frac{Tr}{m_{02}}\right)^2 t^2}. \quad (4.52)$$

If an orbit ratio similar to  $R1$  and  $R2$  but accounting for all orbit radii in between is then introduced as  $R3 = (r/r_i)$  and  $t_{Rmax}$  is substituted into the equation for  $t$ , the location of the maximum orbit ratio,  $R3_{max}$ , with a little simplification can be found as

$$R3_{max} = \frac{R2}{1 - \cos^2(\beta_0)} \quad (4.53)$$

where again  $\beta_0$  is defined in Eq. (4.47). It is of note that this equation, similar to Eq. (4.48), is independent of the spacecraft acceleration, confirming the trajectory is based on geometry alone and the acceleration will only modify the transfer duration. In addition to determining the variation of orbit radius and thrust angle with time, the plane change variation can also be defined as

$$\Delta i = \frac{2}{\pi} \left[ \tan^{-1} \left( \frac{\frac{T_r}{m_{02}} t - \sqrt{\frac{\mu}{r_t}} \sqrt{\frac{R_1}{R_2}} \cos(\beta_0)}{\sqrt{\frac{\mu}{r_t}} \sqrt{\frac{R_1}{R_2}} \sin(\beta_0)} \right) + \frac{\pi}{2} - \beta_0 \right] \quad (4.54)$$

The use of these equations will be demonstrated in the analytical case studies in Chapter 6.

#### 4.5.2.2. *Circular Initial Orbit*

##### 4.5.2.2.1. *HST and Hohmann Critical Specific Impulse Ratio*

Using Eq. (4.46) to represent the velocity requirement for the low thrust phase of the HST, Eq. (4.38) to represent the high-thrust phase of the HST and Eq. (4.18) to represent the Hohmann transfer, the critical specific impulse ratio for a circular initial orbit is

$$\frac{I_{spL}}{I_{spH}} = I_{sp}^{HHL C} = \frac{\sqrt{1 + \frac{R_1}{R_2} - 2\sqrt{\frac{R_1}{R_2}} \cos\left(\frac{\pi \Delta I}{2}\right)}}{\sqrt{R_1} \mathcal{O}_1 + \mathcal{O}_2 - \sqrt{2R_1 - \frac{2R_1}{1+R_2}} + \sqrt{\frac{2R_1}{R_2} - \frac{2R_1}{1+R_2}} - \sqrt{\frac{R_1}{R_2} + \sqrt{R_1}}} \quad (4.55)$$

where

$$\mathcal{O}_1 = \sqrt{1 + \frac{2R_1}{1+R_1} - \sqrt{\frac{8R_1}{1+R_1}} \cos\left(\tan^{-1}\left(\frac{\sin(\Delta I)}{\sqrt{R_1^3 + \cos(\Delta I)}}\right)\right)}$$

$$\mathcal{O}_2 = \sqrt{1 + \frac{2}{1+R_1} - \sqrt{\frac{8}{1+R_1}} \cos\left(\Delta I - \tan^{-1}\left(\frac{\sin(\Delta I)}{\sqrt{R_1^3 + \cos(\Delta I)}}\right)\right)}.$$

The function graph is shown in Section 4.5.2.2.4.

##### 4.5.2.2.2. *HST and Bi-Elliptic Critical Specific Impulse Ratio [1-2]*

For the scenario where the HST, with coupled plane change and spiral-in performed by the low-thrust system, is compared to the bi-elliptic transfer with plane change distributed between the first and second nodes, the high and low-thrust phases of the HST are given in Eqs. (4.38) and (4.46) respectively. The bi-elliptic transfer velocity requirement is defined in

Eq. (4.20). Using these definitions and the orbit ratios previously defined, the critical specific impulse ratio given in Eq. (4.4) can be simplified to give

$$\frac{I_{spL}}{I_{spH}} = I_{sp}^{BHLC} = \frac{\sqrt{1 + \frac{R1}{R2} - 2\sqrt{\frac{R1}{R2}} \cos\left(\frac{\pi\Delta I}{2}\right)}}{\sqrt{\frac{R1}{R2}(\sqrt{R2}\mathcal{P}_1 + \sqrt{2}\mathcal{P}_2 - 1) + \sqrt{\frac{2R2}{R1+R2}} - \sqrt{2R1 - \frac{2R1}{1+R2}} + \sqrt{\frac{2R1}{R2} - \frac{2R1}{1+R2}} - 1}} \quad (4.56)$$

where

$$\mathcal{P}_1 = \sqrt{1 + \frac{2R2}{1+R2} - \sqrt{\frac{8R2}{1+R2}} \cos\left(\tan^{-1}\left(\frac{\sin(\Delta I)}{\frac{\sqrt{R2^3\sqrt{R1+R2}}}{\sqrt{2R1}} + \cos(\Delta I)}\right)\right)}$$

$$\mathcal{P}_2 = \sqrt{\frac{R1}{R1+R2} + \frac{1}{1+R2} - \sqrt{\frac{4R1}{R1+R2}} \sqrt{\frac{1}{1+R2}} \cos\left(\Delta I - \tan^{-1}\left(\frac{\sin(\Delta I)}{\frac{\sqrt{R2^3\sqrt{R1+R2}}}{\sqrt{2R1}} + \cos(\Delta I)}\right)\right)}.$$

The function graph is shown in Section 4.5.2.2.4.

#### 4.5.2.2.3. HST and Bi-Elliptic Critical Specific Impulse Ratio [2-3]

The high and low-thrust phases of the HST are defined in Eqs. (4.38) and (4.46) respectively. The bi-elliptic velocity requirement, with plane change performed at the second and third impulses, is defined in Eq. (4.22). The critical specific impulse ratio equation is then defined using these equations and the orbit ratios defined previously as

$$\frac{I_{spL}}{I_{spH}} = I_{sp}^{B_{23}HLC} = \frac{\sqrt{1 + \frac{R1}{R2} - 2\sqrt{\frac{R1}{R2}} \cos\left(\frac{\pi\Delta I}{2}\right)}}{\sqrt{R1\sqrt{\frac{2R2}{1+R2}} + \sqrt{\frac{R1}{R2}}(Q_1 - 1) + Q_2 - \sqrt{2R1 - \frac{2R1}{1+R2}} + \sqrt{\frac{2R1}{R2} - \frac{2R1}{1+R2}}}} \quad (4.57)$$

where

$$Q_1 = \sqrt{\frac{2}{1+R2} + \frac{2R1}{R1+R2} - \sqrt{\frac{8}{1+R2}} \sqrt{\frac{2R1}{R1+R2}} \cos\left(\tan^{-1}\left[\frac{\sin(\Delta I)}{\sqrt{\frac{2}{1+R2}} \sqrt{\frac{R1^3}{R2^3}} + \cos(\Delta I)}\right]\right)}$$

$$Q_2 = \sqrt{1 + \frac{2R_2}{R_1+R_2} - \sqrt{\frac{8R_2}{R_1+R_2}} \cos\left(\Delta I - \tan^{-1}\left[\frac{\sin(\Delta I)}{\sqrt{\frac{2}{1+R_2}\sqrt{\frac{R_1^3}{R_2^3} + \cos(\Delta I)}}}\right]\right)}.$$

The function graph is shown in Section 4.5.2.2.4.

#### 4.5.2.2.4. *Circular Initial Orbit function Graphs*

The graphs in this section demonstrate the evolution of the critical specific impulse ratios comparing the Hohmann and bi-elliptic equations with the HST with coupled low-thrust plane change and spiral-in. All graphs represent a circular initial orbit for the compared transfers. Figure 4-22 shows the critical specific impulse ratio of the HST compared with the Hohmann transfer as described in Eq. (4.55). Figure 4-23 corresponds to Eq. (4.56) and represents the HST and bi-elliptic, with plane change at second and third impulses, critical specific impulse ratio. Figure 4-24 represents the critical specific impulse ratio described in Eq. (4.57). All critical ratios generate very similar plots to the other low-thrust plane change methodology described in Section 4.5.1.3. On comparison, it is found that this methodology offers lower critical specific impulse ratios for the transfer scenarios considered. The general trends as discussed earlier are also valid here. That is, the critical specific impulse ratio reduces with increasing  $R_2$  and  $\Delta I$ . As has been discovered in all cases comparing the HST and Hohmann transfer, there is a singularity at small  $R_2$  and  $\Delta I$  which determines in the region beyond, the HST will never outperform the Hohmann transfer.

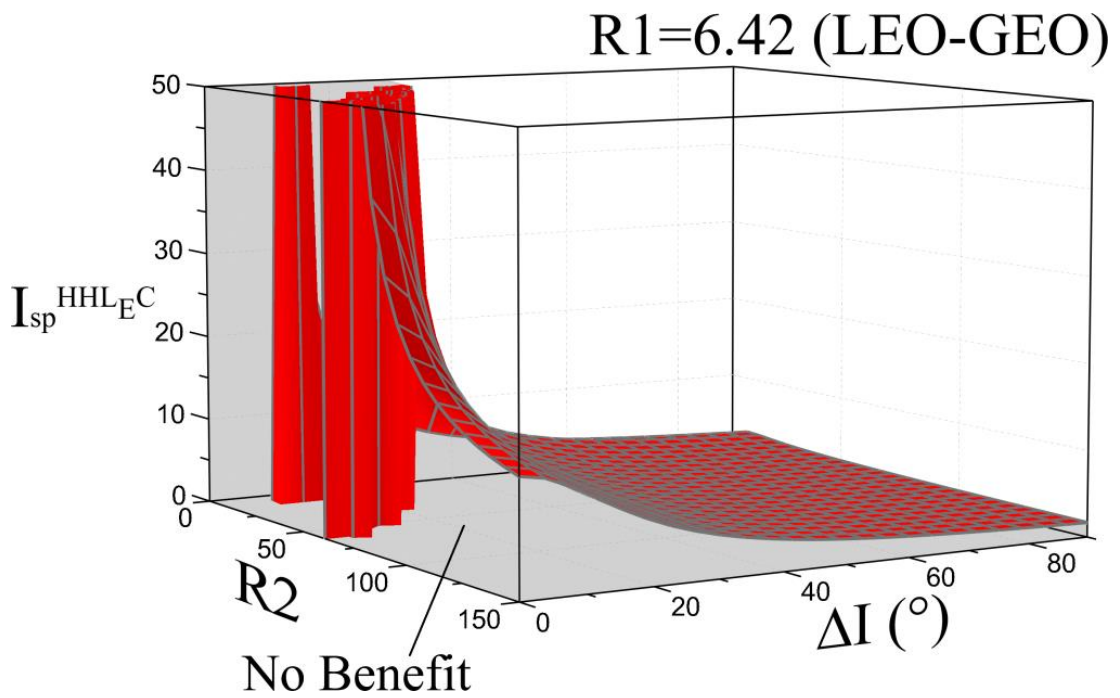


Figure 4-22 HST and Hohmann critical specific impulse ratio, Eq. (4.55), variation for  $R1 = 6.42$  (GTO – GEO)

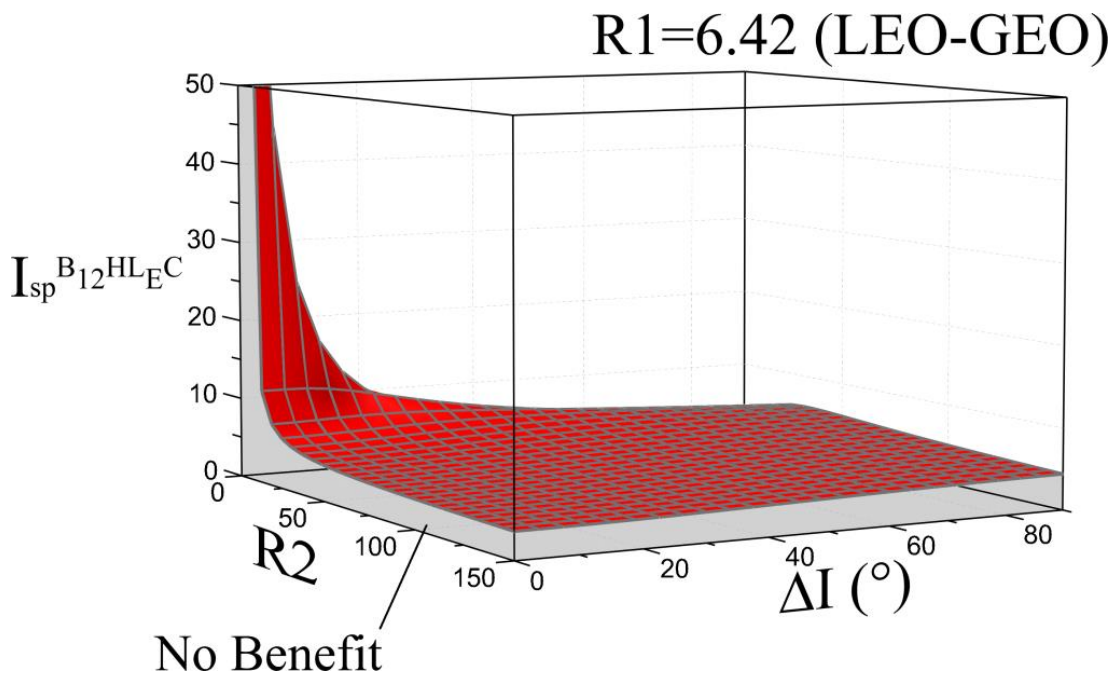


Figure 4-23 HST and Hohmann critical specific impulse ratio, Eq. (4.56), variation for  $R1 = 6.42$  (GTO – GEO)

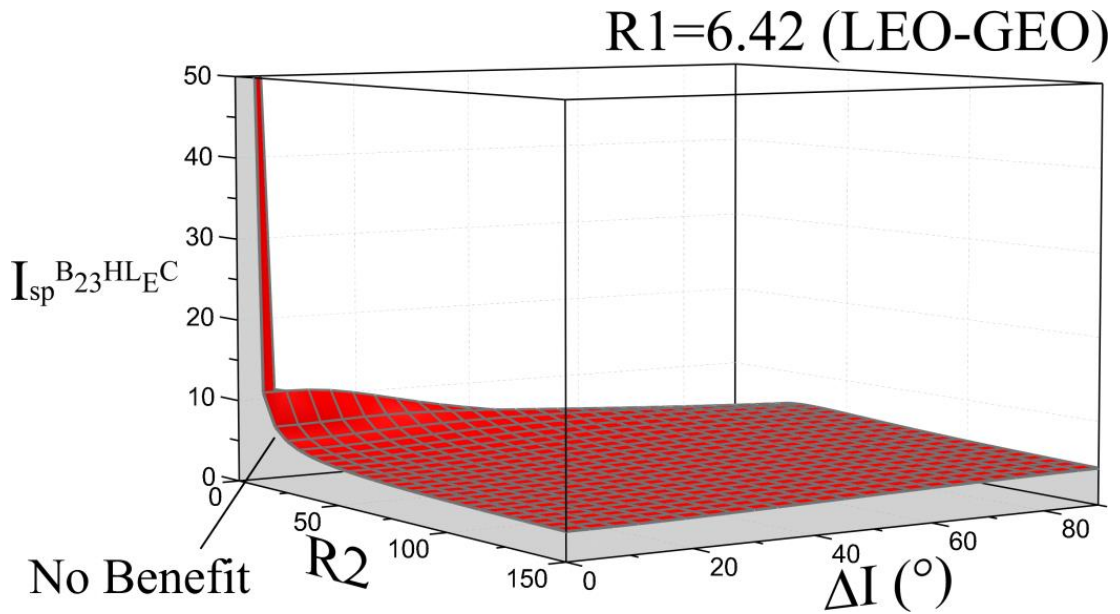


Figure 4-24 HST and Hohmann critical specific impulse ratio, Eq. (4.57), Variation for  $R_1 = 6.42$  (GTO – GEO)

### 4.5.2.3. *Elliptical Initial Orbit*

#### 4.5.2.3.1. *HST and Hohmann Critical Specific Impulse Ratio*

For an elliptical initial orbit, the critical specific impulse ratio comparing the Hohmann transfer and HST, with coupled low-thrust plane change and spiral-in, is given as

$$\frac{I_{spL}}{I_{spH}} = I_{sp}^{HHLE} = \frac{\sqrt{1 + \frac{R_1}{R_2} - 2\sqrt{\frac{R_1}{R_2}} \cos\left(\frac{\pi\Delta I}{2}\right)}}{R_1 - \sqrt{\frac{R_1}{R_2}} \left[ \sqrt{R_2} \left( \sqrt{\frac{2R_2}{1+R_2}} - \sqrt{\frac{2R_1}{1+R_1}} \right) - \sqrt{\frac{2}{1+R_2} + 1} \right]} \quad (4.58)$$

where

$$R_1 = \sqrt{\frac{2}{1+R_1} + 1} - 2\sqrt{\frac{2}{1+R_1}} \cos(\Delta I) .$$

In Eq. (4.58), the Hohmann transfer velocity requirement is previously defined in Eq. (4.24) and the HST high and low-thrust phases are defined in Eqs. (4.42) and (4.46) respectively. The function graph is shown in Section 4.5.2.3.4.

#### 4.5.2.3.2. HST and Bi-Elliptic Critical Specific Impulse Ratio [1-2]

For the scenario comparing the bi-elliptic transfer to the HST using low-thrust to impart the plane change and starting in an elliptical orbit, the velocity requirement for the bi-elliptic transfer has been previously described in Eq. (4.27). The high and low-thrust sections of the HST have been described in Eqns. (4.42) and (4.46) respectively. Using these and the orbit ratios previously defined, the critical specific impulse ratio is

$$\frac{I_{spL}}{I_{spH}} = I_{sp}^{BHLE} = \frac{\sqrt{1 + \frac{R1}{R2} - 2\sqrt{\frac{R1}{R2}} \cos\left(\frac{\pi\Delta I}{2}\right)}}{\sqrt{\frac{R1}{R2} \left( \sqrt{R2} \mathcal{S}_1 + \mathcal{S}_2 - \sqrt{R2} \left[ \sqrt{\frac{2R2}{1+R2}} \sqrt{\frac{2R1}{1+R1}} + 1 - \sqrt{\frac{2}{1+R2}} \right] + \sqrt{\frac{2R2}{R1+R2}} - 1 \right)}} \quad (4.59)$$

where

$$\mathcal{S}_1 = \sqrt{\frac{2R1}{1+R1} + \frac{2R2}{1+R2} - \sqrt{\frac{8R1}{1+R1}} \sqrt{\frac{2R2}{1+R2}} \cos\left(\tan^{-1}\left[\frac{\sin(\Delta I)}{\sqrt{\frac{R2^3(R1+R2)}{1+R1}} + \cos(\Delta I)}\right]\right)}$$

$$\mathcal{S}_2 = \sqrt{\frac{2}{1+R2} + \frac{2R1}{R1+R2} - \sqrt{\frac{8}{1+R2}} \sqrt{\frac{2R1}{R1+R2}} \cos\left(\Delta I - \tan^{-1}\left[\frac{\sin(\Delta I)}{\sqrt{\frac{R2^3(R1+R2)}{1+R1}} + \cos(\Delta I)}\right]\right)}$$

The function graph is shown in Section 4.5.2.3.4.

#### 4.5.2.3.3. HST and Bi-Elliptic Critical Specific Impulse Ratio [2-3]

Considering an elliptical initial orbit for the case when the bi-elliptic, with plane change at the second and third impulses, is compared to the HST, using the low-thrust system to perform the plane change, the velocity requirement equation for the bi-elliptic equation with plane change at the second and third impulses has already been defined in Eq. (4.29). The HST's high and low-thrust phase velocity requirements have also been defined previously in Eqns. (4.42) and (4.46) respectively. The critical specific impulse ratio, using the previously defined orbit ratios and velocity requirements, for this case is then defined as

$$\frac{I_{spL}}{I_{spH}} = I_{sp}^{B_{23}HLE} = \frac{\sqrt{1 + \frac{R1}{R2} - 2\sqrt{\frac{R1}{R2}\cos\left(\frac{\pi\Delta I}{2}\right)}}}{\sqrt{\frac{2R1R2}{1+R2} - \sqrt{\frac{2R1^2}{1+R1}} + \sqrt{\frac{R1}{R2}} \left[ \mathcal{J}_1 - \left( \sqrt{R2} \left( \sqrt{\frac{2R2}{1+R2}} \sqrt{\frac{2R1}{1+R1}} - \sqrt{\frac{2}{1+R2} + 1} \right) \right) \right] + \mathcal{J}_2}} \quad (4.60)$$

where

$$\mathcal{J}_1 = \sqrt{\frac{2}{1+R2} + \frac{2R1}{R1+R2} - \sqrt{\frac{8}{1+R2}} \sqrt{\frac{2R1}{R1+R2}} \cos\left(\tan^{-1}\left[\frac{\sin(\Delta I)}{\sqrt{\frac{2}{1+R2}\sqrt{\frac{R1^3}{R2^3} + \cos(\Delta I)}}}\right]\right)}$$

$$\mathcal{J}_2 = \sqrt{1 + \frac{2R2}{R1+R2} - \sqrt{\frac{8R2}{R1+R2}} \cos\left(\Delta I - \tan^{-1}\left[\frac{\sin(\Delta I)}{\sqrt{\frac{2}{1+R2}\sqrt{\frac{R1^3}{R2^3} + \cos(\Delta I)}}}\right]\right)}$$

The function graph is shown in Section 4.5.2.3.4.

#### 4.5.2.3.4. *Elliptical Initial Orbit function Graphs*

This section shows the critical specific impulse ratio functions for an elliptical initial orbit. All critical ratios compare the HST with combined low-thrust plane change and spiral-in as described earlier. Figure 4-25 shows Eq. (4.58) which represents the HST compared with the Hohmann transfer. Figure 4-26 highlights Eq. (4.59) which represents the HST compared with the bi-elliptic transfer with plane change at the first and second impulses. Finally, Figure 4-27 illustrates Eq. (4.60) which represents the HST compared with the bi-elliptic transfer with plane change performed at the second and third impulses. As was the case for the circular initial orbit, all critical ratios generate plots which are similar to the other low-thrust plane change methodology described in Section 4.5.1.4. As was the case for the circular initial orbit, it is found that this low-thrust plane change methodology offers lower critical specific impulse ratios than the plane change performed at the largest orbit radius methodology for the transfer scenarios considered. It can be seen in all figures that the critical specific impulse ratios reduce with increasing  $R2$  and  $\Delta I$ . As has been shown in all

cases comparing the HST and Hohmann transfer, a singularity exists at small  $R2$  and  $\Delta I$  and confirms in the region beyond, the HST will never outperform the Hohmann transfer.

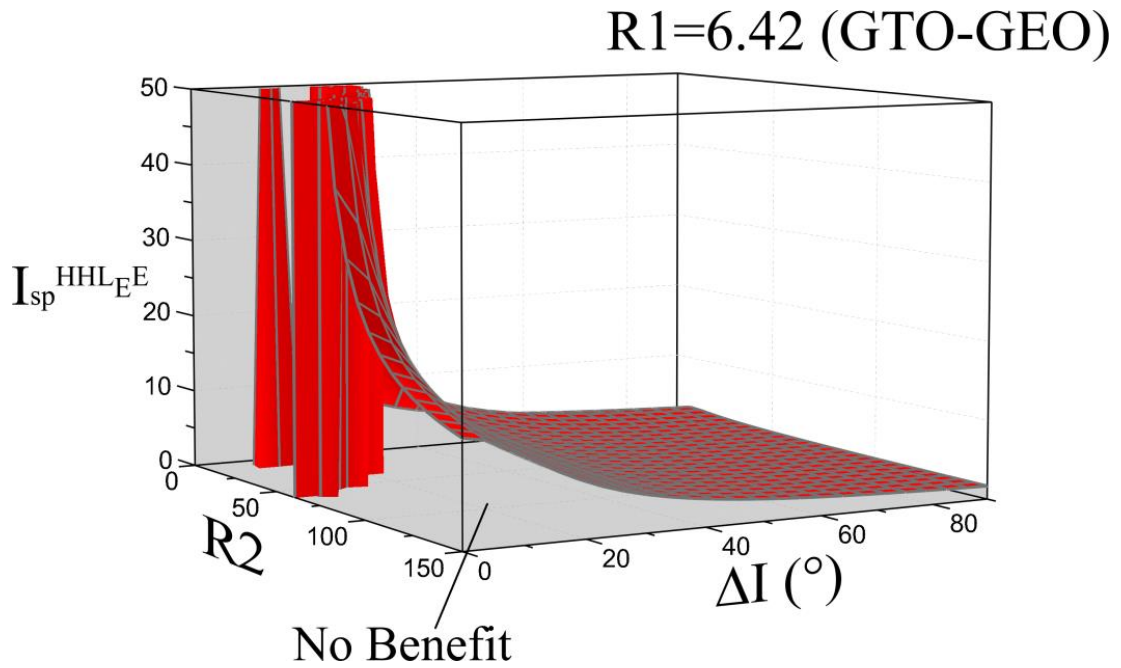


Figure 4-25 HST and Hohmann critical specific impulse ratio, Eq. (4.58), variation for  $R1 = 6.42$  (GTO – GEO)

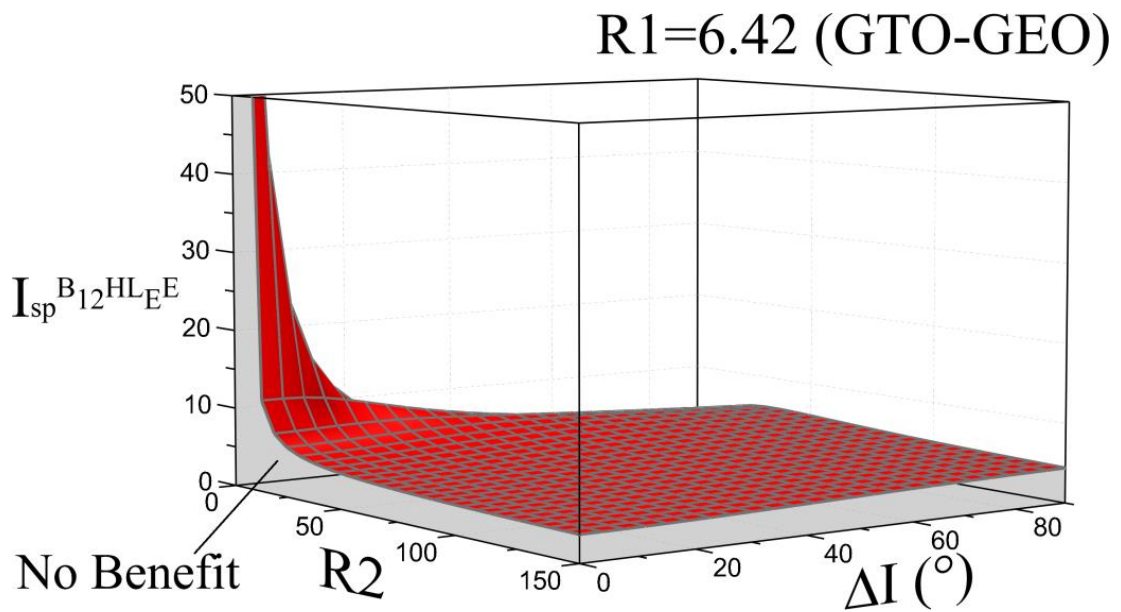


Figure 4-26 HST and Hohmann critical specific impulse ratio, Eq. (4.59), variation for  $R1 = 6.42$  (GTO – GEO)

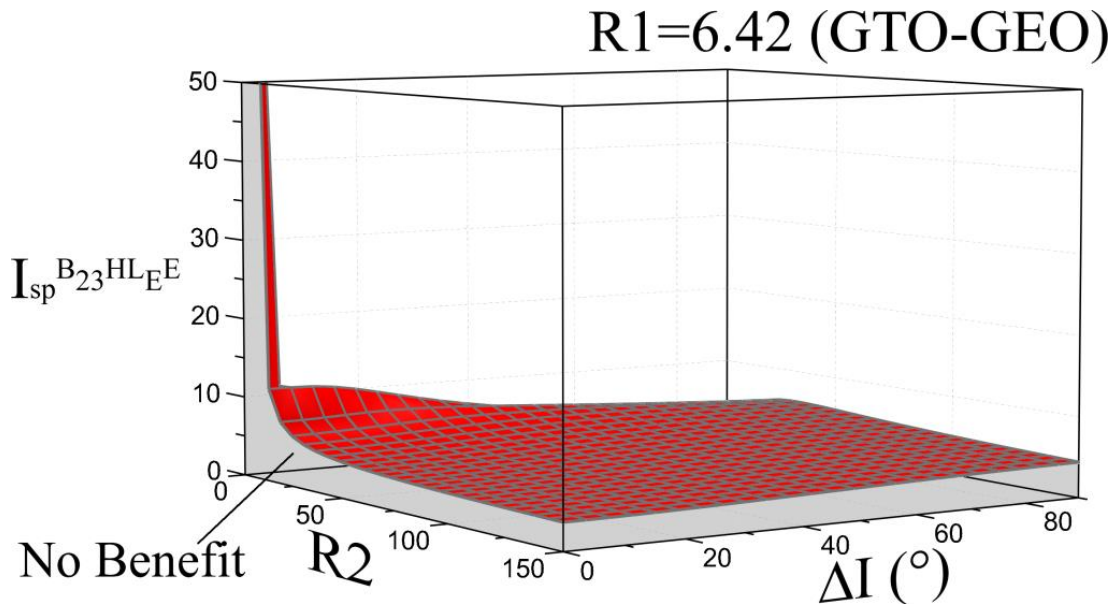


Figure 4-27 HST and Hohmann critical specific impulse ratio, Eq. (4.60), variation for  $R1 = 6.42$  (GTO – GEO)

## 4.6. HST Only Critical Ratio

To determine when the HST using high-thrust plane change or HST using low thrust plane change should be used, an additional critical specific impulse ratio can be defined which, used in collaboration with the previously defined critical ratios, will give a full overview of the system. The critical ratio can be derived by comparing the fuel mass fraction, given in Eq. (4.2), for each HST transfer configuration. The critical ratio, with little simplification, is then defined as

$$\left. \frac{I_{spL}}{I_{spH}} \right|_{HST} = \frac{\Delta V_{HSTSL} - \Delta V_{HSTL}}{\Delta V_{HSTHCP(C/E)} - \Delta V_{HSTHP(C/E)}}. \quad (4.61)$$

Equation (4.61) is relevant for both a circular and elliptical initial orbit, as well as both plane change methodologies as only the velocity requirement equations will vary.

## 4.6.1. Plane Change at Greatest Radius

### 4.6.1.1. *HST with High-Thrust Plane Change and HST with Low-Thrust Plane Change Critical Ratio (Circular Initial Orbit)*

For the case of a circular initial orbit and the low-thrust plane change performed in full at the largest orbit radius, the critical specific impulse ratio comparing the HST using high-thrust plane change with its low-thrust plane change counterpart is defined as

$$\frac{I_{spL}}{I_{spH}} \Big|_{HST} = I_{sp}^{HSHRC} = \frac{-\frac{\pi}{2} \sqrt{\frac{R_1}{R_2}} \Delta I}{\sqrt{2R_1 - \frac{2R_1}{1+R_2}} - \sqrt{\frac{2R_1}{R_2} - \frac{2R_1}{1+R_2}} - u_1 + u_2} \quad (4.62)$$

where

$$u_1 = \sqrt{R_1} \left[ 1 + \sqrt{1 + \frac{2R_2}{1+R_2} - \sqrt{\frac{8R_2}{1+R_2}} \cos \left( \tan^{-1} \left[ \frac{\sin(\Delta I)}{\sqrt{(R_2)^3 + \cos(\Delta I)}} \right] \right)} \right]$$

$$u_2 = \sqrt{\frac{R_1}{R_2}} \left[ 1 - \sqrt{1 + \frac{2}{1+R_2} - \sqrt{\frac{8}{1+R_2}} \cos \left( \Delta I - \tan^{-1} \left[ \frac{\sin(\Delta I)}{\sqrt{(R_2)^3 + \cos(\Delta I)}} \right] \right)} \right].$$

In Eq. (4.62), Eqs. (4.37) and (4.5) define the low-thrust system velocity requirement with ( $\Delta V_{HSTL}$ ) and without ( $\Delta V_{HSTSL}$ ) plane change respectively. Equations (4.17) and (4.38) define the high-thrust system velocity requirement with ( $\Delta V_{HSTHPC}$ ) and without ( $\Delta V_{HSTHCPC}$ ) plane change respectively. The function graph is shown in Section 4.6.1.3.

#### 4.6.1.2. *HST with High-Thrust Plane Change and HST with Low-Thrust Plane Change Critical Ratio (Elliptical Initial Orbit)*

The critical specific impulse ratio, comparing the HST using high-thrust plane change and its low-thrust counterpart for an elliptical initial orbit is defined as

$$\frac{I_{spL}}{I_{spH}} \Big|_{HST} = I_{sp}^{HSHRE} = \frac{-\frac{\pi}{2} \sqrt{\frac{R1}{R2}} \Delta I}{\sqrt{\frac{R1}{R2}} \left[ \sqrt{R2} \left( \sqrt{\frac{2R2}{1+R2}} - \sqrt{\frac{2R1}{1+R1}} \right) - \sqrt{\frac{2}{1+R2} + 1} \right] - \sqrt{R1} v_2} \quad (4.63)$$

where

$$v_1 = \sqrt{1 + \frac{2}{1+R2} - \sqrt{\frac{8}{1+R2}} \cos \left( \Delta I - \tan^{-1} \left[ \frac{\sin(\Delta I)}{\sqrt{\frac{2R1R2^3}{1+R1} + \cos(\Delta I)}} \right] \right)}$$

$$v_2 = \left[ 1 - \sqrt{\frac{2R1}{1+R1} + \frac{2R2}{1+R2} - \sqrt{\frac{8R1}{1+R1}} \sqrt{\frac{2R2}{1+R2}} \cos \left( \tan^{-1} \left[ \frac{\sin(\Delta I)}{\sqrt{\frac{2R1R2^3}{1+R1} + \cos(\Delta I)}} \right] \right)} \right]$$

Again the HST with low-thrust plane change assumes the full plane change is performed at the largest radius and as such the velocity requirement is the same as defined in the previous section; Eqs. (4.37) and (4.5) for with and without plane change respectively. Equations (4.25) and (4.42) define the HST's high-thrust phase velocity requirement with ( $\Delta V_{HSTHPE}$ ) and without ( $\Delta V_{HSTHCE}$ ) plane change respectively. The function graph is shown in Section 4.6.1.3.

#### 4.6.1.3. *Function Graphs*

The graphs of the HST only critical specific impulse ratios for a circular and elliptical initial orbit are shown in Figure 4-28 and Figure 4-29 respectively. Figure 4-28 represents Eq. (4.62) and Figure 4-29 represents Eq. (4.63). The critical specific impulse ratios derived here

are fundamentally different from that derived previously. If the spacecraft specific impulse ratio exceeds the critical ratio, then the HST with low-thrust plane change should be selected instead of the HST with high-thrust plane change. Conversely, if the spacecraft specific impulse ratio is less than the critical ratio then the HST with high-thrust plane change should be selected instead of the HST with low-thrust. This is demonstrated for both initial orbits in Figure 4-28 and Figure 4-29. Using these critical specific impulse ratios with the previous ratios comparing the HST with different transfers allows an overview of the system in which it can be seen which transfer is more fuel effective.

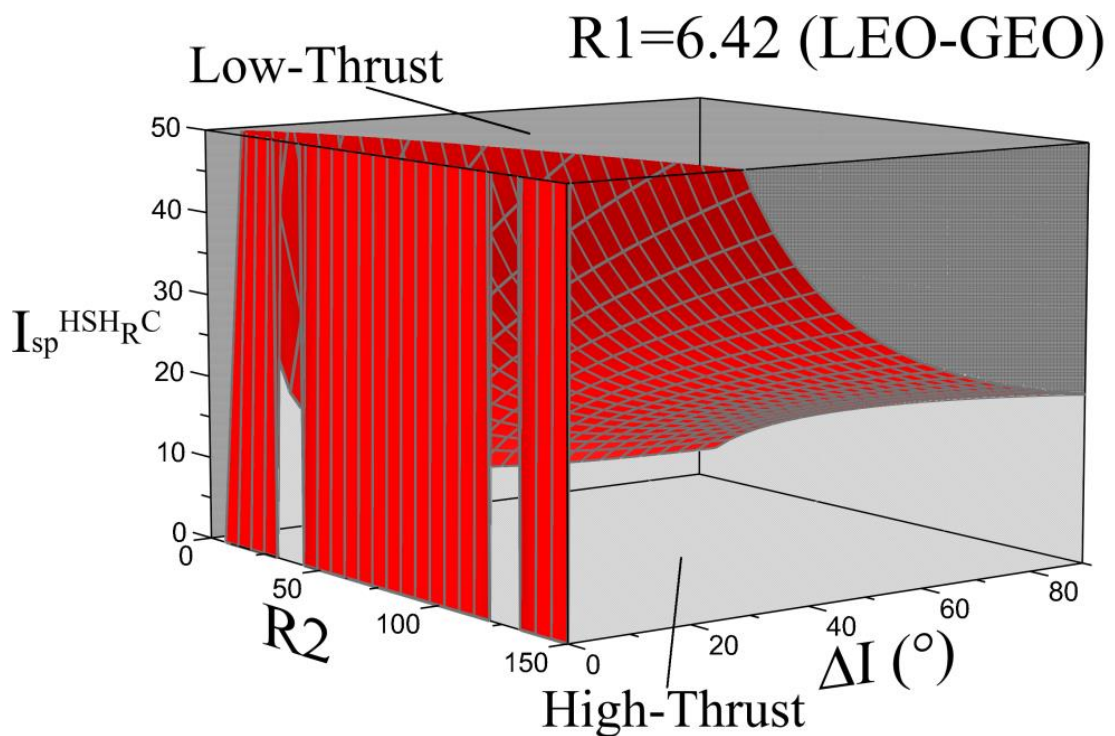


Figure 4-28 HST only critical specific impulse ratio variation for  $R_1 = 6.42$  (LEO – GEO), plane change performed at largest orbit radius

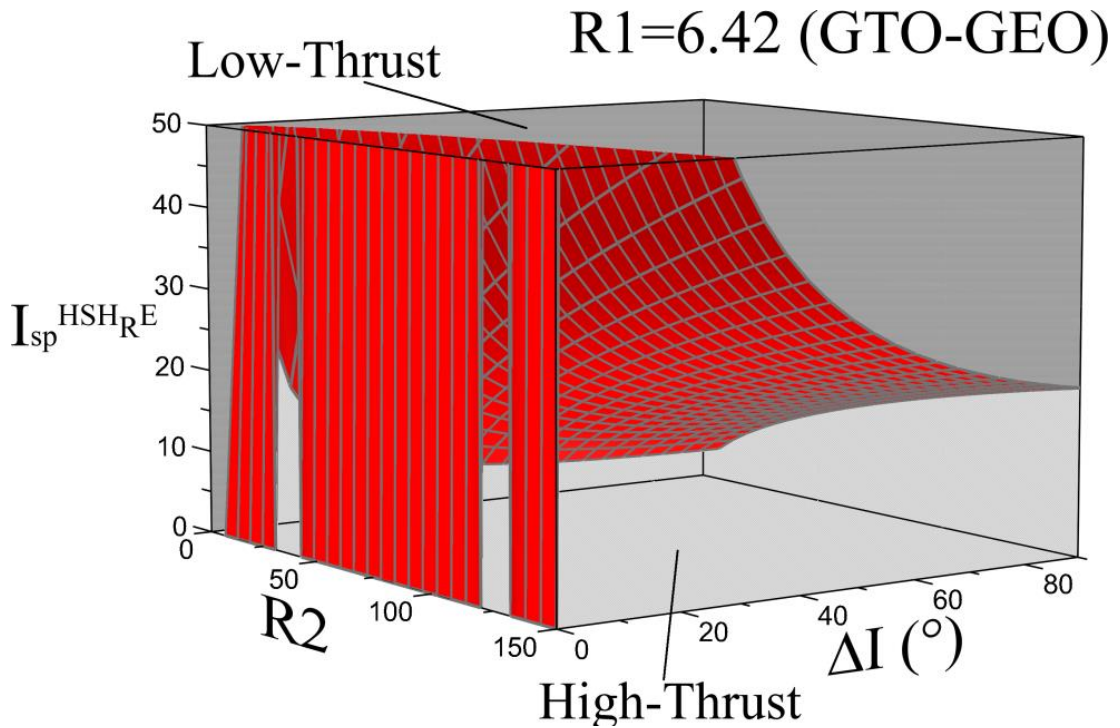


Figure 4-29 HST only critical specific impulse ratio variation for  $R_1 = 6.42$  (GTO – GEO), plane change performed at largest orbit radius

## 4.6.2. Edelbaum’s Method (Combined Plane Change and Orbit Raise Manoeuvre)

### 4.6.2.1. *HST with High-Thrust Plane Change and HST with Low-Thrust Plane Change Critical Ratio (Circular Initial Orbit)*

Comparing the HST, with high thrust plane change, and HST, with low-thrust plane change and spiral-in combined, the critical specific impulse ratio for a circular initial orbit is given as

$$\frac{I_{spL}}{I_{spH}} \Big|_{HST} = I_{sp}^{HSH_{EC}} = \frac{1 - \sqrt{\frac{R_1}{R_2}} \sqrt{1 + \frac{R_1}{R_2} - 2\sqrt{\frac{R_1}{R_2}} \cos\left(\frac{\pi\Delta I}{2}\right)}}{\sqrt{2R_1 - \frac{2R_1}{1+R_2} - \sqrt{\frac{2R_1}{R_2} - \frac{2R_1}{1+R_2}} - W_1 + W_2}} \quad (4.64)$$

where

$$\mathcal{W}_1 = \sqrt{R_1} \left[ 1 + \sqrt{1 + \frac{2R_2}{1+R_2} - \sqrt{\frac{8R_2}{1+R_2}} \cos \left( \tan^{-1} \left[ \frac{\sin(\Delta I)}{\sqrt{(R_2)^3 + \cos(\Delta I)}} \right]} \right)} \right]$$

$$\mathcal{W}_1 = \sqrt{\frac{R_1}{R_2}} \left[ 1 - \sqrt{1 + \frac{2}{1+R_2} - \sqrt{\frac{8}{1+R_2}} \cos \left( \Delta I - \tan^{-1} \left[ \frac{\sin(\Delta I)}{\sqrt{(R_2)^3 + \cos(\Delta I)}} \right]} \right)} \right].$$

For this equation the velocity requirement for the low-thrust phase with plane change is given in Eq. (4.46). The equation for low-thrust phase without plane change is defined in Eq. (4.5). The HST high-thrust phase with and without plane change velocity requirement is defined in Eqs. (4.17) and (4.38) respectively. The function graph is shown in Section 4.6.2.3.

#### 4.6.2.2. *HST with High-Thrust Plane Change and HST with Low-Thrust Plane Change Critical Ratio (Elliptical Initial Orbit)*

For an elliptical initial orbit, the critical specific impulse ratio comparing the HST, with high-thrust plane change, and HST, with the low-thrust plane change combined with the spiral-in manoeuvre, is defined as

$$\frac{I_{spL}}{I_{spH}} \Big|_{HST} = I_{sp}^{HSH_{EE}} = \frac{1 - \sqrt{\frac{R_1}{R_2}} \sqrt{1 + \frac{R_1}{R_2} - 2\sqrt{\frac{R_1}{R_2}} \cos\left(\frac{\pi\Delta I}{2}\right)}}{\sqrt{\frac{R_1}{R_2}} \left[ \sqrt{R_2} \left( \sqrt{\frac{2R_2}{1+R_2}} - \sqrt{\frac{2R_1}{1+R_1}} \right) - \sqrt{\frac{2}{1+R_2} + 1} \right] - \mathcal{X}_1} - \sqrt{R_1} \mathcal{X}_2 \quad (4.65)$$

where

$$\mathcal{X}_1 = \sqrt{1 + \frac{2}{1+R_2} - \sqrt{\frac{8}{1+R_2}} \cos \left( \Delta I - \tan^{-1} \left[ \frac{\sin(\Delta I)}{\sqrt{\frac{2R_1R_2^3}{1+R_1} + \cos(\Delta I)}} \right]} \right)}$$

$$\mathcal{X}_2 = \left[ 1 - \sqrt{\frac{2R1}{1+R1} + \frac{2R2}{1+R2} - \sqrt{\frac{8R1}{1+R1}} \sqrt{\frac{2R2}{1+R2}} \cos \left( \tan^{-1} \left[ \frac{\sin(\Delta I)}{\sqrt{\frac{2R1R2^3}{1+R1} + \cos(\Delta I)}} \right]} \right)} \right].$$

As was the case for the circular initial orbit, the HST velocity requirement, with a combined low-thrust plane change and spiral-in manoeuvre, is defined in Eq. (4.46). The HST low-thrust phase without plane change velocity requirement is given in Eq. (4.5). Equations (4.25) and (4.42) define the HST's velocity requirement for the high-thrust phase with and without plane change. The function graph is shown in Section 4.6.2.3.

### 4.6.2.3. *Function Graphs*

The graphs of Eqs. (4.64) and (4.65) are shown in Figure 4-30 and Figure 4-31 respectively. It can be seen that the graphs exhibit similar trends compared to the graphs showing the critical ratios representative of a low-thrust plane change at the largest radius in Section 4.6.1.3, however the scales are very different. This suggests that for the scenario under consideration,  $R1 = 6.42$ , combining the plane change and spiral-in manoeuvres proves more effective than performing the full plane change at the largest radius and then spiralling-in. As was discussed in Section 4.6.1.3, and can be seen in both figures here, there are clear regions in which each version of the HST should be used.

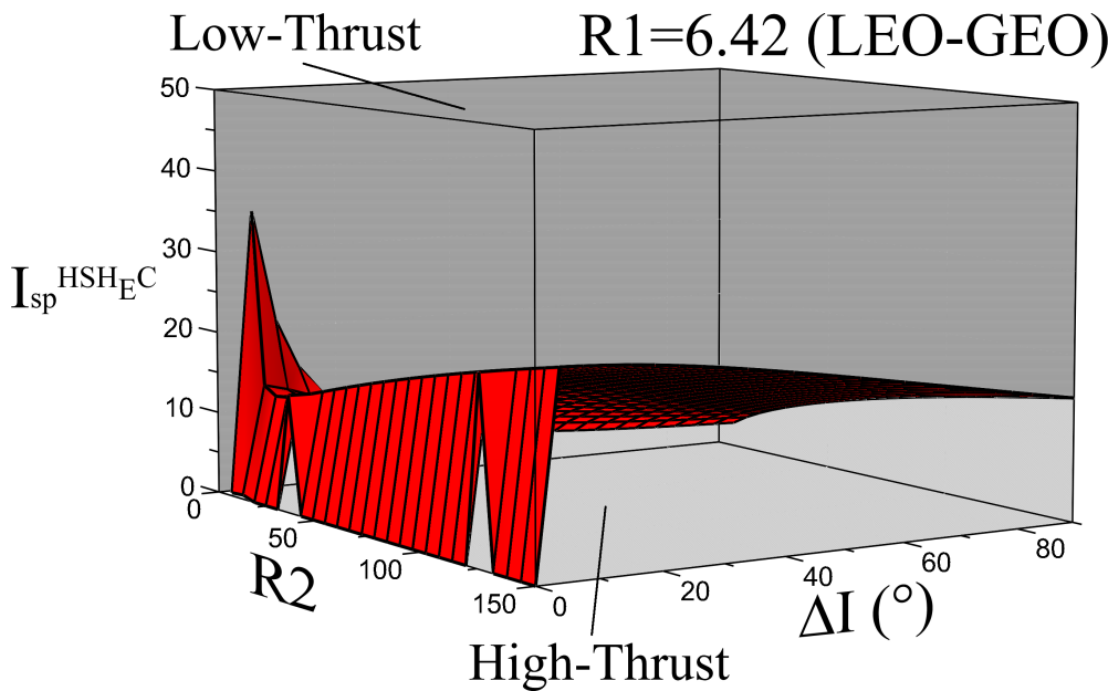


Figure 4-30 HST only critical specific impulse ratio variation for  $R1 = 6.42$  (LEO – GEO)

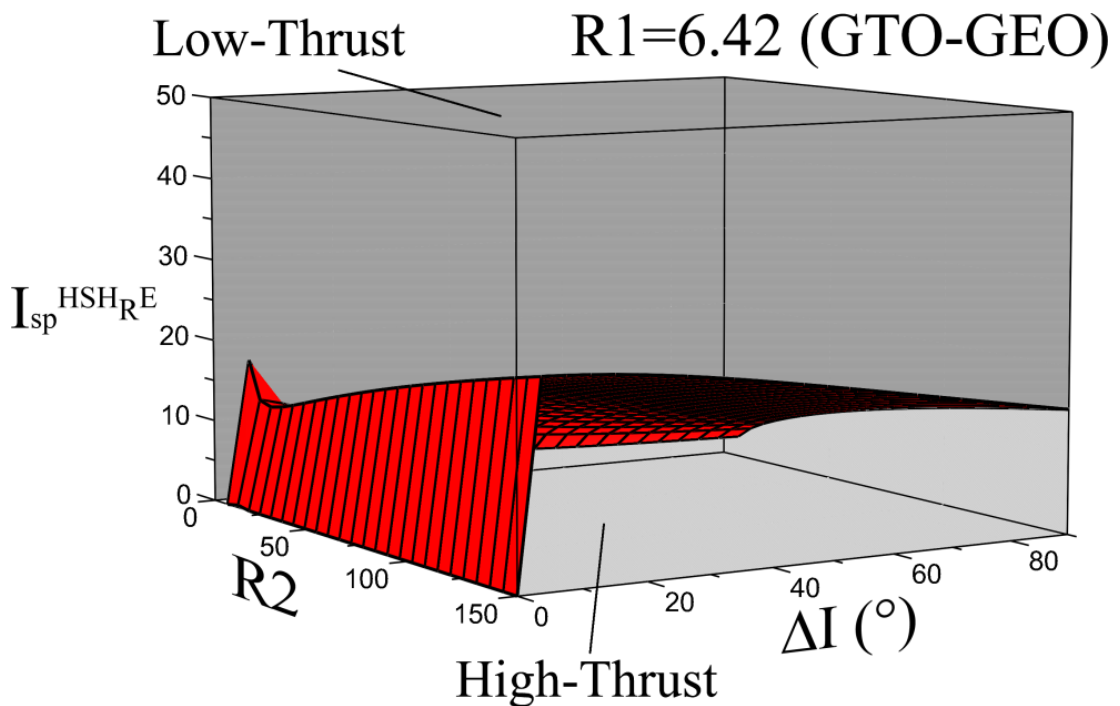


Figure 4-31 HST only critical specific impulse ratio variation for  $R1 = 6.42$  (GTO – GEO)

## 4.7. Critical Ratio Comparisons

As was discussed in the co-planar section of this chapter; when comparing different critical specific impulse ratios i.e. HST and Hohmann and HST and bi-elliptic, the largest ratio must

be taken into account to assure the HST offers a fuel mass saving against the most efficient transfer. After the most fuel efficient transfer has been identified, it can then be determined whether the HST with high or low-thrust plane change offers the largest fuel mass saving compared to the high-thrust only transfer. This section will briefly discuss the process that can be used to determine when each system should be used. The process is valid for all comparisons of the same type and as such only the HST and Hohmann critical specific impulse ratios for an elliptical initial orbit, with high and low-thrust, will be compared here. Figure 4-32 shows all critical ratios and the regions in which each version of the HST should be used. The black line on the diagram is the limit of an example system configuration with a specific impulse ratio of  $I_{spL}/I_{spH} = 12$ . Above this limit line is the forbidden region as the system cannot produce a specific impulse ratio in this region. To the left of the point  $R2 = 40.35$ , below the black limit line and above the red and blue dotted lines, is the region in which the HST with low-thrust plane change should be used. To the right of  $R2 = 40.35$ , below the black and red lines and above the solid blue line is where a HST with high-thrust plane change should be used.

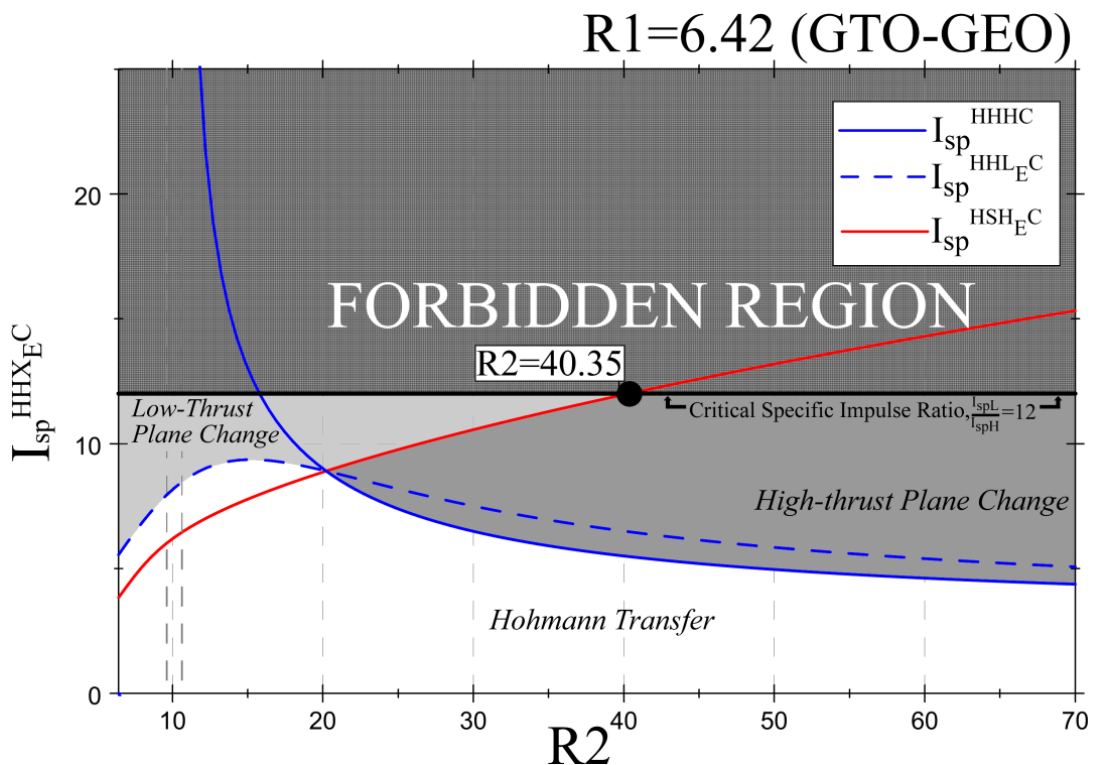


Figure 4-32 Comparison of critical specific impulse ratios, HST and Hohmann with high and low-thrust plane changes for  $R1 = 6.42$  (GTO – GEO)

## 4.8. Low-Thrust Plane Change Method

### Comparison

It was suggested previously in Section 4.6.2.3 that the low-thrust plane change method in which the plane change and spiral-in manoeuvres are combined is more efficient than performing the full plane change at the largest orbit radius before spiralling in for an initial orbit ratio of  $R1 = 6.42$ . Comparing the critical ratios for a circular and elliptical initial orbit in Figure 4-33 and Figure 4-34 respectively, it can be seen in both figures that the critical specific impulse ratio which compares the HST with high-thrust plane change and the HST with low-thrust plane change performed at the largest Radius, represented in red, is the larger of the two ratios for a varying  $R2$  and  $\Delta I$ . This confirms that combining the plane change and spiral-in manoeuvres is more efficient than performing the full plane change at the largest orbit radius.

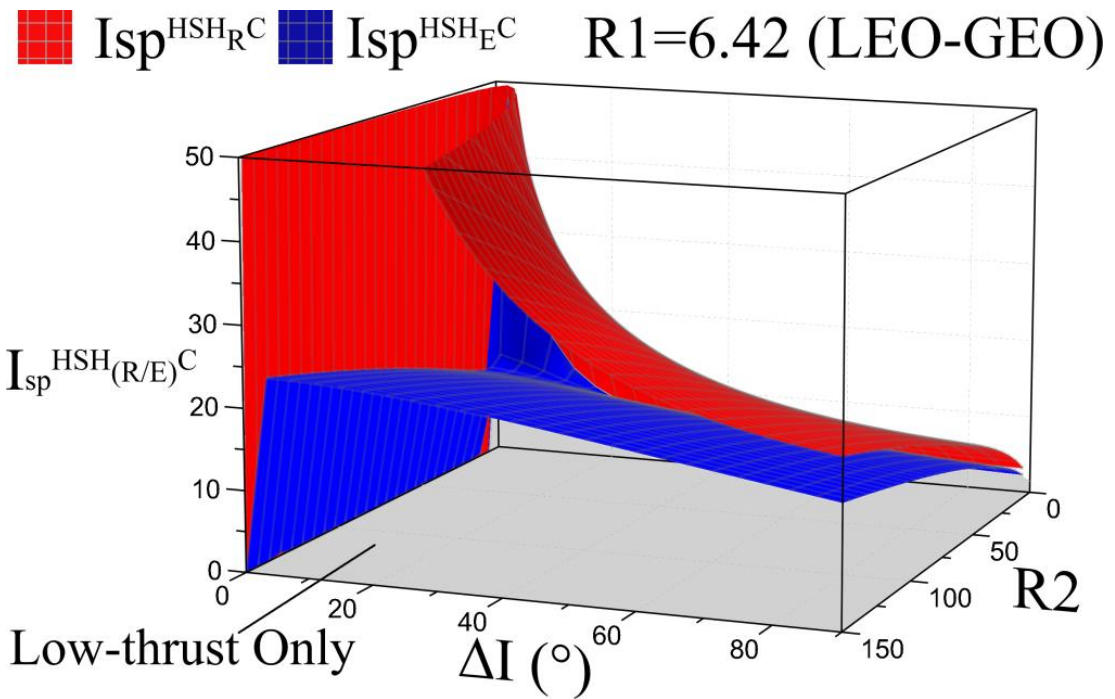


Figure 4-33 HST only critical ratio with both low-thrust plane change methods, circular initial orbit,  $R1 = 6.42$  (LEO - GEO)

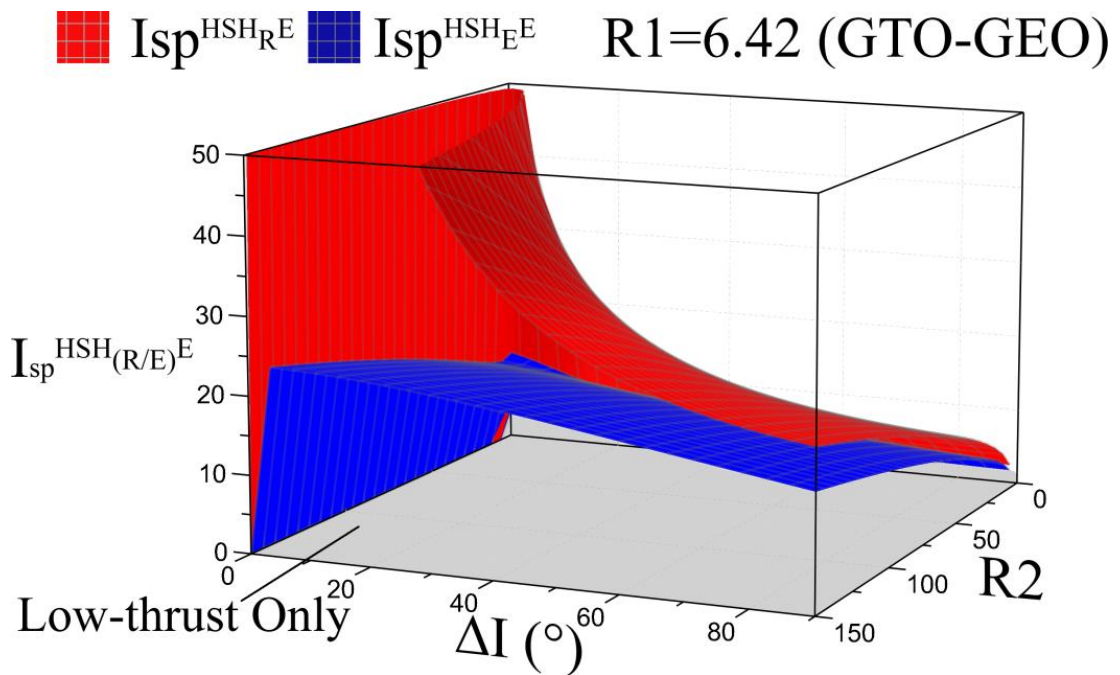


Figure 4-34 HST only critical ratio with both low-thrust plane change methods, elliptical initial orbit,  $R1 = 6.42$  (GTO - GEO)

It is necessary to consider if this is the case for different orbits of interest. Both a LEO to Medium Earth Orbit (MEO) and Sun Synchronous Orbit (SSO) are therefore investigated next. The LEO - MEO transfer is shown in Figure 4-35 with  $R1 = 3.21$  as this gives a 12

hour orbital period; a common location for Global Positioning System (GPS) satellites. This is half the orbital period of a GEO satellite and as such, the orbit ratio,  $R1$ , is half of that used in the previous GEO example. It can be seen that the trend is very similar to the LEO – GEO transfer in Figure 4-33 and shows for a LEO - MEO it is also better to perform the plane change and spiral-in manoeuvre together with the low-thrust plane change as opposed to performing the full plane change at the largest radius before spiralling in. Figure 4-36 shows both critical ratios for a transfer from a LEO – SSO, with an altitude of 800 km and inclination of  $98.6^\circ$  as detailed in the Ariane 5 User Manual [122, Sec. 2.5]. This results in  $R1 = 1.09$ . As this is a fixed plane change, the plot is shown for varying  $R2$  only. As was the case for the LEO – MEO transfer, it is found that it is more efficient to combine the plane change and spiral-in manoeuvres as opposed to performing the full plane change at the largest orbit radius and then spiralling in, when using the low-thrust system for plane change. As such, for the analytical case studies in Chapter 6, only the critical ratios which use the HST with low-thrust plane change (plane change and spiral-in manoeuvres combined) will be used.

■  $I_{sp}^{HSH_{R^C}}$ 
■  $I_{sp}^{HSH_{E^C}}$ 
R1=3.21 (LEO-MEO)

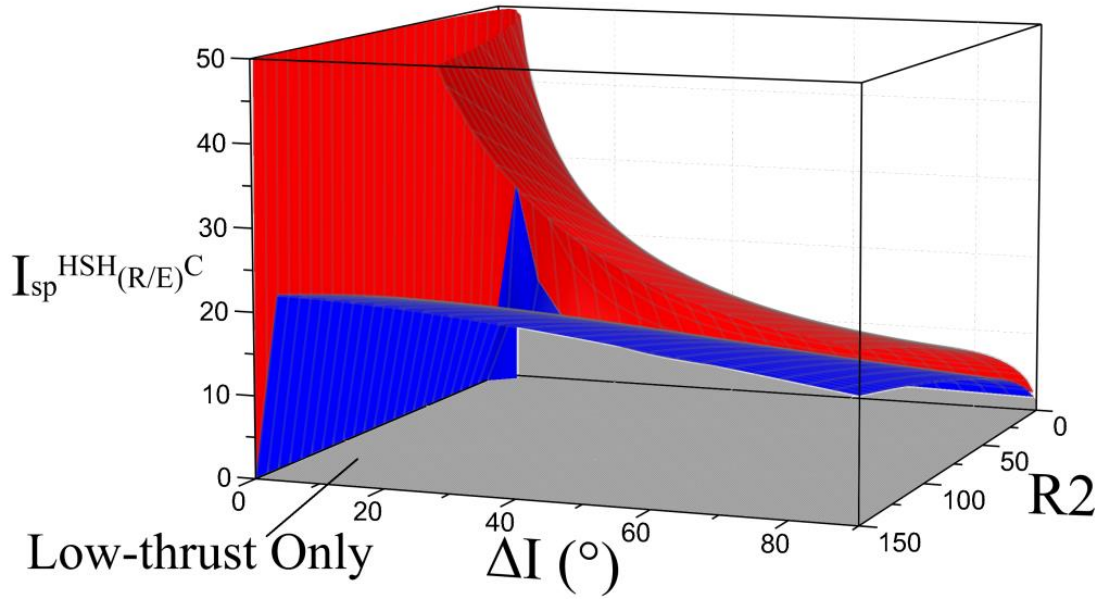


Figure 4-35 HST only critical ratio with both low-thrust plane change methods, circular initial orbit,  $R1 = 3.21$  (LEO - MEO)

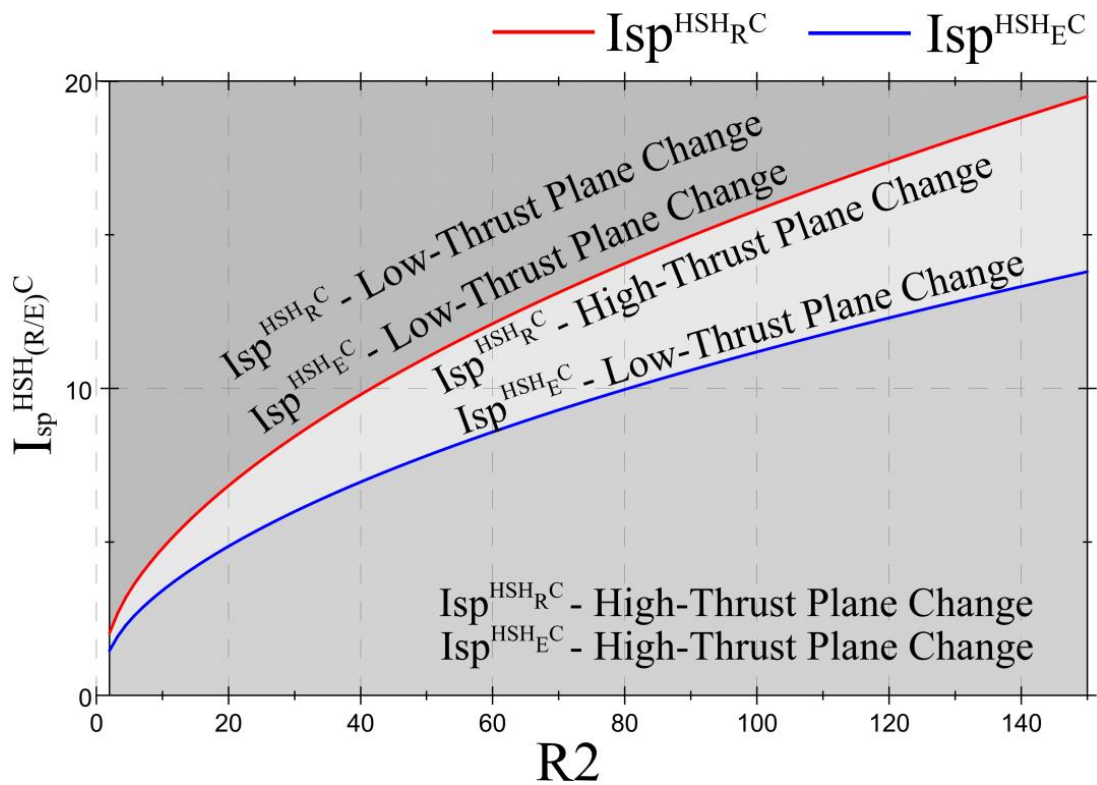


Figure 4-36 HST Only critical ratio with both low-thrust plane change methods, circular initial orbit,  $R1 = 1.09, \Delta I = 98.6$  (LEO - SSO)

## 4.9. Time Restricted Transfers

To understand the HST fully, it is necessary to introduce the transfer time into the analysis. This section therefore introduces the equations for all variations of the HST transfer after first introducing the general case. The total transfer time of the HST can be defined as

$$t_{HST(C/E)} = t_{HSTH} + t_{HSTL}, \quad (4.66)$$

where  $t_{HSTH}$  represents the high-thrust phase and  $t_{HSTL}$  represents the low-thrust phase. For both co-planar and non-co-planar cases, the high-thrust phase will always be defined as

$$t_{HSTH} = \frac{\pi}{\sqrt{\mu}} \sqrt{\left[ \frac{r_t}{2R_1} (1 + R_2) \right]^3}. \quad (4.67)$$

As the analytical analysis assumes the spacecraft acceleration is constant over the low-thrust phase, and is therefore dependent on the spacecraft mass at the beginning of phase two, the low-thrust phase transfer time can be defined as

$$t_{HSTL} = \frac{m_{02}}{T_r} \Delta V_{HSTL}, \quad (4.68)$$

where

$$m_{02} = m_{wet} e^{\frac{-\Delta V_{HSTH(C/E)}}{g^{lspH}}}.$$

As can be seen from Eq. (4.68), the transfer time will vary dependent on the initial orbit configuration and which propulsion system performs the plane change. In the case that the low-thrust propulsion system performs the plane change, the transfer time will also vary depending on which method is used. This section will therefore define the transfer time equations for the co-planar and non-co-planar scenarios, accounting for all possible variations. For a comparison however, it is necessary to define the transfer time of the Hohmann and bi-elliptic transfers. These equations were given in Chapter 2 but are defined

again respectively in Eqs. (4.69) and (4.70) with the inclusion of the orbit ratios  $R1$  and  $R2$ .

They are valid for both circular and elliptical initial orbits, with and without a plane change.

$$t_H = \frac{\pi}{\sqrt{\mu}} \sqrt{\left[ \frac{r_t}{2R1} (1 + R1) \right]^3} \quad (4.69)$$

$$t_B = \frac{\pi}{\sqrt{\mu}} \left( \sqrt{\left[ \frac{r_t}{2R1} (1 + R2) \right]^3} + \sqrt{\left[ \frac{r_t}{2} \left( 1 + \frac{R2}{R1} \right) \right]^3} \right) \quad (4.70)$$

## 4.9.1. Co-planar

For the co-planar scenario, the transfer time equation for a circular orbit can be defined as

$$t_{HSTC} = \frac{\pi}{\sqrt{\mu}} \sqrt{\left[ \frac{r_t}{2R1} (1 + R2) \right]^3} + \frac{\sqrt{\frac{\mu}{r_t}} \left[ 1 - \sqrt{\frac{R1}{R2}} \right] m_{wet} e \frac{-\frac{\pi}{\sqrt{r_t}} \sqrt{R1} \left[ \sqrt{\frac{2R2}{1+R2}} + \sqrt{\frac{1}{R2}} - \sqrt{\frac{2}{R2(1+R2)}} - 1 \right]}{g^{I_{sp}} H}}{Tr}, \quad (4.71)$$

in which the HST low and high-thrust velocity requirements are defined in Eqs. (4.5) and (4.6) respectively. As before, the orbit ratios  $R1$  and  $R2$  have also been introduced to simplify the equation. The transfer time for the elliptical initial orbit can be defined using Eqs. (4.5) and (4.12) for the HST's low and high thrust velocity requirements respectively as

$$t_{HSTE} = \frac{\pi}{\sqrt{\mu}} \sqrt{\left[ \frac{r_t}{2R1} (1 + R2) \right]^3} + \frac{\sqrt{\frac{\mu}{r_t}} \left[ 1 - \sqrt{\frac{R1}{R2}} \right] m_{wet} e \frac{-\frac{\mu}{\sqrt{r_t}} \sqrt{\frac{R1}{R2}} \sqrt{R2} \left( \sqrt{\frac{2R2}{1+R2}} - \sqrt{\frac{2R1}{1+R1}} \right) - \sqrt{\frac{2}{1+R2} + 1}}{g^{I_{sp}} H}}{Tr}. \quad (4.72)$$

## 4.9.2. Non Co-Planar

### 4.9.2.1. High-thrust Plane Change

For the HST with the high-thrust system performing the plane change and initiating in a circular orbit, the transfer time is defined as

$$t_{HSTC} = \frac{\pi}{\sqrt{\mu}} \sqrt{\left[ \frac{r_t}{2R1} (1 + R2) \right]^3} + \frac{\sqrt{\frac{\mu}{r_t}} \left[ 1 - \sqrt{\frac{R1}{R2}} \right] m_{wet} e \frac{-\frac{\pi}{\sqrt{r_t}} \sqrt{R1} \left[ A_1 + \sqrt{\frac{1}{R2}} A_2 \right]}{g^{I_{sp}} H}}{Tr} \quad (4.73)$$

where

$$\mathbb{A}_1 = \sqrt{1 + \frac{2R_2}{1+R_2} - \sqrt{\frac{8R_2}{1+R_2}} \cos \left( \tan^{-1} \left[ \frac{\sin(\Delta I)}{\sqrt{(R_2)^3 + \cos(\Delta I)}} \right] \right)}$$

$$\mathbb{A}_2 = \sqrt{1 + \frac{2}{1+R_2} - \sqrt{\frac{8}{1+R_2}} \cos \left( \Delta I - \tan^{-1} \left[ \frac{\sin(\Delta I)}{\sqrt{(R_2)^3 + \cos(\Delta I)}} \right] \right)}.$$

For the case of an elliptical initial orbit and the high-thrust system performing the plane change, the transfer time is given as

$$t_{HSTE} = \frac{\pi}{\sqrt{\mu}} \sqrt{\left[ \frac{r_t}{2R_1} (1 + R_2) \right]^3} + \frac{\sqrt{\frac{\mu}{r_t}} \left[ 1 - \sqrt{\frac{R_1}{R_2}} \right] m_{wet} e^{-\frac{\sqrt{\frac{\mu}{r_t}} \frac{R_1}{R_2} [\sqrt{R_2} \mathbb{B}_1 + \mathbb{B}_2]}{g^I_{spH}}}}}{Tr} \quad (4.74)$$

where

$$\mathbb{B}_1 = \sqrt{\frac{2R_1}{1+R_1} + \frac{2R_2}{1+R_2} - \sqrt{\frac{8R_1}{1+R_1}} \sqrt{\frac{2R_2}{1+R_2}} \cos \left( \tan^{-1} \left[ \frac{\sin(\Delta I)}{\sqrt{\frac{2R_1 R_2^3}{1+R_1} + \cos(\Delta I)}} \right] \right)}$$

$$\mathbb{B}_2 = \sqrt{1 + \frac{2}{1+R_2} - \sqrt{\frac{8}{1+R_2}} \cos \left( \Delta I - \tan^{-1} \left[ \frac{\sin(\Delta I)}{\sqrt{\frac{2R_1 R_2^3}{1+R_1} + \cos(\Delta I)}} \right] \right)}.$$

#### 4.9.2.2. Low-Thrust Plane Change

##### 4.9.2.2.1. Plane Change at Largest Orbit Radius

For a circular initial orbit the HST with the low-thrust system performing the plane change at the largest radius transfer time is defined as

$$t_{HSTC} = \frac{\pi}{\sqrt{\mu}} \sqrt{\left[ \frac{r_t}{2R_1} (1 + R_2) \right]^3} + \frac{\sqrt{\frac{\mu}{r_t}} \left[ 1 - \sqrt{\frac{R_1}{R_2}} + \sqrt{\frac{R_1 \pi}{R_2^2} \Delta I} \right] m_{wet} e^{-\frac{\sqrt{\frac{\mu}{r_t}} \sqrt{R_1} \left[ \sqrt{\frac{2R_2}{1+R_2}} + \sqrt{\frac{1}{R_2}} - \sqrt{\frac{2}{R_2(1+R_2)}} - 1 \right]}{g^I_{spH}}}}}{Tr}. \quad (4.75)$$

For the case of an elliptical initial orbit and the low-thrust system performing the plane change at the largest orbit radius, the transfer time can be defined as

$$t_{HSTE} = \frac{\pi}{\sqrt{\mu}} \sqrt{\left[ \frac{r_t}{2R_1} (1 + R_2) \right]^3} + \frac{\sqrt{\frac{\mu}{r_t}} \left[ 1 - \sqrt{\frac{R_1}{R_2}} + \sqrt{\frac{R_1 \pi \Delta I}{R_2^2}} \right] m_{wet} e^{-\frac{\sqrt{\frac{\mu}{r_t}} \sqrt{\frac{R_1}{R_2}} \sqrt{R_2} \left( \sqrt{\frac{2R_2}{1+R_2}} - \sqrt{\frac{2R_1}{1+R_1}} \right) - \sqrt{\frac{2}{1+R_2} + 1}}}{g^{I_{sp} H}}}}{Tr} \quad (4.76)$$

#### 4.9.2.2.2. *Edelbaum's Method (Combined Plane Change and Spiral-In Manoeuvre)*

For a circular initial orbit and the HST performing the plane change with the low-thrust system but combined with the spiral in-phase, the transfer time is defined as

$$t_{HSTC} = \frac{\pi}{\sqrt{\mu}} \sqrt{\left[ \frac{r_t}{2R_1} (1 + R_2) \right]^3} + \frac{\sqrt{\frac{\mu}{r_t}} \left[ 1 + \frac{R_1}{R_2} - 2 \sqrt{\frac{R_1}{R_2}} \cos\left(\frac{\pi \Delta I}{2}\right) \right] m_{wet} e^{-\frac{\sqrt{\frac{\mu}{r_t}} \sqrt{R_1} \left[ \sqrt{\frac{2R_2}{1+R_2}} + \sqrt{\frac{1}{R_2}} - \sqrt{\frac{2}{R_2(1+R_2)} - 1} \right]}{g^{I_{sp} H}}}}{Tr} \quad (4.77)$$

For the elliptical initial orbit case, the HST transfer time can be defined as

$$t_{HSTE} = \frac{\pi}{\sqrt{\mu}} \sqrt{\left[ \frac{r_t}{2R_1} (1 + R_2) \right]^3} + \frac{\sqrt{\frac{\mu}{r_t}} \left[ 1 + \frac{R_1}{R_2} - 2 \sqrt{\frac{R_1}{R_2}} \cos\left(\frac{\pi \Delta I}{2}\right) \right] m_{wet} e^{-\frac{\sqrt{\frac{\mu}{r_t}} \sqrt{\frac{R_1}{R_2}} \sqrt{R_2} \left( \sqrt{\frac{2R_2}{1+R_2}} - \sqrt{\frac{2R_1}{1+R_1}} \right) - \sqrt{\frac{2}{1+R_2} + 1}}}{g^{I_{sp} H}}}}{Tr} \quad (4.78)$$

## 4.10. Analytical Limit Analysis

As the HST requires a large intermediate orbit radius and the analytical analysis is based on a quasi-circular transfer assumption, it is necessary to compare the spacecraft thrust at this large radius to local gravity, and hence determine the effect it has on the resultant trajectory. It is understood that with increasing intermediate orbit radius, the spacecraft will tend to enter an eccentric orbit while transferring towards the target orbit and so a critical limit must be defined which beyond, a numerical analysis should be used. It is of note that this occurs at a radius less than the Earth's sphere of influence ( $\approx 156$  Earth Radii [20, Sec. 7.4]), as will be shown in this section, and is therefore relevant to most low-thrust analytical analyses. With this in mind, it is worthwhile noting that the author has found no such analysis in the

literature. It is noted that in practical terms the actual sphere of influence of the Earth in the Sun-Earth system will be altered due to the effect of the Moon, however for the purpose of this dissertation, this analysis will provide a reasonable limit to the analytical approach. Only the case where the spacecraft spirals inward with no plane change is considered as the results are provided in terms of the spacecraft acceleration only and are therefore relevant to the different HST configurations. For the case where the low-thrust system performs a coupled plane change and spiral-in manoeuvre however, only the acceleration used to control the semi-major axis can be related to the limits derived in this section and not the total magnitude of spacecraft acceleration. The maximum allowable eccentricity, dependent on an error deemed acceptable by the mission designer, is calculated by first defining the eccentricity,

$$e = \frac{r_a - r_p}{r_a + r_p} \quad (4.79)$$

To achieve a circular final orbit,  $r_a = r_p = 0 \therefore e = 0$ . However if it is assumed that the orbit apogee is achieved and the perigee is specified as an acceptable relative error,  $e_{re}$ , then

$$e_{re} = \frac{r_a - r_p}{r_a} \quad (4.80)$$

and by substituting Eq. (4.80) into Eq. (4.79) yields

$$e = \frac{r_a - r_a(1 - e_{re})}{r_a + r_a(1 - e_{re})} \quad (4.81)$$

$$e = \frac{e_{re}}{2 - e_{re}}$$

The error can then be specified to give a maximum acceptable final orbit eccentricity. As there is no analytical methodology available to implement this error into the analysis, a numerical method is used and then compared with the analytical analysis for verification. For this analysis the orbit parameters are defined in Table 4-4. It should be noted that this analysis applies specifically to a target that is GEO. GEO was chosen as it is an orbit of great

interest for many commercial activities and accounts for a large proportion of the satellites in orbit, as has been discussed previously in this dissertation. It can be assumed that if a target of lower altitude than GEO is required, the limits determined in this analysis are invalid. In this scenario they would be lower and hence this process should be repeated to determine the correct limits. Conversely, if the target orbit is higher than the altitude of GEO, then the limits determined in this analysis are valid but somewhat conservative.

**Table 4-4 Critical limit validation study parameters**

Gravitational constant, $\mu$ ( $m^3/s^2$ )	$3.986004418 \times 10^{14}$
Target orbit radius, $r_t$ (m)	42,164,000
Spacecraft acceleration range $a_s$ ( $m/s^2$ )	$3 \times 10^{-4} \rightarrow 0.15 \times 10^{-4}$

The numerical trajectory is calculated with the use of control laws defined in modified equinoctial elements in Section 2.6 using the trajectory generation model specified in Section 5.1.

To determine a maximum orbit radius at which the analytical analysis is valid it is first necessary to define an acceptable error. For this analysis, a relative error of 5% and 10% is considered. By substituting these values into Eq. (4.81) the maximum allowable eccentricities are 0.0256 and 0.0526. By now considering the numerical analysis, the eccentricity of the target orbit for varying spacecraft accelerations is shown in comparison with the initial orbit radius in Figure 4-37. The acceleration range is  $3 \times 10^{-4} \rightarrow 0.15 \times 10^{-4} m/s^2$  which with a spacecraft thrust of approximately 300mN, would represent a spacecraft mass range at the beginning of phase 2 of 1000  $\rightarrow$  20,000 kg.

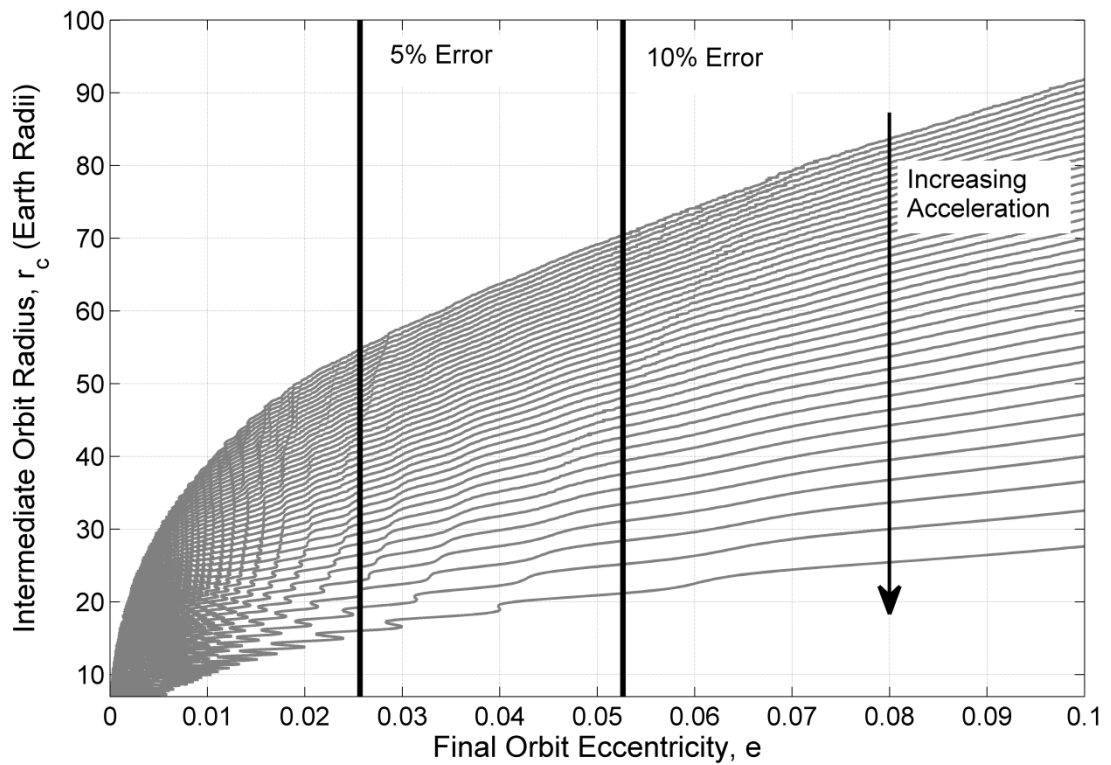


**Figure 4-37 Critical orbit radius at specified eccentricity error tolerances with varying spacecraft acceleration**

From Figure 4-37, it can be seen with increasing spacecraft acceleration, the maximum achievable intermediate orbit radius which can be achieved within the specified error margins reduces. The spacecraft acceleration range, as specified in Table 4-4, can be plotted against the critical orbit radius determined from Figure 4-37 dependent on the specified 5 or 10% relative error. This is shown in Figure 4-38 with the relevant final orbit eccentricity errors defined as the shaded regions. As noted previously, these limits are well within the Earth's sphere of influence.

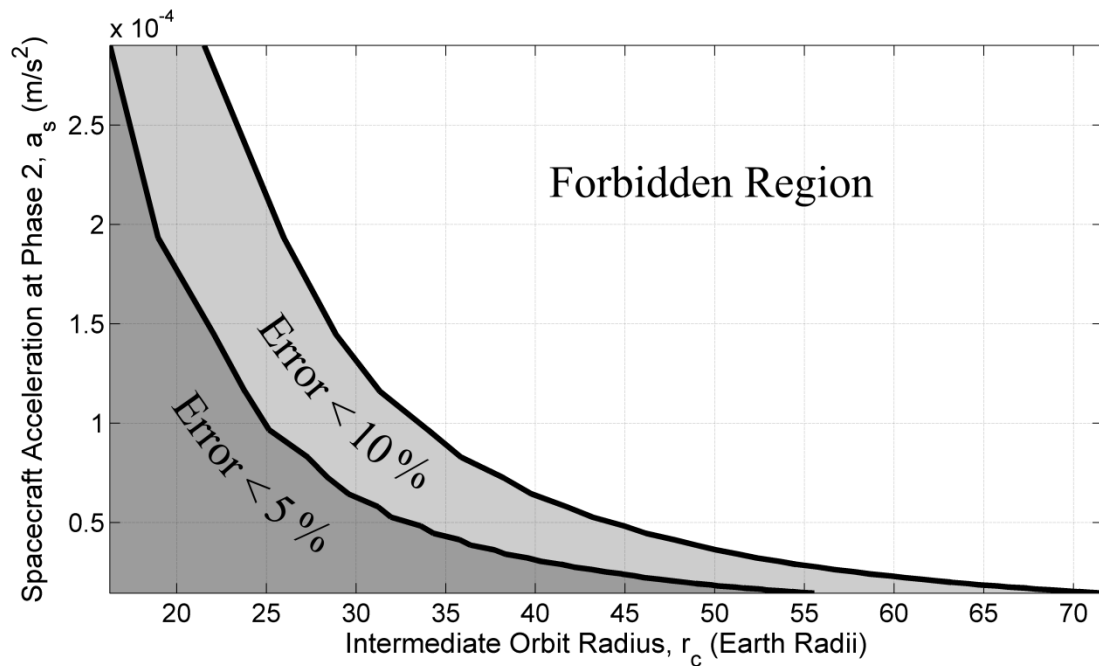


Figure 4-38 Maximum initial orbit radius with varying spacecraft acceleration. Error represents final orbit eccentricity

## 4.11. Summary

This chapter has introduced the Hohmann Spiral Transfer (HST); a transfer method incorporating both high and low-thrust propulsion systems. The chapter has presented the general theory of the transfer and used this to derive critical specific impulse ratios which determine when the transfer outperforms a high-thrust only transfer. Critical specific impulse ratios have been derived for both co-planar and non-co-planar transfers. For non-co-planar transfers, critical specific impulse ratios are derived for the case when a plane change is performed by either the high or low-thrust system. For a low-thrust plane change, two methods have been considered: either perform the full plane change at the largest orbit radius and then spiral-in towards the target or combine the plane change and spiral-in manoeuvres together. On comparison, it was found that combining the plane change and spiral-in sections is always more efficient and as such it is this method that is used in any analytical analysis performed using the HST. It has been shown that the HST offers the greatest fuel mass savings at large  $R2$  and  $\Delta I$ . Time restrictions have been imposed to enable more detailed

mission analysis and design of the HST. In addition, critical orbit ratios have been determined that identify the maximum orbit ratios the HST can achieve to maintain an acceptable final orbit with almost zero eccentricity; therefore obeying the quasi-circular assumption of the analytical approach.

# Chapter 5

---

## NUMERICAL ANALYSIS AND OPTIMISATION

This chapter builds on Chapter 4, which introduced the HST analytically, by introducing a numerical method which can be used as part of an optimisation study. Defining the numerical method allows analytical constraints to be removed, allowing a more realistic investigation of the transfer. The key differences are that the intermediate orbit is allowed to be eccentric as opposed to circular and the orbit eccentricity can also be controlled throughout the transfer with the use of the locally optimal control law defined in Section 2.6. This removes the need for the limiting intermediate orbit radius described in Section 4.10. Another advantage of implementing the numerical method is that full thrust profiles are determined for any given trajectory; allowing a detailed analysis of the spacecraft propulsion requirements. Finally, the numerical analysis accounts for fuel depletion over the duration of the transfer and therefore accounts for an increasing acceleration assuming constant thrust.

### 5.1. Numerical Integration Procedure

The equations of motion are defined in modified equinoctial which are derived in [123] and validated in [110]. These are used to propagate the trajectory as they are non-singular except for rectilinear orbits when the inclination,  $i, = \pi$  radians and provide runtime improvements over classical elements for certain orbit transfers [123]. The numerical method propagates the spacecraft position in time using an explicit variable step size Runge-Kutta (4,5) formula known as the Dormand-Prince pair [124]. It is a one-step solver, meaning it only requires the solution at the immediately preceding time point to solve the current point. A relative and

absolute tolerance of  $10^{-5}$  was initially chosen for all trajectory propagation and optimisation studies to allow rapid analysis without loss of accuracy. The trajectory is modified using the locally optimal control laws defined in Section 2.6, which control the thrust direction vector via the control law blending method also defined in Section 2.6. The number of control laws used for the determination of the thrust direction vector changes dependent on the mission specification. For the scenario where the high-thrust phase performs the plane change and there are no orbit insertion requirements, only the semi-major axis, eccentricity and radius of perigee control laws are required. For the case where the low-thrust system performs the plane change and there are no orbit insertion requirements then the inclination control law is introduced in addition to the three previously described. If there are specific orbit insertion requirements then additional control laws, such as the argument of perigee and longitude of ascending node, can be introduced.

## 5.2. Optimisation method

The trajectory optimisation process is primarily aimed at optimising the complex low-thrust section of the HST, however it can be modified to include an optimisation of the high-thrust section so that the HST can be optimised as a full hybrid transfer. This allows the optimiser to choose the ‘best’ scenario without the need for experienced engineering judgement when splitting the high and low-thrust phases. This section therefore details the procedure for the full HST optimisation, accounting for the different configurations of the HST. The optimisation algorithm selected uses a constrained nonlinear optimisation technique adapting a sequential quadratic programming (SQP) method. This is selected as it has a strict feasibility with respect to the bounds meaning every iterative step is taken within the specified limits [125]. This is necessary for this study as the parameters to be optimised cannot be negative otherwise the trajectory generation will fail. The algorithm is employed

through the optimisation tool, `fmincon`, which is part of the Matlab<sup>®</sup> mathematical programming software suite. The optimisation problem can be specified as

$$\min_{W_\sigma, R2, e} \{m_{HSTF}\} \quad (5.1)$$

where  $W_\sigma$  represents each of the locally optimal control law constants required for the generation of the low-thrust phase,  $R2$  is the intermediate orbit to initial orbit radius ratio and  $e$  is the intermediate orbit eccentricity. When the intermediate orbit is elliptical, the orbit ratio  $R2$  is the ratio of the intermediate orbit apogee to initial orbit radius. When the initial orbit is elliptical, the orbit ratio  $R2$  is the ratio of the intermediate orbit apogee to the initial orbit perigee. Each term is explained in full in the proceeding sections. The optimisation parameters are subject to the following bounds

$$\begin{aligned} W_{\sigma L} &\leq W_\sigma \leq W_{\sigma U} \\ R2_L &\leq R2 \leq R2_U \\ e_L &\leq e \leq e_U \end{aligned} \quad (5.2)$$

and the following active inequality constraints,

$$t - t_{MAX} \leq 0 \quad (5.3)$$

$$\left| \frac{a}{a_{target}} \right| - 0.01 \leq 0 \quad (5.4)$$

$$e - 0.001 \leq 0 \quad (5.5)$$

$$|i| - 0.001^\circ \leq 0, \quad (5.6)$$

where  $t_{MAX}$  is the maximum allowable transfer time and is determined by the mission specification.  $a_{target}$  is the target semi-major axis which is used to scale the large semi-major axis value. It should be noted that there are no active equality constraints for the optimisation studies in this dissertation.

## 5.2.1. High-Thrust Phase

It is assumed the high-thrust section is conducted through one or two impulsive burns; accounting for a circular or elliptical initial orbit respectively. As was discussed in Chapter 4, this is based on the minimum energy Hohmann transfer. The first burn is used to enter the transfer orbit which takes the spacecraft beyond the target orbit. In the case where the low-thrust system is activated at the apogee of this orbit, i.e. the low-thrust phase begins with the eccentricity of the transfer orbit, this is the only high-thrust burn performed unless a plane change is required. In the case where the spacecraft enters an intermediate orbit at the transfer orbit apogee, a second high-thrust impulse, incorporating any plane change, is used to achieve this before the low-thrust system is activated. It is worthwhile noting again that the analytical analysis assumes that the spacecraft enters a circular intermediate orbit at this far away point. The HST high-thrust phase optimisation involves two variables, the orbit ratio  $R2$  and the intermediate orbit eccentricity,  $e$ . The optimiser can vary  $R2$  to increase/decrease the intermediate orbit apogee in order to reduce the velocity requirement of the high-thrust phase. Additionally, the eccentricity,  $e$ , of this intermediate orbit can also be modified by the optimiser to lower the velocity requirement of the high-thrust phase.

## 5.2.2. Adaptation of Intermediate Orbit

To include the intermediate orbit eccentricity as an optimisation parameter, it is necessary to modify the equation representing the intermediate orbit velocity. The definitions for the radius of perigee and apogee can be defined respectively as

$$r_p = (1 - e)a \quad (5.7)$$

$$r_a = (1 + e)a. \quad (5.8)$$

The semi-major,  $a$ , is defined as

$$a = \frac{r_p + r_a}{2}. \quad (5.9)$$

By substituting Eqs (5.7) and (5.8) into Eq. (5.9), the radius of perigee, for the intermediate orbit with apogee radius,  $r_c$ , is defined as

$$r_p = r_X = r_c \left( \frac{2}{1+e} - 1 \right). \quad (5.10)$$

Note that this orbit perigee will be defined as  $r_X$  from this point forward. It is noted when  $e = 0$ ,  $r_X = r_c$  as expected. This parameter can then be used when deriving the high-thrust phase velocity requirement for each HST case, as is shown in the proceeding sections.

### 5.2.3. High-thrust Plane Change

A schematic of the HST, starting in a circular orbit and using a high-thrust plane change, is shown in Figure 5-1. It can be seen that the intermediate orbit apogee and perigee are variable; thus removing the circular intermediate orbit constraint. The Hohmann and bi-elliptic transfers are also shown as these are what the HST is compared to in the case studies in Chapter 6. When the high-thrust propulsion system performs the plane change, it is assumed that the orbit raise and plane change manoeuvres are combined as this has been proven to be more fuel effective, discussed in detail in Chapter 2. The plane change is distributed over two impulses; one at the initial/transfer orbit node and the second at the transfer/intermediate orbit node with the optimal split determined by numerically solving Eq. (3.8) in Chapter 3. This plane change methodology is also applied to the compared transfer; Hohmann or bi-elliptic as shown in Figure 5-1.

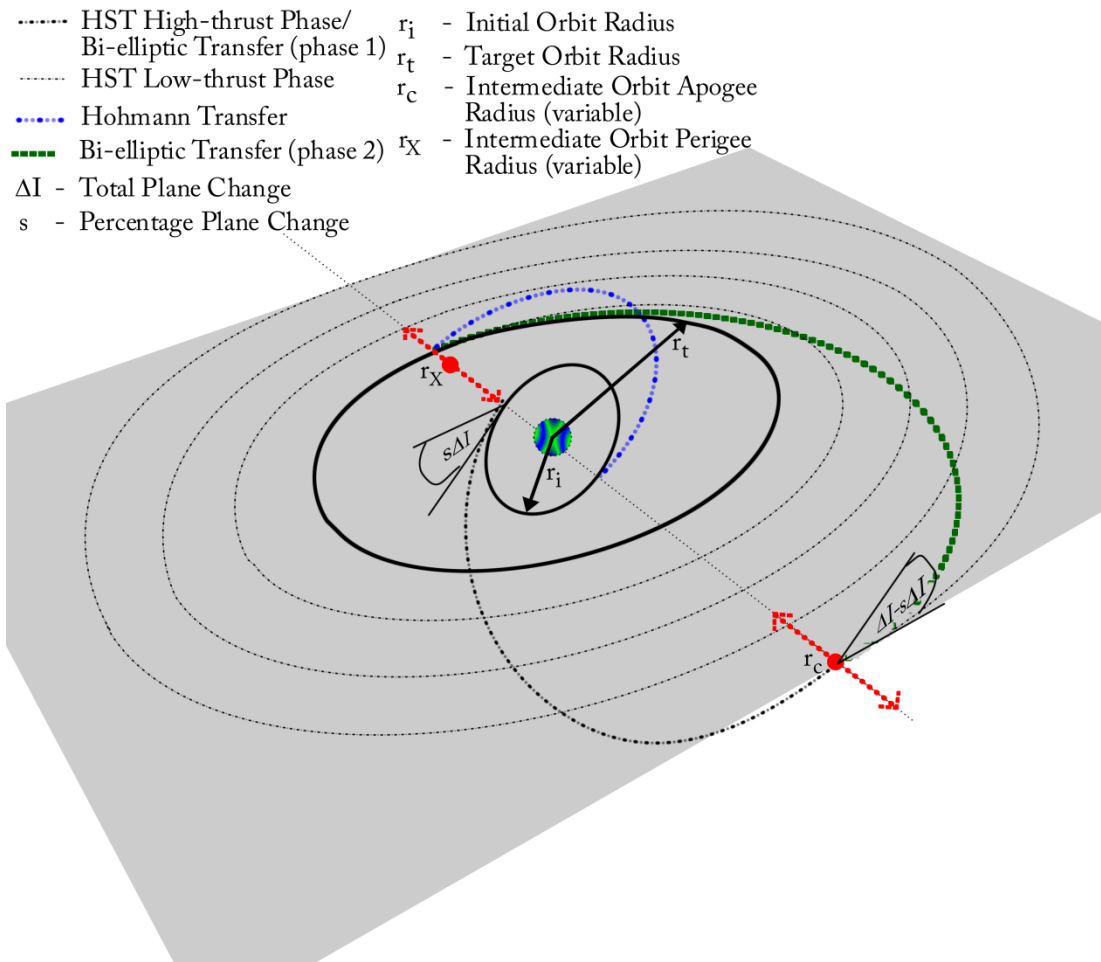


Figure 5-1 HST optimisation method with high-thrust plane change

### 5.2.3.1. Circular Initial Orbit

For the case where the high-thrust system performs the plane change and the initial orbit is circular, the velocity requirement, with the inclusion of  $r_x$  as described in Section 5.2.2, is defined as

$$\Delta V_{HSTHC} = \sqrt{\frac{\mu}{r_t}} \sqrt{R1} \left[ \sqrt{1 + \frac{2R2}{1+R2} - \sqrt{\frac{8R2}{1+R2}} \cos(s\Delta I)} + \sqrt{\frac{1-e}{R2} + \frac{2}{R2^2+R2} - \sqrt{\frac{1-e}{R2}} \sqrt{\frac{8}{R2^2+R2}} \cos((1-s)\Delta I)} \right] \quad (5.11)$$

The optimum plane change split is calculated as described previously in Eq. (3.8) in Chapter 3, with the orbit velocities relevant to the transfer being considered.

### 5.2.3.2. *Elliptical Initial Orbit*

For the HST with high-thrust plane change initiating in an elliptical orbit, the velocity requirement of the high-thrust phase, using  $r_X$  as detailed previously, is defined as

$$\Delta V_{HSTHE} = \sqrt{\frac{\mu}{r_t}} \sqrt{\frac{R1}{R2}} \left[ \sqrt{R2} \sqrt{\frac{2R1}{1+R1} + \frac{2R2}{1+R2} - \sqrt{\frac{8R1}{1+R1}} \sqrt{\frac{2R2}{1+R2}} \cos(s\Delta I)} + \sqrt{1 - e + \frac{2}{1+R2} - \sqrt{\frac{8(1-e)}{1+R2}} \cos((1-s)\Delta I)} \right] \quad (5.12)$$

Again the optimum plane change split is determined with the use of Eq. (3.8) in Chapter 3.

## 5.2.4. Low-thrust Plane Change

The velocity requirements of the high-thrust phase will obviously differ when the low-thrust system is used to perform the plane change. As such, it is necessary to define these equations for a circular and elliptical initial orbit. The HST transfer with low-thrust plane change is shown in Figure 5-2 where it can be seen the co-planar high-thrust phase still allows for a variable intermediate orbit. Depending on the intermediate orbit selected, the low-thrust system is activated at the apogee and proceeds to spiral-in while changing the plane of the orbit to match that of the target. The optimisation process for the low-thrust phase is discussed in detail in Section 5.2.5.

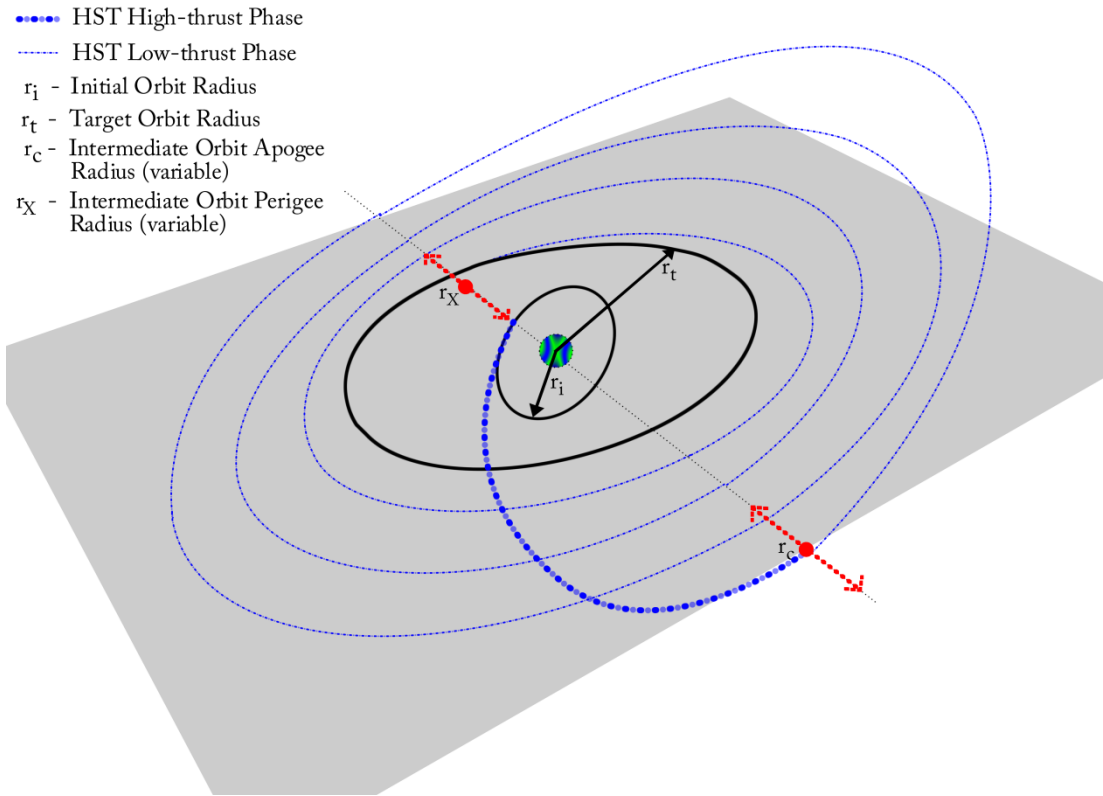


Figure 5-2 HST optimisation method with low-thrust plane change

#### 5.2.4.1. *Circular Initial Orbit*

For the case when the low-thrust phase of the HST performs the plane change and the initial orbit is circular, the high-thrust phase velocity requirement, with substitution of  $r_X$  as described in Section 5.2.2 is defined as

$$\Delta V_{HSTHC} = \sqrt{\frac{\mu}{r_t}} \sqrt{R1} \left[ \sqrt{\frac{2R2}{1+R2}} + \sqrt{\frac{1-e}{R2}} - \sqrt{\frac{2}{R2^2+R2}} - 1 \right]. \quad (5.13)$$

#### 5.2.4.2. *Elliptical Initial Orbit*

The high-thrust phase velocity requirement for the case where the initial orbit is elliptical and the low-thrust phase of the HST performs the plane change, is defined, using  $r_X$  as before, as

$$\Delta V_{HSTHE} = \sqrt{\frac{\mu}{r_t}} \sqrt{R1} \left[ \sqrt{\frac{2R2}{1+R2}} + \sqrt{\frac{1-e}{R2}} - \sqrt{\frac{2R1}{1+R1}} - \sqrt{\frac{2}{R2^2+R2}} \right]. \quad (5.14)$$

## 5.2.5. Low-thrust Phase

The HST low-thrust phase optimisation involves a maximum of four variables, or weighting constants as described previously in the discussion regarding control law blending in Section 2.6. For the case where the high-thrust phase performs the plane change, only three constants are required and are applied to the semi-major axis, eccentricity and radius of perigee control laws. These constants are applied by the optimiser to effectively prioritise each control law dependent on the mission specification. For the case where the low-thrust system performs the plane change, four constants are used. In addition to the three control laws discussed previously, the inclination control law is also given a constant. The use of these constants reduces optimisation complexity as each control law is prioritised before each trajectory calculation as opposed to each control law being prioritised at every time-step. Removing the time dependency also allows this controller to be used as an autonomous guidance system. It should be noted however that by implementing this method, a degree of accuracy is sacrificed as these constants are general for a whole trajectory as opposed to being variable to suit the spacecraft position at each individual time step.

## 5.3. Summary

This chapter has introduced the optimisation and trajectory generation method used within this dissertation. It has been shown that a low-thrust trajectory model can be coupled with a simple high-thrust transfer model to develop an effective hybrid propulsion transfer optimiser. A locally optimal solution method is used and as such can provide rapid optimisation results. As the process optimises control law constants independent of time, the system could also be used as an autonomous guidance controller.

# Chapter 6

---

## CASE STUDIES

### 6.1. Analytical

#### 6.1.1. LEO - GEO

To gain an understanding of when each transfer should be used it is necessary to compare all the critical ratios and their respective transfer times. As an example, a transfer from LEO – GEO is considered, with the launch site selected as Xichang, China. Xichang is one of China's main launch sites for spacecraft bound for GEO and as it requires a large plane change penalty due to its geographical location, it is ideal to demonstrate the HST. Table 6-1 provides a detailed specification of the mission and thruster data. The initial orbital data is based on the Long March Rocket (LM-3A) launch series vehicle capability [126, Ch. 3]. The high-thrust system specific impulse is based on the 500N Bipropellant European Apogee Motor<sup>2</sup> and the low-thrust system thruster data is based on two T6 thruster used in a dual configuration[82], [83]. The wet masses have been chosen to cover a wide range of transfers. The largest mass, 9100 kg, is the maximum achievable wet mass from Xichang using the LM3C launch vehicle [127, Ch. 3]. For the other wet masses, 2000 kg and 5000 kg, the LM3A launch vehicle could be used as its maximum achievable wet mass to a LEO is 6000 kg [127, Ch. 3] or the LM3C could also be used to launch the 5000 kg and 2000 kg wet masses together to reduce launch costs.

---

<sup>2</sup> <http://cs.astrium.eads.net/sp/spacecraft-propulsion/apogee-motors/500n-apogee-motor.html> - date accessed - December 2013

**Table 6-1 Circular initial orbit case study specification (LEO-GEO) from Xichang launch port**

Gravitational constant, $\mu$ ( $\text{m}^3/\text{s}^2$ )	3.986004418x10 <sup>14</sup>		
Mean Earth Radius <sup>3</sup> , $r_E$ (m)	6,378,100		
Initial Orbit, $r_i$ (m)	6,578,100 (200 km altitude)		
Target Orbit, $r_t$ (m)	42,164,100 (35,786 km altitude)		
Target/Initial Orbit Ratio, $R1$	6.41		
Initial Mass, $m_{wet}$ (kg)	9100	5000	2000
High-Thrust System Specific Impulse, $I_{spH}$ (s)	325		
Low-Thrust System Specific Impulse, $I_{spL}$ (s)	4300		
Critical Specific Impulse Ratio, $I_{sp}^{XXX-}$	13.23		
Thrust, $Tr$ (mN)	290 (2x145)		
Plane Change, $\Delta I$ (rad)	0.497 (28.5°)		

Firstly, it is necessary to compare the critical specific impulse ratios of different transfer comparisons to determine which should be considered to offer the largest fuel mass transfer. In Figure 6-1, it can be seen that the critical specific impulse ratios which compare the Hohmann and HST transfers are defined in blue. The green lines represent the critical specific impulse ratios of the bi-elliptic, with plane change performed at the first and second nodes, and HST transfer comparisons. The orange lines represent the critical specific impulse ratios of the bi-elliptic, with plane change performed at the second and third nodes, and HST transfer comparisons. In all cases, the solid line represents a high-thrust plane change and the dashed line represents a low-thrust plane change using Edelbaum's method. The red line represents the HST only critical ratio comparison and identifies the regions in which either a high or low-thrust plane change should be used. As discussed in Section 4.7, when comparing different transfers, i.e. Hohmann and HST critical ratio and bi-elliptic and

<sup>3</sup> <http://nssdc.gsfc.nasa.gov/planetary/factsheet/earthfact.html> - Date accessed - December 2013

HST critical ratio, the largest critical specific impulse ratio should be used to determine when the HST outperforms all compared transfers. When comparing the same transfer but with different plane change methods, i.e. high or low-thrust, then if the specific impulse ratio achievable by the propulsion system is above the red line, a low-thrust plane change method should be used. Conversely, if the specific impulse ratio achievable by the propulsion system is below the red line, a high-thrust plane change method should be used. In Figure 6-1 the solid black line represents the specific impulse ratio achievable by the propulsion system for this specific case study and as such the entire region above this is unachievable and labelled the 'Forbidden Region'. The region to the left of the ratio  $R2 = 44.48$ , below the black line and above the red line is where a HST with low-thrust plane change should be used. Conversely, the region to the right of the ratio  $R2 = 44.48$ , below the red and black lines and above the orange solid line is where a HST with high-thrust plane change should be used. The largest difference between the system specific impulse ratio line and the critical specific impulse ratio will give the greatest fuel mass saving with respect to the compared transfer.

It is evident, based on information in the previous paragraph, only the critical specific impulse ratios comparing the Hohmann and HST transfers can be considered. Figure 6-2 therefore only shows the critical specific impulse ratios comparing the Hohmann and HST transfers.

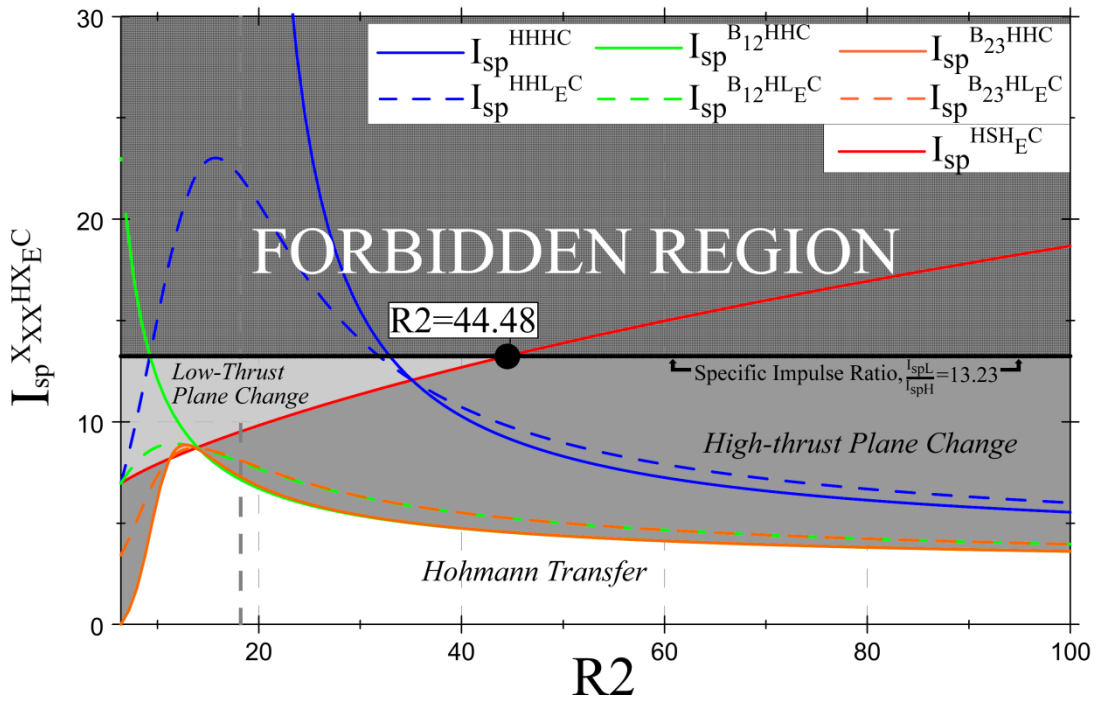


Figure 6-1 Critical specific impulse ratio comparison

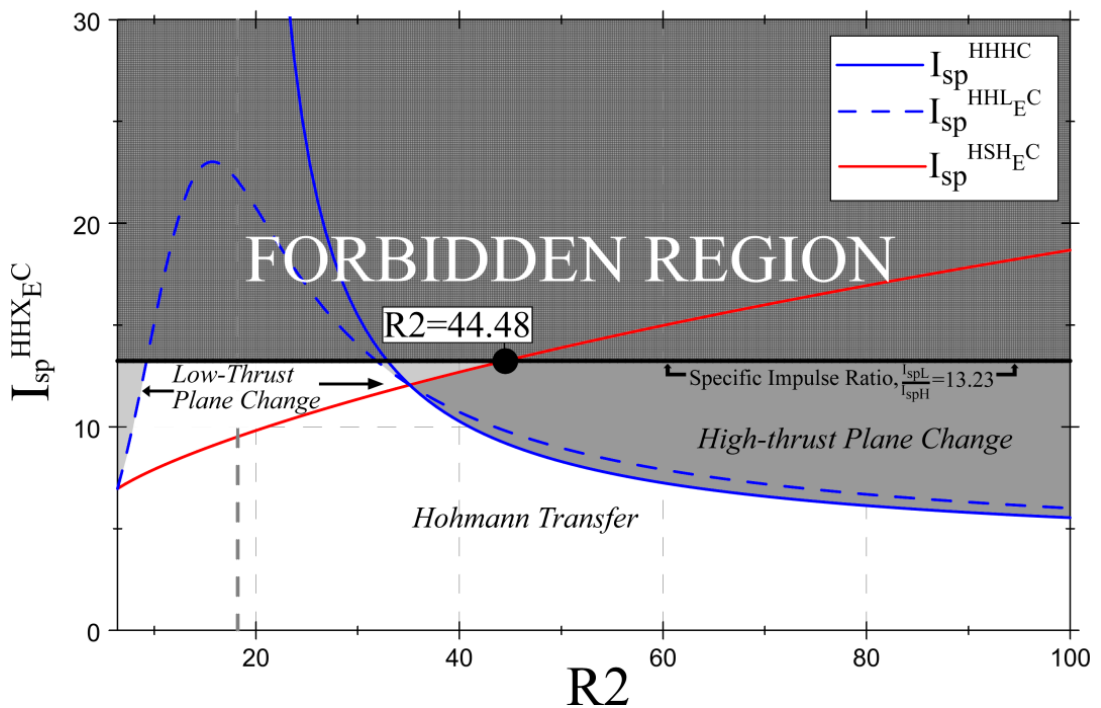


Figure 6-2 Hohmann and HST only critical specific impulse ratio comparison

It is now necessary to determine the maximum achievable  $R2$ , taking into account the analytical limit analysis detailed in Section 4.8. To do this, it is necessary to consider the spacecraft acceleration after the high-thrust phase of the HST so that a comparison can be

made to Figure 4-38 to determine the maximum achievable  $R2$  which satisfies either a 5% or 10% error in the final orbit radius. For this case study, only the 10% error will be considered. For the case where the spacecraft performs the plane change in the low-thrust phase of the transfer using Edelbaum's method, only the acceleration of the spacecraft in the Transverse direction is necessary to determine the critical  $R2$  limit. This is calculated using the thrust angle at the beginning of the low-thrust phase,  $\beta_0$ , as given in Eq (4.47), for a range of  $R2$  values. Figure 6-3 shows a range of spacecraft accelerations for both a high and low-thrust plane change and the critical  $R2$  ratio. The critical ratio, satisfying the 10% final radius error for the specified wet mass and spacecraft thrust is represented as the grey dot and is located where the lines intersect. A summary of the maximum achievable  $R2$  for each case is given in Table 6-2, along with the transfer times for the HST to achieve the target orbit with the specified  $R2$ . The transfer times are calculated using Eq. (4.73) and Eq. (4.77) for the high and low-thrust plane change methods respectively. Where no critical ratio is given, then the spacecraft acceleration is greater than that specified in the limit analysis. In this study, this is the case for the high-thrust plane change case with 2000 kg wet mass and 290 mN thrust. This means the critical  $R2$  for this transfer will be far less than  $R2 = 44.48$  shown in Figure 6-2: the ratio that has to be exceeded for the HST with high-thrust plane change to become more effective than the HST with low-thrust plane change. As such, no further analysis of this system is required. For clarification, any  $R2 < 44.48$  means a low-thrust plane change should be used and for any  $R2 > 44.48$ , a high-thrust plane change should be used. If  $R2 = 44.48$  then a HST with high-thrust plane change will offer the same fuel mass saving as a HST with low-thrust plane change; compared with a Hohmann transfer.

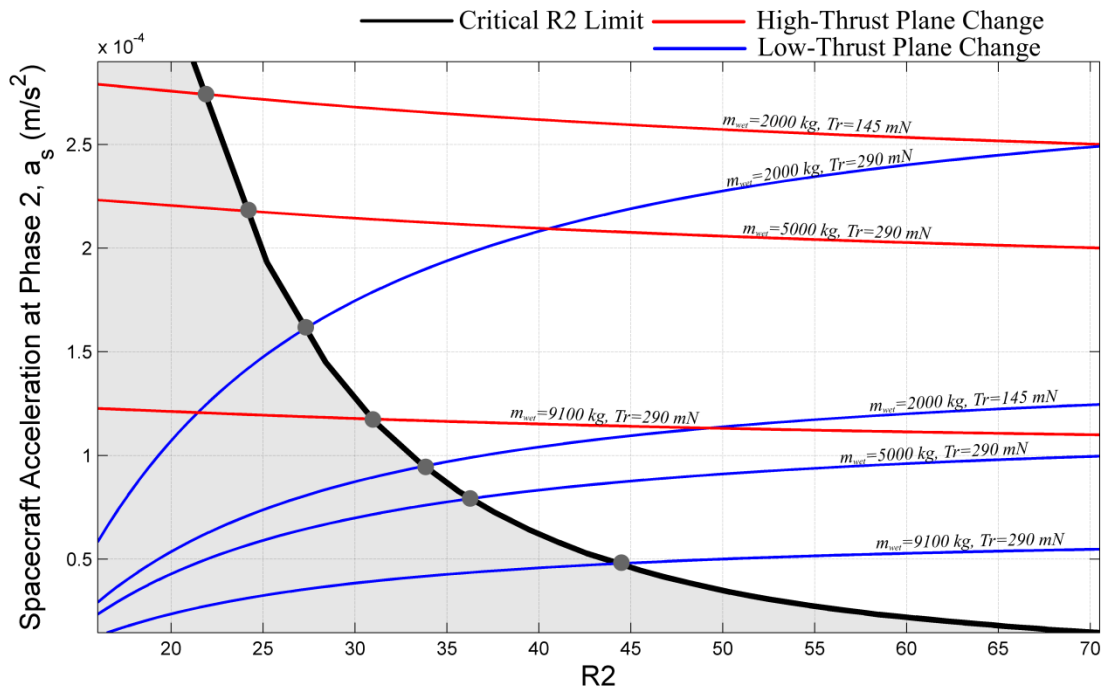


Figure 6-3 Critical  $R2$  limit for varying spacecraft accelerations at the beginning of phase 2

Table 6-2 Critical  $R2$  and transfer time for specified wet mass and thrust

Wet Mass, $m_{wet}$ (kg)	2000	2000	5000	9100	
Thrust, $Tr$ (mN)	145	290	290	290	
Critical $R2$	HT Plane Change	21.85	-	24.18	30.96
	LT Plane Change	33.77	27.32	36.31	44.36
Transfer Time, $t_{HSTC}$ (days)	HT Plane Change	60.78	-	80.7	167.15
	LT Plane Change	105.23	51.42	132.8	248.82

By comparing the remaining critical  $R2$  values in Table 6-2 with high-thrust plane change only, it is evident none of the critical  $R2$  values are greater than 44.48 meaning the HST with a high-thrust plane change should not be used as the HST with low-thrust plane change will be more efficient.

Considering Figure 6-2 and the  $I_{sp}^{HHL_{EC}}$  ratio (HST with low-thrust plane change and Hohmann transfer critical specific impulse ratio), and taking into account the critical  $R2$ , it is

evident that the largest fuel mass saving will occur at  $R2 = R1 = 6.41$ . If the critical  $R2$  was not imposed it can be seen that the fuel mass saving could be increased by transferring to an orbit ratio of approximately  $R2 \geq 55$  and using the HST with high-thrust plane change, resulting in a standard HST. To highlight the benefit of this, the advantage of performing a standard HST will also be shown in addition to the analysis performed in adherence with the critical orbit ratio.

By obeying the critical ratio and using  $R2 = R1 = 6.41$ , the high-thrust system is used to propel the spacecraft from the initial to target orbit before activating the low-thrust engine to complete the transfer. As the low-thrust section adopts Edelbaum's methodology, and this has the capacity to enlarge and shrink the orbit as part of an enhanced HST, it is necessary to follow the analysis procedure detailed in Section 4.5.2.1.1 to determine the characteristics of the low-thrust phase. It is worth noting that as the orbit ratio,  $R2 = R1$  for this case study, which is nowhere near any of the low-thrust plane change critical  $R2$  orbit ratios identified in Figure 6-3, the error associated with the final orbit eccentricity will be minimal. It should also be recognised that only the transfer time is affected with the varying initial wet masses and thrust values used meaning the orbital parameters' histories calculated here are valid for all cases considered. Firstly, it is necessary to determine if  $R2 = 6.41$  is the largest orbit ratio achieved throughout the duration of the transfer. To do this it is necessary to calculate the value of  $R2$  at which the initial thrust angle  $\beta_0 = 90^\circ$  as this suggests that at this orbit ratio, and any greater, the spacecraft will only shrink the orbit as opposed to expanding and then shrinking it. If  $\beta_0 = 90^\circ$  at  $R2 = 6.41$ , then the low-thrust system must perform a plane change only manoeuvre at  $R2 = 6.41$  with no increase or decrease in the orbit ratio. The orbit ratio  $R2$  at which the spacecraft will only shrink the orbit is calculated using Eq. (4.48) and is found to be  $R2_{max} = 12.73$  which suggests for this case study that the low-thrust system must expand and contract the orbit while performing the plane change. As such, it is then necessary to determine the largest orbit ratio experienced throughout this case study

transfer and ensure that this does not exceed the critical orbit ratio. It is found  $R3_{max} = 7.5$  using Eq. (4.53) which confirms the maximum orbit ratio is well below the critical orbit ratios shown in Table 6-2. It is then possible to show the variation of orbital parameters with time using the equations defined in Section 4.5.2.1.1. As all transfers follow the same trajectory, only the plots for  $m_{wet} = 5000$  kg are shown; however, the transfer time shown is only relevant for this specific example. The plot of the orbital radius is given in Figure 6-4 where it can be seen the maximum orbit ratio,  $R3_{max} = 7.5$ , is also labelled. The maximum orbit ratio occurs at  $t_{HSTL} = 68.02$  days which is exactly half the total transfer time for the low thrust phase (136.04 days). It should be noted that the plots shown only consider the low-thrust phase transfer time. If the total HST transfer time is required then the reader is directed back to Table 6-2. The variation of the thrust angle over the duration of the low-thrust phase is given in Figure 6-5. It is observed that  $R3_{max}$  occurs at a thrust angle of  $\beta = 90^\circ$  as expected. The plane change variation over time is given in Figure 6-6 where again  $R3_{max}$  is labelled to highlight the maximum orbit ratio location. It is found that at this point  $\Delta i = 7.08^\circ$  meaning the majority of plane change is performed in the second half of the low-thrust phase.

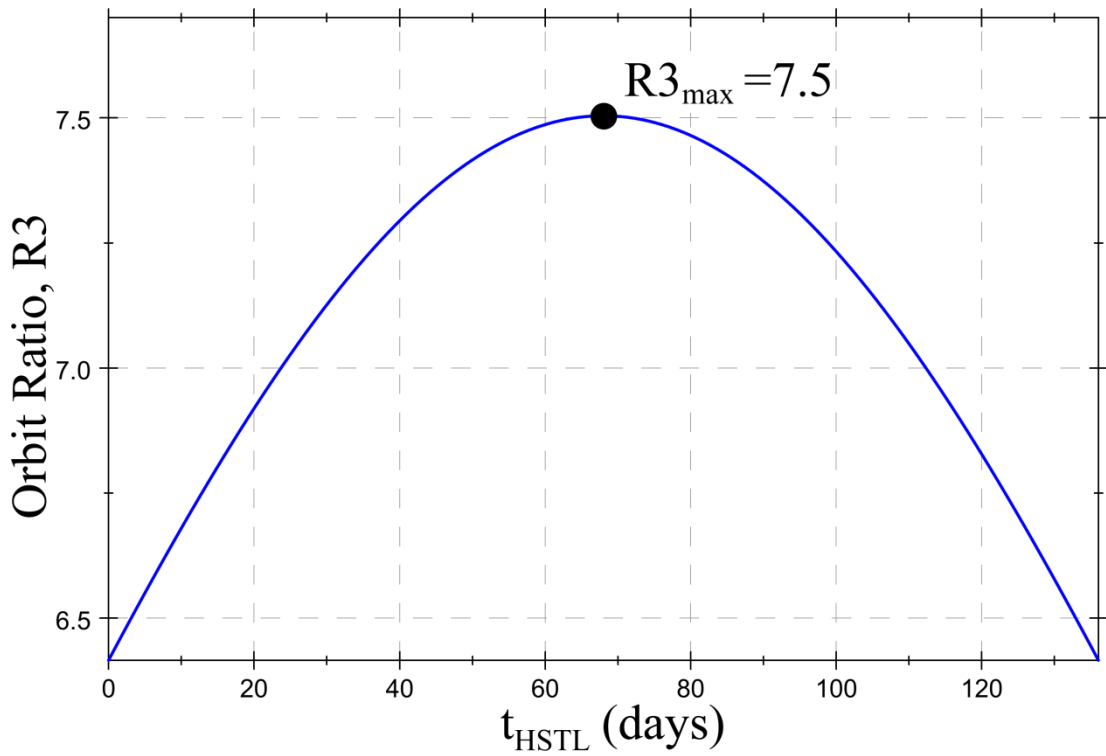


Figure 6-4 Orbit ratio,  $R3$ , variation over low-thrust phase for wet mass of 5000 kg

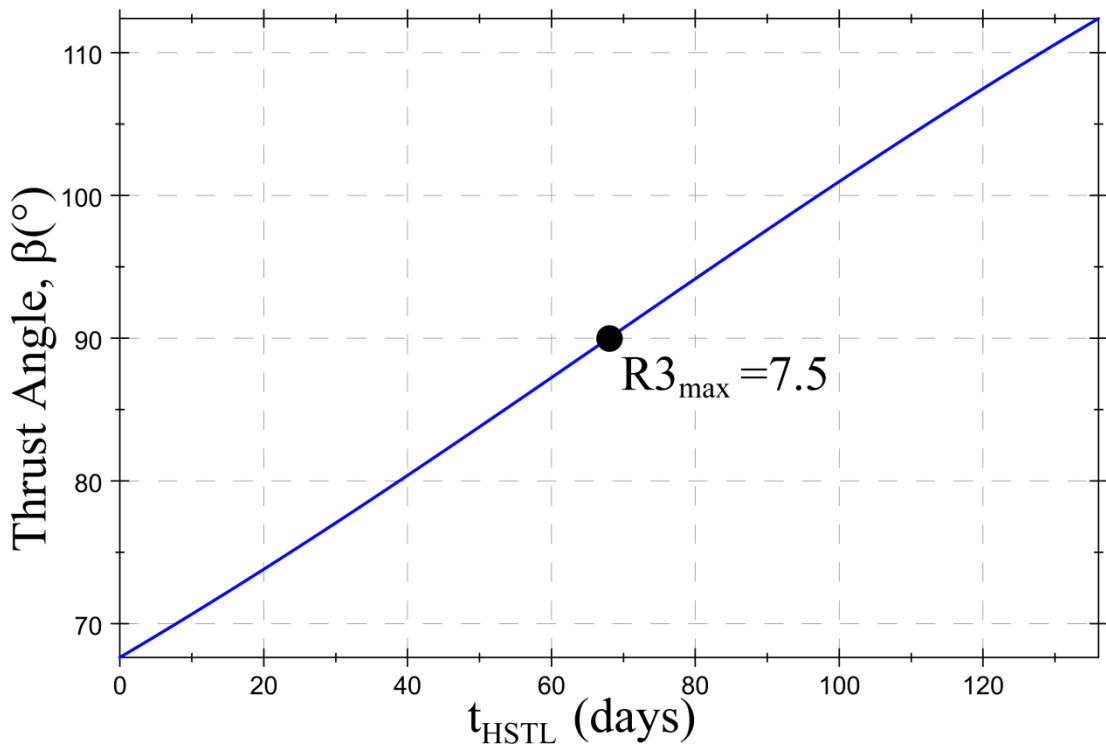
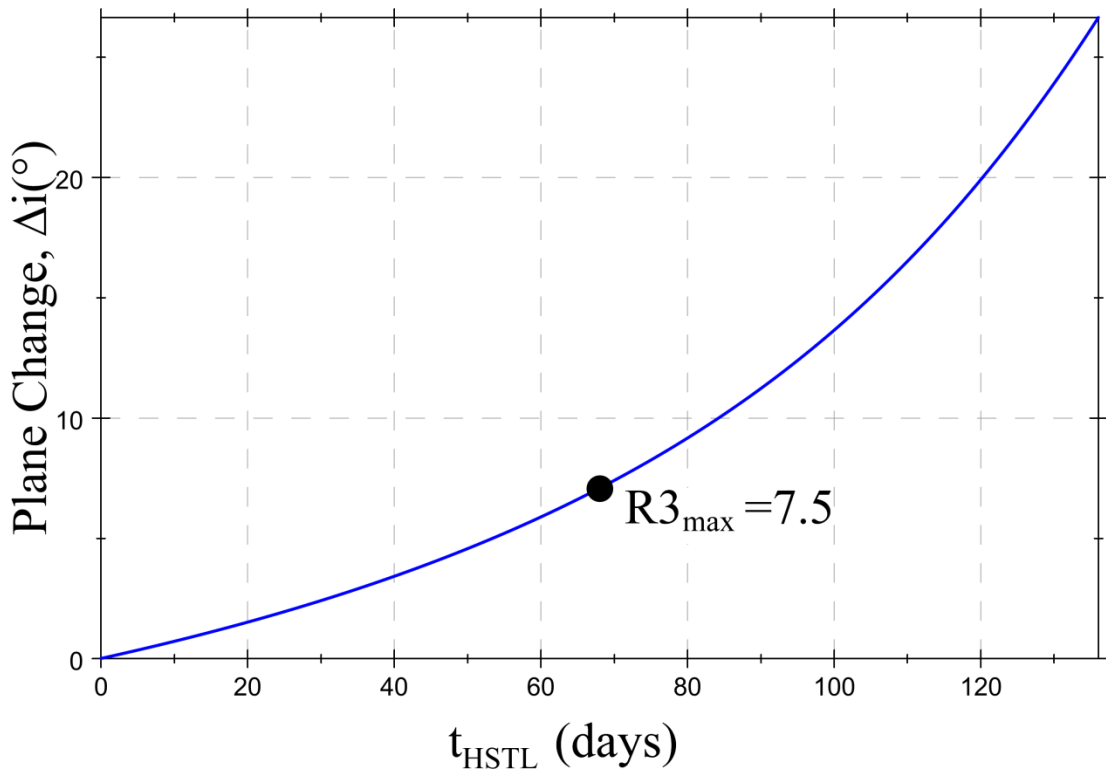


Figure 6-5 Thrust angle,  $\beta$ , variation over low-thrust phase for wet mass of 5000 kg



**Figure 6-6 Plane change,  $\Delta i$ , variation over low-thrust phase for wet mass of 5000 kg**

The total fuel mass of the HST can then be determined using Eq. (4.2) with Eq. (4.38) and (2.10) representing the velocity requirement of the HST's high and low-thrust phases respectively. To calculate the fuel mass saving achieved by using the HST, its fuel mass can be compared with the Hohmann fuel mass which is calculated using Eq. (4.1) with Eq. (4.18) representing the velocity requirement of the transfer. Table 6-3 provides a summary of each wet mass considered; providing the HST fuel mass, the fuel mass saving compared to the Hohmann transfer, the subsequent dry mass and the transfer time.

Table 6-3 HST performance for different wet masses

Wet Mass, $m_{wet}$ (kg)/ Thrust (mN)	2000/(145)	2000/(290)	5000/(290)	9100/(290)
Fuel Mass, $m_{HSTF}$ (kg)	1449.18	1449.18	3622.96	6593.78
Fuel Mass Saving w.r.t. Hohmann (kg/ % of $m_{wet}$ )	26.9/1.34	26.9/1.34	67.24/1.34	122.37/1.34
Dry Mass, $m_{dry}$ (kg)	550.82	550.82	1377.04	2506.22
Total Transfer Time, $t_{HSTC}$ (days)	109.05	54.64	136.26	247.82

If there is a time restriction imposed on the transfer then this can be included in the analysis in order to determine the accompanying maximum wet mass. The maximum wet mass is determined by re-arranging the HST transfer time defined in Eq. (4.77) to give

$$m_{wetMAX} = \frac{Tr \left[ t_{HSTC} - \frac{\pi}{\sqrt{\mu}} \sqrt{\left[ \frac{r_t}{2R_1} (1+R_2) \right]^3} \right]}{\sqrt{\frac{\mu}{r_t}} \sqrt{1 + \frac{R_1}{R_2} - 2\sqrt{\frac{R_1}{R_2}} \cos\left(\frac{\pi\Delta l}{2}\right)} e^{-\frac{\pi}{\sqrt{r_t}} \sqrt{R_1} \left[ \sqrt{\frac{2R_2}{1+R_2} + \sqrt{\frac{1}{R_2} - \sqrt{\frac{2}{R_2(1+R_2)}} - 1}} \right]} gI_{spH}} \quad (6.1)$$

where  $t_{HSTC}$  will be the maximum allowable transfer time. Figure 6-7 shows a plot of the maximum wet mass against specified transfer time, detailing  $m_{wetMAX}$  for a transfer time of 90 days, 120 days and 150 days.

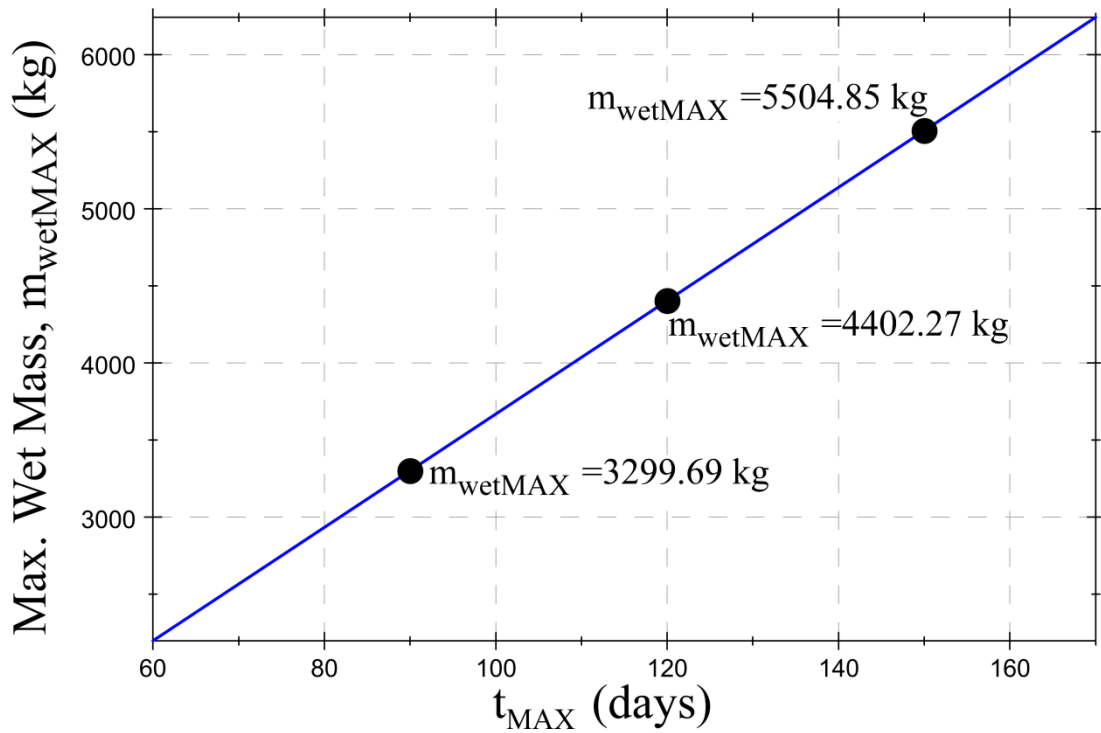


Figure 6-7 Maximum allowable wet mass for specified transfer time

A summary of the HST performance for the chosen maximum allowable wet masses is provided in Table 6-4. As before, the fuel mass saving as a percentage of the initial wet mass is 1.34% for each case. The table also shows the total transfer time if only a low-thrust transfer using Edelbaum's method from the initial to target orbit is used to achieve the calculated dry mass using the HST. The resultant transfer time saving using the HST is also shown.

Table 6-4 HST performance for maximum allowable wet masses

Specified Transfer Time, $t_{HSTC}$ (days)	90	120	150
Wet Mass, $m_{wet}$ (kg)/ Thrust (mN)	3299.69/(290)	4402.27/(290)	5504.85/(290)
Fuel Mass, $m_{HSTF}$ (kg)	2390.93	3189.85	3988.76
Fuel Mass Saving w.r.t. Hohmann (kg/ % of $m_{wet}$ )	44.37/1.34	59.2/1.34	74.03/1.34
Dry Mass, $m_{dry}$ (kg)	908.76	1212.42	1516.09
Transfer Time of Low-Thrust Only (Edelbaum's Method) to Achieve Dry Mass (days)	251.28	335.25	419.22
Transfer Time Saving using HST compared to Low-Thrust Only (Edelbaum's Method) (days)	161.28	185.25	269.22

If the critical orbit ratio is removed and a normal HST is used then additional mass saving can be achieved while satisfying the same time restrictions as detailed in Table 6-4. The maximum  $R2$  achievable to suit the time restrictions of 90 days, 120 days and 150 days is calculated using Eq. (4.73) as it is noted in Figure 6-2 that the HST with high-thrust plane change will be the most efficient HST with  $R2 > 44.48$ . Equation (4.73) is set equal to each time restriction and solved for  $R2$  with

$$m_{wet} = \frac{m_{dry}}{\frac{-\Delta V_{HSTHC}}{e^{g_{spL}}} \frac{-\Delta V_{HSTL}}{e^{g_{spH}}}} \quad (6.2)$$

which is a form of Eq. (4.2) with  $m_{HSTF} = m_{wet} - m_{dry}$ . The velocity requirements of the HST's high and low-thrust phases are defined in Eq. (4.17) and Eq. (4.5) respectively. For each respective transfer time, the dry masses shown in Table 6-4 are used when solving for the maximum  $R2$ . Table 6-5 shows the results using the HST with high-thrust plane change; specifying the maximum achievable  $R2$  which satisfies the time constraint for each dry mass. The additional fuel mass saving compared with that found in Table 6-4 is also shown. The

fuel mass of the HST in this case has been calculated using Eq. (4.2) with Eq. (4.17) and Eq. (4.5) representing the high and low-thrust velocity requirement respectively.

**Table 6-5 HST performance for specified dry masses using HST with high-thrust plane change**

<b>Specified Transfer Time, <math>t_{HSTC}</math> (days)</b>	<b>90</b>	<b>120</b>	<b>150</b>
<b>Maximum Achievable Orbit Ratio, <math>R_2</math></b>	74.31	79.38	83.15
<b>Dry Mass, <math>m_{dry}</math> (kg)</b>	908.76	1212.42	1516.09
<b>Wet Mass, <math>m_{wet}</math> (kg)</b>	3283.04	4360.26	5435
<b>Fuel Mass, <math>m_{HSTF}</math> (kg)</b>	2374.28	3147.84	3919
<b>Fuel Mass Saving w.r.t. Hohmann (kg/ % of <math>m_{wet}</math>)</b>	47.68/1.45	68.69/1.58	90.34/1.66
<b>Additional Fuel Mass Saving compared to Table 6-4 (kg)</b>	3.31	9.49	16.31

### 6.1.2. GTO – GEO

As the previous study focused on a circular initial orbit, or rather a LEO – GEO transfer, it is necessary to perform a comparison of the HST and high-thrust only transfers with an elliptical initial orbit, or rather a study from GTO – GEO as this is also a very common transfer used for GEO bound spacecraft.

As the results are similar to the circular initial orbit, this case study will not re-consider all the graphs previously shown, instead it will comment on relevant differences between the two. This case study considers the Xichang launch centre in China again with the same spacecraft configuration as detailed in Table 6-1. The initial wet masses are different however as the capability of the different launchers available at Xichang reduces the maximum mass to GTO. The new wet masses to be considered are 2600 kg for the LM3A launch vehicle, 5500 kg for the LM3BE launch vehicle and 3800 kg for the LM3C launch

vehicle [126, Ch. 3]. These are the maximum achievable wet masses for each launch vehicle. As before, only the HST and Hohmann transfer critical specific impulse ratio can be considered as the Hohmann outperforms both variations of the bi-elliptic and hence the HST must outperform this to ensure it is the most fuel efficient transfer. The critical ratio characteristics are very similar to the LEO – GEO transfer and are shown in Figure 6-8. In Figure 6-8, the orbit ratio  $R2 = 44.92$  defines the point at which a larger ratio would mean the HST with high-thrust plane change is more efficient and conversely a lower ratio is where the HST with low-thrust plane change is more efficient. As before, the areas where this holds true are identified. The specific impulse ratio of the spacecraft configuration ( $I_{spL}/I_{spH} = 13.23$ ) is again shown as the solid black line and above this is the forbidden region as the spacecraft cannot achieve a specific impulse ratio in this region.

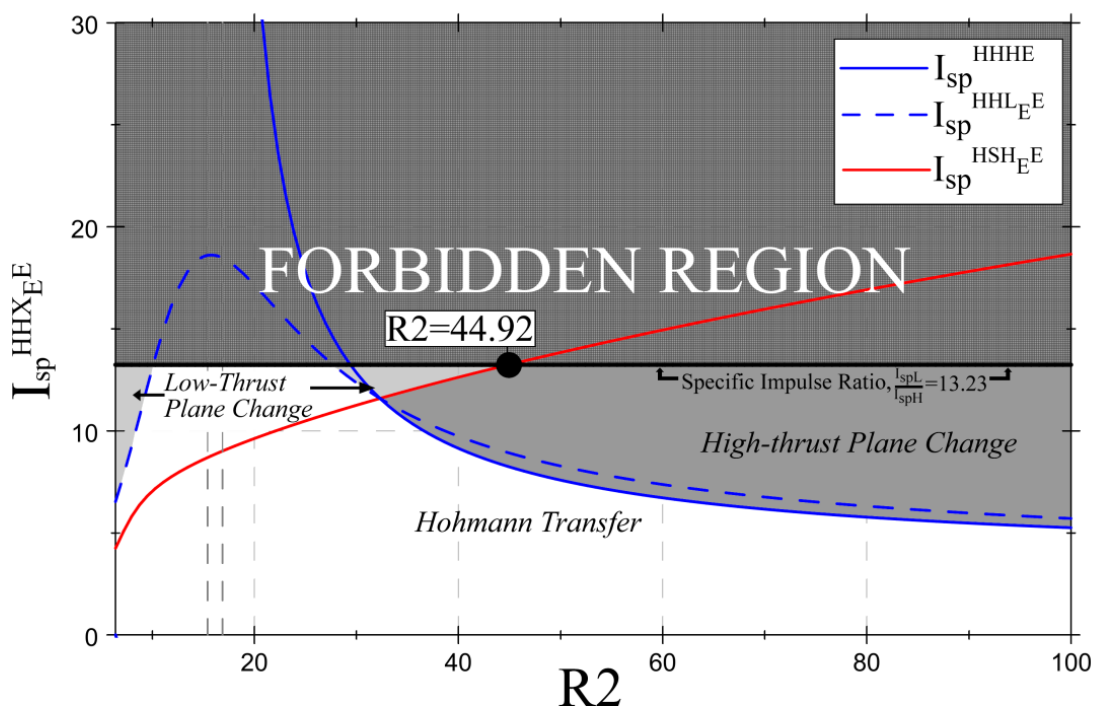


Figure 6-8 Hohmann and HST only critical specific impulse ratio comparison

As was the case for the LEO – GEO transfer, it is necessary to determine the critical  $R2$  orbit ratio. The graph for this case study will not be shown as it follows the same process as that shown in Figure 6-3. The critical orbit ratios however, along with the HST transfer times, are

given in Table 6-6. The HST with high and low-thrust plane change transfer times are calculated using Eqs. (4.74) and (4.78) respectively. The critical ratios for the 2600 kg and 3800 kg wet masses with high-thrust plane change are not given as they are out with the acceleration range used for the study. As the critical  $R2$  will be far less than 44.92, which is the ratio to be exceeded before the HST with high-thrust plane change outperforms the HST with low-thrust plane change, these cases can be discounted and no further analysis is required.

**Table 6-6 Critical  $R2$  and transfer time for specified wet mass and thrust**

<b>Wet Mass, <math>m_{wet}</math> (kg)</b>	<b>2600</b>	<b>2600</b>	<b>3800</b>	<b>5500</b>	
<b>Thrust, <math>Tr</math> (mN)</b>	145	290	290	290	
<b>Critical <math>R2</math></b>	<b>HT Plane Change</b>	33.83	-	-	34.64
	<b>LT Plane Change</b>	47.58	37.73	42.79	48.5
<b>Transfer Time, <math>t_{HSTE}</math> (days)</b>	<b>HT Plane Change</b>	165.92	-	-	378.79
	<b>LT Plane Change</b>	239.69	115.99	292.79	542.51

Comparing the remaining critical  $R2$  ratios given in Table 6-6 for the HST with high-thrust plane change, it is found that none of them exceed the orbit ratio  $R2 = 44.92$  shown in Figure 6-8. As was the case in the LEO – GEO transfer, this means that the HST with low-thrust plane change is the only system that should be considered as it is most efficient. By comparing the difference between the system ratio ( $I_{spL}/I_{spH} = 13.23$ ) and the critical specific impulse ratio for the HST with low-thrust plane change at the different critical  $R2$  orbit ratios, it is clear for all mass and thrust variations that the difference is largest at  $R2 = R1 = 6.41$ . As such, the low-thrust phase trajectory will be the same as the LEO – GEO transfer with only the transfer times varying. The orbit ratio ( $R3$ ), thrust angle ( $\beta$ ) and plane change ( $\Delta i$ ) histories are therefore defined in Figure 6-4, Figure 6-5 and Figure 6-6

respectively. A summary of the transfer for the given wet masses and thrust is provided in Table 6-7.

Table 6-7 HST performance for different wet masses

Wet Mass, $m_{wet}$ (kg)/ Thrust (mN)	2600/(145)	2600/(290)	3800/(290)	5500/(290)
Fuel Mass, $m_{HSTF}$ (kg)	1052.79	1052.79	1538.7	2227.06
Fuel Mass Saving w.r.t. Hohmann (kg/ % of $m_{wet}$ )	85.84/3.3	85.84/3.3	125.45/3.3	181.58/3.3
Dry Mass, $m_{dry}$ (kg)	1547.21	1547.21	2261.3	3272.94
Total Transfer Time, $t_{HSTE}$ (days)	305.93	153.07	223.62	323.57

It is worth noting that the fuel mass saving for the GTO – GEO transfer has increased to 3.3% of  $m_{wet}$  from 1.34% of  $m_{wet}$  for the LEO-GEO transfer. The elliptical initial orbit for this case offers a substantial fuel mass saving compared to the circular initial orbit which is a direct result of the reduced velocity requirement for the high-thrust phase of the HST. By comparing these results with the LEO – GEO results shown in Table 6-3, it can be seen that the 2600 kg wet mass delivers a dry mass greater than that of the 5000 kg wet mass in the LEO – GEO case. Similarly, the 5500 kg wet mass delivers a larger dry mass than the 9100 kg wet mass in the LEO – GEO case. This can be attributed to the additional velocity requirement to account for the circular initial orbit. This does however have an adverse effect on the total transfer time of the elliptical case studies as can be seen by comparing Table 6-3 and Table 6-7. If a transfer time restriction is to be imposed on the GTO – GEO transfer, then the maximum achievable wet mass, which accommodates the time restriction, can be calculated by re-arranging Eq. (4.78) to give

$$m_{wetMAX} = \frac{Tr \left[ t_{HSTE} - \frac{\pi}{\sqrt{\mu}} \sqrt{\frac{r_t}{2R1} (1+R2)} \right]^3}{\sqrt{\frac{\mu}{r_t}} \sqrt{1 + \frac{R1}{R2} - 2 \sqrt{\frac{R1}{R2}} \cos\left(\frac{\pi \Delta I}{2}\right)} e^{-\frac{\mu}{r_t} \sqrt{\frac{R1}{R2}} \left[ \sqrt{R2} \left( \sqrt{\frac{2R2}{1+R2}} \sqrt{\frac{2R1}{1+R1}} - \sqrt{\frac{2}{1+R2+1}} \right) \right]} g^{I_{sp}H}} \quad (6.3)$$

where  $t_{HSTE}$  will be the maximum allowable transfer time. Similar to the LEO-GEO case study, three transfer times of 90 days, 120 days and 150 days are used to determine the maximum achievable wet mass. A summary of the HST performance for the specified time restrictions is provided in Table 6-8 where it can be seen the fuel mass saving, as a percentage of the initial wet mass, is 3.3% for each case. It should be noted that no comparison to Edelbaum's low-thrust only transfer is made here as it is only valid for circular to circular transfers and hence cannot be used for an initial GTO.

**Table 6-8 HST performance for maximum allowable wet masses**

<b>Specified Transfer Time, <math>t_{HSTE}</math> (days)</b>	<b>90</b>	<b>120</b>	<b>150</b>
<b>Wet Mass, <math>m_{wet}</math> (kg)/ Thrust (mN)</b>	1527.13/(290)	2037.42/(290)	2547.7/(290)
<b>Fuel Mass, <math>m_{HSTF}</math> (kg)</b>	618.37	824.99	1031.62
<b>Fuel Mass Saving w.r.t. Hohmann (kg/ % of <math>m_{wet}</math>)</b>	50.42/3.3	67.26/3.3	84.11/3.3
<b>Dry Mass, <math>m_{dry}</math> (kg)</b>	908.76	1212.42	1516.09

Similar to the LEO – GEO transfer, if the critical orbit ratio is ignored then additional fuel mass savings can be identified by utilising the HST with high-thrust plane change and a large  $R2$  for a given dry mass and transfer time. Table 6-9 shows the results of using this transfer where it is noted the maximum achievable  $R2$  is the same as that for the LEO – GEO transfer. In this case it is calculated using Eq. (4.74) in a similar fashion to that in the LEO – GEO transfer with Eq. (6.2) used to represent  $m_{wet}$  and Eq. (4.25) used to represent the high-thrust phase velocity requirement for an elliptical initial orbit. The fuel mass of the HST is calculated using Eq. (4.2) where Eqs. (4.25) and (4.5) represent the high and low-thrust

velocity requirement equations respectively. Table 6-9 shows the fuel mass saving compared to the Hohmann as well as the additional fuel mass saving possible in comparison to that identified in Table 6-8.

**Table 6-9 HST performance for specified dry masses using HST with high-thrust plane change**

<b>Specified Transfer Time, <math>t_{HSTE}</math> (days)</b>	<b>90</b>	<b>120</b>	<b>150</b>
<b>Maximum Achievable Orbit Ratio, <math>R2</math></b>	74.31	79.38	83.15
<b>Dry Mass, <math>m_{dry}</math> (kg)</b>	908.76	1212.42	1516.09
<b>Wet Mass, <math>m_{wet}</math> (kg)</b>	1520.2	2019.08	2516.85
<b>Fuel Mass, <math>m_{HSTF}</math> (kg)</b>	611.44	806.66	1000.76
<b>Fuel Mass Saving w.r.t. Hohmann (kg/ % of <math>m_{wet}</math>)</b>	53.7/3.54	76.68/3.8	100.3/3.99
<b>Additional Fuel Mass Saving compared to Table 6-8 (kg)</b>	3.28	9.42	16.19

### 6.1.3. Analytical Study Comparison

Analytical case studies have highlighted the mass saving possible using the HST instead of a conventional high-thrust only transfer. The case studies have demonstrated fuel mass savings are possible, 1.34% of  $m_{wet}$  for a LEO – GEO transfer and 3.3% of  $m_{wet}$  for a GTO – GEO, launching from the Xichang launch site in China with a relative plane change of  $\Delta I = 28.5^\circ$  and adhering to critical orbit ratio constraints. Without the critical orbit ratio limit, it can be shown that the HST can offer additional fuel mass savings by transferring to an even larger orbit ratio,  $R2$ , and using the high-thrust system to perform the plane change. The low-thrust system in this case is simply used to spiral back towards the target. The increase in fuel mass saving when using the GTO initial orbit can be attributed to the additional velocity requirement in the high-thrust phase to account for a circular initial orbit in the LEO case. The fuel mass savings identified in both cases are substantial enough to allow an additional

payload on the platform or perhaps extend the life of the platform by carrying additional fuel for on orbit manoeuvres. The case studies have demonstrated the use of the analytical equations derived in Chapter 4 for an applied mission analysis problem and it has been shown that the analytical analysis has the flexibility to accommodate differing mission priorities e.g. transfer time or wet mass. Additionally, the HST has been shown to offer a large reduction in transfer time compared to a low-thrust only transfer. Due to the transfer duration restrictions that are sometimes specified for satellite transfers, specifically GEO bound platforms, the HST offers a suitable alternative which can provide a substantial fuel mass saving at an acceptable transfer time. Although the transfer time is far greater than the high-thrust transfer alone, it is possible that the in-orbit commissioning could be performed while the HST is underway, allowing the spacecraft to arrive at the orbit ready for operation.

## 6.2. Numerical Optimisation

### 6.2.1. LEO/GTO – GEO

Using the analytical analysis determined there is an advantage using the HST over conventional transfer methods. It also identified additional fuel mass savings could be achieved if the critical  $R2$  orbit ratio accounting for orbit eccentricity was removed. It is therefore necessary to study the HST using a full numerical method, allowing the analytical constraints to be removed, to determine if there are further fuel mass savings possible. This case study will therefore consider the transfer to GEO from both LEO and GTO initial orbits: allowing a comparison to the analytical studies carried out in Section 6.1, so that the removal of the analytical constraints can be quantitatively measured. The transfer and spacecraft specification are therefore defined again in Table 6-1. The specific wet masses and maximum allowable transfer times to be considered for both the LEO and GTO initial orbits are defined in Table 6-10 and are based on the results from the analytical case studies. The numerical case study will therefore use these in order to determine if there is any further

improvement on the analytical results. It is noted that all cases considered here use two T6 thrusters in dual configuration.

**Table 6-10 Numerical study parameters**

LEO - GEO			GTO - GEO		
Wet Mass, $m_{wet}$ (kg)	Dry Mass, $m_{dry}$ (kg)	Transfer Time, $t_{HSTC}$ (days)	Wet Mass, $m_{wet}$ (kg)	Dry Mass, $m_{dry}$ (kg)	Transfer Time, $t_{HSTE}$ (days)
2000	550.82	54.64	2600	1547.21	153.07
5000	1377.04	136.26	3800	2261.3	223.62
9100	2506.22	247.82	5500	3272.94	323.27
3299.69	908.76	90	1527.13	908.76	90
4402.27	1212.42	120	2037.42	1212.42	120
5504.85	1516.09	150	2547.7	1516.09	150

The tolerances used in the optimisation procedure apply to the objective, function and constraint parameters. The objective tolerance is used as a lower bound on the optimisation step size. The function tolerance is a lower bound on the change in the objective function. The constraint function is an upper bound and measures the magnitude of the constraint violation. A tolerance of  $1 \times 10^{-9}$  was used for each parameter unless otherwise stated. The optimisation stops if the objective or function tolerances alone are satisfied, however it will not stop if the constraint function only is satisfied. The possibility then arises that the optimisation will halt without the constraint function being satisfied which was found to be the case for the majority of cases bar two using a tolerance of  $1 \times 10^{-5}$ . A tolerance of  $1 \times 10^{-9}$  was introduced to rectify this, ensuring all cases satisfied the constraint tolerance. For the GTO – GEO cases with wet masses of 2600 kg and 5500 kg, the constraint tolerance of  $1 \times 10^{-5}$  was satisfied with the results providing a larger fuel mass saving than what was

found using the tolerance of  $1 \times 10^{-9}$ . As such, it is this result which is used within this study. In contrast to the analytical study, it was found that the HST with high-thrust plane change offered a larger fuel mass saving than the HST with low-thrust plane change. Table 6-11 - Table 6-13 detail the results of each numerical study, comparing it with the HST with low-thrust plane change and the analytical results. Details of some of the orbit characteristics are also provided.

**Table 6-11 2000 kg wet mass specified LEO – GEO comparison. A – Analytical, HTPC – High-Thrust Plane Change, LTPC – Low-Thrust Plane Change**

<b>Wet Mass, <math>m_{wet}</math> (kg)</b>	<b>2000</b>		
	<b>A</b>	<b>HTPC</b>	<b>LTPC</b>
<b>Transfer</b>			
HST Dry Mass (kg)	550.82	684.10	594.94
HST Transfer Time (days)	54.64	54.63	54.58
Hohmann Dry Mass (kg)	523.92	523.67	523.67
HST Fuel Mass (kg)	1449.18	1315.90	1405.06
<i>R2</i>	6.41	8.48	12.13
Intermediate Orbit Eccentricity	0	0.73	0.37
<b>Saving compared to Hohmann (kg)</b>	26.90	160.43	71.28
<b>Saving compared to Hohmann (% of <math>m_{wet}</math>)</b>	1.34	8.02	3.56

**Table 6-12 5000 kg wet mass specified LEO – GEO comparison. A – Analytical, HTPC – High-Thrust Plane Change, LTPC – Low-Thrust Plane Change**

Wet Mass, $m_{wet}$ (kg)	5000			
	Transfer	A	HTPC	LTPC
HST Dry Mass (kg)	1377.04	1715.92	1419.78	
HST Transfer Time (days)	136.26	136.25	135.82	
Hohmann Dry Mass (kg)	1309.81	1309.17	1309.17	
HST Fuel Mass (kg)	3622.96	3284.08	3580.22	
$R2$	6.41	8.27	10.81	
Intermediate Orbit Eccentricity	0	0.73	0.24	
<b>Saving compared to Hohmann (kg)</b>	67.24	406.76	110.62	
<b>Saving compared to Hohmann (% of <math>m_{wet}</math>)</b>	1.34	8.14	2.21	

**Table 6-13 9100 kg wet mass specified LEO – GEO comparison. A – Analytical, HTPC – High-Thrust Plane Change, LTPC – Low-Thrust Plane Change**

Wet Mass, $m_{wet}$ (kg)	9100			
	Transfer	A	HTPC	LTPC
HST Dry Mass (kg)	2506.22	3126.14	2642.39	
HST Transfer Time (days)	247.82	247.59	246.98	
Hohmann Dry Mass (kg)	2383.85	2382.68	2382.68	
HST Fuel Mass (kg)	6593.78	5973.86	6457.61	
$R2$	6.41	8.16	10.25	
Intermediate Orbit Eccentricity	0	0.73	0.28	
<b>Saving compared to Hohmann (kg)</b>	122.37	743.46	259.71	
<b>Saving compared to Hohmann (% of <math>m_{wet}</math>)</b>	1.34	8.17	2.85	

It can be seen in Table 6-11 - Table 6-13 that both the HST with a high and low-thrust plane change outperforms the analytical analysis by a considerable margin. This can be attributed

to the removal of the analytical constraint, which ensures the intermediate orbit radius is circular, and the fact the thrust vector can now be controlled throughout the low-thrust phase. It can also be seen in the results that the HST with high-thrust plane change has a far larger intermediate orbit eccentricity than the HST with low-thrust plane change; suggesting it is much more sensitive to the intermediate orbit eccentricity assumption used throughout the analytical analysis than the HST with low-thrust plane change. Considering the fuel mass savings, it can be seen that the HST with low-thrust plane change offers approximately double the analytical HST with low-thrust plane change value while the HST with high-thrust plane change offers over six times the analytical fuel mass saving. Considering the HST with high-thrust plane change only as this is the best transfer, it is shown in Table 6-11 - Table 6-13 that it offers a fuel mass saving of 160.43 kg, 406.76 kg and 743 kg compared to the standard Hohmann transfer for the 2000 kg, 5000 kg and 9100 kg wet masses respectively. This translates as a saving of 8.02 %, 8.14 % and 8.17 % of each respective wet mass. The mass savings are approximately constant which was also found in the analytical HST with low-thrust plane change analysis. Considering the intermediate orbit characteristics which are also detailed in Table 6-11 - Table 6-13, there is a clear distinction between the high and low-thrust plane change variations of the HST. The HST with high-thrust plane change uses an eccentricity of 0.73 for all cases, which is the maximum value allowed to ensure the spacecraft does not collide with Earth. The HST with low-thrust plane change uses an orbit eccentricity of approximately 0.3 for all wet mass cases. Considering the intermediate orbit radius ratio,  $R2$ , the HST with high-thrust plane change uses  $R2 \approx 8$  for all wet mass cases while the HST with low-thrust plane change uses  $R2 \geq 10$  for all cases. The optimisation results for the wet mass cases related to the time specified transfers of 90 days, 120 days and 150 days all produce similar results to that shown in Table 6-11 - Table 6-13 and as such are provided in APPENDIX A. Figure 6-9, Figure 6-10 and Figure 6-11 show the variation in eccentricity, fuel mass saving and  $R2$  respectively for all the wet

masses considered. It is interesting to note that the intermediate orbit eccentricity seems to have a direct effect on the total fuel mass saving of the HST with both high and low-thrust plane changes. The HST with high-thrust plane change fuel mass saving is approximately constant for each case with the eccentricity also being constant. Similarly, the HST with low-thrust plane change fuel mass fluctuates with the orbit eccentricity, where generally the larger the eccentricity the larger the fuel mass saving. The question then arises as to why the eccentricity is not larger for the HST with low-thrust plane change? This can be directly attributed to the spacecraft acceleration distribution. As the thrust direction also has to account for the plane change, the acceleration available to control an eccentric orbit is reduced; therefore, limiting the maximum intermediate orbit eccentricity at the beginning of the low-thrust phase.

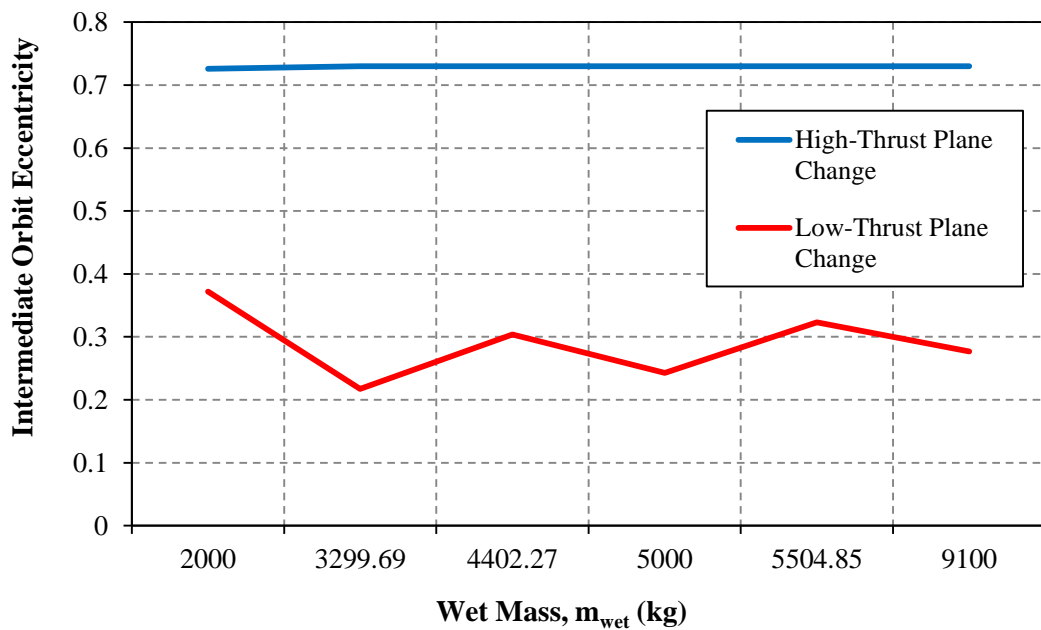


Figure 6-9 LEO – GEO, intermediate orbit eccentricity for wet masses specified in ascending order

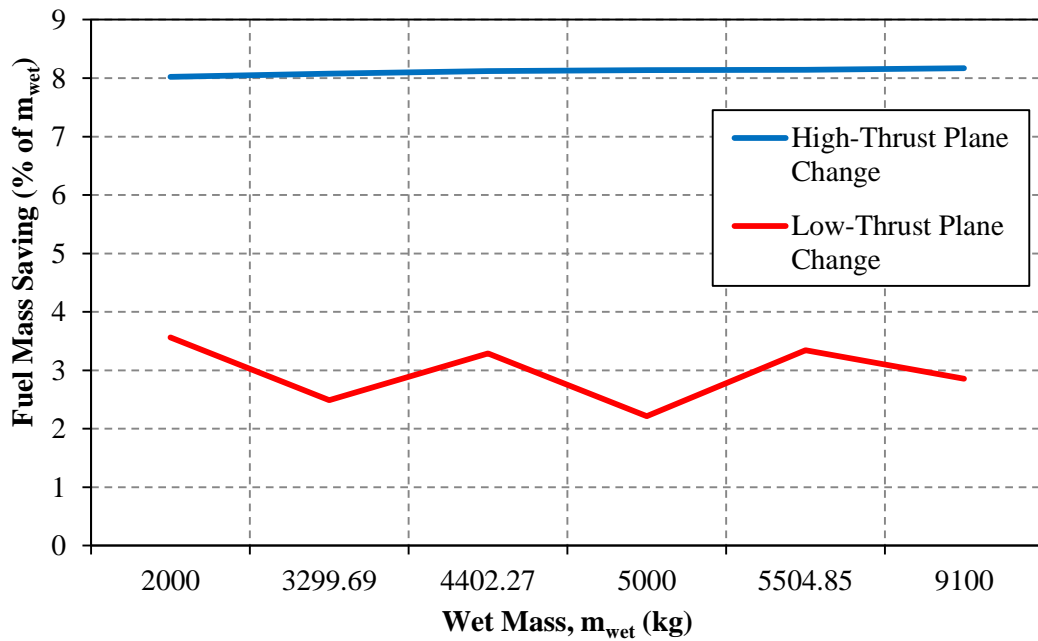


Figure 6-10 LEO – GEO, percentage fuel mass savings for wet masses specified in ascending order

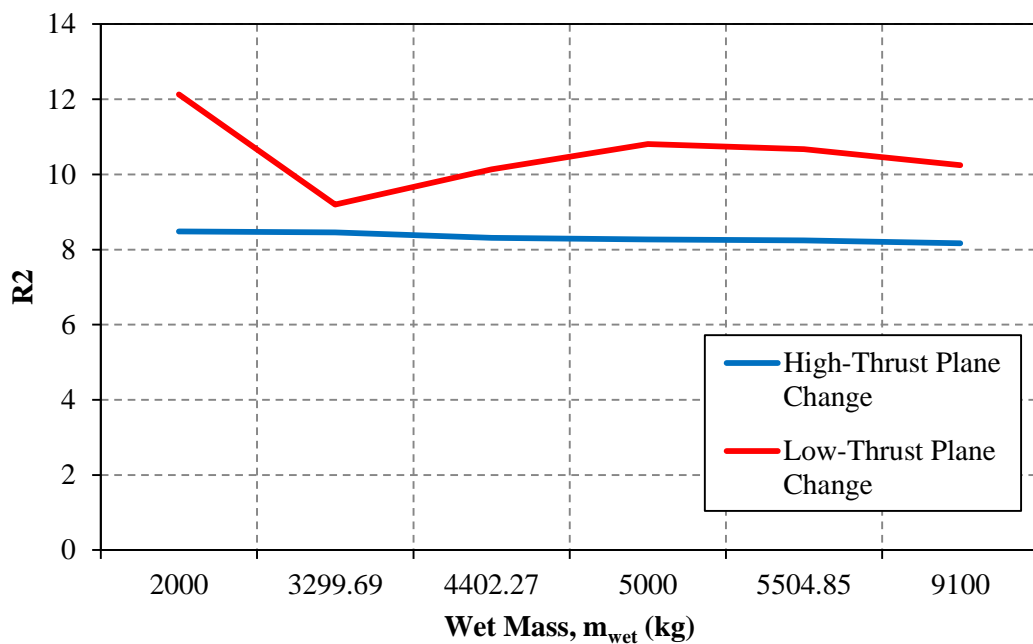


Figure 6-11 LEO – GEO, r2 for wet masses specified in ascending order

Considering the GTO-GEO transfer, the results for the specified wet mass cases are given in Table 6-14 - Table 6-16. As was the case for the LEO-GEO transfer, the HST with high-thrust plane change offers the largest fuel mass saving compared to the Hohmann transfer at approximately 17.5 % of  $m_{wet}$ . This equates to 454.94 kg, 665.63 kg and 965.48 kg for the

wet masses of 2600 kg, 3800 kg and 5500 kg. Considering the HST with low-thrust plane change, it can be seen that although it doesn't offer the same fuel mass saving as the HST with high-thrust plane change, there is a substantial increase compared to the analytical HST with low-thrust plane change.

**Table 6-14 2600 kg wet mass specified GTO – GEO Comparison. A – Analytical, HTPC – High-Thrust Plane Change, LTPC – Low-Thrust Plane Change**

<b>Wet Mass, <math>m_{wet}</math> (kg)</b>	<b>2600</b>		
	<b>A</b>	<b>HTPC</b>	<b>LTPC</b>
<b>Transfer</b>			
HST Dry Mass (kg)	1547.21	1915.42	1675.88
HST Transfer Time (days)	153.07	153.01	152.97
Hohmann Dry Mass (kg)	1461.37	1460.48	1460.48
HST Fuel Mass (kg)	1052.79	684.58	924.12
$R_2$	6.41	8.14	11.29
Intermediate Orbit Eccentricity	0	0.73	0.36
<b>Saving compared to Hohmann (kg)</b>	85.84	454.94	215.39
<b>Saving compared to Hohmann (% of <math>m_{wet}</math>)</b>	3.30	17.50	8.28

**Table 6-15 3800 kg wet mass specified GTO – GEO Comparison. A – Analytical, HTPC – High-Thrust Plane Change, LTPC – Low-Thrust Plane Change**

Wet Mass, $m_{wet}$ (kg)	3800		
Transfer	A	HTPC	LTPC
HST Dry Mass (kg)	2261.30	2800.17	2491.02
HST Transfer Time (days)	223.62	223.24	223.29
Hohmann Dry Mass (kg)	2135.85	2134.55	2134.55
HST Fuel Mass (kg)	1538.70	999.83	1308.98
$R2$	6.41	8.11	12.23
Intermediate Orbit Eccentricity	0	0.73	0.42
<b>Saving compared to Hohmann (kg)</b>	125.45	665.63	356.47
<b>Saving compared to Hohmann (% of <math>m_{wet}</math>)</b>	3.30	17.52	9.38

**Table 6-16 5500 kg wet mass specified GTO – GEO Comparison. A – Analytical, HTPC – High-Thrust Plane Change, LTPC – Low-Thrust Plane Change**

Wet Mass, $m_{wet}$ (kg)	5500		
Transfer	A	HTPC	LTPC
HST Dry Mass (kg)	3279.94	4054.96	3381.38
HST Transfer Time (days)	323.57	323.49	323.54
Hohmann Dry Mass (kg)	3091.36	3089.48	3089.48
HST Fuel Mass (kg)	2227.06	1445.04	2118.62
$R2$	6.41	8.03	8.77
Intermediate Orbit Eccentricity	0	0.73	0.19
<b>Saving compared to Hohmann (kg)</b>	181.58	965.48	291.90
<b>Saving compared to Hohmann (% of <math>m_{wet}</math>)</b>	3.30	17.55	5.31

Considering the intermediate orbit characteristics, the trends for the GTO-GEO transfer are very similar to the LEO-GEO case. The eccentricity for the HST with high-thrust plane

change again stays at the limit of 0.73 while the HST with low-thrust plane change is always less than 0.5. The orbit ratio,  $R2$ , for the HST with high-thrust plane change is approximately  $R2 = 8$  for all wet mass cases while the orbit ratio for the HST with low-thrust plane change varies for each case but is always larger than the HST with high-thrust plane change; as was the case in the LEO-GEO study. The results of the time specified cases are given in APPENDIX A as they exhibit similar trends to the results just discussed. The intermediate orbit eccentricity, fuel mass savings and orbit ratio,  $R2$ , for all wet mass cases considered are shown in Figure 6-12, Figure 6-13 and Figure 6-14 respectively. As was found for the LEO – GEO, the HST with high-thrust plane change uses approximately the same intermediate orbit eccentricity of 0.73 and  $R2 \approx 8$  and therefore offers approximately the same fuel mass saving of  $\approx 17\%$  of  $m_{wet}$ . For the HST with low-thrust case it can be seen there is a direct correlation between the intermediate orbit eccentricity,  $R2$  and the fuel mass saving. Figure 6-12 and Figure 6-14 highlight that the orbit is more eccentric at large orbit ratios which has a direct effect on the fuel mass saving as shown in Figure 6-13. This differs slightly from the LEO-GEO case as a correlation between the fuel mass saving and  $R2$  is not obvious. In general however, it can be said that a larger intermediate orbit eccentricity for both the LEO and GTO – GEO transfers results in a larger fuel mass saving.

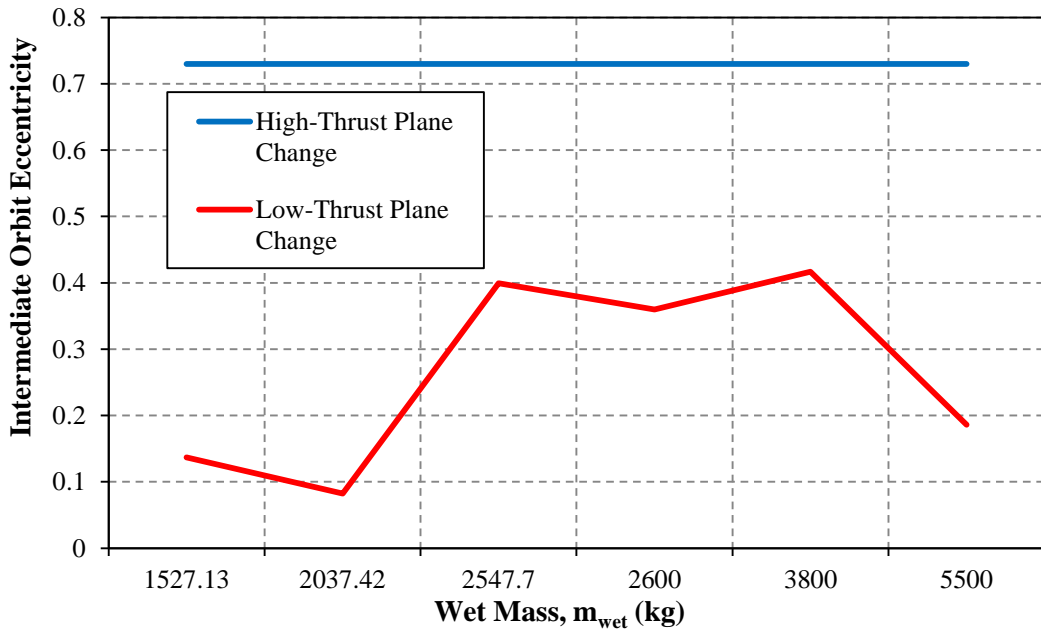


Figure 6-12 GTO – GEO, intermediate orbit eccentricity for wet masses specified in ascending order

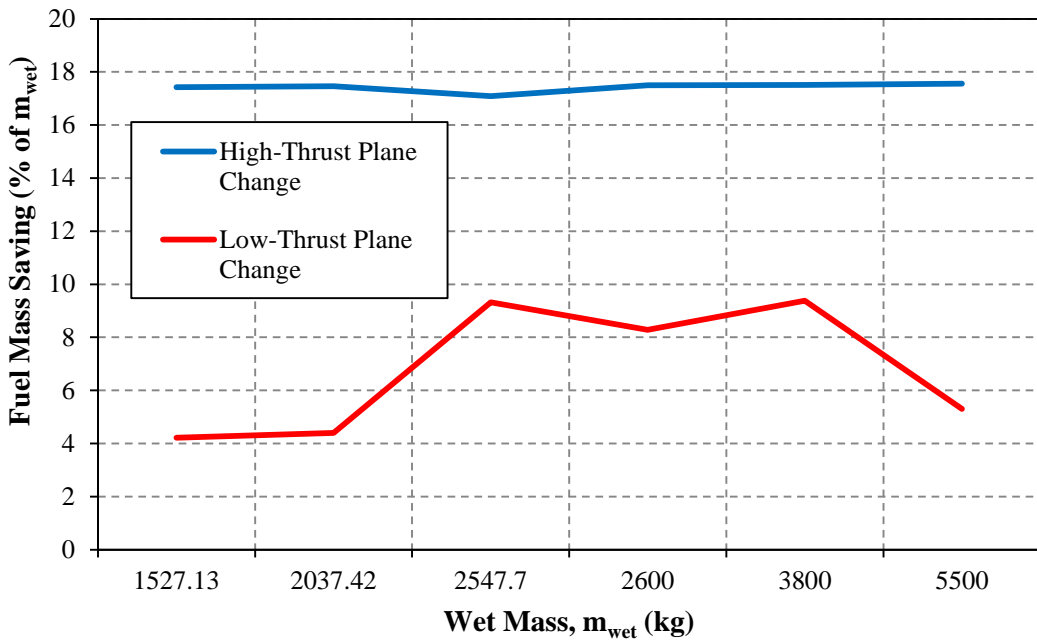


Figure 6-13 GTO – GEO, percentage fuel mass savings for wet masses specified in ascending order

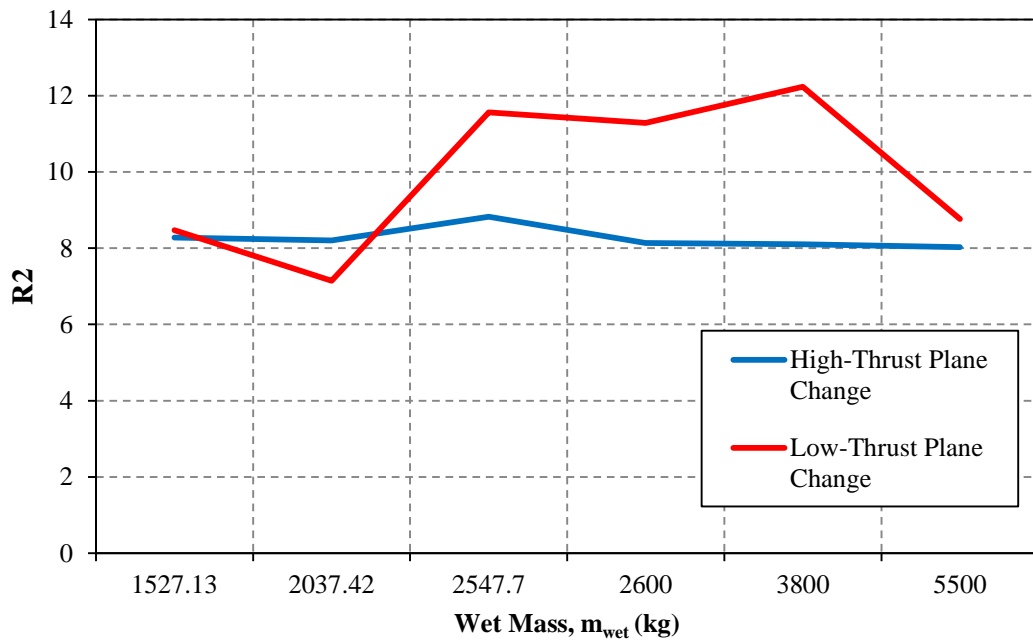
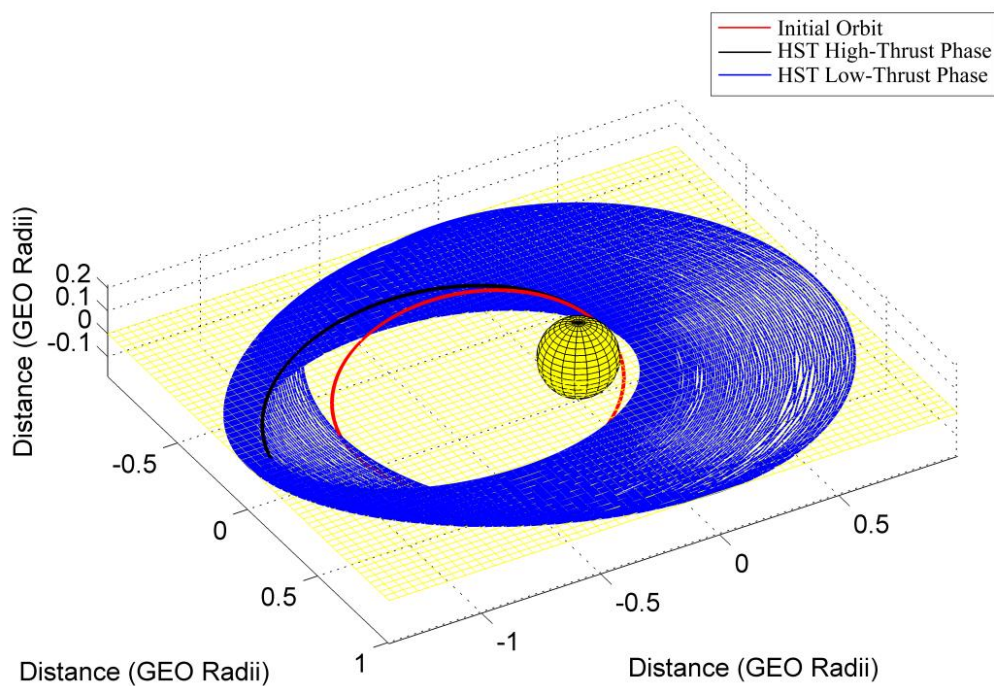


Figure 6-14 GTO – GEO, R2 for wet masses specified in ascending order

As these results were gathered using the numerical analysis, it is possible to determine the transfer history of different orbit characteristics. As there are several wet mass studies, only the results for  $m_{wet} = 1527.13$  kg and  $m_{wet} = 2547.7$  kg for the GTO – GEO transfer with high and low-thrust plane change respectively will be discussed in the text to highlight the differences in the transfers. The orbital transfer histories for the remaining time-specified cases, including the LEO – GEO transfer cases, are given in APPENDIX A. Figure 6-15 and Figure 6-16 show the HST transfer with high and low-thrust plane change respectively. The red line represents the initial orbit which in this case is GTO. The black line represents the high-thrust phase of the HST while the blue line represents the low-thrust section. The differences between the two transfer types are obvious due to the variation in intermediate orbit eccentricity. As was discussed previously, the HST with low-thrust plane change has a smaller eccentricity compared to the HST with high-thrust plane change. This can be attributed to the smaller acceleration available due to the low-thrust system performing the plane change as is highlighted in Figure 6-17 and Figure 6-18 which show the acceleration in the Radial, Transverse and Normal directions for the HST with high and low-thrust plane

change respectively. In Figure 6-17 it can be seen that the acceleration in the Radial and Transverse directions has a maximum magnitude of approximately  $2.4 \times 10^{-4} m/s^2$ . Comparing this to Figure 6-18, it is evident that neither the Radial or Transverse accelerations can achieve this magnitude and as previously discussed, this has a direct effect on the intermediate orbit eccentricity. It can be seen in Figure 6-18 that the Normal acceleration dominates throughout the majority of the low-thrust phase suggesting plane change is the priority in this transfer.



**Figure 6-15 GTO – GEO, HST with high-thrust plane change**

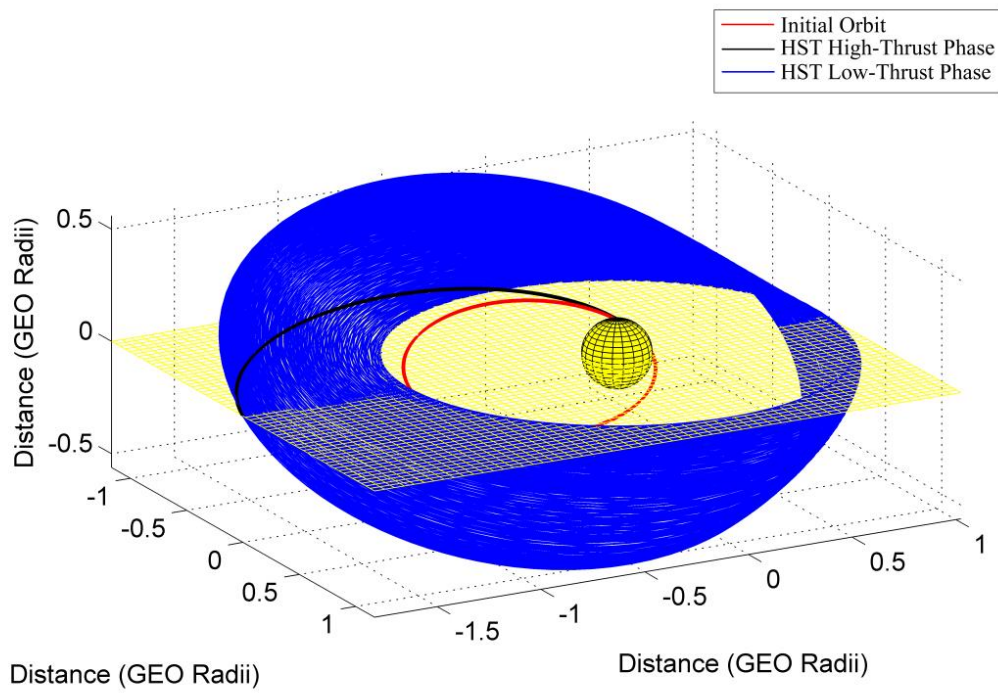


Figure 6-16 GTO-GEO, HST with low-thrust plane change

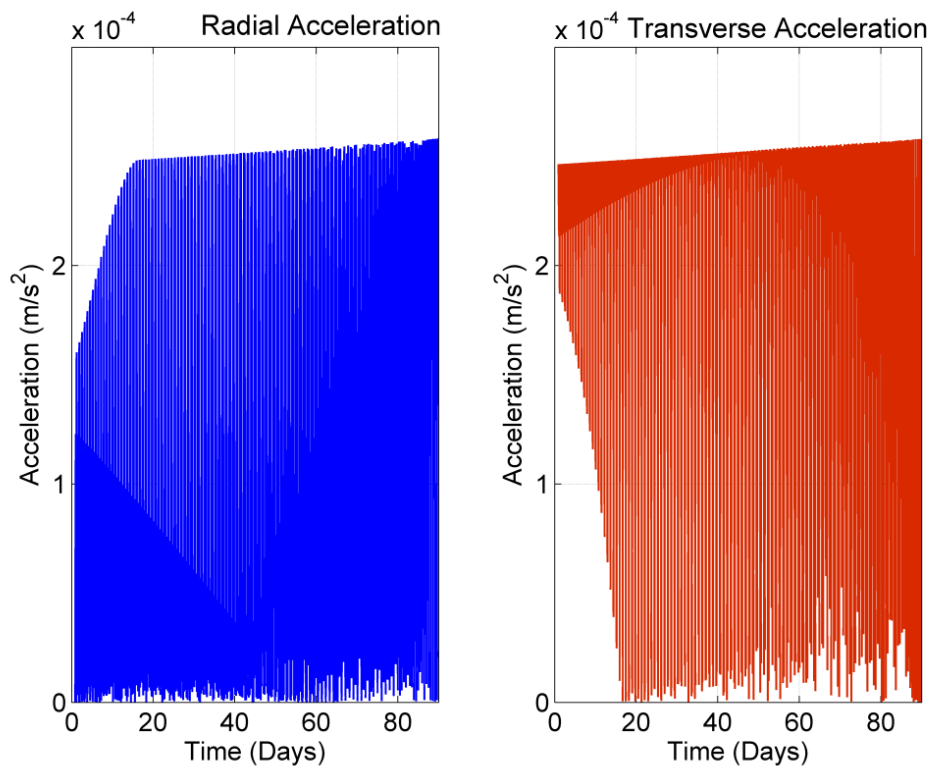
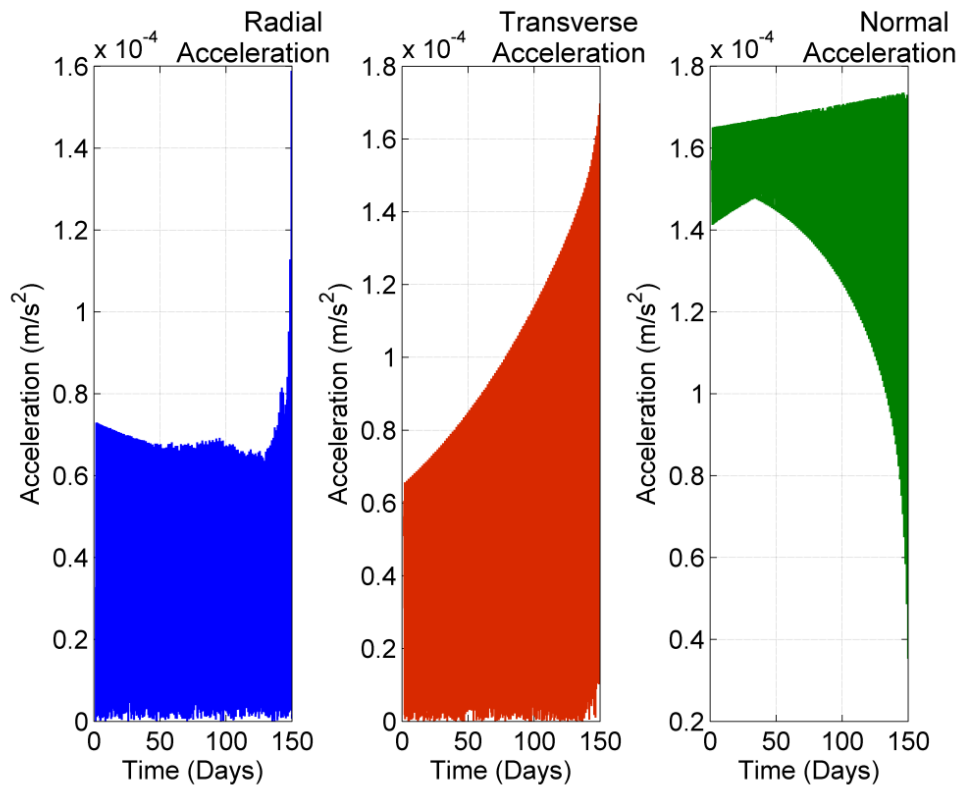


Figure 6-17 GTO – GEO, HST with high-thrust plane change acceleration profiles



**Figure 6-18 GTO – GEO, HST with low-thrust plane change acceleration profiles**

The orbit radius profiles of the HST with high and low-thrust plane changes are given in Figure 6-19 and Figure 6-20 respectively. It is of note that the intermediate orbit in the high-thrust plane change case is similar to a SuperSynchronous Transfer Orbit (SSTO), which has been used in previous high-thrust only missions to reduce the velocity requirement when a large plane change is required [128]. A difference however is that the optimiser in this case chooses to raise the apogee further than that of the intermediate orbit with the low-thrust system as is shown in Figure 6-19. A similar result was also found when considering a two-dimensional electric propulsion transfer to GEO [129] which started from an initial orbit with perigee and apogee below GEO radius. In this work it was noted the semi-major axis was always below that of GEO; also true for this case study as shown in Figure 6-21. A hybrid propulsion transfer designed in [130] also recognised the advantages of a SSTO when combining two propulsion systems, however it did not recognise that increasing the apogee further with the low-thrust propulsion system could improve the fuel mass savings.

Conversely, the HST with low-thrust plane change, which starts from a larger apogee radius due to a larger orbit ratio,  $R_2$ , is constantly reducing the orbit apogee while raising the perigee radius as shown in Figure 6-20. A similar interesting result in this case is that the HST with low-thrust plane change increases the orbit perigee beyond that of the target over the course of the transfer.

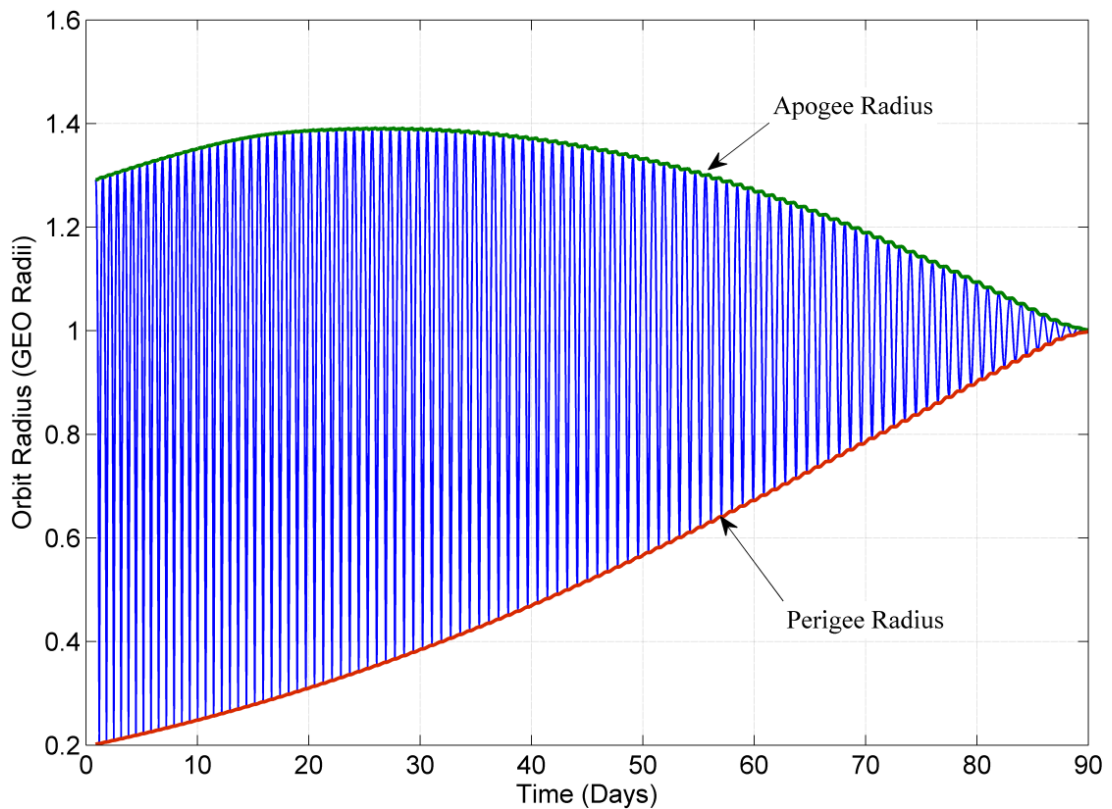


**Figure 6-19 GTO – GEO, HST with high-thrust plane change orbit radius profile**

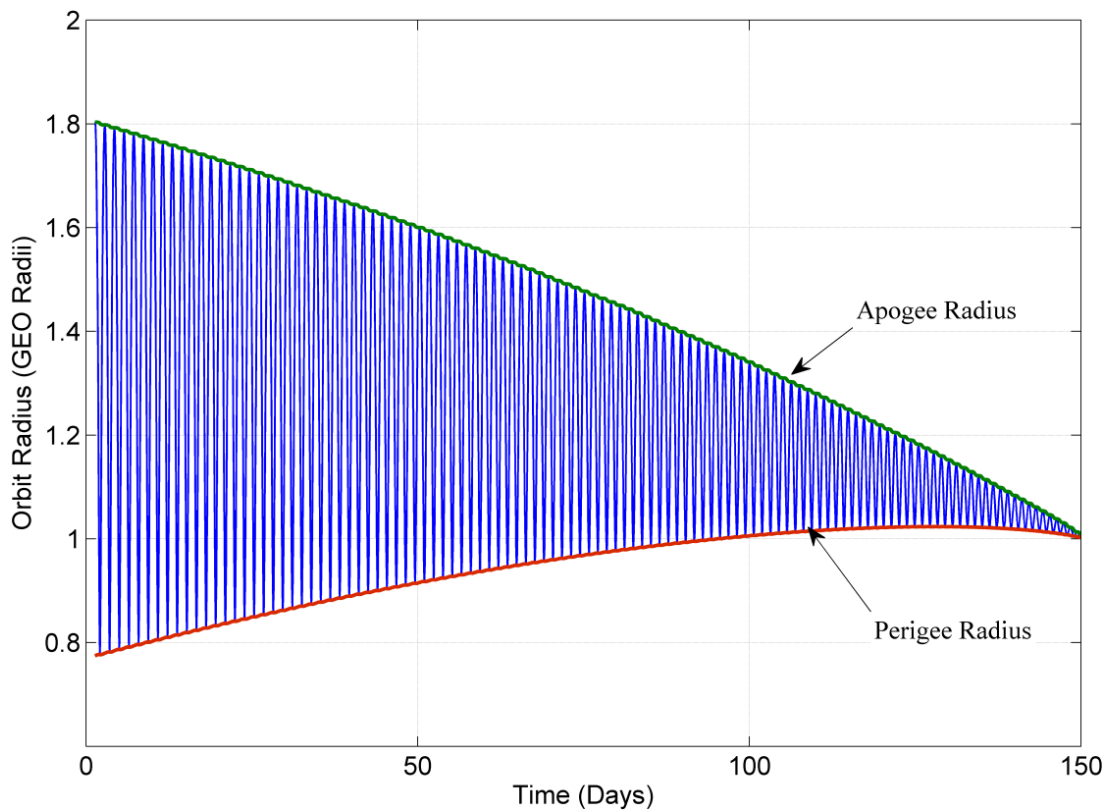


**Figure 6-20 GTO – GEO, HST with low-thrust plane change orbit radius profile**

The semi-major axis and eccentricity profiles for the HST with high-thrust plane change are shown in Figure 6-21. Similarly, the semi-major axis, eccentricity and inclination profiles for the HST with low-thrust plane change are given in Figure 6-22. Comparing only the semi-major axis for each transfer type, it can be seen that the HST with high-thrust plane change is always increasing the semi-major axis while the HST with low-thrust plane change is constantly decreasing the semi-major axis. For the HST with high-thrust plane change, the rate of change of the semi major axis is largest in the first half of the low-thrust transfer with the opposite being true for the HST with low-thrust plane change. The eccentricity in both cases is decreasing as expected. The inclination profile for the HST with low-thrust plane change is also decreasing at a constant rate.

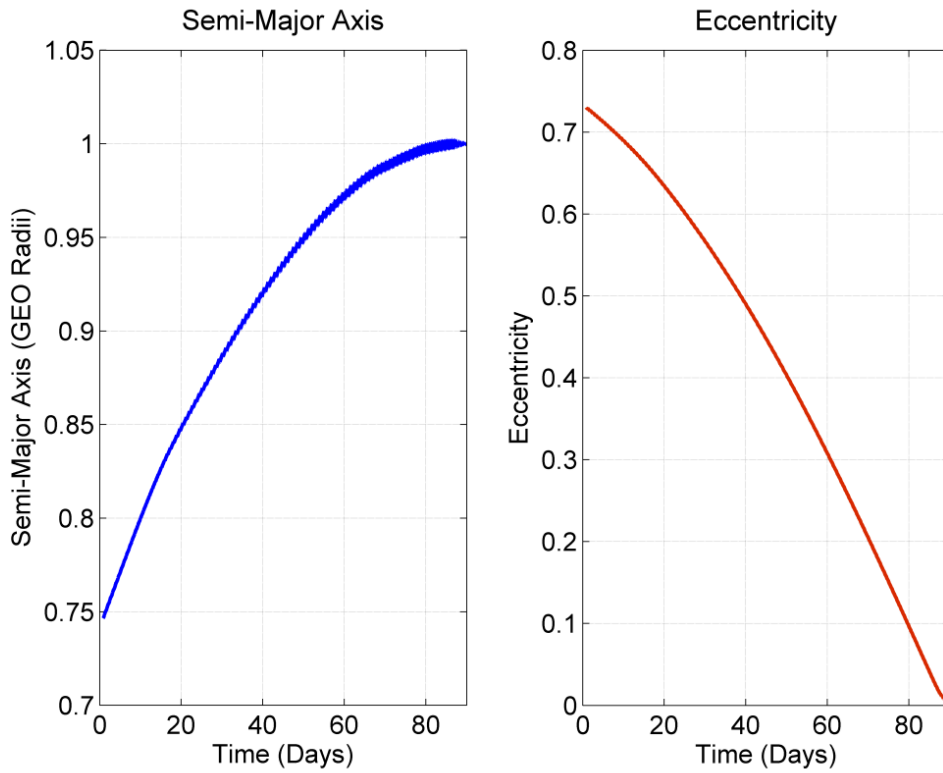


Figure 6-21 GTO – GEO, HST with high-thrust plane change orbital element profiles

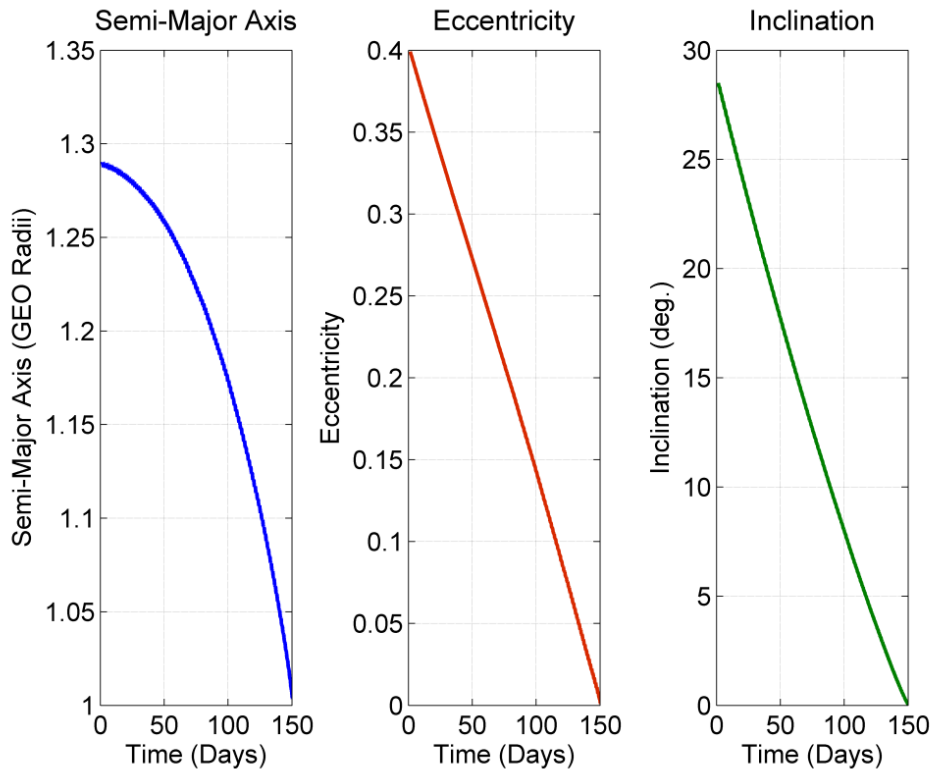


Figure 6-22 GTO – GEO, HST with low-thrust plane change orbital element profiles

The velocity requirement and fuel mass for each phase of each transfer is shown in Table 6-17 where it can be seen for both cases the high-thrust phase velocity requirement is smaller than the low-thrust phase but the fuel mass of the low-thrust phase is smaller than the high-thrust phase. This of course can be attributed to the much larger specific impulse achievable by the low-thrust system.

**Table 6-17 GTO – GEO velocity requirement and fuel mass phase breakdown. HTPC – High-Thrust Plane Change, LTPC – Low-Thrust Plane Change**

	1527.13 kg (HTPC)		2547.7 kg (LTPC)	
	High-thrust phase	Low-thrust phase	High-thrust phase	Low-thrust phase
<b>Velocity Requirement (m/s)</b>	829.56	1943.87	1183.48	2175.48
<b>Fuel Mass (kg)</b>	350.25	53	790.85	88.31

Furthermore, Table 6-18 details the total computational time, number of iterations and number of function evaluations for the two optimisation studies discussed. When the high-thrust system is used to perform the plane change the computational time, number of iterations and function evaluations are less than when the low-thrust system performs the plane change. This is due to the reduced complexity of the optimisation problem when the high-thrust system performs the plane change as there is one less constant to be optimised. The platform used to perform the optimisation had an Intel ® Core ™ i7-3615QM CPU @ 2.30 GHz with 8.00 GB of RAM.

**Table 6-18 Optimisation data. HTPC – High-Thrust Plane Change, LTPC – Low-Thrust Plane Change**

Wet Mass	Computational Time (s)	Iterations	Function Evaluations
<b>1527.13 kg (HTPC)</b>	804	176	12
<b>2547.7 kg (LTPC)</b>	1560	473	18

This numerical optimisation study has considered a LEO and GTO – GEO transfer for a HST using both high and low-thrust plane change manoeuvres. It has been shown that the largest

fuel mass saving is offered by the HST with high-thrust plane change for the LEO – GEO and GTO – GEO cases. The largest fuel mass saving is offered by the GTO – GEO case study, which is approximately 17.5 % of wet mass in all cases considered. As a result the GTO – GEO case study offers a dry mass of approximately 73 % of each wet mass considered compared to only 34 % for the LEO – GEO. The differences between the analytical and numerical studies can be attributed to the constraints required for the analytical analysis. This is highlighted by the fact that both high and low-thrust plane change variations have a significant eccentricity over the course of the low-thrust phase which is not possible within the analytical analysis. When comparing the high and low-thrust plane change transfers, it has been found that the transfers are very different in their make-up; for a high-thrust plane change, the best fuel mass saving is found when the intermediate orbit is highly eccentric whereas for a low-thrust plane change the eccentricity is approximately 0.4. The difference in eccentricity of each plane change case can be attributed to the fact the acceleration in the low-thrust plane change has to perform the plane change as well as the spiral-in and as such the available acceleration to control a large eccentric orbit is reduced.

### 6.2.2. SSO – Highly Elliptical Polar Orbit

A recent study concerning the design of a polar observation satellite has considered the Soyuz launcher with fregat upper stage as the method of insertion into its highly elliptical 90° working orbit [131]. The satellite is currently proposed to have only low-thrust propulsion on-board however this study aims to demonstrate, with the addition of a simple high-thrust booster, the HST can offer substantial fuel mass savings compared to only using the fregat upper stage. Two highly elliptical orbits are considered; 12 hour and 16 hour, with apogee and perigee altitude as shown in Table 6-19.

**Table 6-19 Highly elliptical polar observation orbit**

---

---

	<b>12 Hour Orbit</b>	<b>16 Hour Orbit</b>
<b>Perigee Altitude (m)</b>	300,000	10,000,000
<b>Apogee Altitude (m)</b>	40,170,000	41,740,000
<b>Orbit Inclination (deg.)</b>	90	90

---

---

The work in [131] found that the Soyuz could deliver a dry mass of 1250 kg to the 12 hour orbit, while 859 kg could be delivered to the 16 hour orbit. It is therefore an increase in these values which drives this analysis.

The optimisation study considers a high-thrust system with specific impulse equivalent to that of the fregat upper stage (330s) [132, Ch. 2]. It is assumed the Soyuz launch system places the spacecraft in a 95.4° SSO as due to azimuth restrictions from the Baikonur launch site, this is the closest orbit to 90° that offers the largest payload mass when targeting a polar orbit [132, Ch. 2]. The HST will then consider using the high and low-thrust systems to perform the orbit transfer and accompanying plane change to reach the desired orbit and inclination. The initial mass given in Table 6-20 is extrapolated data based on the Soyuz launch manual minus the fregat mass of 1000 kg which is assumed to be jettisoned after reaching SSO [133]. The low-thrust propulsion system considers two T6 thrusters in dual configuration [10]. The T6 thruster is identified as a suitable propulsion system to specifically enable the 12 hour orbit due to its large thrust [131]. The transfer time is specified as 120 days.

**Table 6-20 Transfer specification and propulsion system performance**

<b>Gravitational constant, <math>\mu</math> (<math>\text{m}^3/\text{s}^2</math>)</b>	3.986004418x10 <sup>14</sup>
<b>Earth Radius <math>r_E</math> (m)</b>	6,378
<b>Initial Orbit, <math>r_i</math> (m)</b>	6,578,000 (200 km altitude)
<b>Initial Mass, <math>m_{wet}</math> (kg)</b>	5275
<b>High-Thrust System Specific Impulse, <math>I_{spH}</math> (s)</b>	330
<b>Low-Thrust System Specific Impulse, <math>I_{spL}</math> (s)</b>	4300
<b>Thrust, <math>Tr</math> (mN)</b>	290 (2x145)
<b>Plane Change, <math>\Delta I</math> (rad)</b>	0.094 (5.4°)
<b>Specified Transfer Time, <math>t_{HST}</math> (days)</b>	120

One fundamental difference between this case study and the previous transfer to GEO is that the line of apsides does not coincide with the perigee and apogee of the high-thrust transfer orbit. This affects the HST with high-thrust plane change quite dramatically as the high-thrust phase now requires an extra impulse at the ascending node to reduce the orbit inclination from 95.4° to 90°. In order to calculate the correct velocity requirement it is assumed an impulse is performed to enter the transfer orbit at the perigee. It is then necessary to perform a pure inclination change at the ascending node before a final impulse is required at the transfer orbit apogee to enter the intermediate orbit. Note that the optimiser still has the flexibility to choose the intermediate orbit eccentricity and as such the third and final burn is not always used if the eccentricity is not changed from that of the transfer orbit. For this transfer case, the transfer orbit radius at the ascending node location is simply the semi-latus rectum. As such, the velocity requirement for the high-thrust phase orbit raise and plane change, with the inclusion of the intermediate orbit eccentricity through Eq. (5.10), is defined as

$$\Delta V_{HSTHC} = \sqrt{\frac{2\mu}{r_i} - \frac{2\mu}{r_i+r_c}} + \sqrt{\frac{\mu(1+e)}{r_c}} - \sqrt{\frac{2\mu}{r_c} - \frac{2\mu}{r_i+r_c}} - \sqrt{\frac{\mu}{r_i}} + 2\sqrt{\frac{2\mu}{r_i} - \frac{2\mu}{r_i+r_c}} + 2\sqrt{\frac{2\mu}{r_i+r_c} \left( \frac{2}{1-e^2} - 1 \right)} \sin\left(\frac{\Delta I}{2}\right). \quad (6.4)$$

The results of the optimisation study are provided in Table 6-21 which details the final dry mass of the HST and the associated mass saving compared to the fregat upper stage transfer. The transfer time of each optimisation is also specified where it can be seen the 120 day transfer limit is satisfied with an error or less than 1%. The intermediate orbit eccentricities for each case are approximately 0.6 with the low-thrust plane change case for the 12 hour orbit the largest at 0.65. The intermediate to initial orbit ratio for each high-thrust plane change case is approximately  $R2 = 4.5$  whereas for the low-thrust plane change it is approximately  $R2 = 5.3$ . It can be seen for both the 12 and 16 hour cases the low-thrust system offers the largest fuel mass saving; 1185.75 kg ( $\approx 22.5\%$  of  $m_{wet}$ ) for the 12 hour and 1448.31 kg ( $\approx 27.5\%$  of  $m_{wet}$ ) for the 16 hour orbit transfer. This is different to the GEO case studies where it was found the HST with high-thrust plane change always outperformed the HST with low-thrust plane change. This can be attributed to the plane change having to be performed at the ascending node as opposed to being optimally split between the first and second impulses, with the majority being performed at the largest orbit radius for maximum efficiency. It should be noted that for this relatively small plane change of  $\Delta I = 5.4^\circ$ , the burn required is approximately 30% of the velocity requirement for the orbit raise manoeuvre for both the 12 and 16 hour transfer cases. It is therefore recommended that the HST with low-thrust plane change should be used for this mission. The addition of a high-thrust propulsion system to the spacecraft should not substantially increase the complexity or risk of the mission as it will only be required to perform two burns to provide the initial orbit raise. It can then be jettisoned at the beginning of the low-thrust phase, increasing the acceleration of the spacecraft and resulting in a reduced transfer time to what is detailed in Table 6-21.

Table 6-21 Optimisation results for 12 and 16 hour orbit transfers

Transfer	12 Hour Orbit		16 Hour Orbit	
	HTPC	LTPC	HTPC	LTPC
Dry Mass, $m_{dry}$ (kg)	2059.53	2435.75	2108.22	2307.31
Total Transfer Time, $t_{HSTC}$ (days)	120.85	120.09	120.20	120.15
Fuel Mass, $m_{HSTF}$ (kg)	3215.47	2839.25	3166.78	2967.69
Dry Mass Increase w.r.t. Fregat (kg)	809.53	1185.75	1249.22	1448.31
Dry Mass Increase w.r.t. Fregat ( % of $m_{wet}$ )	15.35	22.48	23.68	27.46
R2	4.51	5.29	4.30	5.29
Intermediate Orbit Eccentricity, $e$	0.60	0.65	0.60	0.59

The transfer characteristics of the HST with low-thrust plane change for the 12 hour orbit and HST with high-thrust plane change for 16 hour orbits are discussed hereafter. The remaining case studies for each orbit transfer are detailed in APPENDIX A. Figure 6-23 and Figure 6-24 show the HST trajectories to the 12 and 16 hour polar orbits respectively. Figure 6-25 and Figure 6-26 detail the orbit radius profiles for the specified transfers. It can be seen in Figure 6-25 that the apogee radius is constantly increasing while the perigee is raised beyond the target over the course of the transfer. The same trend in Figure 6-26 is observed however the perigee is lowered rapidly at the very end of the transfer. As one of the reasons for the 16 hour orbit is to minimise time spent in the Van Allen radiation belts, it may be necessary to modify the transfer to raise the perigee at the very beginning of the transfer to avoid spending approximately 100 days in the inner belt which extends to approximately 2.5 Earth radii [134]. However, the advantages of performing such a manoeuvre would have to be compared against the fuel mass increase to determine if this is required or if some form of component hardening would be more economical. Figure 6-27 shows the semi-major axis

and eccentricity are constantly increased while the inclination is constantly decreased for the HST with low-thrust plane change. The orbital element profiles for the 16 hour target orbit detailed in Figure 6-28 show that the semi-major axis increases at an approximately constant rate towards the target. The eccentricity of the orbit however is found to decrease at a constant rate to a value lower than the target, where at approximately 115 days it is increased rapidly to meet the target value. The acceleration profiles for the 12 and 16 hour transfers are shown in Figure 6-29 and Figure 6-30 respectively. For the HST with low-thrust plane change it is shown the Normal acceleration is the largest at the beginning of the transfer while the Radial and Transverse accelerations increase steadily over the duration of the transfer. For the HST with high-thrust plane change, it is found that the Transverse acceleration is larger for the majority of the transfer however the Radial acceleration increases towards the end of the transfer, coinciding with the rapid increase in eccentricity as shown in Figure 6-28.

By performing this case study, it is evident that a substantial fuel mass saving can be achieved when using the HST from the initial SSO instead of the Soyuz upper stage fregat. Although the transfer time is increased when using the HST instead of the fregat, it is still less than what would be required for a low-thrust only transfer. For this particular transfer it is therefore a trade-off between dry mass delivered to orbit and time to service of the spacecraft. As this spacecraft's primary mission is scientific it is likely that the time to service is not the major priority it may be for a commercial spacecraft for example. However, as the spacecraft will most likely require some form of commissioning in the space environment before becoming fully operational, it may be possible to coincide this with the transfer so that the spacecraft can enter service as soon as it arrives at the working orbit.

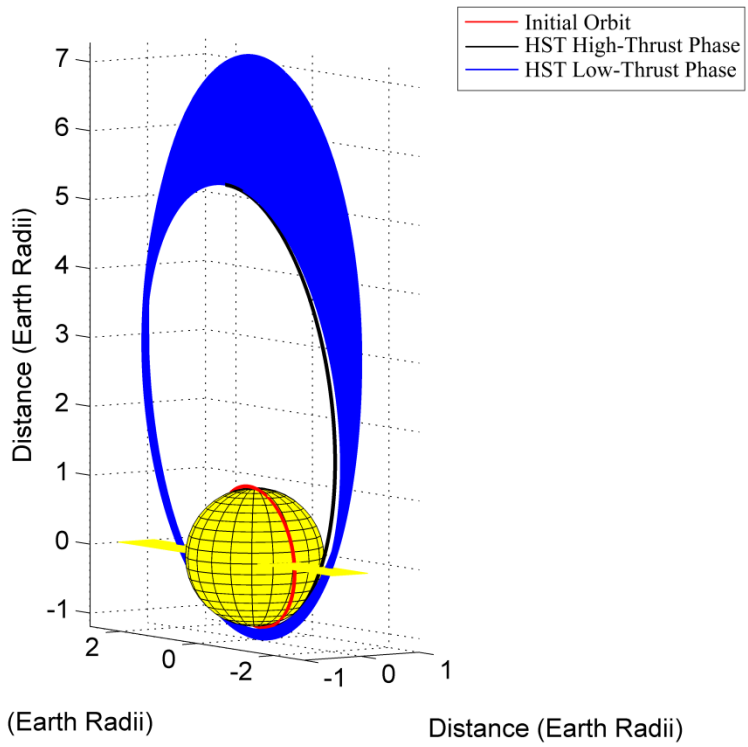


**Figure 6-23 12 hour polar orbit transfer, HST with low-thrust plane change**

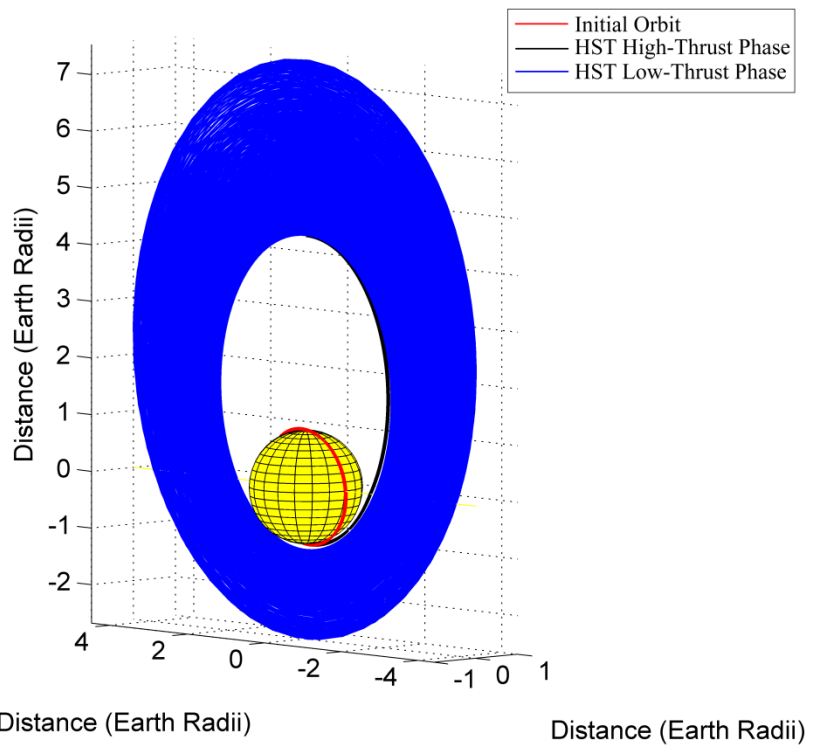


**Figure 6-24 16 hour polar orbit transfer, HST with high-thrust plane change**

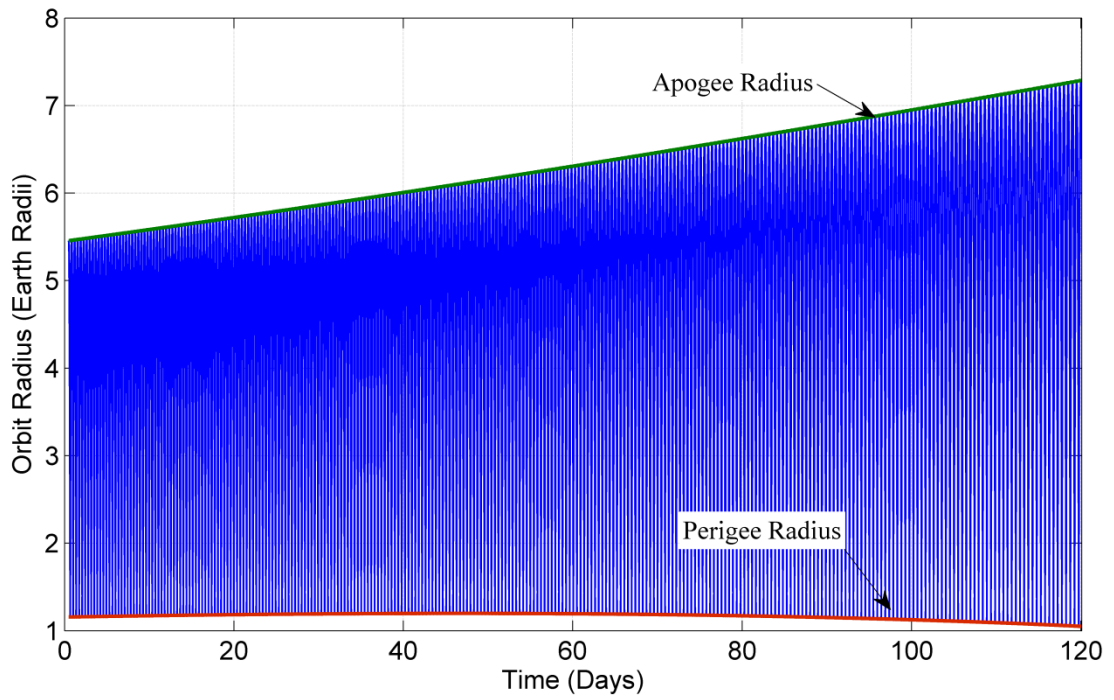


Figure 6-25 12 hour polar orbit transfer, HST with low-thrust plane change orbit radius profile

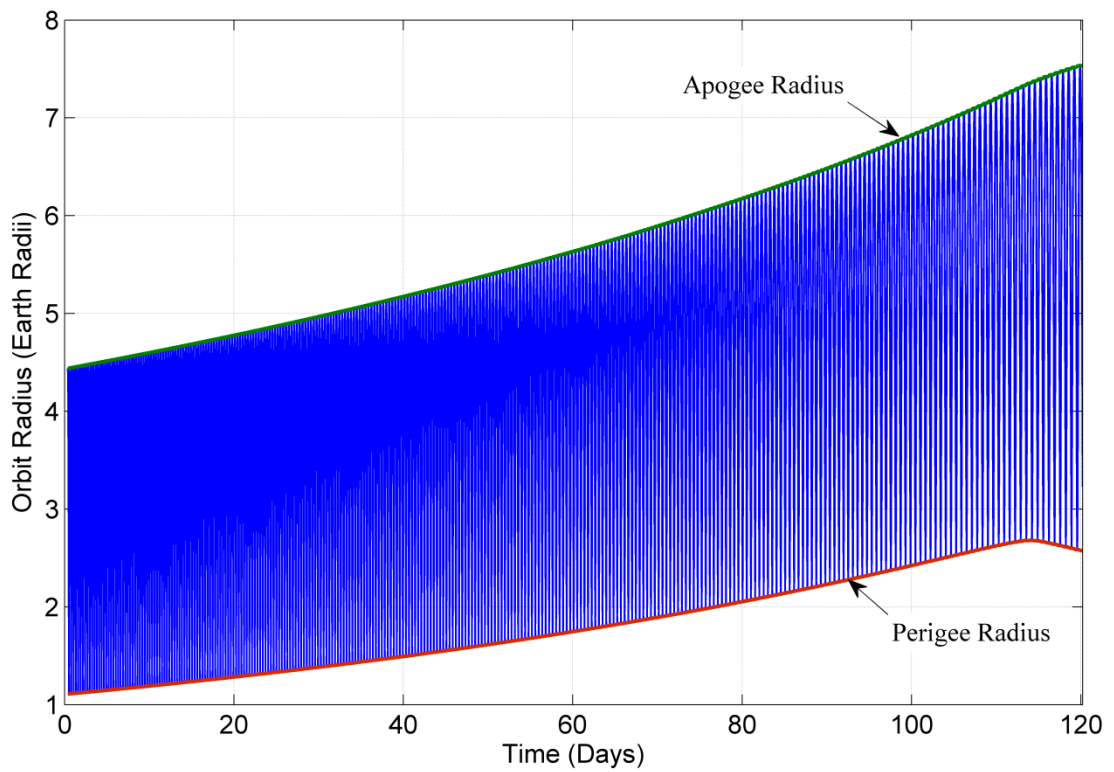


Figure 6-26 16 hour polar orbit transfer, HST with high-thrust plane change radius profile

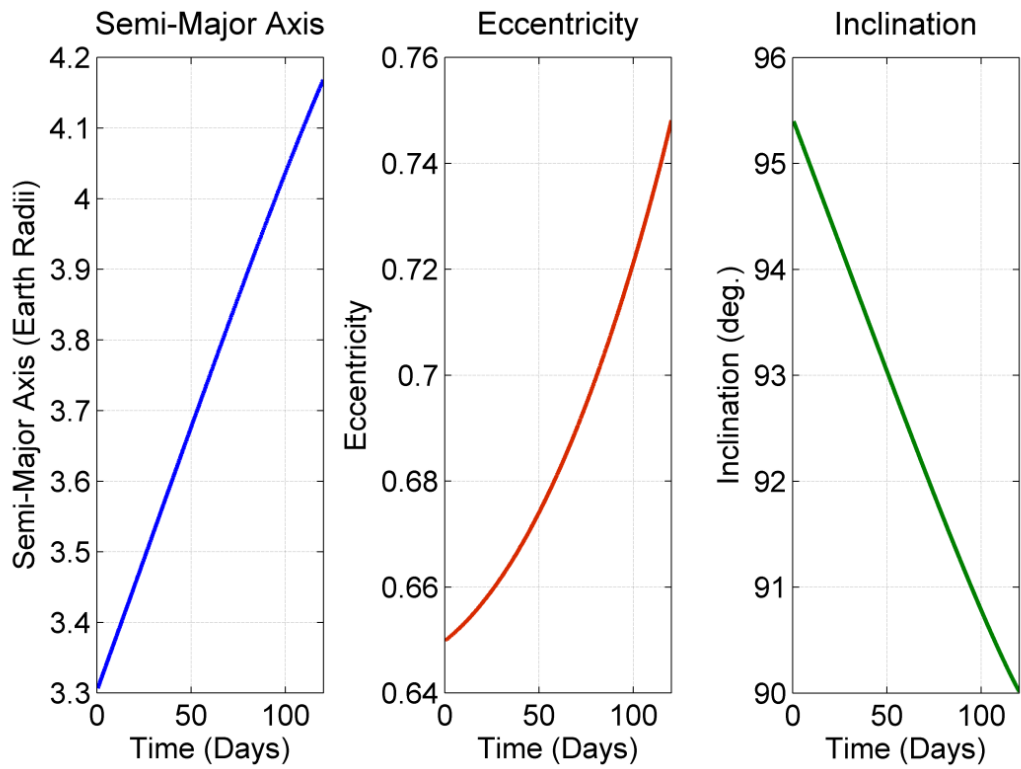


Figure 6-27 12 hour polar orbit transfer, HST with low-thrust plane change orbit element profiles

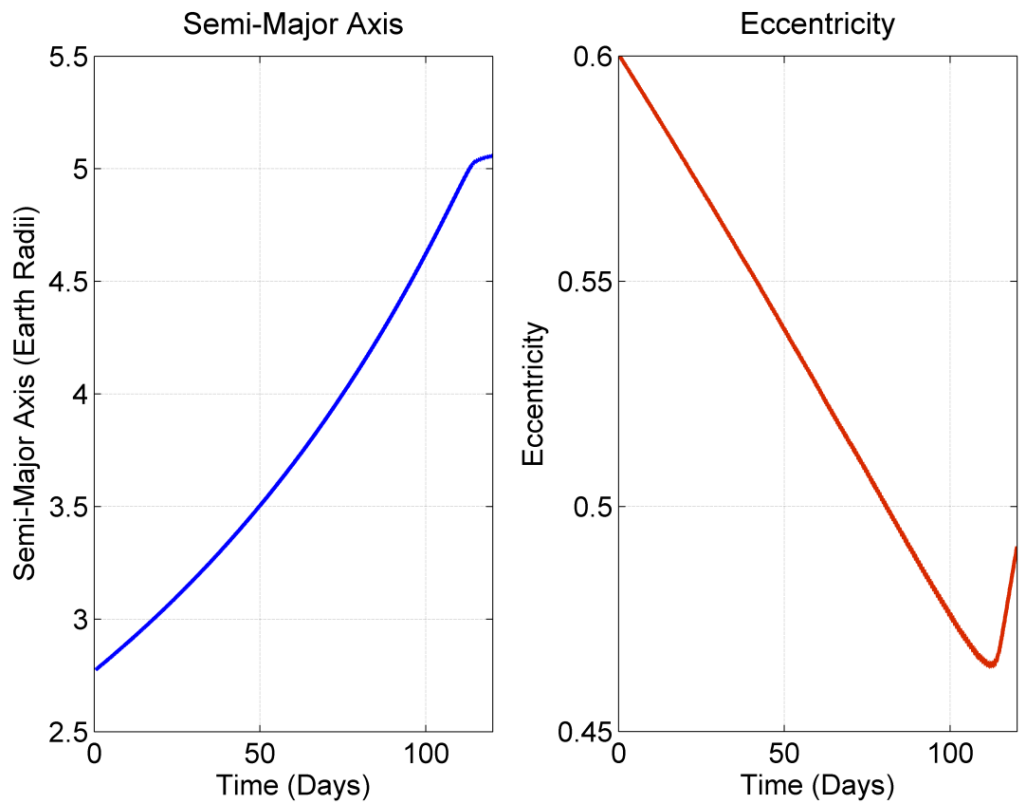


Figure 6-28 16 hour polar orbit transfer, HST with high-thrust plane change orbital element profiles

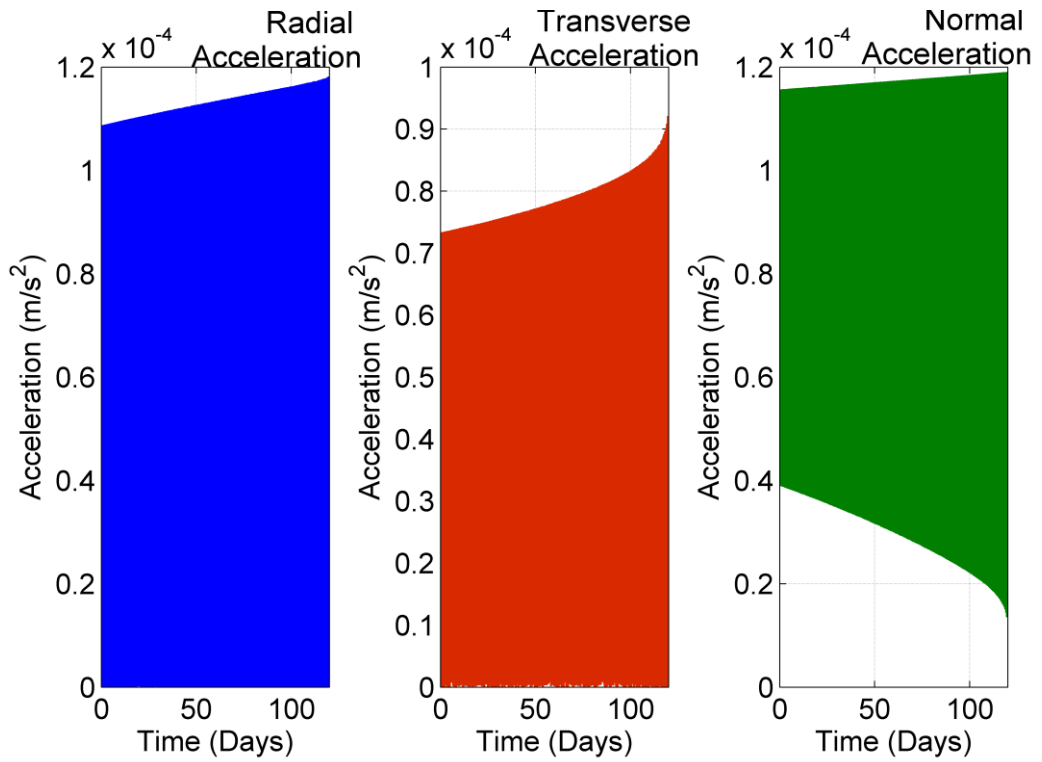


Figure 6-29 12 hour polar orbit transfer, HST with low-thrust plane change acceleration profiles

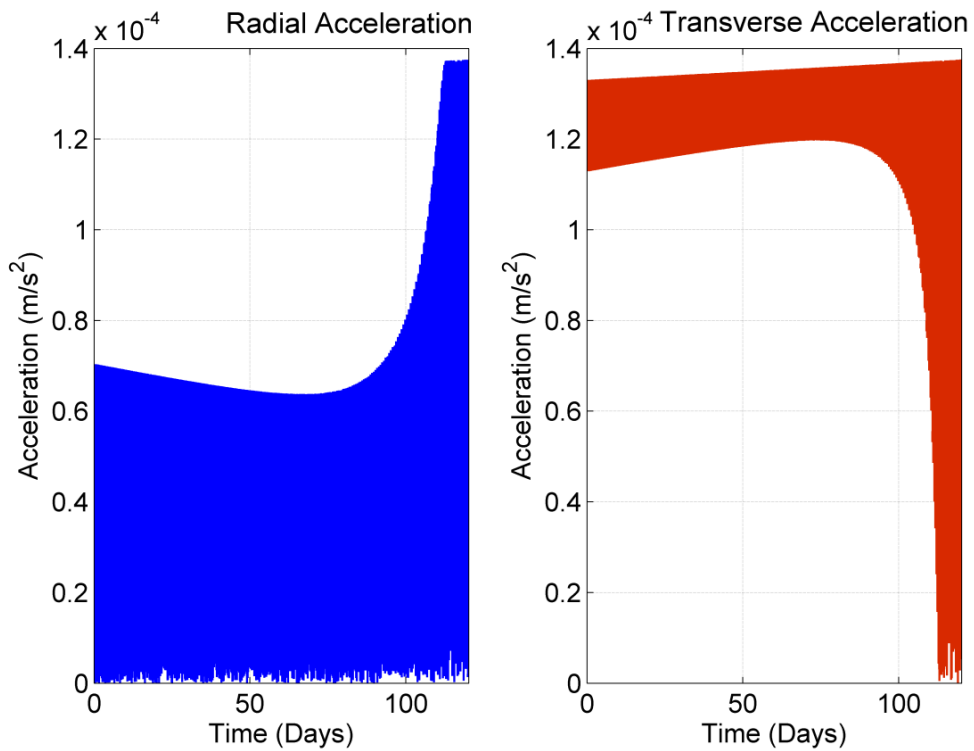


Figure 6-30 16 hour polar orbit transfer, HST with high-thrust plane change acceleration profiles

## 6.3. Summary

This chapter has considered the application of the analytical and numerical analysis tools developed within this dissertation to describe the HST. In the analytical case, it was found substantial fuel mass savings are possible when using the HST instead of a high-thrust only transfer. The analytical analysis tools also demonstrated the flexibility to handle different mission constraints i.e. specified dry mass or transfer time.

The numerical optimisation method allowed the removal of the constraints necessary in the analytical analysis. By doing this, it was shown the fuel mass savings were improved considerably and this is mainly due to the introduction of an eccentric intermediate orbit which can be controlled by the thrust direction vector. As such, the analytical and numerical resultant transfer trajectories are very different. It is therefore suggested that the analytical analysis be only used as a method of determining whether any benefit can be gained from using the HST. If a benefit is identified, then the numerical optimisation method should be used to perform a detailed study and determine the actual fuel mass savings and trajectory. If no benefit is identified in the analytical analysis but the results indicate the HST and high-thrust transfers' performance to be close, then the numerical method should be implemented to determine if the introduction of an eccentric intermediate orbit can offer a fuel mass saving.

By comparing the different case studies performed in this chapter it has been shown that the most efficient HST is entirely dependent on the specified transfer. For the case of a GEO transfer it has been shown the HST with high-thrust plane change offers the largest fuel mass saving however for the SSO to highly elliptical polar orbit it has been shown that the HST with low-thrust plane change is always more efficient. It is of note that the optimisation model uses a locally optimal method and as such any result cannot be taken as a globally optimal solution. If a globally optimal study is necessary then the solution calculated in the

locally optimal method could be used as an initial guess to a globally optimal solver which should improve convergence probability.

# Chapter 7

---

## CONCLUSIONS AND FUTURE WORK

### 7.1. Conclusions

The work conducted in this dissertation has extended the knowledge on high-thrust only transfers and addressed the current trend of dual propulsion platforms. Two critical limits, dependent on the final to initial orbit radius ratio and plane change, have been found that determine whether a Hohmann or bi-elliptic transfer has the lowest velocity requirement. A reference graph has been produced using these critical limits which can be used to determine the transfer with the lowest velocity requirement for any given orbit specification. This is achieved through the use of simple analytic expressions that negate the need for a numerical analysis of each transfer case considered. It is found that the critical limits change with increasing plane change and converge on a point where both the Hohmann and bi-elliptic transfers offer the same velocity requirement. This critical point is defined by the orbit ratio of 4.68 and plane change of  $44.8^\circ$ . An Area Of Uncertainty (AOU) exists between the critical limits in which a test is required to determine the transfer offering the lowest velocity requirement. Beyond the critical point a second AOU emerges in which another similar test is required to determine the transfer with the lowest velocity requirement. The effectiveness of the bi-elliptic transfer is found to increase with increasing plane change. This is due to a reduction in the critical limit that represents an orbit ratio of 15.58 for a co-planar transfer and 4.68 with a plane change of  $44.8^\circ$ , described previously. For dual propulsion platforms, it is found through numerical case studies that the Hohmann Spiral Transfer (HST) can offer an increase in dry mass of 17% (of wet mass) for a transfer to Geostationary Earth Orbit (GEO). An increase of 27% (of wet mass) has also been identified for a transfer from a Sun-

Synchronous Orbit (SSO) to a highly elliptical polar orbit. In the analytical analysis, a critical orbit ratio is determined which cannot be exceeded to ensure the zero eccentricity assumption of the analysis is valid. This results in variation between the analytical and numerical case studies. For a transfer to GEO, the increase of dry mass is identified as 3.3% (of wet mass) compared to 17% for the numerical case. The sensitivity of the analysis to this eccentricity assumption is demonstrated as the analytical analysis used the low-thrust system to achieve the largest fuel mass saving whereas the numerical analysis used the high-thrust system. For comparison, when the eccentricity assumption is removed the analytical analysis offered an increased dry mass of up to 4% (of wet mass) and used the high-thrust plane change method. In the numerical SSO study, the low-thrust system is used to provide the largest fuel mass saving, highlighting the sensitivity of the analysis to the orbit transfer specification. Furthermore, a transfer time reduction of approximately 64% can be achieved when comparing the HST to a low-thrust only transfer from Low Earth Orbit to GEO.

## 7.2. Recommendations and Future Work

This section considers additional work which could be performed to compliment the analyses within this dissertation. It can be split into two sections as shown.

### 7.2.1. Analytical

As was demonstrated within this dissertation, the analytical analysis can provide a general insight into the HST performance. When this is compared to the numerical analysis however it is found that there are significant differences which can be attributed to the analytical eccentricity constraints. It is therefore recommended to consider the effect of orbit eccentricity in the analytical analysis. It should be noted however that this will complicate the analysis and prevent the use of the simple critical specific impulse ratio as a means of determining when the HST will outperform the high-thrust only transfer.

## 7.2.2. Numerical

Several modifications could be made to the numerical optimisation method which could compliment the work carried out in this dissertation. These are as follows:

**Radiation Model:** It would be beneficial to include the effect of radiation, specifically from the Inner and Outer Van Allen belts, on the spacecraft's low-thrust propulsion system while utilising the HST. The resultant trajectory is expected to be affected and this would be of particular interest to an in-depth mission analysis study considering transfers which may spend long periods of time within the radiation belts.

**Thrust Arcs Model:** The implementation of thrust arcs into the optimisation study would also be a worthy addition as this could significantly improve the fuel mass savings without drastically increasing the transfer time.

# REFERENCES

- [1] Baker, J. M., “Orbit transfer and rendezvous maneuvers between inclined circular orbits,” *Journal of Spacecraft and Rockets*, vol. 3, no. 8, pp. 1216–1220, Aug. 1966, doi:10.2514/3.28630.
- [2] Barrar, R. B., “Two-Impulse vs One-Impulse Transfer-Analytic Theory,” *AIAA Journal*, vol. 1, no. 1, pp. 65–68, Jan. 1963, doi:10.2514/3.1470.
- [3] ALTMAN, S. and J. PISTINER, “Minimum velocity increment solution for two-impulse coplanar orbital transfer,” *AIAA Journal*, vol. 1, no. 2, pp. 435–442, Feb. 1963, doi:10.2514/3.1551.
- [4] Barrar, R., “An analytic proof that the Hohmann-type transfer is the true minimum two-impulse transfer,” *Astronautica Acta*, vol. 9, no. 1, pp. 1–11, 1962.
- [5] El Mabsout, B., O. M. Kamel, and A. S. Soliman, “The optimization of the orbital Hohmann transfer,” *Acta Astronautica*, vol. 65, no. 7–8, pp. 1094–1097, Oct. 2009, doi:10.1016/j.actaastro.2009.03.010.
- [6] Gardner Moyer, H., “Minimum impulse coplanar circle-ellipse transfer,” *AIAA Journal*, vol. 3, no. 4, pp. 723–726, Apr. 1965, doi:10.2514/3.2954.
- [7] Hazelrigg, G., “The use of Green’s theorem to find globally optimal solutions to a class of impulsive transfers.” 1968.
- [8] Hoelker, R. and R. Silber, “The bi-elliptical transfer between circular coplanar orbits,” Alabama, 1959.

- [9] Escobal, P. R., “Optimum Planetocentric,” in *Methods of Astrodynamics*, 1st ed., New York: John Wiley & Sons, Inc., 1968, pp. 57–93.
- [10] Vallado, D., *Fundamentals of astrodynamics and applications*. 2001.
- [11] Tsiolkovsky, K. E., “The exploration of cosmic space by means of reaction devices,” *Issledovanie mirovykh prostranstv reaktivnymi ....* 1903.
- [12] Chobotov, V., “Orbital mechanics third edition.” 2002.
- [13] Hohmann, W., *The attainability of heavenly bodies (Die Erreichbarkeit der Himmelskoerper)*, no. November. Washington: NASA, 1960.
- [14] Palmore, J., “An Elementary Proof Of the Optimality of Hohmann Transfers,” *Journal of Guidance, Control, and Dynamics*, vol. 7, no. 5, pp. 629–630, Sep. 1984, doi:10.2514/3.56375.
- [15] Prussing, J. E., “Simple proof of the global optimality of the Hohmann transfer,” *Journal of Guidance, Control, and Dynamics*, vol. 15, no. 4, pp. 1037–1038, Jul. 1992, doi:10.2514/3.20941.
- [16] Horner, J., “Optimum impulsive orbital transfers between coplanar orbits,” *ARS Journal*, vol. 32, no. 7, pp. 1082–1089, Jul. 1962, doi:10.2514/8.6209.
- [17] Ting, L., “Optimum Orbital Transfer by Impulses,” *ARS Journal*, vol. 30, no. 11, pp. 1013–1018, Nov. 1960, doi:10.2514/8.5305.
- [18] Munick, H., R. McGill, and G. . Taylor, “Analytic solutions to several optimum orbit transfer problems,” *Journal of the Astronautical Sciences*, vol. 7, no. 4. 1960.

- [19] Lawden, D., "Entry into circular orbits," *Journal of British Interplanetarry Society*, vol. 10, no. 1. pp. 5–7, 1951.
- [20] Bate, R. R., D. D. Mueller, and J. E. White, *Fundamentals of Astrodynamics*. Dover Pubns, 1971, p. 198.
- [21] Lawden, D., "Optimal transfers between coplanar elliptical orbits," *Journal of guidance, control, and dynamics*, vol. 15, no. 3. pp. 788–792, 1992.
- [22] Lawden, D., "Impulsive transfer between elliptical orbits," *Optimization Techniques*. 1962.
- [23] Lawden, D., "Time-closed optimal transfer by two impulses between coplanar elliptical orbits," *Journal of guidance, control, and dynamics*, vol. 16, no. 3. pp. 16–18, 1993.
- [24] Ehricke, K. A., "Interplanetary Mission Profiles," San Diego, 1958.
- [25] Shternfel'd, A. A., *Soviet Space Science*, 2nd ed. New York: Basic books Inc, 1959, pp. 109–111.
- [26] Robbins, H., "An analytical study of the impulsive approximation.," *AIAA journal*, no. August. pp. 1417–1423, 1966.
- [27] McIntyre, J. E., "Optimal transfer of a thrust limited vehicle between coplanar circular orbits," Princeton University, 1964.
- [28] Rider, L., "Characteristic Velocity Requirements for Impulsive Thrust Transfers Between Non Co-Planar Circular Orbits," *ARS Journal*, vol. 31, no. 3, pp. 345–351, Jan. 1961, doi:10.2514/8.5478.

- [29] Roth, H. L., “Bi-elliptic Transfer with Plane Change,” Defense Technical Information Center, Los Angeles, California, 1965.
- [30] Edelbaum, T. N., “Propulsion Requirements for Controllable Satellites,” *ARS Journal*, vol. 31, no. 8, pp. 1079–1089, Aug. 1961, doi:10.2514/8.5723.
- [31] Y., J. E. and R. G. Choueiri, “Electric Propulsion,” *Encyclopedia of Physical Science and Technology*, vol. 5. Academic Press, pp. 125–141, 2002.
- [32] Kuninaka, H., K. Nishiyama, I. Funakai, Tetsuya, Y. Shimizu, and J. Kawaguchi, “Asteroid Rendezvous of HAYABUSA Explorer Using Microwave Discharge Ion Engines,” in *29th International Electric Propulsion Conference*, 2005, pp. 1–10.
- [33] Dankanich, J., “Low-thrust Propulsion Technologies, Mission Design, and Application,” in *Aerospace Technologies Advancements*, no. January, Arif, T. T., Ed. InTech, 2010, pp. 219–240.
- [34] Rayman, M., P. Varghese, D. Lehman, and L. Livesay, “Results from the Deep Space 1 technology validation mission,” *Acta Astronautica*. 2000.
- [35] Estublier, D., G. Saccoccia, and J. G. Del Amo, “Electric propulsion on SMART-1-a technology milestone,” *ESA bulletin*. 2007.
- [36] Goebel, D. and I. Katz, *Fundamentals of electric propulsion: ion and Hall thrusters*. 2008.
- [37] Tsien, H., “Take-off from satellite orbit,” *Journal of the American Rocket Society*, vol. 44, no. 44. pp. 233–236, 1953.
- [38] Wiesel, W. and S. Alfano, “Optimal many-revolution orbit transfer,” *Journal of Guidance, Control, and Dynamics*. pp. 155–157, 1985.

- [39] Casalino, L. and G. Colasurdo, “Improved Edelbaum’s Approach to Optimize Low Earth/Geostationary Orbits Low-Thrust Transfers,” *Journal of Guidance, Control, and Dynamics*, vol. 30, no. 5, pp. 1504–1511, Sep. 2007, doi:10.2514/1.28694.
- [40] Kluever, C. A., “Geostationary Orbit Transfers Using Solar Electric Propulsion with Specific Impulse Modulation,” *Journal of Spacecraft and Rockets*, vol. 41, no. 3. 2004.
- [41] Cass, J., “Discontinuous low thrust orbit transfer,” U.S. Air Force Inst. of Technology, 1983.
- [42] Kechichian, J., “Reformulation of Edelbaum’s low-thrust transfer problem using optimal control theory,” *Journal of Guidance, Control, and Dynamics*, vol. 20, no. 5, pp. 988–994, Sep. 1997, doi:10.2514/2.4145.
- [43] Oh, D. Y. and D. Landau, “Simple Semi-Analytic Model for Optimized Interplanetary Low-Thrust Trajectories Using Solar Electric Propulsion,” *Journal of Spacecraft and Rockets*, vol. 50, no. 3, pp. 609–619, May 2013, doi:10.2514/1.A32326.
- [44] Edelbaum, T., “The use of high-and low-thrust propulsion in combination for space missions,” *Journal of the Astronautical Sciences*, vol. 9. pp. 49–60, 1962.
- [45] Choueiri, E., “A critical history of electric propulsion: the first 50 years (1906-1956),” *Journal of Propulsion and Power*. 2004.
- [46] Fimple, W., “An Improved Theory of the Use of High- and Low-Thrust Propulsion in Combination,” *Journal of the Astronautical Sciences*, vol. 10. pp. 107–113, 1963.

- [47] Horsewood, J., “Interplanetary Trajectory Analysis for Combined High and Low-Thrust Propulsion Systems,” *Preprint*. 1966.
- [48] Hazelrigg, G. A., “Optimal space flight with multiple propulsion systems.,” *Journal of Spacecraft and Rockets*, no. October. pp. 1233–1235, 1968.
- [49] Dickerson, W. and D. Smith, “Trajectory optimization for solar-electric powered vehicles.,” *Journal of Spacecraft and Rockets*, vol. 5, no. August. 1968.
- [50] Fishbach, L. H., “Multiple Thrust Level Trajectories for Minimum Propellant Consumption,” Case Institute of Technology, Cleveland, Ohio, 1967.
- [51] Willis Jr., E. A. and L. H. Fischbach, “Comment on ‘Optimal Space Flight with Multiple Propulsion Systems,’” *Journal of Spacecraft and Rockets*, vol. 6, no. 6. p. 1969, 1969.
- [52] Kluever, C., “Spacecraft optimization with combined chemical-electric propulsion,” *Journal of Spacecraft and Rockets*, vol. 32, no. Compendex. AIAA, Washington, DC, United States, pp. 378–380, 1995.
- [53] Kluever, C., “Optimal Earth-moon trajectories using combined chemical-electric propulsion,” *Journal of guidance, control, and dynamics*, vol. 20, no. Compendex. pp. 253–258, 1997.
- [54] Kluever, C. and B. Pierson, “Optimal earth-moon trajectories using nuclear electric propulsion,” *Journal of guidance, control, and dynamics*, vol. 20, no. 2. 1997.
- [55] Oleson, S., R. Myers, and C. Kluever, “Advanced propulsion for geostationary orbit insertion and north-south station keeping,” *Journal of Spacecraft ...*, vol. 2. 1997.

- [56] Kluever, C. a., “Optimal Geostationary Orbit Transfers Using Onboard Chemical–Electric Propulsion,” *Journal of Spacecraft and Rockets*, vol. 49, no. 6, pp. 1174–1182, Nov. 2012, doi:10.2514/1.A32213.
- [57] Oh, D. Y., T. Randolph, and S. Kimbrell, “End to End Optimization of Chemical–Electric Orbit Raising Missions,” *Journal of Spacecraft and Rockets*, vol. 41, no. 5, pp. 831–839, 2004, doi:10.2514/1.13096.
- [58] Mailhe, L. and S. Heister, “Design of a hybrid chemical/electric propulsion orbital transfer vehicle,” *Journal of spacecraft and rockets*, vol. 39, no. 1. pp. 131–139, 2002.
- [59] Miele, a, T. Wang, and P. . Williams, “Computation of optimal Mars trajectories via combined chemical/electrical propulsion, part 1: baseline solutions for deep interplanetary space,” *Acta Astronautica*, vol. 55, no. 2, pp. 95–107, Jul. 2004, doi:10.1016/j.actaastro.2004.01.053.
- [60] Miele, a., T. Wang, and P. N. Williams, “Computation of optimal Mars trajectories via combined chemical/electrical propulsion, Part 2: Minimum time solutions with bounded thrust direction,” *Acta Astronautica*, vol. 57, no. 11, pp. 819–828, Dec. 2005, doi:10.1016/j.actaastro.2005.04.007.
- [61] Miele, a., T. Wang, and P. N. Williams, “Computation of optimal Mars trajectories via combined chemical/electrical propulsion, Part 3: Compromise solutions,” *Acta Astronautica*, vol. 57, no. 11, pp. 829–840, Dec. 2005, doi:10.1016/j.actaastro.2005.04.008.

- [62] Baig, S. and C. McInnes, “Artificial Three-Body Equilibria for Hybrid Low-Thrust Propulsion,” *Journal of Guidance, Control, and Dynamics*, vol. 31, no. 6, pp. 1644–1655, Nov. 2008, doi:10.2514/1.36125.
- [63] Mengali, G. and A. a. Quarta, “Tradeoff Performance of Hybrid Low-Thrust Propulsion System,” *Journal of Spacecraft and Rockets*, vol. 44, no. 6, pp. 1263–1270, Nov. 2007, doi:10.2514/1.30298.
- [64] Heiligers, J., C. R. McInnes, J. D. Biggs, and M. Ceriotti, “Displaced geostationary orbits using hybrid low-thrust propulsion,” *Acta Astronautica*, vol. 71, pp. 51–67, Feb. 2012, doi:10.1016/j.actaastro.2011.08.012.
- [65] Mengali, G. and A. a. Quarta, “Trajectory Design with Hybrid Low-Thrust Propulsion System,” *Journal of Guidance, Control, and Dynamics*, vol. 30, no. 2, pp. 419–426, Mar. 2007, doi:10.2514/1.22433.
- [66] Ceriotti, M. and C. R. McInnes, “Generation of Optimal Trajectories for Earth Hybrid Pole Sitters,” *Journal of Guidance, Control, and Dynamics*, vol. 34, no. 3, pp. 847–859, May 2011, doi:10.2514/1.50935.
- [67] Anderson, P. and M. Macdonald, “Static, Highly Elliptical Orbits Using Hybrid Low-Thrust Propulsion,” *Journal of Guidance, Control, and Dynamics*, vol. 36, no. 3, pp. 870–880, May 2013, doi:10.2514/1.56636.
- [68] Turner, M., *Rocket and spacecraft propulsion: principles, practice and new developments*, Third. New York: Springer, Praxis, 2009.
- [69] Stuhlinger, E., *Ion propulsion for space flight*. McGraw-Hill, 1964.

- [70] Sovey, J., V. Rawlin, and M. Patterson, "Ion propulsion development projects in US: space electric rocket test I to deep space 1," *Journal of Propulsion and Power*. 2001.
- [71] Rayman, M., P. Chadbourne, J. Culwell, and S. Williams, "Mission design for deep space 1: A low-thrust technology validation mission," *Acta Astronautica*. 1999.
- [72] Rayman, M. and P. Varghese, "The deep space 1 extended mission," *Acta Astronautica*, vol. 705, no. 5. pp. 693–705, 2001.
- [73] Rayman, M., T. Fraschetti, C. Raymond, and C. Russell, "Dawn: A mission in development for exploration of main belt asteroids Vesta and Ceres," *Acta Astronautica*, vol. 58, no. 11, pp. 605–616, Jun. 2006, doi:10.1016/j.actaastro.2006.01.014.
- [74] Kim, V., G. Popov, and B. Arkhipov, "Electric propulsion activity in Russia," *IEPC* .... pp. 15–19, 2001.
- [75] Kuninaka, H., K. Nishiyama, and I. Funaki, "Powered flight of electron cyclotron resonance ion engines on Hayabusa explorer," *Journal of propulsion* .... 2007.
- [76] Dudney, R. S., "Rescue in Space," *Air Force Magazine*, no. January, 2012.
- [77] Smith, A., R. Muench, W. Wimmer, D. Heger, X. Marc, F. Bosquillon de Freschville, M. Rosengren, T. Morley, S. Pallashke, B. Smeds, C. Sollazzo, and A. McDonald, "Lost in Space? -ESOC Always Comes to the Rescue," *ESA bulletin*, vol. 117, no. february. pp. 54–63, 2004.
- [78] Boeing, "Boeing 702 Spacecraft," 2013. [Online]. Available: [http://www.boeing.com/assets/pdf/defense-space/space/bss/factsheets/702/bkgd\\_702sp.pdf](http://www.boeing.com/assets/pdf/defense-space/space/bss/factsheets/702/bkgd_702sp.pdf).

- [79] Wallace, N. C. and M. Fehringer, “The ESA GOCE Mission and the T5 Ion Propulsion Assembly,” in *31st International Electric Propulsion Conference*, 2009.
- [80] Wallace, N., C. Saunders, and M. Fehringer, “The In-Orbit Performance and Status of the GOCE Ion Propulsion Assembly (IPA),” in *Space Propulsion 2010 Conference*, 2010.
- [81] Edwards, C. and N. Wallace, “The T5 ion propulsion assembly for drag compensation on GOCE,” *Proc. 2nd int. GOCE user ...*, vol. 2004, no. March. pp. 8–10, 2004.
- [82] Snyder, J. S., D. M. Goebel, R. R. Hofer, J. E. Polk, N. C. Wallace, and H. Simpson, “Performance Evaluation of the T6 Ion Engine,” *Journal of Propulsion and Power*, vol. 28, no. 2, pp. 371–379, Mar. 2012, doi:10.2514/1.B34173.
- [83] Clark, S., N. Wallace, Q. S. Division, and F. Guarducci, “Qualification of the T6 Ion Thruster for the BepiColombo Mission to the Planet Mercury,” in *32nd International Electric Propulsion Conference*, 2011, pp. 1–23.
- [84] Fearn, D., “The development of ion propulsion in the UK: a historical perspective,” in *29th International Electric Propulsion Conference*, 2005, pp. 1–10.
- [85] Huddleson, J., J. Brandon-Cox, N. Wallace, and J. Palencia, “An Overview of the T6 Gridded Ion Propulsion System Pre-development Activities for Alpha-Bus,” in *4th Int. Spacecraft Propulsion Conference, ESASP.555E.72H*, 2004.
- [86] Toki, K., Y. Shimizu, and K. Kuriki, “Development of An MPD thruster system for the EPEX Space Test,” in *23rd International Electric Propulsion Conference*, 1993, pp. 554–561.

- [87] Toki, K., Y. Shimizu, K. Kuriki, and H. Kuninaka, "An MPD Arcjet Thruster System for Electric Propulsion Experiment (EPEX) in Space," in *30th Joint Propulsion Conference and Exhibit*, 1994.
- [88] Toki, K., Y. Shimizu, and K. Kuriki, "Electric propulsion experiment (EPEX) of a repetitively pulsed MPD thruster system onboard space flyer unit (SFU)," in *25th International Electric Propulsion Conference*, 1997, pp. 749–755.
- [89] Petropoulos, A. and J. Longuski, "Shape-based algorithm for the automated design of low-thrust, gravity assist trajectories," *Journal of Spacecraft and Rockets*, vol. 41, no. 5. 2004.
- [90] Wall, B. J. and B. a. Conway, "Shape-Based Approach to Low-Thrust Rendezvous Trajectory Design," *Journal of Guidance, Control, and Dynamics*, vol. 32, no. 1, pp. 95–101, Jan. 2009, doi:10.2514/1.36848.
- [91] Wall, B., "Shape-Based Approximation Method for Low-Thrust Trajectory Optimization," in *AIAA/AAS Astrodynamics Specialist Conference and Exhibit*, American Institute of Aeronautics and Astronautics, 2008.
- [92] Taheri, E. and O. Abdelkhalik, "Shape-Based Approximation of Constrained Low-Thrust Space Trajectories Using Fourier Series," *Journal of Spacecraft and Rockets*, vol. 49, no. 3, pp. 535–545, May 2012, doi:10.2514/1.A32099.
- [93] Novak, D. M. and M. Vasile, "Improved Shaping Approach to the Preliminary Design of Low-Thrust Trajectories," *Journal of Guidance, Control, and Dynamics*, vol. 34, no. 1, pp. 128–147, Jan. 2011, doi:10.2514/1.50434.
- [94] Conway, B., *Spacecraft trajectory optimization*. Cambridge University Press, 2010.

- [95] Marec, J. and N. Vinh, "Optimal low-thrust, limited power transfers between arbitrary elliptical orbits," *Acta Astronautica*, vol. 4, no. October 1976. pp. 511–540, 1977.
- [96] Haissig, C., K. Mease, and N. Vinh, "Minimum-fuel, power-limited transfers between coplanar elliptical orbits," *Acta Astronautica*, vol. 29, no. I. pp. 1–15, 1993.
- [97] McInnes, C., "Low-Thrust Orbit Raising with Coupled Plane Change and J Precession," *Journal of guidance, control, and dynamics*, vol. 20, no. 3. pp. 607–609, 1997.
- [98] Geffroy, S. and R. Epenoy, "Optimal low-thrust transfers with constraints---generalization of averaging techniques," *Acta Astronautica*, vol. 41, no. 3. 1997.
- [99] Kechichian, J., "The treatment of the earth oblateness effect in trajectory optimization in equinoctial coordinates," *Acta astronautica*, vol. 40, no. 1. pp. 69–82, 1997.
- [100] Gao, Y. and C. Kluever, "Analytic orbital averaging technique for computing tangential-thrust trajectories," *Journal of guidance, control, and dynamics*, vol. 28, no. 6. pp. 2–5, 2005.
- [101] Yang, G., "Earth-moon Trajectory Optimization Using Solar Electric Propulsion," *Chinese Journal of Aeronautics*, vol. 20, no. 5, pp. 452–463, Oct. 2007, doi:10.1016/S1000-9361(07)60067-3.
- [102] Spencer, D. B. and R. D. Culp, "Designing continuous-thrust low-Earth-orbit to geosynchronous-Earth-orbit transfers," *Journal of Spacecraft and Rockets*, vol. 32, no. 6, pp. 1033–1038, Nov. 1995, doi:10.2514/3.26726.

- [103] Kluever, C. and S. Oleson, "Direct approach for computing near-optimal low-thrust earth-orbit transfers," *Journal of Spacecraft and Rockets*, vol. 97. Sun Valley, ID, United states, pp. 1783–1800, 1998.
- [104] Kluever, C., "Simple guidance scheme for low-thrust orbit transfers," *Journal of Guidance Control and Dynamics*, vol. 21, no. 6. pp. 19–21, 1998.
- [105] McInnes, C., *Solar sailing: technology, dynamics and mission applications*, First. London: Springer, Praxis, 2004.
- [106] Macdonald, M. and C. McInnes, "Analytical Control Laws for Planet-Centered Solar Sailing," *Journal of Guidance, Control, and Dynamics*, vol. 28, no. 5, pp. 1038–1048, Sep. 2005, doi:10.2514/1.11400.
- [107] Macdonald, M. and C. McInnes, "Realistic earth escape strategies for solar sailing," *Journal of Guidance, Control, and Dynamics*, vol. 28, no. 2, pp. 315–323, Mar. 2005, doi:10.2514/1.5165.
- [108] Macdonald, M., C. R. M. Innes, and Q. City, "Analytic Control Laws for Near-Optimal Geocentric Solar Sail Transfers AAS / AIAA Astrodynamics Specialists Conference." 2001.
- [109] Macdonald, M., C. McInnes, and B. Dachwald, "Heliocentric solar sail orbit transfers with locally optimal control laws," *Journal of Spacecraft and Rockets*, vol. 44, no. 1, pp. 273–276, Jan. 2007, doi:10.2514/1.17297.
- [110] Walker Ireland, B and Owens, J, M. J. H., "A Set of Modified Equinoctial Orbit Elements," in *Celestial Mechanics 36*, D. Reidel Publishing Company, 1985, pp. 409–419.

- [111] Betts, J., “Optimal interplanetary orbit transfers by direct transcription,” *Journal of the Astronautical Sciences*, vol. 42, no. 3, pp. 247–268, 1994.
- [112] Battin, R. H., *An Introduction to the Mathematics and Methods of Astrodynamics, Revised Edition*, Revised Ed. American Institution of Aeronautics and Astronautics, 1999, p. 799.
- [113] Roy, A., *Orbital motion*, Fourth. IOP Publishing, 2005.
- [114] Petropoulos, A. E., “Simple Control Laws for Low-Thrust Orbit Transfers,” in *AAS/AIAA Astrodynamics Specialists Conference*, 2003.
- [115] Sackett, L., L. Malchow, and T. Edelbaum, “Solar electric geocentric transfer with attitude constraints: analysis,” 1975.
- [116] Vallado, D. A., “Orbit Maneuvering,” in *Fundamentals of Astrodynamics and Applications*, 2nd ed., El Segundo and Dordrecht: Microcosm Press and Springer and Kluwer Academic Publishers, 2004, pp. 305–402.
- [117] Edelbaum, T., “How many impulses?,” *Astronautics and Aeronautics*, vol. 5, no. 11, pp. 64–69, 1967.
- [118] Loney, S. L., “Sides and Angles of a Triangle,” in *Plane Trigonometry*, Clay, C. J. and M. A. and Sons, Eds. Cambridge: Cambridge University Press, 1893, pp. 173–188.
- [119] Burden, R. L. and J. D. Faires, “Solutions of Equations in One Variable,” in *Numerical Analysis*, 9th ed., Canada: Cengage Learning, 2011, 2011, pp. 47–104.
- [120] Sidi, M. J., *Spacecraft dynamics and control: a practical engineering approach*, Cambridge . Cambridge University Press, 1997, pp. 73–76.

- [121] Norris, B. J., “Systems human factors: how far have we come?,” *BMJ quality & safety*, vol. 21, no. 9, pp. 713–4, Sep. 2012, doi:10.1136/bmjqs-2011-000476.
- [122] arianespace service and solutions, “Ariane 5 User ’ s Manual,” Boulevard de l’Europe, 2011.
- [123] Broucke, R. and P. Cefola, “On the equinoctial orbit elements,” *Celestial Mechanics*. 1972.
- [124] Dormand, J. R. and P. J. Prince, “A family of embedded Runge-Kutta formulae,” *Journal of Computational and Applied Mathematics*, vol. 6, no. 1, pp. 19–26, Mar. 1980, doi:10.1016/0771-050X(80)90013-3.
- [125] Nocedal, J. and S. J. Wright, *Numerical Optimization*. Springer, 2003, pp. 77–94.
- [126] Various, “LM-3A Series Launch Vehicle User’s Manual,” in *China Academy of Launch Vehicle Technology*, 3rd ed., Beijing: China Academy of Launch Vehicle Technology, 2011, pp. 3.1 – 3.36.
- [127] “LM-3A Series Launch Vehicle User’s Manual,” in *China Academy of Launch Vehicle Technology*, 3rd ed., 2011, pp. 3.1 – 3.36.
- [128] Walters, I., J. Baker, and I. Shurmer, “ORION: A Supersynchronous Transfer Orbit mission,” *Flight Mechanics/Estimation* .... 1995.
- [129] Kimbrel, M., “Optimization of electric propulsion orbit raising.” 2002.
- [130] Spitzer, A., “Novel orbit raising strategy makes low thrust commercially viable,” *IEPC Paper*. 1995.

- [131] Anderson, P., M. Macdonald, and B. Dobke, “Geostationary Equivalent Space-Based Polar Remote Sensing,” 2014.
- [132] Starsem, “Soyuz Launch Manual,” 2001.
- [133] Heiligers, J., M. Ceriotti, C. R. McInnes, and J. D. Biggs, “Design of optimal earth pole-sitter transfers using low-thrust propulsion,” *Acta Astronautica*, vol. 79, pp. 253–268, Oct. 2012, doi:10.1016/j.actaastro.2012.04.025.
- [134] Dyer, C., “Radiation Effects on spacecraft & aircraft,” *Solspa 2001, Proceedings of the Second Solar Cycle ...*, no. 1. 2002.

# APPENDIX A

## A.1. Optimisation Study Results

### A.1.1. LEO-GEO

Table A-1 3299.69 kg wet mass time specified LEO – GEO comparison. A – Analytical, HTPC – High-Thrust Plane Change, LTPC – Low-Thrust Plane Change

Wet Mass, $m_{wet}$ (kg)		3299.69		
Transfer	A	HTPC	LTPC	
HST Dry Mass (kg)	908.76	1130.49	946.15	
HST Transfer Time (days)	90.00	89.92	89.65	
Hohmann Dry Mass (kg)	864.39	863.97	863.97	
HST Fuel Mass (kg)	2390.93	2169.20	2353.54	
$R2$	6.41	8.46	9.20	
Intermediate Orbit Eccentricity	0	0.73	0.22	
<b>Saving compared to Hohmann (kg)</b>	44.37	266.52	82.18	
<b>Saving compared to Hohmann (% of <math>m_{wet}</math>)</b>	1.34	8.08	2.49	

**Table A-2 4402.27 kg wet mass time specified LEO – GEO comparison. A – Analytical, HTPC – High-Thrust Plane Change, LTPC – Low-Thrust Plane Change**

<b>Wet Mass, <math>m_{wet}</math> (kg)</b>	<b>4402.27</b>		
<b>Transfer</b>	<b>A</b>	<b>HTPC</b>	<b>LTPC</b>
HST Dry Mass (kg)	1212.42	1510.16	1297.43
HST Transfer Time (days)	120.00	119.96	119.45
Hohmann Dry Mass (kg)	1153.23	1152.66	1152.66
HST Fuel Mass (kg)	3189.85	2892.11	3104.84
<i>R2</i>	6.41	8.31	10.14
Intermediate Orbit Eccentricity	0	0.73	0.30
<b>Saving compared to Hohmann (kg)</b>	59.20	357.50	144.77
<b>Saving compared to Hohmann (% of <math>m_{wet}</math>)</b>	1.34	8.12	3.29

**Table A-3 5504.85 kg wet mass time specified LEO – GEO comparison. A – Analytical, HTPC – High-Thrust Plane Change, LTPC – Low-Thrust Plane Change**

<b>Wet Mass, <math>m_{wet}</math> (kg)</b>	<b>5504.85</b>		
<b>Transfer</b>	<b>A</b>	<b>HTPC</b>	<b>LTPC</b>
HST Dry Mass (kg)	1516.09	1889.61	1625.42
HST Transfer Time (days)	150.00	149.99	149.70
Hohmann Dry Mass (kg)	1442.06	1441.35	1441.35
HST Fuel Mass (kg)	3988.76	3615.24	3879.43
<i>R2</i>	6.41	8.25	10.67
Intermediate Orbit Eccentricity	0	0.73	0.32
<b>Saving compared to Hohmann (kg)</b>	74.03	448.25	184.07
<b>Saving compared to Hohmann (% of <math>m_{wet}</math>)</b>	1.34	8.14	3.34

## A.1.2. GTO-GEO

**Table A-4 1527.13 kg wet mass time Specified GTO – GEO Comparison. A – Analytical, HTPC – High-Thrust Plane Change, LTPC – Low-Thrust Plane Change**

Wet Mass, $m_{wet}$ (kg)	1527.13		
Transfer	A	HTPC	LTPC
HST Dry Mass (kg)	908.76	1123.88	922.20
HST Transfer Time (days)	90.00	89.99	89.88
Hohmann Dry Mass (kg)	858.35	857.82	857.82
HST Fuel Mass (kg)	618.37	403.25	604.93
$R_2$	6.41	8.28	8.47
Intermediate Orbit Eccentricity	0	0.73	0.14
<b>Saving compared to Hohmann (kg)</b>	50.42	266.05	64.37
<b>Saving compared to Hohmann (% of <math>m_{wet}</math>)</b>	3.30	17.42	4.22

**Table A-5 2037.42 kg wet mass time Specified GTO – GEO Comparison. A – Analytical, HTPC – High-Thrust Plane Change, LTPC – Low-Thrust Plane Change**

<b>Wet Mass, <math>m_{wet}</math> (kg)</b>			
<b>2037.42</b>			
<b>Transfer</b>	<b>A</b>	<b>HTPC</b>	<b>LTPC</b>
HST Dry Mass (kg)	1212.42	1500.36	1234.05
HST Transfer Time (days)	120.00	120.06	119.98
Hohmann Dry Mass (kg)	1145.16	1144.47	1144.47
HST Fuel Mass (kg)	824.99	537.06	803.37
<i>R2</i>	6.41	8.20	7.14
Intermediate Orbit Eccentricity	0	0.73	0.08
<b>Saving compared to Hohmann (kg)</b>	<b>67.26</b>	<b>355.90</b>	<b>89.59</b>
<b>Saving compared to Hohmann (% of <math>m_{wet}</math>)</b>	<b>3.30</b>	<b>17.47</b>	<b>4.40</b>

**Table A-6 2547.7 kg wet mass time Specified GTO – GEO Comparison. A – Analytical, HTPC – High-Thrust Plane Change, LTPC – Low-Thrust Plane Change**

<b>Wet Mass, <math>m_{wet}</math> (kg)</b>	<b>2547.7</b>		
<b>Transfer</b>	<b>A</b>	<b>HTPC</b>	<b>LTPC</b>
HST Dry Mass (kg)	1516.09	1866.54	1668.54
HST Transfer Time (days)	150.00	149.72	149.86
Hohmann Dry Mass (kg)	1431.67	1431.10	1431.10
HST Fuel Mass (kg)	1031.62	681.16	879.16
<i>R2</i>	6.41	8.83	11.56
Intermediate Orbit Eccentricity	0	0.73	0.40
<b>Saving compared to Hohmann (kg)</b>	84.11	435.44	237.44
<b>Saving compared to Hohmann (% of <math>m_{wet}</math>)</b>	3.30	17.09	9.32

## A.2. Transfer Profiles

### A.2.1. LEO-GEO

#### A.2.1.1. High-Thrust Plane Change

##### A.2.1.1.1. Wet Mass = 3299.69 kg

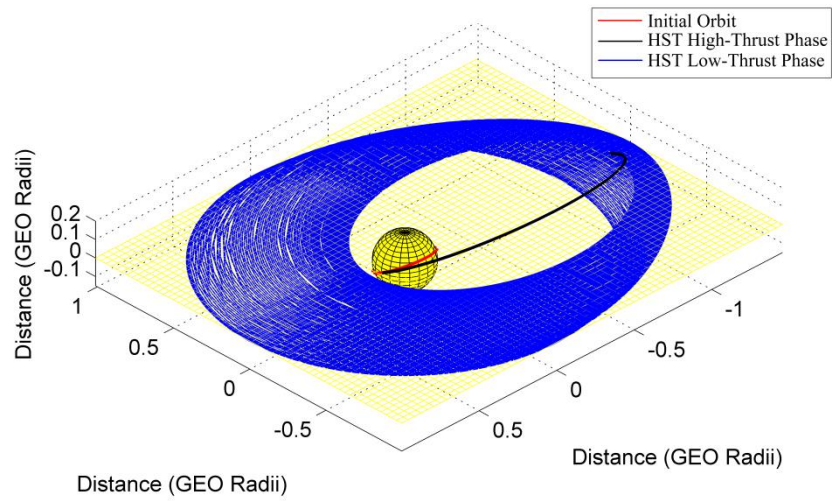


**Figure A-1 LEO – GEO, HST with High-Thrust Plane Change**

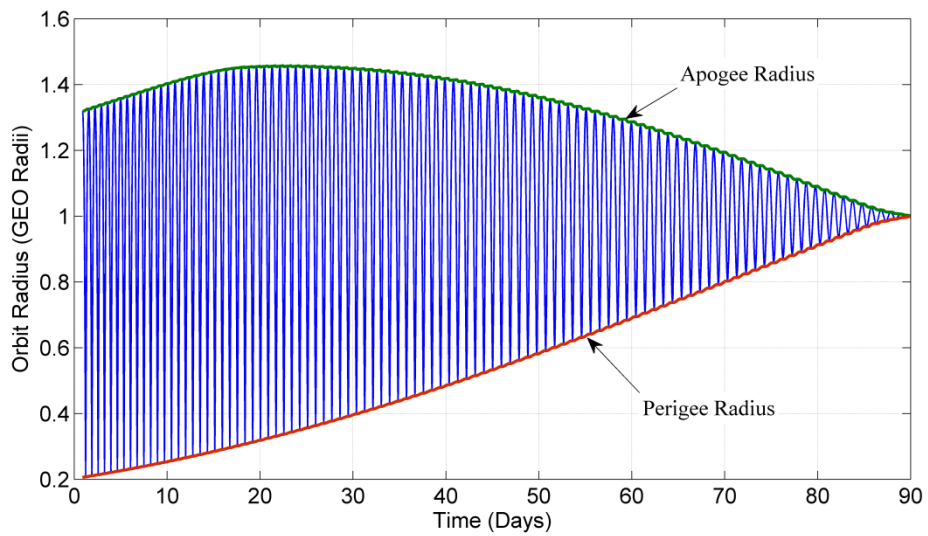


**Figure A-2 LEO – GEO, HST with High-Thrust Plane Change Orbit Radius Profile**

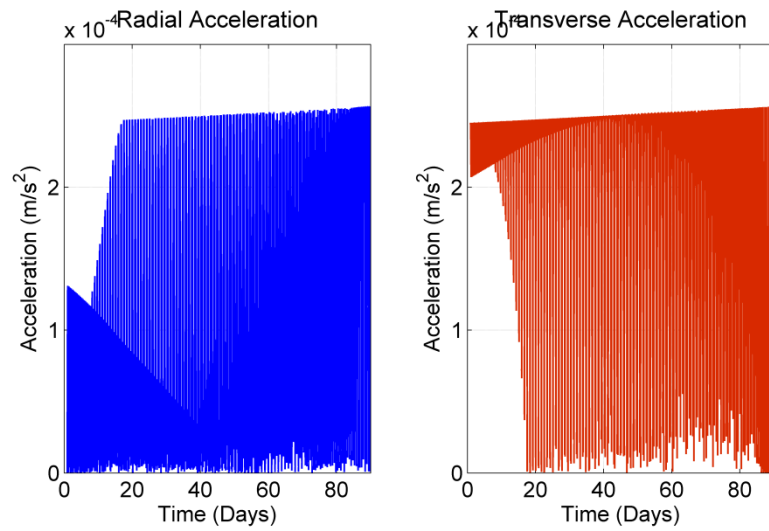


**Figure A-3 LEO – GEO, HST with High-Thrust Plane Change Acceleration Profile**

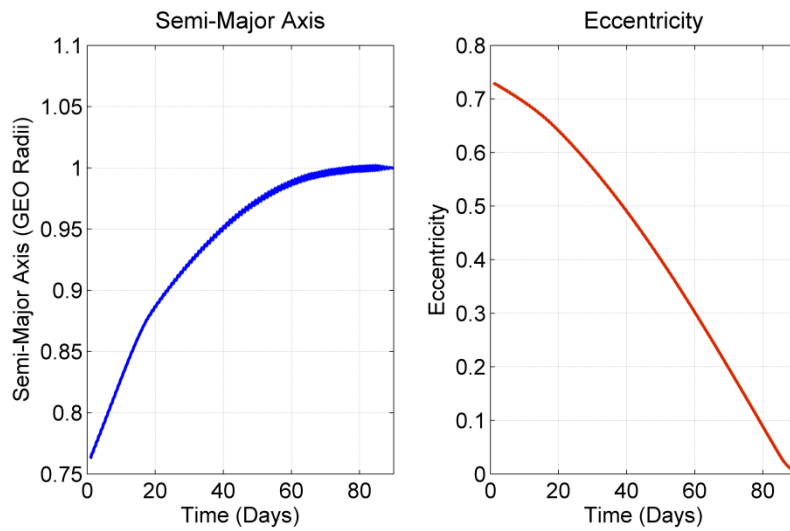


Figure A-4 LEO – GEO, HST with High-Thrust Plane Change Orbital Element Profiles

A.2.1.1.2. Wet Mass = 4402.27 kg

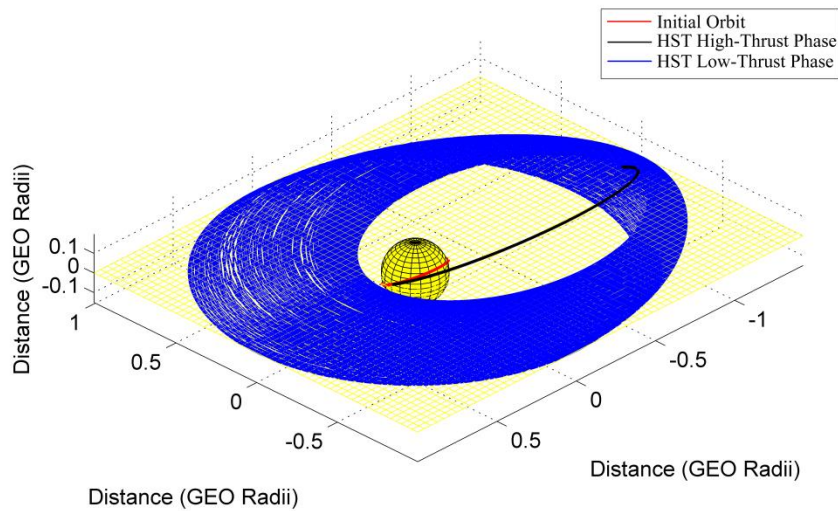
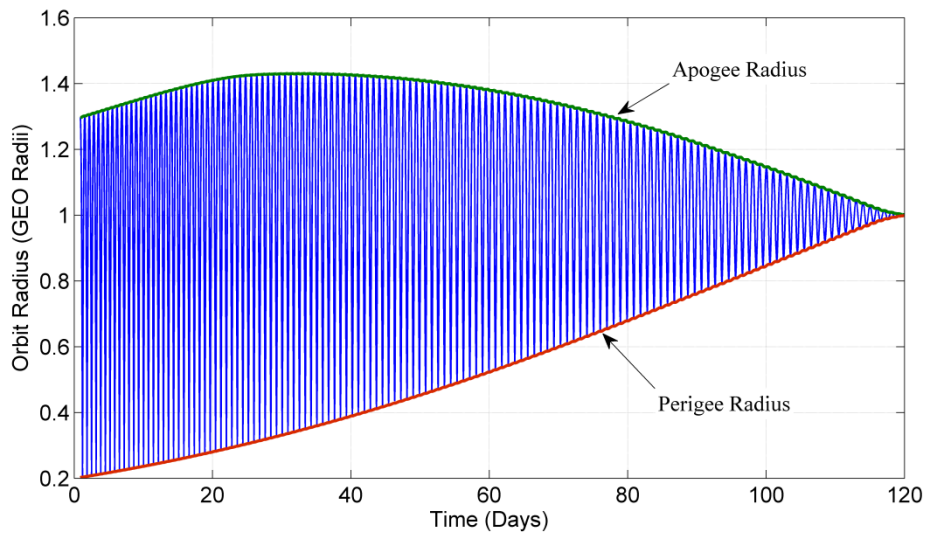
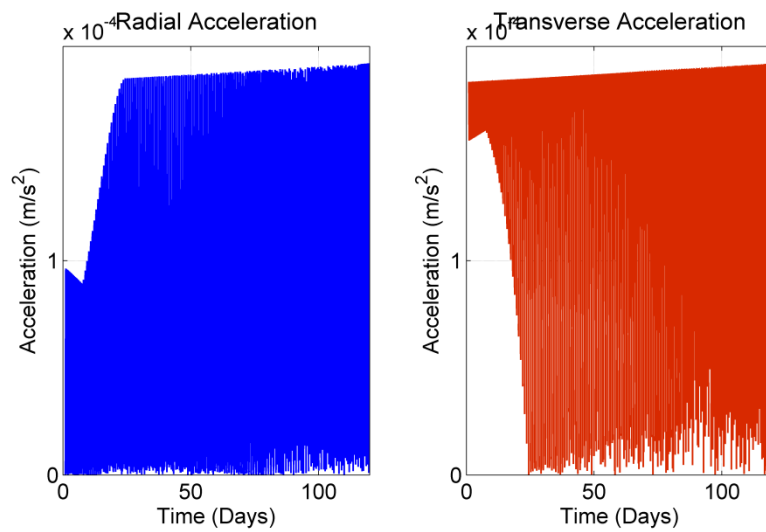


Figure A-5 LEO – GEO, HST with High-Thrust Plane Change



**Figure A-6 LEO – GEO, HST with High-Thrust Plane Change Orbit Radius Profile**



**Figure A-7 LEO – GEO, HST with High-Thrust Plane Change Acceleration Profile**

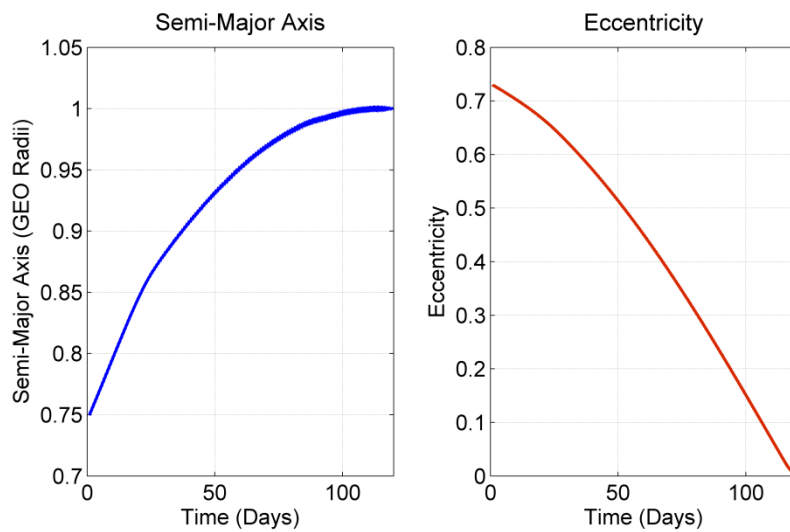


**Figure A-8 LEO – GEO, HST with High-Thrust Plane Change Orbital Element Profiles**

### A.2.1.1.3. Wet Mass = 5504.85 kg

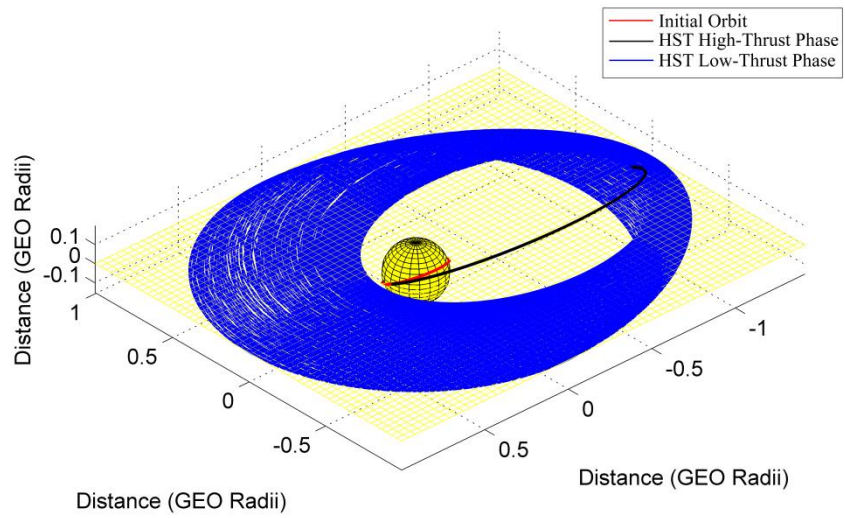


**Figure A-9 LEO – GEO, HST with High-Thrust Plane Change**

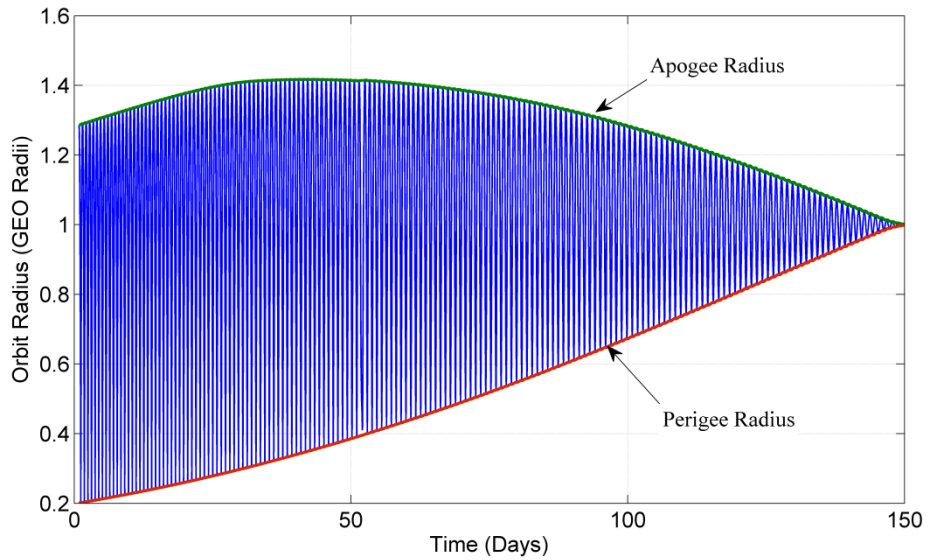


**Figure A-10 LEO – GEO, HST with High-Thrust Plane Change Orbit Radius Profile**

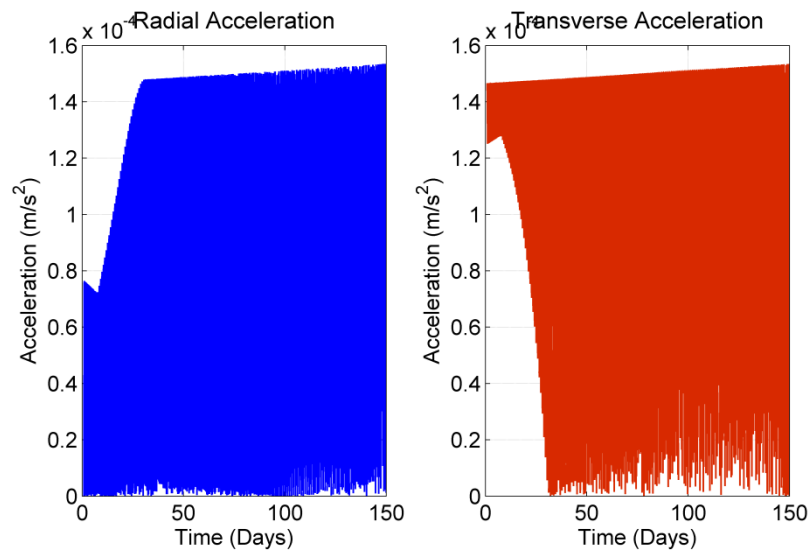


Figure A-11 LEO – GEO, HST with High-Thrust Plane Change Acceleration Profile

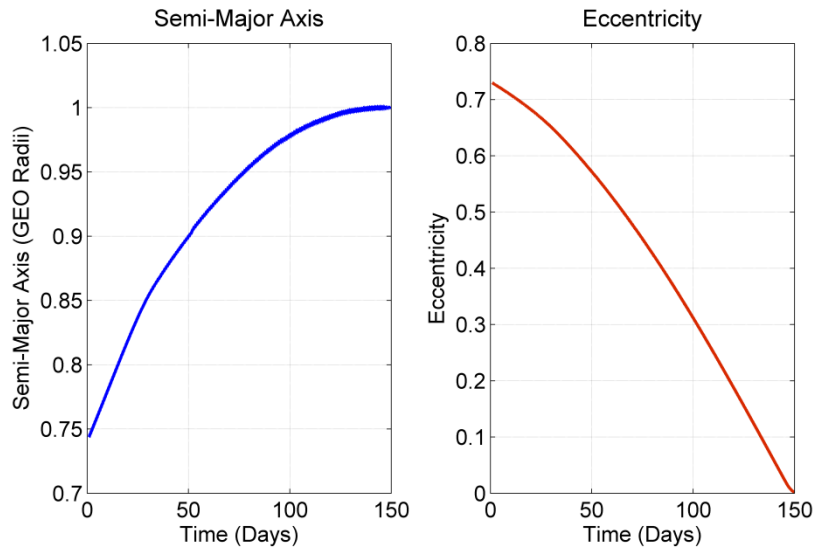
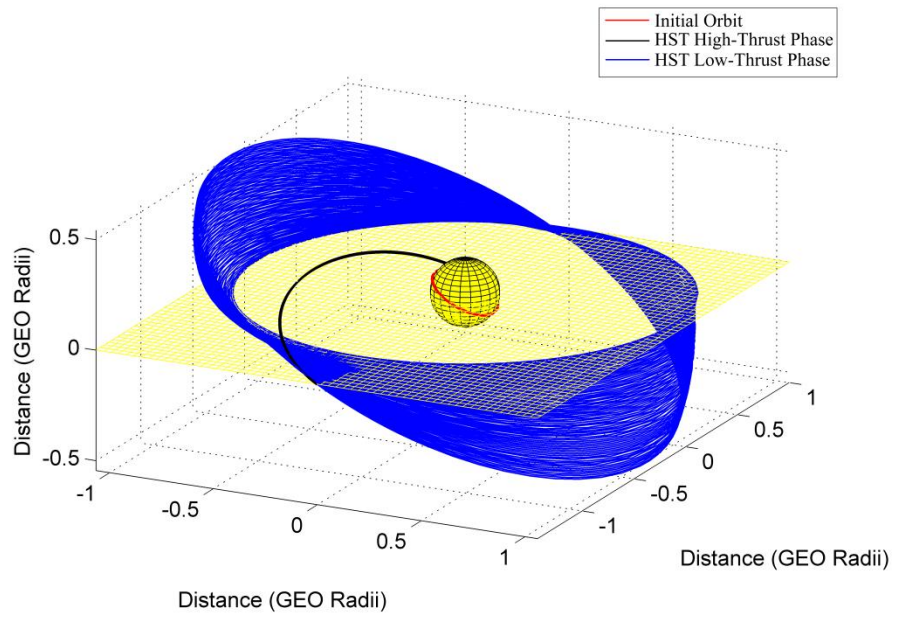


Figure A-12 LEO – GEO, HST with High-Thrust Plane Change Orbital Element Profiles

## A.2.1.2. Low-Thrust Plane Change

### A.2.1.2.1. Wet Mass = 3299.69 kg



**Figure A-13 LEO – GEO, HST with Low-Thrust Plane Change**

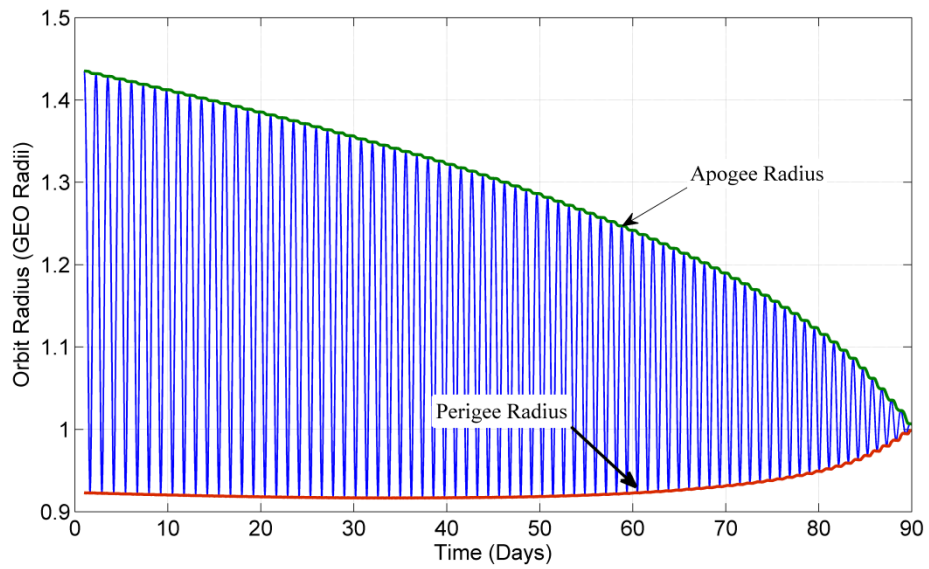


**Figure A-14 LEO – GEO, HST with Low-Thrust Plane Change Orbit Radius Profile**

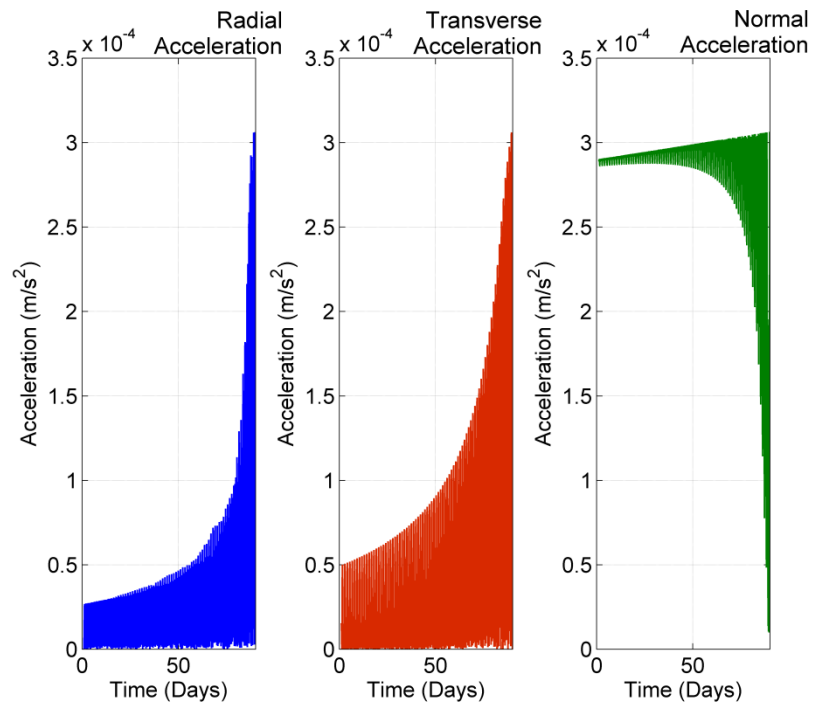


Figure A-15 LEO – GEO, HST with Low-Thrust Plane Change Acceleration Profile

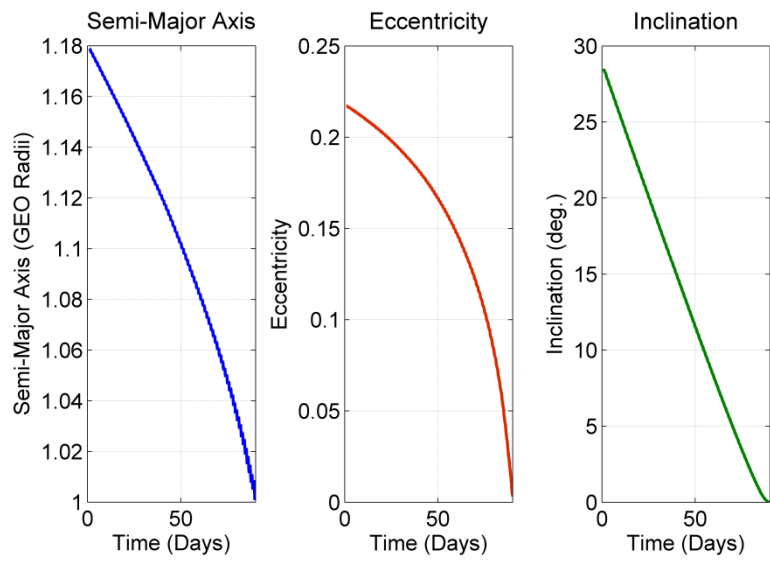
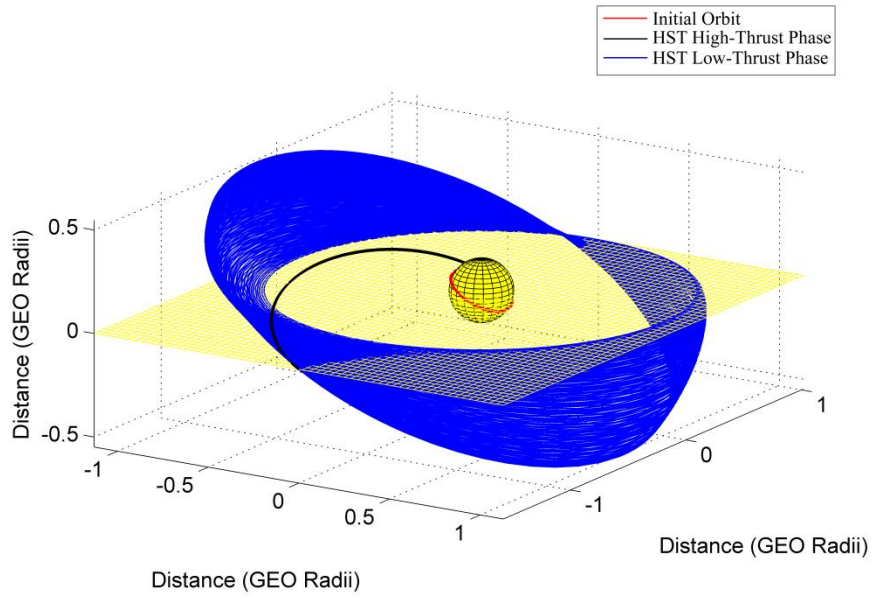
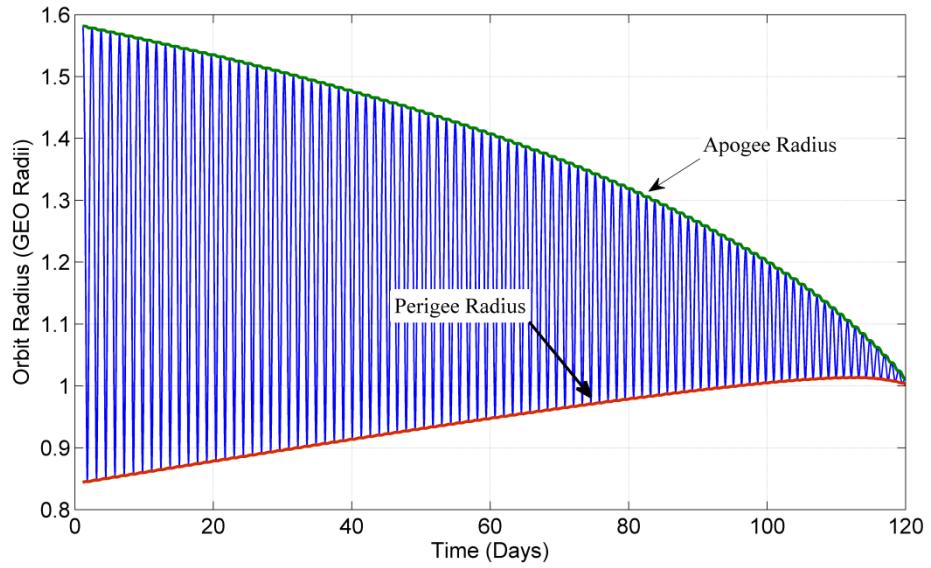


Figure A-16 LEO – GEO, HST with Low-Thrust Plane Change Orbital Element Profiles



**Figure A-17 LEO – GEO, HST with Low-Thrust Plane Change**



**Figure A-18 LEO – GEO, HST with Low-Thrust Plane Change Orbit Radius Profile**

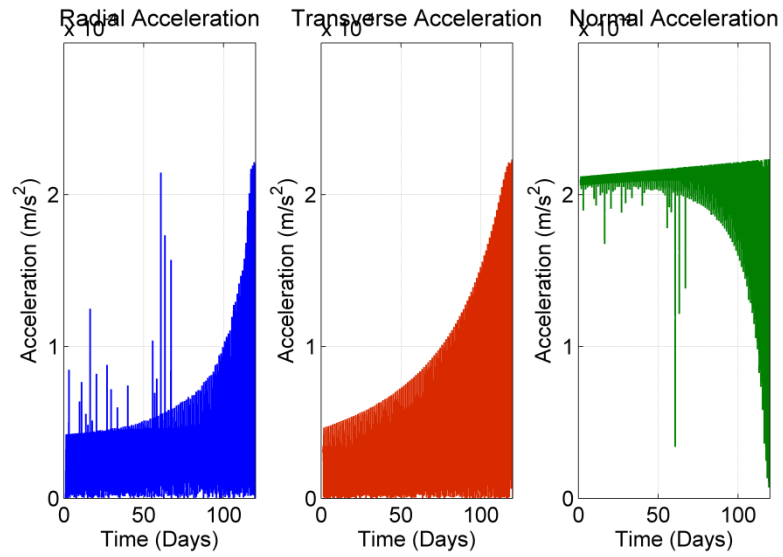


Figure A-19 LEO – GEO, HST with Low-Thrust Plane Change Acceleration Profile

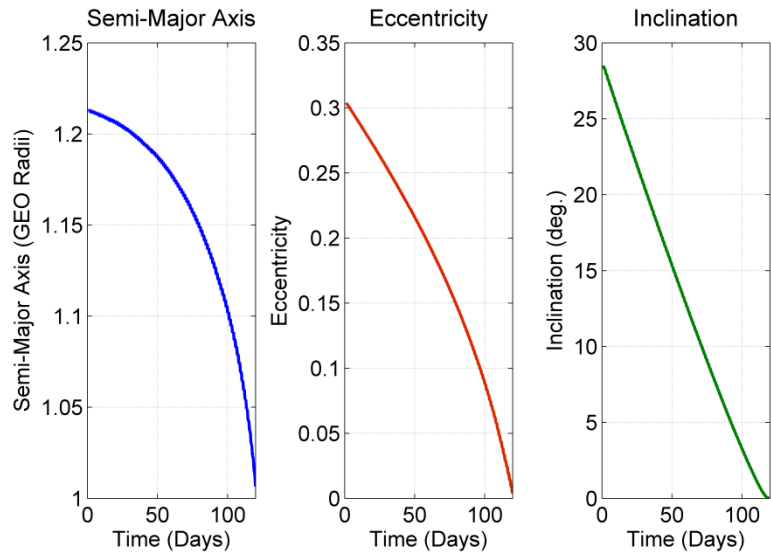
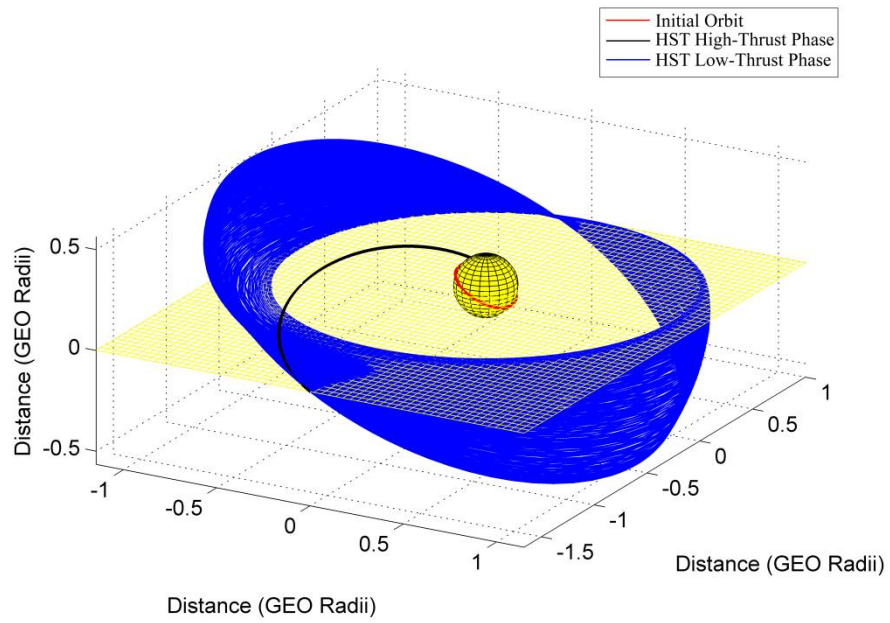
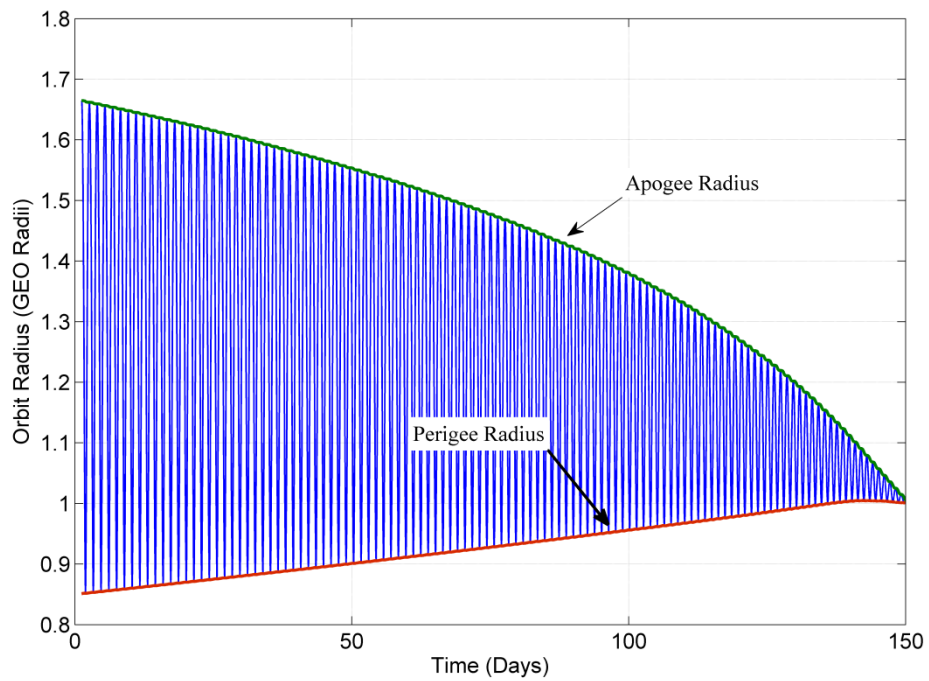


Figure A-20 LEO – GEO, HST with Low-Thrust Plane Change Orbital Element Profiles

A.2.1.2.2. Wet Mass = 5504.85 kg



**Figure A-21 LEO – GEO, HST with Low-Thrust Plane Change**



**Figure A-22 LEO – GEO, HST with Low-Thrust Plane Change Orbit Radius Profile**

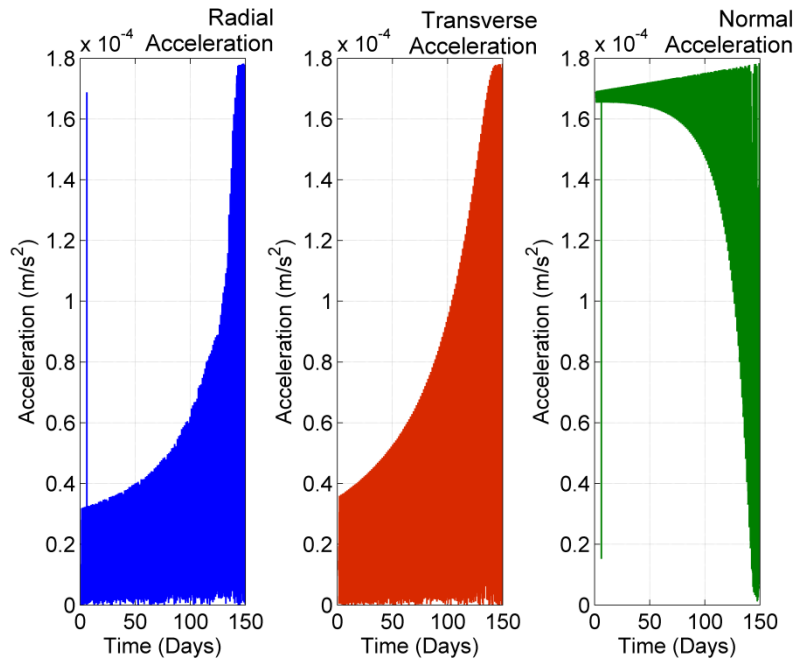


Figure A-23 LEO – GEO, HST with Low-Thrust Plane Change Acceleration Profile

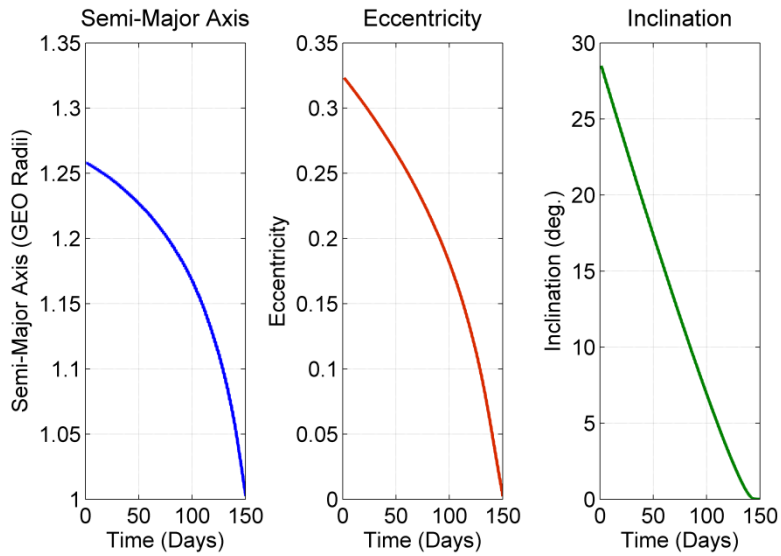
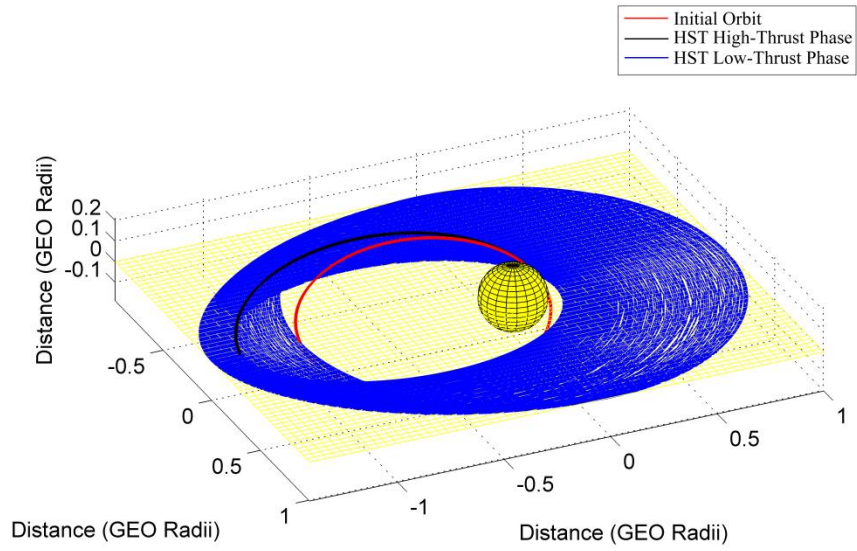


Figure A-24 LEO – GEO, HST with Low-Thrust Plane Change Orbital Element Profiles

## A.2.2. GTO-GEO

### A.2.2.1. High-Thrust Plane Change

#### A.2.2.1.1. Wet Mass = 2037.42 kg



**Figure A-25 GTO – GEO, HST with High-Thrust Plane Change**

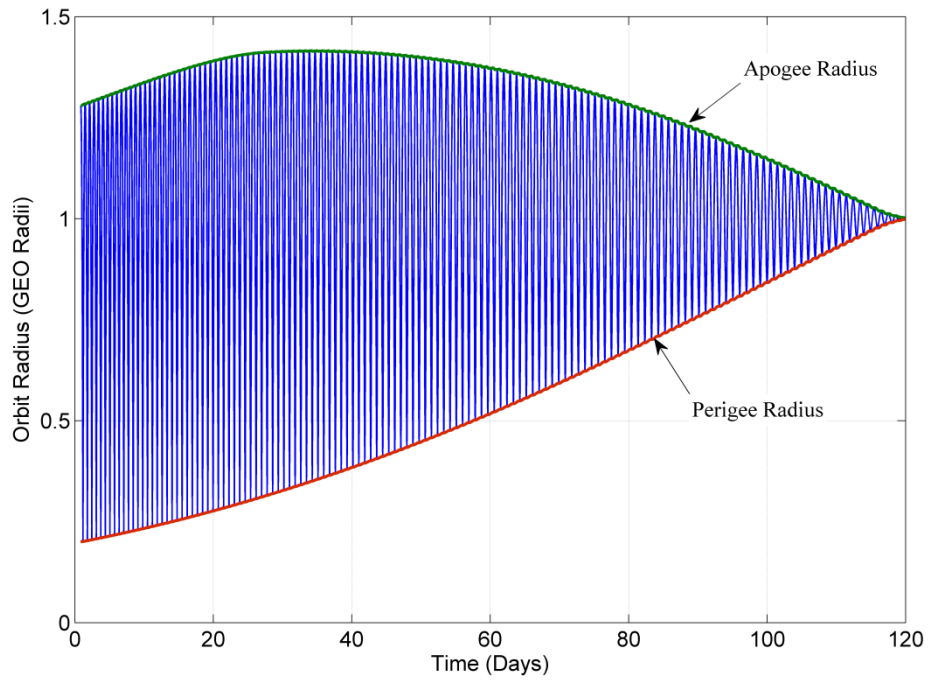


**Figure A-26 GTO – GEO, HST with High-Thrust Plane Change Orbit Radius Profile**

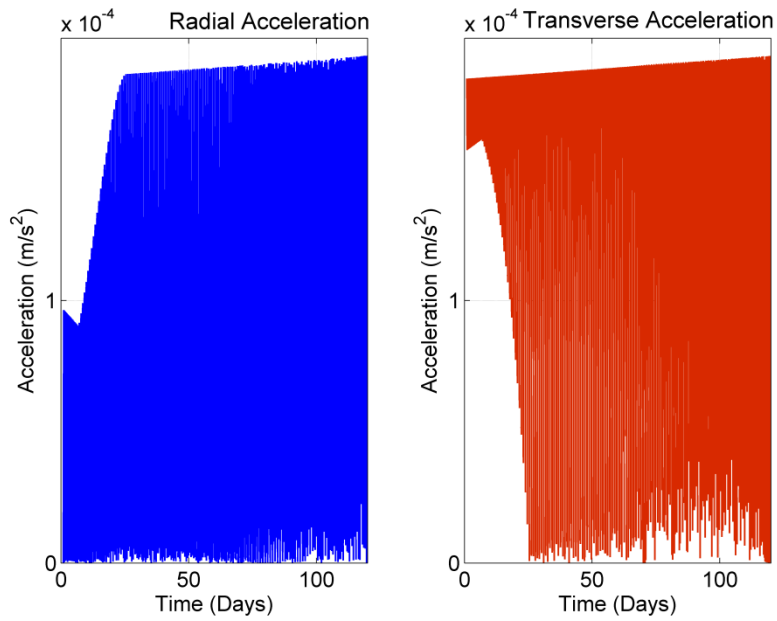


Figure A-27 GTO – GEO, HST with High-Thrust Plane Change Acceleration Profile

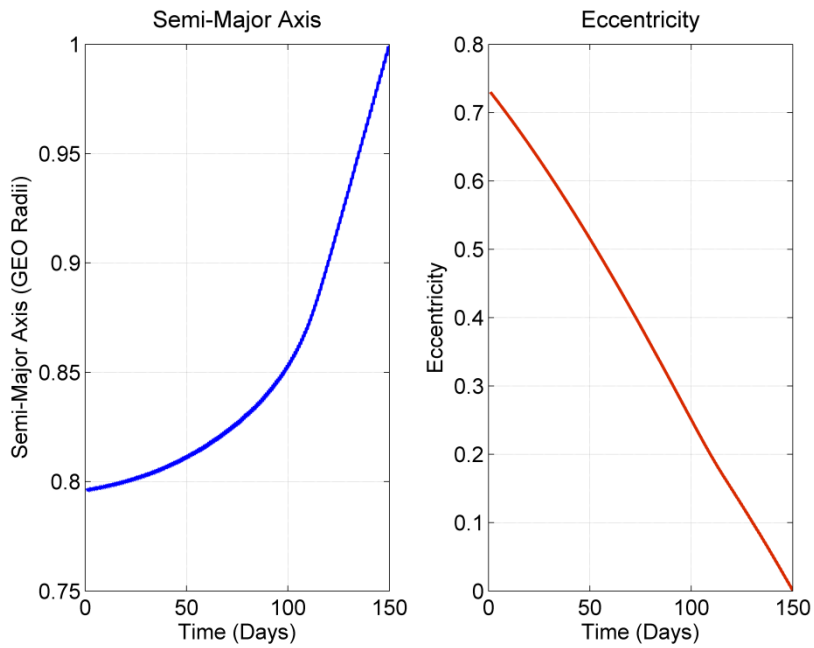
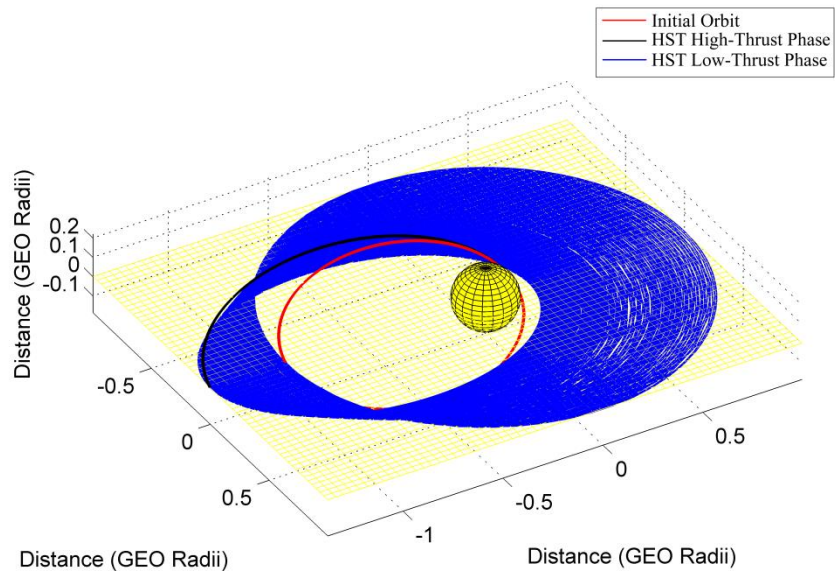
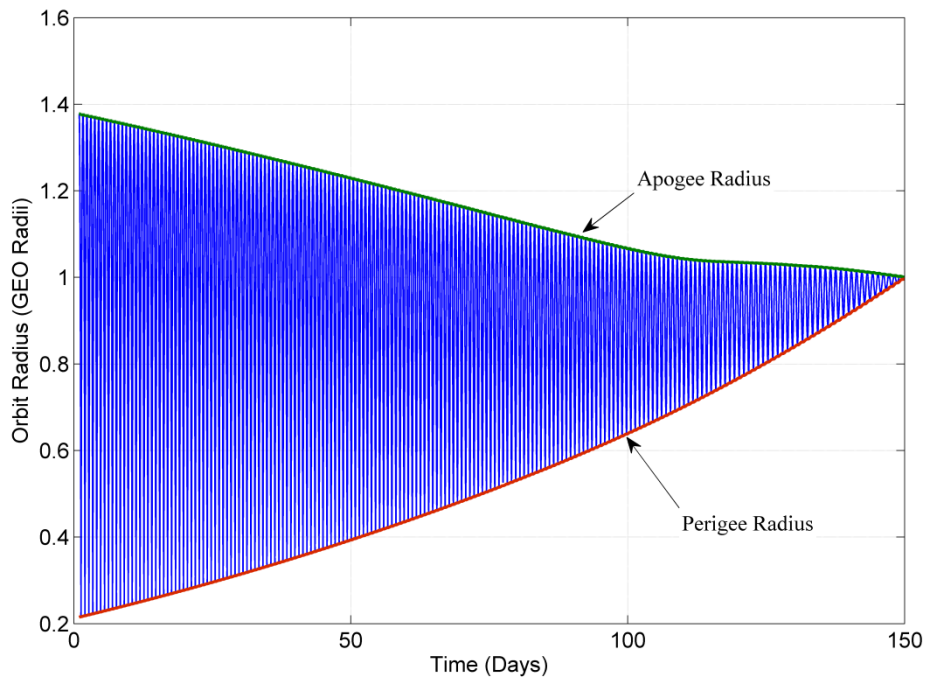


Figure A-28 GTO – GEO, HST with High-Thrust Plane Change Orbital Element Profiles

A.2.2.1.2. Wet Mass = 2547.7 kg



**Figure A-29 GTO – GEO, HST with High-Thrust Plane Change**



**Figure A-30 GTO – GEO, HST with High-Thrust Plane Change Orbit Radius Profile**

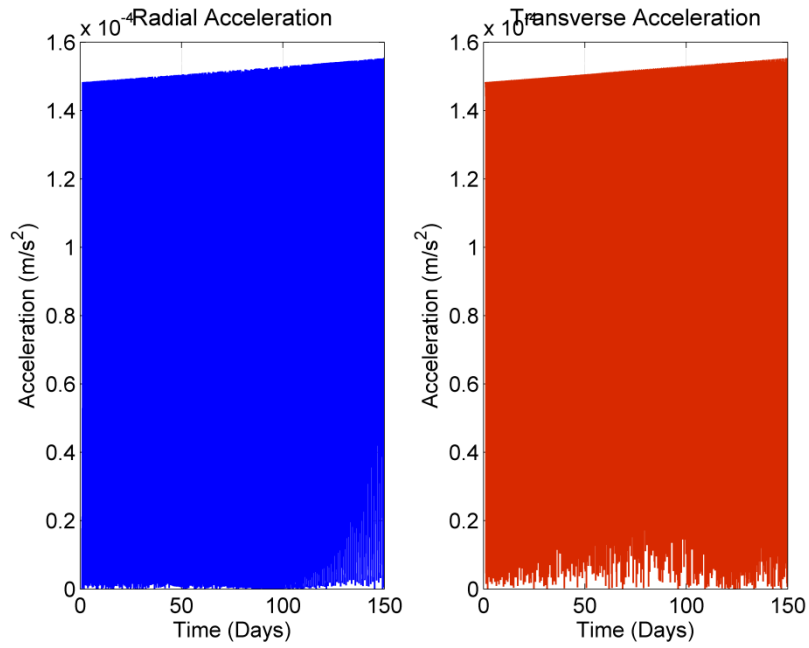


Figure A-31 GTO – GEO, HST with High-Thrust Plane Change Acceleration Profile

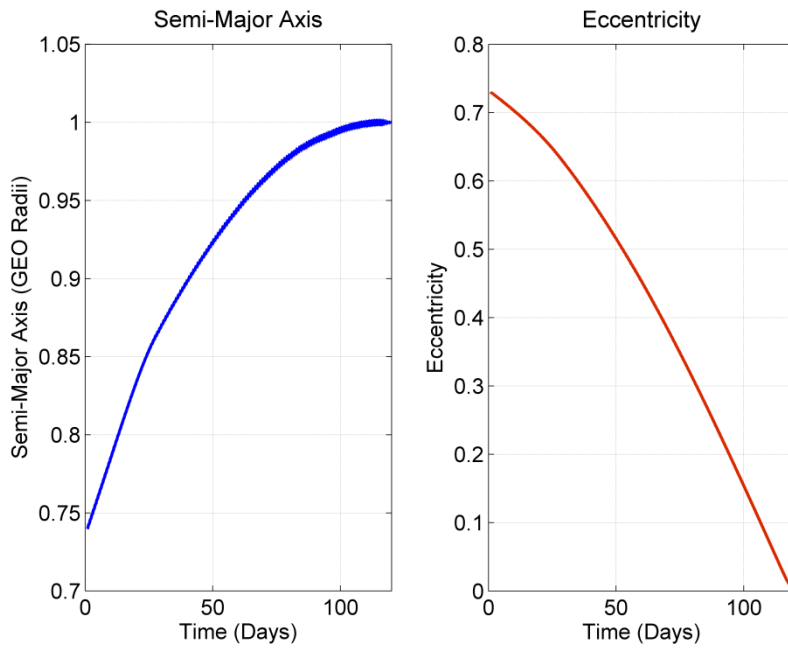
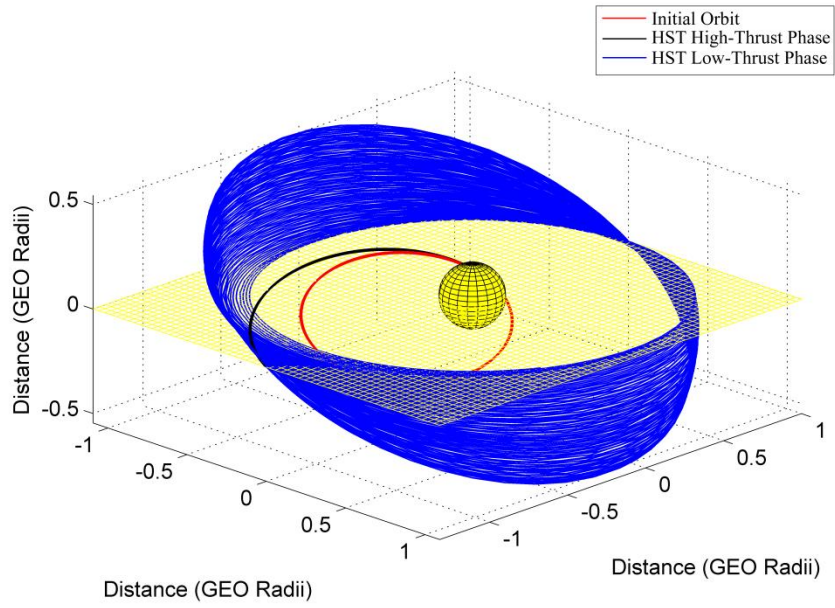


Figure A-32 GTO – GEO, HST with High-Thrust Plane Change Orbital Element Profiles

## A.2.2.2. Low-Thrust Plane Change

### A.2.2.2.1. Wet Mass = 1527.13 kg



**Figure A-33 GTO – GEO, HST with Low-Thrust Plane Change**

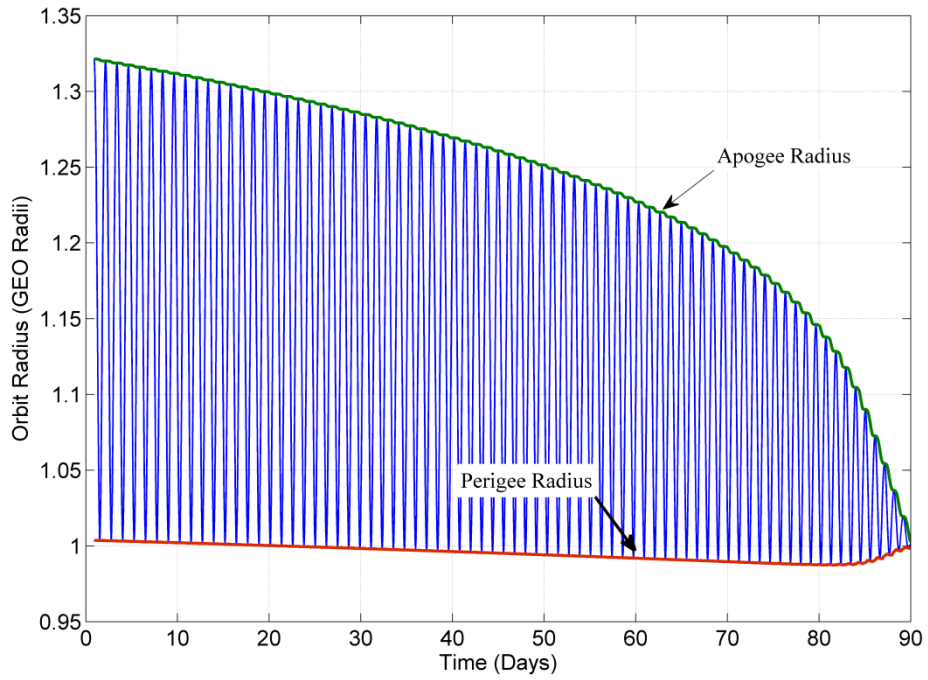


**Figure A-34 GTO – GEO, HST with Low-Thrust Plane Change Orbit Radius Profile**

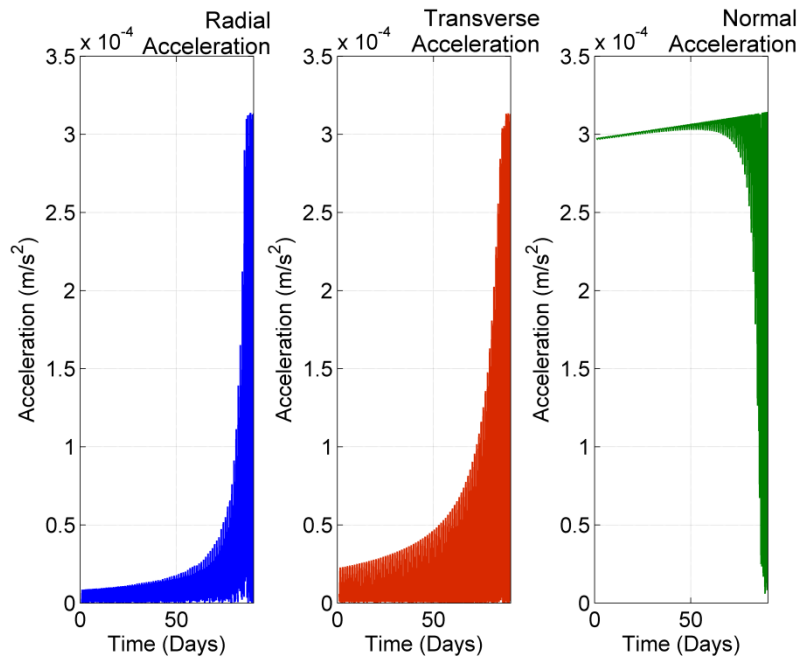


Figure A-35 GTO – GEO, HST with Low-Thrust Plane Change Acceleration Profile

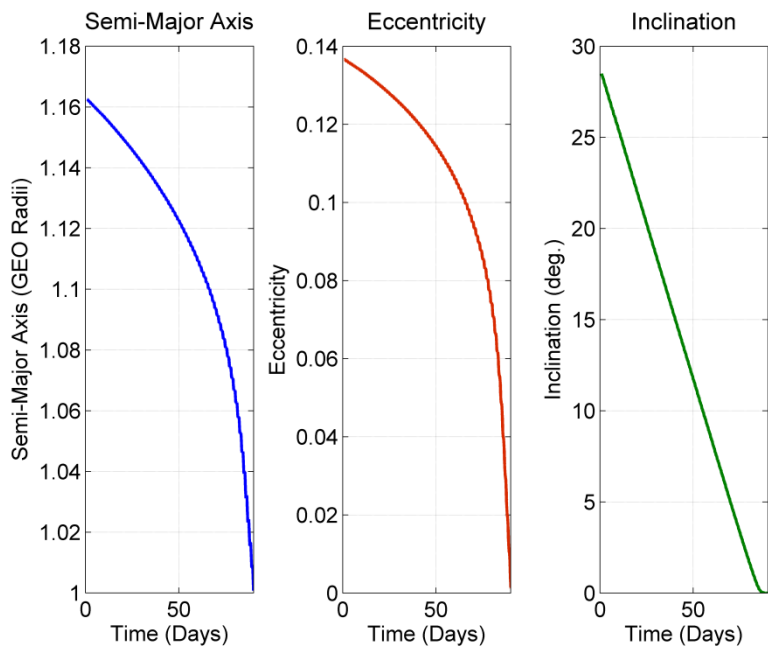
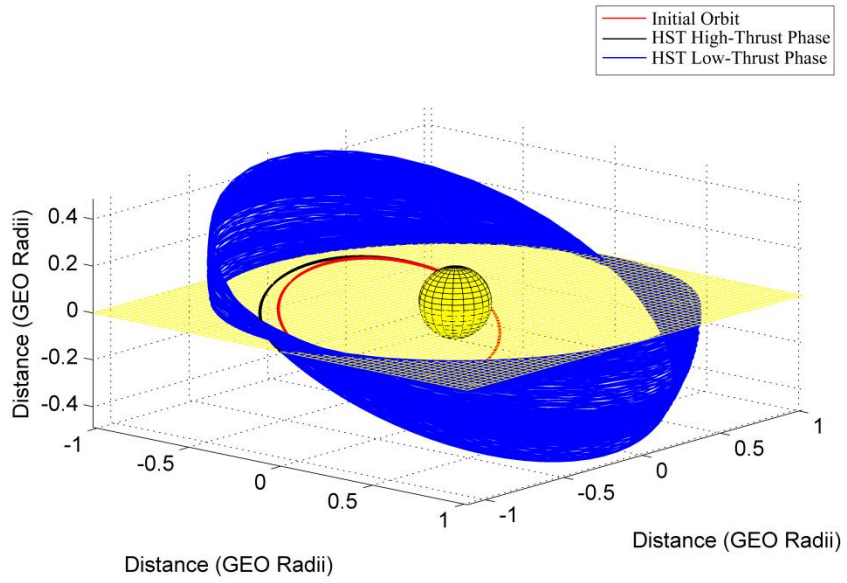
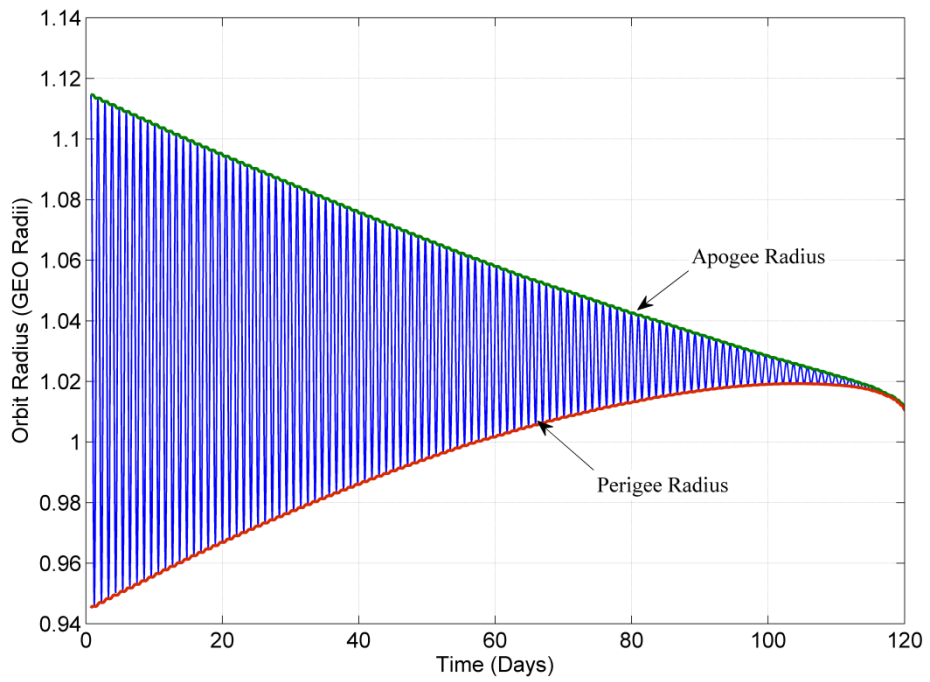


Figure A-36 GTO – GEO, HST with Low-Thrust Plane Change Orbital Element Profiles

A.2.2.2.2. Wet Mass = 2037.42 kg



**Figure A-37 GTO – GEO, HST with Low-Thrust Plane Change**



**Figure A-38 GTO – GEO, HST with Low-Thrust Plane Change Orbit Radius Profile**

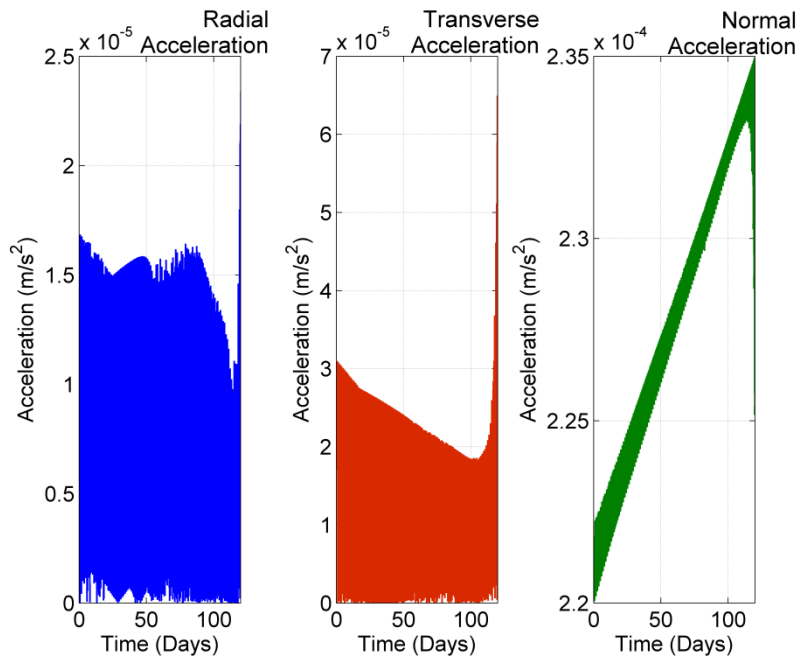


Figure A-39 GTO – GEO, HST with Low-Thrust Plane Change Acceleration Profile

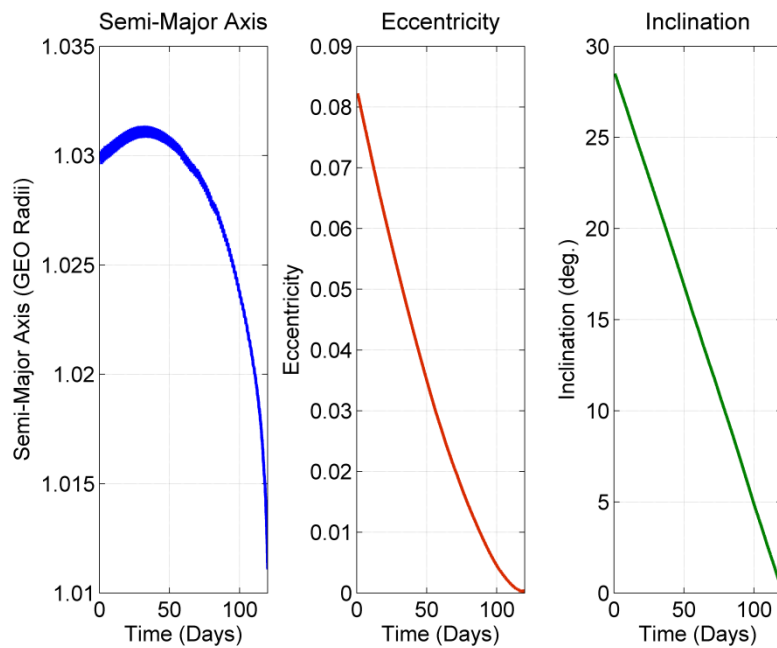
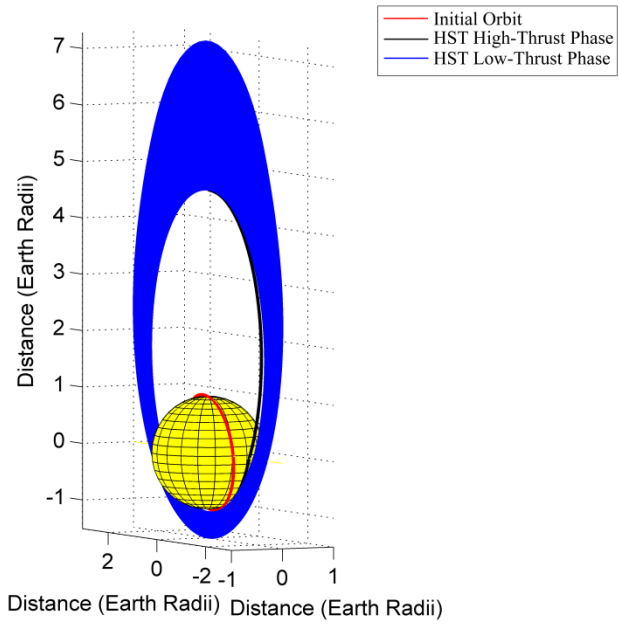


Figure A-40 GTO – GEO, HST with Low-Thrust Plane Change Orbital Element Profiles

## A.2.3. SSO – Highly Elliptical Polar Orbit

### A.2.3.1. 12 hour Orbit - HST with High-Thrust Plane Change



**Figure A-41 SSO – Highly Elliptical 12 Hour Polar Orbit, HST with High-Thrust Plane Change**

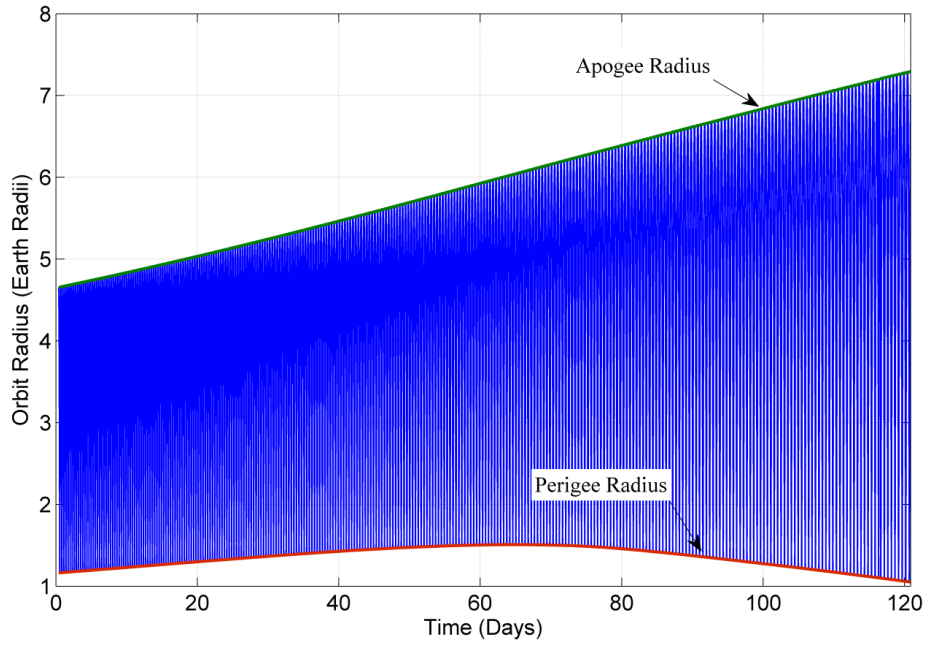


**Figure A-42 SSO – Highly Elliptical 12 Hour Polar Orbit, HST with High-Thrust Plane Change Orbit Radius Profile**

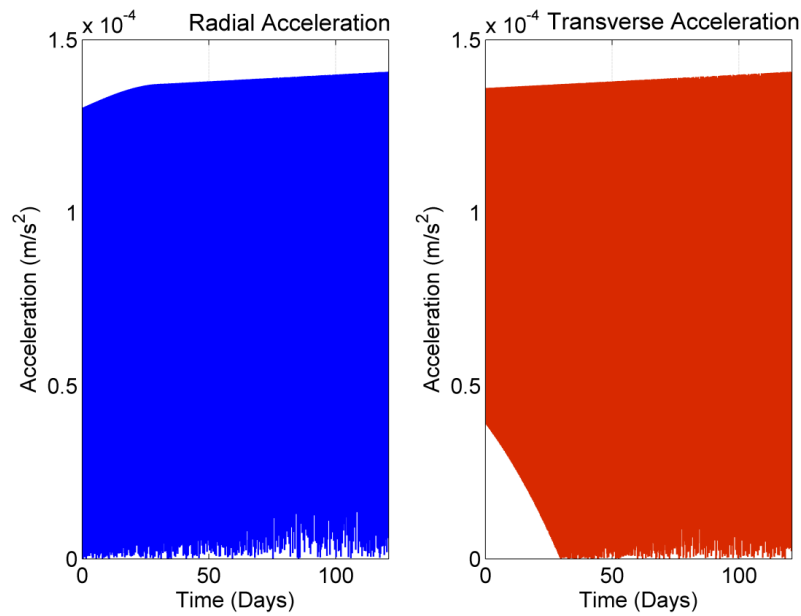


**Figure A-43 SSO – Highly Elliptical 12 Hour Polar Orbit, HST with High-Thrust Plane Change Acceleration Profile**

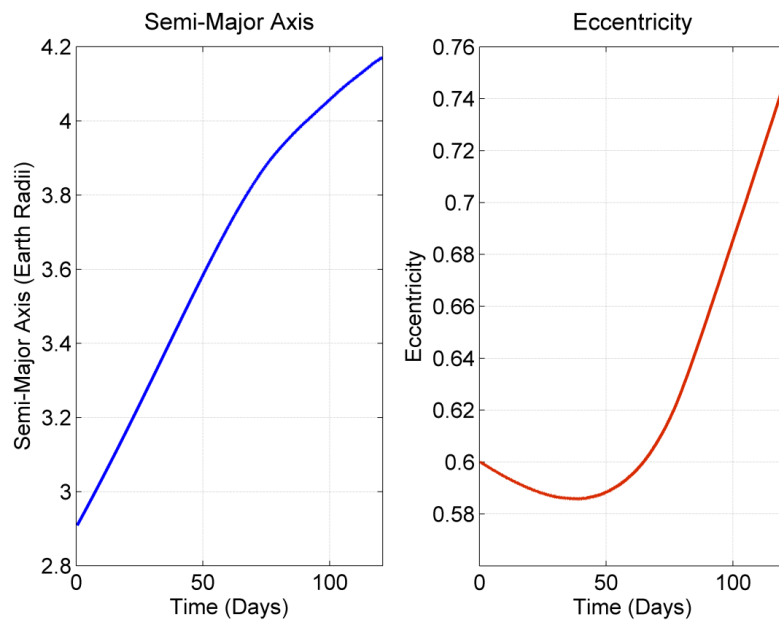


**Figure A-44 SSO – Highly Elliptical 12 Hour Polar Orbit, HST with High-Thrust Plane Change Orbital Element Profiles**

### A.2.3.2. 16 hour Orbit - HST with Low-Thrust Plane Change

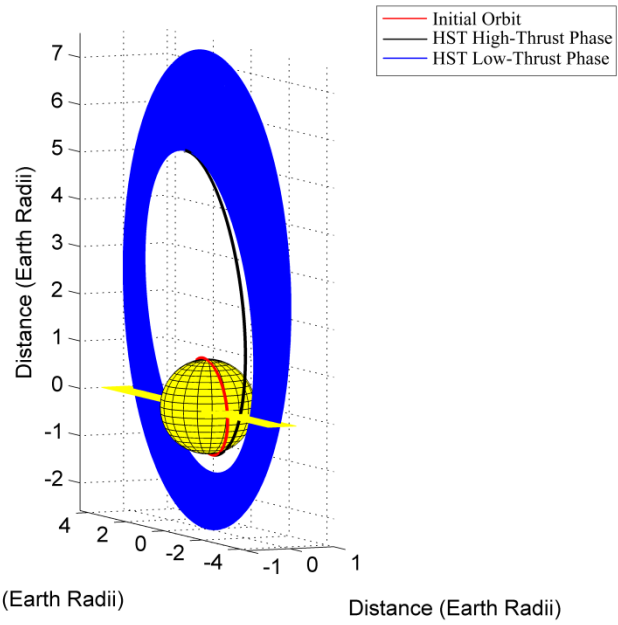


**Figure A-45 SSO – Highly Elliptical 16 Hour Polar Orbit, HST with Low-Thrust Plane Change**

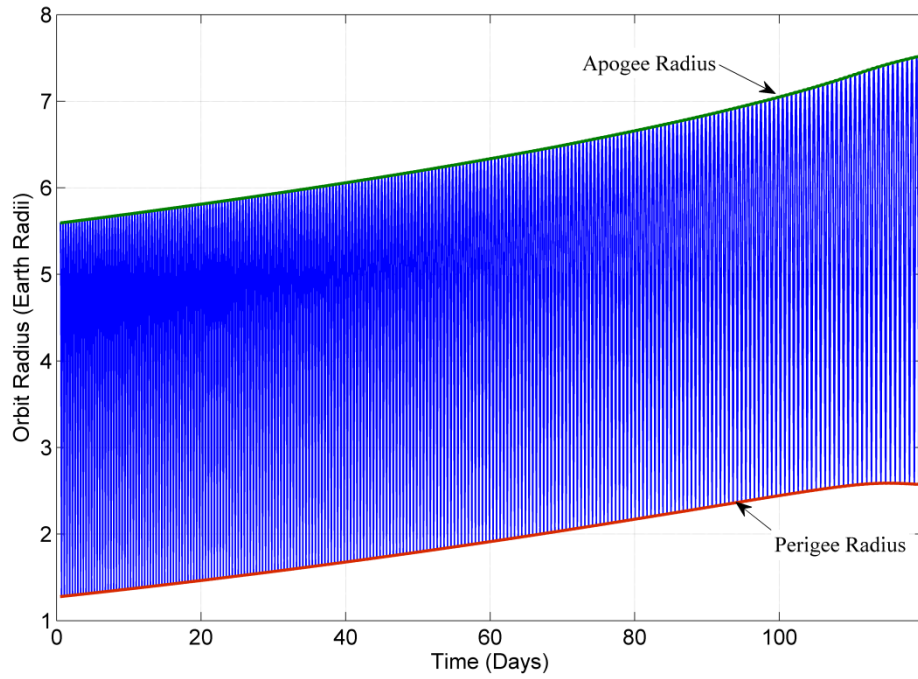


**Figure A-46 SSO – Highly Elliptical 16 Hour Polar Orbit, HST with Low-Thrust Plane Change Orbit Radius Profile**

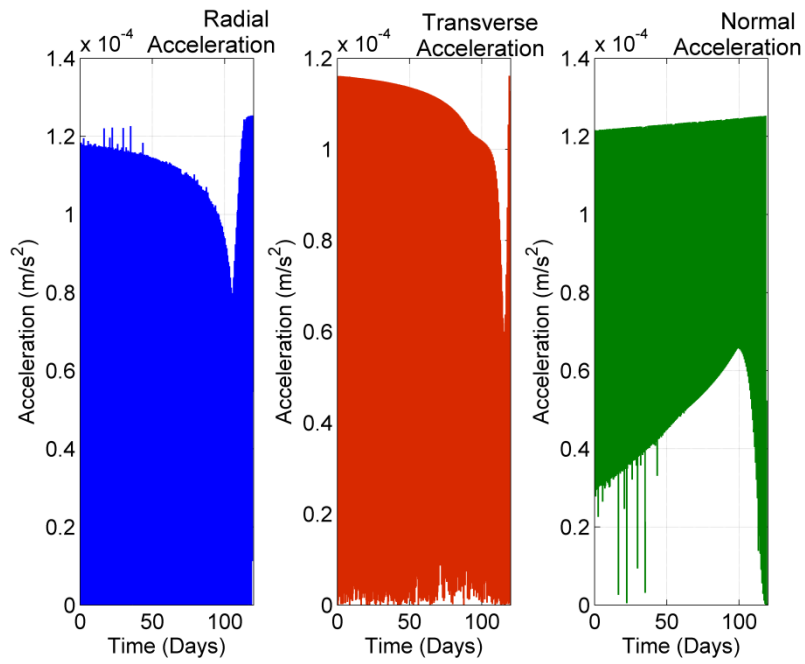


**Figure A-47 SSO – Highly Elliptical 16 Hour Polar Orbit, HST with Low-Thrust Plane Change Acceleration Profile**

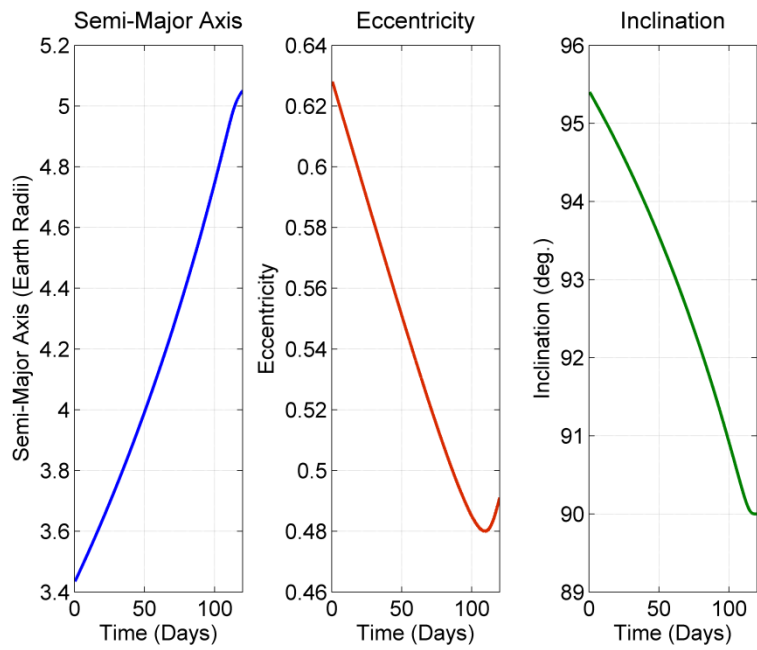


**Figure A-48 SSO – Highly Elliptical 16 Hour Polar Orbit, HST with Low-Thrust Plane Change Orbital Element Profiles**